UNIVERSITAT DE VALÈNCIA

Facultad de Física

Departamento de Física de la Tierra y Termodinámica

Study of the anisotropy of thermal infrared emissivity of inorganic bare soils at different moisture levels

TESIS DOCTORAL

VICENTE GARCÍA SANTOS

D. ENRIC VALOR i MICÓ, Profesor Titular de Física de la Tierra, en el departamento de Física de la Tierra y Termodinámica de la Facultad de Física, Universitat de València Y

D. VICENTE CASELLES MIRALLES, Catedrático de Física de la Tierra en el departamento de Física de la Tierra y Termodinámica de la Facultad de Física, Universitat de València,

CERTIFICAN: Que la presente memoria "*Study of the anisotropy of thermal infrared emissivity of inorganic bare soils at different moisture levels*", presentada por Vicente García Santos ha sido realizada bajo su dirección constituyendo su Tesis Doctoral para optar al grado de Doctor en Teledetección por la Universitat de València.

Y para que así conste, en cumplimiento de la legislación vigente, firman el presente certificado en Burjassot, a 7 de julio de 2013

Fdo.: Enric Valor i Micó Fdo.: Vicente Caselles Miralles

Este trabajo ha sido posible gracias a la financiación económica recibida por parte de:

El Proyecto EL USO DE LA TELEDETECCIÓN PARA MEJORAR LA OBSERVACIÓN DE LA ATMÓSFERA Y EL CLIMA (CLIMATEL) (CGL2007-64666/CLI), financiado por el Ministerio de Educación y Ciencia (MEC), así como de su acción complementaria CGL2007-29819-E/CLI.

El Proyecto EL CAMBIO CLIMATICO A TRAVES DE LA TELEDETECCION (CGL2010-17577), financiado por el Ministerio de Ciencia e Innovación (MICINN).

El Proyecto EL USO DE LA TELEDETECCIÓN PARA UNA MEJOR COMPRENSIÓN DEL CAMBIO CLIMÁTICO (PROMETEO/2009/086), financiado por el Generalitat Valenciana, Conselleria d'Educació i Ciència, en el marco del Programa Prometeo (I+D) para grupos de investigación de excelencia.

La ayuda para la Formación del Personal Investigador (FPI) de carácter predoctoral, englobada en el marco del Plan Nacional de Investigación Científica, Desarrollo e Innovación Tecnológica 2008-2011 por el Ministerio de Ciencia e Innovación (MICINN), con efectos económicos y administrativos del 1 de septiembre de 2008 al 31 de agosto de 2012.

Al contrato como Técnico Superior en Investigación por la Universitat de València, englobado en el proyecto EL CAMBIO CLIMATICO A TRAVES DE LA TELEDETECCION (CGL2010-17577), financiado por el Ministerio de Ciencia e Innovación (MICINN), con efectos económicos y administrativos del 1 de noviembre de 2012 al 31 de Octubre de 2013.

Llegado el final de este ciclo de mi vida, me gustaría plasmar en las siguientes líneas la especial gratitud que siento hacia todas aquellas personas que me han servido de apoyo e inspiración.

En primer lugar, al Profesor Vicente Caselles, Catedrático de Física de la Tierra y jefe del Grupo de Teledetección Térmica al que pertenezco. Agradecerle el haberme iniciado en la senda de la investigación científica, depositando en mí una confianza incondicional en cada paso que daba.

A mi director de Tesis, el Profesor Enric Valor i Micó, agradecerle haberme guiado durante toda mi reciente carrera investigadora de forma tan paternal, estando pendiente de mi evolución e iluminando con coherencia y sentido común todos aquellos puntos oscuros que aparecieron durante el camino.

Al Profesor César Coll, agradecerle ser capaz de mostrar la visión más crítica en mi trabajo mejorándolo sustancialmente y posteriormente ser un compañero más con el que compartir risas y bromas…*Espero que algún día reconozca que fui y seré su mejor pareja de pádel universitario*.

Al profesor José Antonio Martínez Lozano, director del departamento de Física de la Tierra y Termodinámica, agradecerle su disposición en todo momento a facilitar cualquier inconveniente.

Quiero hacer constar en las sucesivas líneas y de forma detallada la incondicional gratitud que siento hacia mi familia. Hacia mi hermano mayor Julio agradecerle el enorme cuidado y preocupación que ha tenido siempre por el resto de los hermanos menores. A mi hermano Gonzalo agradecerle su inquietud por mi presente y futuro, animándome a que emprenda nuevas aventuras en el futuro y disfrute de todo lo que haga. A mi hermano Ricardo, agradecerle el cuidado que ha tenido siempre de mí protegiéndome cual ángel de la guarda y compartiendo conmigo las inquietudes de la vida con el mejor sentido del humor. A mis padres agradecerles desde lo más profundo de mi corazón el esfuerzo realizado para que pudiéramos, tanto mis hermanos como yo, perseguir nuestros deseos e ilusiones animándonos a continuar más allá después de cada meta alcanzada. Agradecer especialmente a mi madre por haberme dotado con su fortaleza mental, su espíritu de lucha y el respeto al prójimo, cualidades que espero sigan acompañándome durante toda mi vida. Hacer extensible mi afecto también a todos los restantes miembros de la familia.

Al Dr. Juan Manuel Sánchez Tomás, agradecerle su empeño y ánimo en los trabajos de colaboración mutua, así como su visión siempre optimista de la vida, espero poder seguir colaborando contigo muchos años más, y por supuesto mantener tu amistad.

A la Dra. Raquel Niclòs, agradecerle su plena confianza en mi trabajo, así como sus siempre ventajosos consejos. También espero alargar tantos años como sea posible nuestra colaboración laboral.

To Dr. Andy French, thanks for your warm-hearted welcome during my short-stay in 2011 and 2012 at the Arid Land Agricultural Center (Arizona, USA). And thanks also for give me the chance to collaborate in the HyspIRI mission, ambitious NASA Project. I want also thank my ALARC working colleagues, Elizabete, Greg and Nick.

Agradecer a mis compañeros de despacho: Carol, Edu, Celia y la nueva llegada Xusa, llenar de alegría y compañerismo el día a día, compartiendo vivencias tanto en el despacho como a la hora de comer. Querría expresar un agradecimiento especial a Carol, agradecerle la amistad que hemos ido forjando día a día, así como su constante apoyo y extrema generosidad, compartiendo aventuras y desventuras conmigo durante casi 6 años.

También me gustaría recordar a otros compañeros de despacho ya no tan asiduos. Joan Miquel Galve, la Dra. Maria Mira y la Dra. Mar Bisquert, agradecerles su afecto y amistad que espero sea duradera pese al tiempo y la distancia.

A mis dos mejores amigos, Alberto y Pere, por estar presentes en mi vida desde hace casi dos décadas (y espero que sean muchas más) y que con el tiempo me han llegado a considerar un hermano más. Y por supuesto a sus padres, Pedro y Mariló, cuyo trato hacia mí no lo diferencio respecto al de sus hijos.

Agradecer a María y su familia el trato afectivo y cariñoso que me dispensaron durante una parte importante del período de doctorado…*no creo en puntos finales, sino en seguidos*.

Agradecer con todas mis fuerzas a mis compañeros de batalla: Alex Buil y Felipe Beltrán, cuyas circunstancias de la vida les hicieron partir a lugares suficientemente remotos como para dejarme un importante vacío fraternal. Espero que mantengamos durante toda una vida la amistad que forjamos en los pocos años que compartimos en Valencia. Felipe haz extensible mi afecto a Bruna y a la pequeña Manu.

A Quique Villaescusa, Amparo Sebastià y Vicente Marín. Agradecerles haberme hecho empezar el día con el mejor humor posible las múltiples veces que los he encontrado en cafetería, así como solventar cualquier consulta administrativa que surgiera. Sin duda todo ello no está pagado con un…*arnadí*.

En general deseo agradecer los momentos de diversión vividos con compañeros de departamento, presentes o pasados: Álvaro, Emilio, Ana, Sara, Jose Luis, Guillem, Rosa, Carlos, Víctor Estellés, Jorge, Almu, Cecilia, Aurelio, Níobe, María, Facundo, Jorgiana, Amparo, Oreto, Gema, Paula, Roberto, Maura (haciéndolo extensible a su marido Jesús)… *y todos aquellos que no recuerde mi memoria ahora*.

Querría agradecerte a ti, mi *musa anónima*, haber llenado de afecto y cariño los momentos buenos y malos de mi vida, contigo he llegado a sentir una felicidad plena.

En general me gustaría decir GRACIAS a todos los que leáis estos agradecimientos y me conozcáis, sin duda el espacio y la memoria han hecho que me olvide de ti…*pero mi corazón no*.

Index

RESUMEN

I. Introducción

La técnica responsable de obtener información de un objeto lejano sin contacto físico con éste, se llama Teledetección. Esta técnica ha demostrado ser una alternativa muy ventajosa frente a otros métodos cuya adquisición de datos es más lenta y costosa. La Teledetección usa sensores a bordo de satélites, para medir la radiación emitida por las superficies terrestres en diferentes partes del espectro electromagnético, con la intención de entender mejor los procesos físicos ocurridos en tierra, océanos o atmósfera. El intercambio de energía superficie-atmosfera, estimaciones de la evapotranspiración, monitorización del efecto invernadero o estudios de desertificación y degradación del suelo, son algunas de las aplicaciones más importantes en Teledetección y todas ellas tienen un factor común, el conocimiento previo de la temperatura.

La medida precisa de la temperatura superficial es uno de los campos de estudio más interesantes en Teledetección. Las superficies terrestres emiten su radiación máxima, siguiendo la Ley de Planck, en el intervalo espectral llamado Infrarrojo Térmico, el cual comprende el rango de longitudes de onda desde 3 hasta 20 μm. Es por eso que los sensores satelitales encargados de medir la temperatura trabajan en este intervalo espectral. No obstante obtener un valor preciso de la temperatura, requiere un conocimiento previo de la contribución radiativa atmosférica y de la emisividad de la superficie.

Un preciso conocimiento de la emisividad es fundamental a la hora de obtener la temperatura de una superficie, especialmente en la llamada ventana atmosférica situada entre los 8-14 μm. En este intervalo espectral la contribución atmosférica es débil, permitiendo el paso de la radiación superficial de forma casi transparente. Por tanto el efecto de la emisividad es mucho más importante en la medida de la temperatura realizada por aquellos sensores que operen en dicha ventana. El conocimiento preciso de la emisividad superficial no es sencillo, este parámetro varía en su magnitud con la longitud de onda o con el tipo de composición del suelo, pero también han aparecido estudios que demostraron que la emisividad variaba con la humedad del suelo o con la geometría de observación de la superficie. La presente Tesis centra su meta en el estudio de la anisotropía de la emisividad térmica de suelos inorgánicos no vegetados bajo diferentes niveles de humedad. Los objetivos estipulados para llevar a cabo dicho estudio fueron:

1. Coleccionar un conjunto de muestras de suelos inorgánicos sin vegetación, lo suficientemente representativo de los diferentes tipos de texturas presentes en la Tierra, con la finalidad de realizar un estudio de la anisotropía de la emisividad térmica profuso.

2. Dado que dicho estudio está basado en medidas de campo, analizar qué efectos tiene en la precisión de la emisividad obtenida la contribución radiativa de atmósfera y elementos circundantes, evaluando cual es el mejor método de obtención in situ de dicha contribución radiativa envolvente.

3. Una vez estipulada la metodología para llevar a cabo la obtención de la emisividad, analizar como varía, tanto acimutal como cenitalmente, en condiciones de secado completo. Posteriormente estudiar la evolución de dicha anisotropía, a medida que aumenta el nivel de humedad en el suelo.

4. Estudiar la incertidumbre producida al obtener la temperatura de una superficie mediante un algoritmo dependiente de la emisividad, cuando se ignoran efectos angulares y de humedad en la emisividad de los suelos inorgánicos no vegetados. También se estudia el error obtenido en el flujo de onda larga, parámetro importante en la obtención del intercambio de energía entre superficie y atmósfera.

5. Finalmente se intentará obtener una expresión matemática que ayude a predecir el valor de la emisividad de un suelo desnudo, previo conocimiento de la humedad y la geometría de observación.

II. Metodología

Un total de 13 muestras componen el conjunto de suelos inorgánicos no vegetados seleccionados para llevar a cabo el estudio de la anisotropía de la emisividad térmica. Estos suelos representan desde un punto de vista textural, al 75% de los suelos minerales del mundo, fueron extraídos de los primeros 15 cm de la superficie (el llamado horizonte A), y en función de su densidad aparente, fue necesario obtener hasta 17 kg. La procedencia de cada uno de estos suelos fue muy diversa, cinco de ellos proceden de España, otros cinco de Estados Unidos y los tres restantes de Brasil. Los resultados del análisis edafológico mostraron que las muestras utilizadas en este estudio abarcaban intervalos de composición textural arenosa entre el 14% y el 100% y limosa y arcillosa entre el 0%-54%, los 13 suelos se clasifican en 9 de las 12 texturas definidas por el triangulo de textura del *United States Department of Agriculture*. Desde el punto de vista mineralógico las muestras de suelos desnudos utilizadas abarcan un intervalo de cuarzo entre el 0% y el 100%. Y son consideradas inorgánicas dado que su materia orgánica nunca supera el 9%.

El presente estudio intenta analizar la anisotropía de la emisividad térmica en condiciones de campo, por tanto la medida sobre las muestras se realizan a una distancia suficientemente pequeña para verse fuertemente afectadas por el tamaño de la partícula del suelo. Así pues nuestros suelos fueron tamizados a un tamaño de partícula no superior a 0.5 cm, puesto que según el estudio Lagouarde *et al.* (1995), la variación angular de la temperatura de brillo de un suelo cuyo tamaño de la partícula supere 4-5 cm, puede verse afectada por efectos de sombreado del sol. En cambio en el mismo estudio se observó que para un suelo tamizado a tamaños de partícula inferiores a dichos valores, el efecto de la variación angular de la temperatura de brillo solo era posible si se tenían en cuenta anisotropías en la emisividad del suelo.

Una vez completamente secas, las muestras fueron puestas en un recipiente circular de 52 cm de diámetro y 10 cm de altura. Aquí fueron saturadas mediante inundación por un periodo de 24 horas, una vez pasado este tiempo el proceso de secado se realizó de forma natural, tomándose medidas de emisividad sobre la muestra (como se verá posteriormente) a diferentes niveles de humedad, desde la saturación hasta el completo secado. Durante el proceso de secado algunas muestras arcillosas y limosas, presentaron grietas, las cuales fueron selladas siempre que las condiciones de humedad del suelo lo permitieron, en caso contrario no se tomaron medidas de emisividad para evitar posibles efectos de cavidad.

La medida de la humedad en las muestras se realizó mediante un sensor TDR, modelo Delta-T SM200. Este sensor permite obtener una medida de la humedad del suelo con una precisión de ±0.03 $m^3 \cdot m^{-3}$, precisión ratificada mediante una calibración hecha por nosotros en laboratorio. Las medidas de humedad se realizaron pinchando a diferentes puntos de la superficie del suelo antes y después de la medida de la emisividad de la superficie. Además, el proceso de saturación y secado de las muestras se realizó varias veces para obtener una reproducibilidad de los resultados, aparte de obtener nuevos puntos intermedios de humedad.

Centrándonos ahora en la obtención de la emisividad, su medida directa es de extrema dificultad puesto que se necesita conocer la temperatura de la superficie en los primeros micrómetros del suelo. Hoy en día es muy difícil medir dicha temperatura con los termómetros de contacto existentes, por tanto se pensó en una medida alternativa de la emisividad basada en la obtención de su valor relativo entre su valor nadir y una configuración angular dada. Es decir el cociente entre ambas emisividades, que desde el punto de vista radiativo se traduce en la medida simultánea de la radiancia emitida por una superficie en una configuración de ángulos cenital y acimutal, la radiancia de la dicha superficie pero a nadir (ángulo cenital y acimutal iguales a cero) y la medida hemisférica de la radiancia envolvente a la muestra de suelo. Una vez obtenido el valor relativo de la emisividad a una configuración dada obtener su valor absoluto es simple, tan solo hay que multiplicar dicho valor relativo por el valor absoluto a nadir. Este valor absoluto a nadir se puede obtener fácilmente con los métodos actuales conocidos, como el de la caja (Rubio *et al.* 1997; Mira *et al.* 2007) o el TES (*Temperature and Emissivity Separation* method, Mira *et al.* 2009).

La medida relativa de la emisividad se llevó a cabo con la ayuda de dos radiómetros térmicos multiespectrales modelo CIMEL Electronique CE 312-2B. Dichos radiómetros demostraron ser capaces de medir la temperatura de una superficie con una precisión de ±0.19 °C. Ambos radiómetros se dispusieron en los brazos de un goniómetro, de forma que eran capaces de medir la radiancia procedente de una superficie a dos configuraciones angulares distintas, aunque una de ellas siempre fue la del nadir. La medida de la radiancia hemisférica descendente estuvo subyugada a estas dos medidas de superficie, tomándose cada 18 minutos. Este intervalo de tiempo supuso fluctuaciones en dicha radiancia hemisférica del 4%, lo cual suponía cometer un error poco significativo sobre la emisividad relativa (±0.0005).

Las medidas de radiancia angulares se realizaron para ángulos cenitales desde 10° hasta 70°, en intervalos de 10°. Y para ángulos acimutales de 0°, 120° y 240°, girando para ello la muestra 120° cada vez. Se giró la muestra, y no el conjunto goniómetro-radiómetros, con la finalidad de medir más rápidamente y a su vez mantener el mismo pasaje envolvente (incidencia solar y elementos circundantes) a distintos ángulos cenitales. De este modo cualquier variación en la emisividad relativa a distintos acimuts, puede ser atribuida exclusivamente a la muestra.

Como se comentó anteriormente, la medida de la radiancia envolvente a la muestra, estuvo subyugada, tomándose cada 18 minutos, a las medidas angulares sobre el suelo. También se comentó que dicho retardo en su medida no supuso errores importantes en el valor final de emisividad relativa. No obstante, dado que dicho parámetro aparece tanto en el numerador como en el denominador de la expresión de la emisividad relativa, se consideró oportuno realizar una comparación de los métodos conocidos, para obtener in situ dicha radiancia. Los métodos de medida in situ a comparar fueron cuatro. Dos de ellos se basaron en medidas directas a la atmósfera a 53° respecto la vertical (aproximación de Kondratyev; Kondratyev, 1969) y midiendo hacia la vertical, multiplicando posteriormente dicha medida por un factor dependiente tanto del intervalo espectral de medida como del vapor de agua atmosférico (aproximación de Rubio, Rubio et al. 1997). Otro método consistió en procesar un perfil atmosférico de la zona mediante un modelo de transferencia radiativa con la finalidad de obtener un valor simulado de la radiancia hemisférica descendente. El último método a comparar supuso utilizar una panel de reflectividad difusa, capaz de medir directamente la contribución de los elementos circundantes a éste (atmósfera, edificios, arboles, etc.) dada la alta reflectividad en el infrarrojo térmico de su superficie dorada.

Los cuatro métodos expuestos anteriormente fueron comparados bajo tres situaciones de entorno bien distintas: la primera fue en un lugar elevado sin casi presencia de elementos circundantes y para un día completamente despejado, el segundo entrono fue para el mismo día despejado pero en un lugar donde la presencia de elementos circundantes era notable y el tercer y último entorno fue para el mismo lugar del primer entorno, pero bajo un cielo cuya cobertura nubosa era muy variable. Los resultados de la comparación mostraron que para un lugar con mínima contribución envolvente y un cielo completamente despejado, los cuatro métodos son perfectamente válidos con diferencia relativas entre ellas no superiores al 2%, lo cual no supone errores importantes a la hora de obtener la emisividad relativa de un suelo desnudo. No obstante, cuando la presencia de elementos circundantes es notable o cuando la cobertura nubosa es importante, el uso de un panel de reflectividad difusa ofrece valores relativos de la radiancia hemisférica, hasta un 72% superior al resto de métodos. No tener en cuenta este incremento de la radiancia hemisférica supone sobreestimar la emisividad relativa hasta 0.09. Por tanto el uso de un panel de reflectividad difusa se hizo indispensable, pese a que se midió en una zona con mínima contribución atmosférica y en la medida de lo posible se evitaron cielos con presencia de nubes.

III. Resultados

Antes de presentar los resultados, cabe destacar que la metodología empleada para llevar a cabo la medida de la emisividad relativa, permitió obtener valores de dicho parámetro con un error promedio de ±0.003 en un 56% de los casos, independientemente del canal espectral, nivel de humedad, tipo de suelo o ángulo de observación. El error alcanzó un valor de ±0.01 en el 97% de los casos. Por tanto se decidió que sólo cambios de la emisividad superiores a 0.01 serían considerados como significativos, tanto con el ángulo de observación como con el nivel de humedad.

En primer lugar se analizó la variación de la emisividad relativa con el ángulo acimutal, para ello se calculó la diferencia máxima entre las emisividades a distintos acimuts, para un ángulo cenital dado. Los resultados mostraron que el 85% de los valores de estas diferencias no superaban el 0.01, error máximo estipulado para considerar variaciones en la emisividad relativa calculada. Por tanto es factible concluir que los suelos no vegetados pueden ser considerados acimutalmente isótropos.

El estudio de la anisotropía cenital de la emisividad relativa en suelos inorgánicos completamente secos, mostró como resultado general que dicha emisividad decrece con el aumento del ángulo cenital, siendo significativo para todo tipo de suelo inorgánico a partir de los 60°, independientemente del intervalo espectral térmico en que fuera medido. El descenso de la emisividad con el ángulo cenital fue modelizado por McAtee et al. (2003) basándose en la teoría de dispersión de Mie. No obstante este modelo requiere un conocimiento previo del radio medio de la partícula, siendo actualmente imposible obtener esta información mediante medidas satelitales. Por tanto el presente estudio basó sus resultados y conclusiones en datos cuantitativos del suelo capaces de ser obtenidos mediante medidas hechas por satélite, como pueden ser los porcentajes de componentes texturales y minerales (Singh and Kathpalia, 2007; Ninomiya and Fu, 2001; Wu *et al.* 2009) o de humedad del suelo (Misión SMOS, Kerr et al. 2001).

Como se comentó anteriormente, el tipo de composición del suelo o el intervalo de espectral de medida de la emisividad, es un factor importante al evaluar la magnitud de decrecimiento de la emisividad con el ángulo cenital. Así pues los suelos arenosos con alto contenido en cuarzo o yeso, son los que presentan un mayor descenso de la emisividad con el ángulo, pero este descenso viene marcado por intervalo espectral de medida. En toda la ventana atmosférica el descenso de la emisividad de suelos arenosos es significativo a partir de 40°, llegando a un valor un 5% más bajos que a su valor nadir. Sin embargo, a intervalos espectrales más discretos, el descenso de la emisividad de estos suelos desnudos es dispar. Así por ejemplo la emisividad entre 10-12 μm, es significativa a partir de los 50°, llegando a descensos un 4% inferior al nadir pero entre 8-9.4 μm este descenso es significativo a partir de 30°, llegando a valores un 14% más bajos que los registrados a nadir. La explicación de los descensos tan significativos entre 8-9.4 μm se encuentra en el cuarzo, este mineral presenta unas bandas de reflexión llamadas *reststrahlen*, que hacen descender la emisividad del suelo de forma brusca. Para el caso de suelos francos, limosos o arcillosos, el descenso de de la emisividad con el ángulo cenital es menos pronunciado que en el caso de los arenosos, especialmente para el casos de suelos con alto contenido en arcilla.

En resumen, cuando un suelo mineral completamente seco presenta un alto porcentaje de arcilla en su composición textural, su emisividad se vuelve más isótropa con el aumento cenital. Por el contrario a medida que el porcentaje de arena aumenta, esta emisividad decrece más pronunciadamente con el ángulo, siendo muy significativa a partir de valores angulares cenitales bajos, especialmente si entre los minerales del suelo arenoso hay grandes concentraciones de cuarzo o yeso.

Sobre el efecto que tiene la humedad del suelo en la anisotropía de la emisividad relativa, los resultados mostraron conclusiones dispares en función del intervalo espectral de medida y del tipo de composición del suelo.

Así pues en el caso de suelos arenosos, cuando la humedad aumenta, la anisotropía de su emisividad relativa se ve fuertemente influenciada por el intervalo espectral donde ha sido medida. En toda la ventana atmosférica, 8-14 μm y entre 10-12 μm, el efecto de la humedad no es apreciable en el descenso de la emisividad relativa con el ángulo cenital, no obstante en el intervalo 8-9.4 μm, el descenso cenital de la emisividad relativa se ve amortiguado a medida que aumenta el contenido en agua, reduciéndose hasta un 7% respecto a valores en seco y siendo significativa dicha reducción a partir de los 40°.

En el caso de suelos de textura franca, los resultados son opuestos al caso de suelos arenosos, la anisotropía cenital de la emisividad se ve acentuada a medida que aumenta el contenido en agua del suelo, siendo significativa, respecto a sus valores en seco, a partir de los 50° y con descensos de hasta un 3% inferiores a los obtenidos en condiciones de deshidratación del suelo.

Por último el caso de suelos arcillosos es singular, ni el ángulo cenital ni el aumento de la humedad parece afectar el comportamiento casi isotrópico que presenta su emisividad. Solo a partir de 60° y cuando están completamente secos, la emisividad relativa presente descensos significativos respecto a su valor nadir.

En resumen, la presencia de agua retenida tanto en los microporos y macroporos de los suelos minerales estudiados, tiende a homogeneizar el comportamiento de la anisotropía de la emisividad relativa en primera aproximación. Esto se observa al mitigar el decrecimiento de la emisividad relativa en suelos arenosos con alta cantidad de cuarzo en el intervalo espectral 8-9.4 μm o en el acentuado decrecimiento de dicha emisividad respecto a valores en seco, para el caso de suelos francos. No obstante, la casi isotropía en la emisividad de los suelos arcillosos, hace pensar que la relación entre dicho parámetro y el ángulo cenital de medida así como la humedad, no es puramente lineal.

Una vez conocidos los efectos angulares y de humedad sobre las emisividades de los suelos sin vegetación, se profundizó en el impacto de dicha anisotropía en la obtención de otros parámetros, dependientes de la emisividad. En primer término se estudió la imprecisión cometida sobre la medida de la temperatura de la superficie terrestre si no se tenían en cuenta las variaciones de la emisividad del suelo debido a un ángulo cenital y un valor de humedad dados. Para ello se utilizó un algoritmo *split-window* dependiente de la emisividad del suelo (Galve *et al.* 2008), el cual utilizaba las emisividades y temperaturas de brillo del los canales 31 y 32 (10-12 μm) del sensor MODIS a bordo de los satélites TERRA y AQUA. Se estudió la diferencia en temperatura cuando el pixel era medido a nadir o cuando se medía a un ángulo cenital de 65°, ángulo máximo alcanzado por el sensor MODIS. Los errores en la obtención de la temperatura de la superficie si no se tenía en cuenta la anisotropía cenital de la emisividad del pixel, variaba entre ±0.4 K y ±1.8 K, dependiendo del tipo de muestra, para atmósferas con un contenido en vapor de agua menor a 4 cm. Además cuanto más seca era la atmósfera más grande era el error cometido en temperatura.

Otro parámetro afectado por la variación cenital de la emisividad es el flujo de onda larga, parámetro indispensable al estudiar el intercambio de energía entre superficie y atmósfera, energía que entre otras funciones puede llevar a ahorrar un consumo innecesario de agua en el riego de cultivos. Los resultados mostraron que el error relativo cometido en el flujo de onda larga, al no considerar la variación angular de la emisividad, variaba entre el 2% y el 8%, dependiendo del tipo de suelo.

Finalmente con los resultados obtenidos, en el estudio del efecto de la humedad del suelo sobre la anisotropía de la emisividad relativa, se llevó a cabo una parametrización, resultando en que la expresión que mejor encaja fue un polinomio de segundo grado. No obstante, la idea era obtener una expresión global, aplicable a cualquier tipo de suelo inorgánico, por eso se realizó un análisis estadístico que relacionaba los coeficiente del polinomio con los datos texturales y minerales de los suelos estudiados. El resultado del análisis determinó que los coeficientes de dicho polinomio se relacionaban, nuevamente mediante un polinomio de grado dos, con los porcentajes de arcilla y cuarzo en el intervalo espectral 8-9.4 μm. En el intervalo 10-12 μm estos coeficientes se relacionaban con los porcentajes de arcilla y materia orgánica. Finalmente en toda la ventana atmosférica, 8-14 μm, los coeficientes del polinomio se relacionaban, parte de ellos con la arcilla y el cuarzo y el resto con la arcilla y la materia orgánica. El error máximo asociado a esta expresión fue el determinado en el análisis de la sensibilidad del método de obtención de la emisividad relativa, ± 0.01.

IV. Conclusiones

Las principales conclusiones extraídas del estudio que conforma la presente Tesis Doctoral son:

1. Los suelos inorgánicos no vegetados empleados en el presente estudio son representativos de un gran número de suelos presentes en la Tierra, desde el punto de vista textural y mineral. Por tanto los resultados obtenidos en el estudio del efecto de la humedad del suelo

sobre la anisotropía de la emisividad térmica de éstos, puede ser aplicada a un buen número de superficies.

2. La metodología diseñada en este estudio para obtener los valores relativos de la emisividad térmica de los suelos inorgánicos sin vegetación, permitió obtener valores con un error máximo de ± 0.01.

3. La contribución radiativa de la atmósfera y posibles elementos envolventes a la muestra de suelo fue analizada mediante la comparación de cuatro métodos diferentes para obtenerla in situ. Los métodos fueron comparados bajo diferentes condiciones de entorno y las conclusiones más relevantes fueron:

    - En el caso de cielos completamente despejados y en un lugar con una presencia mínima de elementos envolventes, los cuatro métodos producen resultados similares, con diferencias relativas no superiores al 2%. No obstante, cuando la presencia de elementos circundantes es notable o la presencia de nubes en el cielo es elevada, el uso de un panel de reflectividad difusa es la opción más recomendable, puesto que tiene en cuenta dicha contribución evitando cometer infravaloraciones de la contribución radiativa envolvente de hasta un 72%.

    - Al evaluar el efecto de dicha infravaloración en la radiancia hemisférica descendente, sobre la precisión de la emisividad relativa de los suelos, se observaron sobreestimaciones de hasta 0.09 en sus valores. Por tanto, el uso de un panel de reflectividad difusa pasó de ser una opción, a una necesidad indispensable en el presente estudio.

4. Respeto a los conclusiones sobre la anisotropía de le emisividad térmica de los suelos inorgánicos estudiados, las más importantes fueron:

    - La emisividad de dichos suelos puede ser considerada casi invariante acimutalmente, pero no respecto al ángulo cenital, puesto que a partir de 60° el decrecimiento de su emisividad es significativo, independientemente del intervalo espectral de medida o la composición del suelo.

    - No obstante, la magnitud del decrecimiento cenital de la emisividad, está fuertemente influenciado por la composición y el intervalo espectral de medida. La emisividad térmica de suelos presenta un comportamiento cada vez más isótropo frente al aumento cenital a medida que aumenta el contenido en arcilla. Todo lo contrario ocurre para suelos con alto contenido en arena, especialmente en aquellos con alto contenido en cuarzo entre sus minerales, su emisividad decrece más pronunciadamente con el aumento del ángulo cenital, llegando descensos relativos del 14% respecto a su valores a nadir y siendo significativa a partir de ángulos de 30°, como es el caso de la emisividad entre 8-9.4 μm.

    - El efecto de la humedad sobre la anisotropía de la emisividad térmica, también muestra una fuerte dependencia con el tipo de suelo y el intervalo espectral de la medida. Así pues el efecto del incremento del contenido en agua en suelos, provoca que la emisividad decrezca menos pronunciadamente con el ángulo cenital para el caso de suelos arenosos (en el intervalo 8-9.4 μm), pero más pronunciadamente en el caso de suelos francos (en toda la ventana atmosférica). Los suelos arcillosos sin embargo no muestran variación de su emisividad muy significativas, ni con el ángulo de observación ni con la humedad.

5. También se ha demostrado que ignorar efectos angulares en la emisividad puede acarrear errores sistemáticos en la determinación de la temperatura terrestre entre ±0.4 K y ±1.8K, dependiendo del tipo de suelo y para atmósferas con contenido de vapor de aguar inferior a 4cm. También se mostraron errores relativos entre el 2% y 8% para el flujo de onda larga, lo cual puede llevar a estimaciones erróneas de los balances de energía de la superficie.

Por último, comentar que a partir de los resultados del estudio se consiguió obtener una expresión capaz de predecir la emisividad relativa de un suelo desnudo si previamente se conocían tanto el ángulo cenital de observación y la humedad del suelo. Adicionalmente esta expresión puede ser aplicada globalmente a un gran número de suelos, en distintas partes del intervalo espectral térmico 8-14 μm, si previamente se conocen los porcentajes de cuarzo, materia orgánica y arcilla

Chapter 1

Introduction

This first chapter introduces the reader to the emissivity concept, showing how important is this parameter in the thermal infrared spectral region. *State of the art* about emissivity dependence of inorganic bare soils on soil moisture and viewing geometry is exposed, and main objectives pursued detailed at the end of the chapter.

1.1 The Importance of the TIR emissivity in Remote Sensing

The technique responsible for retrieving information from a far object without physical contact is called *Remote Sensing*, it has demonstrated to be an advantageous alternative in place of slow and costly data acquisitions at surface level. This technique uses sensors onboard satellites, to take measurements of the radiation at different ranges of the electromagnetic spectrum, with the aim of better understanding all the processes that happen at terrestrial surfaces, oceans or the atmosphere. Remote Sensing techniques are useful for a wide variety of disciplines such as Biology, Geography, or Physics to give some examples.

Data retrievals for surface-atmosphere energy budget calculations, evapotranspiration estimates, greenhouse effect monitoring, or studies of desertification and soil degradation, are some of the most important applications of Remote Sensing. All of them have a common factor, the land surface temperature (LST) estimates from a satellite, which is one of the most challenging research fields of remote sensing. Temperatures from the Earth surface can be retrieved from measurements at the spectral range called Thermal Infrared (TIR) that covers the spectrum from 3 to 20 μm.

Retrieving an accurate value of LST needs a previous precise knowledge of surface emissivity, especially in the so called atmospheric window, allocated between 7 and 14 μm within the TIR region. Atmospheric emission from this spectral region is weak, therefore highly transparent to the emitted radiation from the surface to the satellite.

Emissivity is the relative ability of a body to emit and absorb energy by radiation. It is the ratio of the energy radiated by a particular body at a given temperature, to the energy radiated by a blackbody at the same temperature. The knowledge of the surface emissivity, in addition to be useful to retrieve accurate values of LST, may be very helpful to develop geological and land use maps using the spectral signatures in the TIR region (Rowan and Mars, 2002; Vaughan *et al.* 2005; Ogawa *et al.* 2008).

Emissivity varies with wavelength but it is also dependent on the type of soil (Salisbury and D’Aria, 1992; Nanni and Demattê, 2006). Soil composition can be considered a relatively static factor over time. However, there are other factors more variable that can have influence on the TIR surface emissivity, some of these factors are the soil moisture (SM) and the viewing geometry. There are several studies focused on the variation of TIR emissivity with SM, as well as with the viewing geometry, which analyze these effects separately. However, there is not a study analyzing both effects jointly.

1.2 Effect of soil moisture on TIR emissivity

Few studies can be found about the variation of TIR emissivity with SM. The first one (Van Bauel and Hillel, 1976) showed a clear increase of emissivity with SM. Afterwards, Chen *et al.* (1989) agreed with the previous conclusion for a silty-clay soil, but they observed differences for the increase of emissivity if soil was just tilled, or if it was tilled and compacted. Salisbury and D'Aria (1992) observed that emissivity between 8 and 9 μm increases around 5% for an increase of 7% for soil water content.

The increase of TIR emissivity with SM was also observed from sensors onboard satellites. Ogawa *et al.* (2006), studying desert soils placed at North of Africa and Arabic Peninsula, found a relation between the emissivity product from Moderate Resolution Imaging Spectroradiometer (MODIS) band 29 (8-9 μm) and SM product retrieved from Advanced Microwave Scanning Radiometer-Earth Observing System (AMSR-E) onboard Aqua. Mira *et al.* (2011) applied Temperature and Emissivity Separation (TES) method (Gillespie *et al.* 1998) to five thermal spectral bands of Advanced Spaceborne Thermal Emission and Reflection (ASTER) at two different places over White Sands National Monument in New Mexico (USA). They observed an increase around 4%-5% in emissivity product of ASTER band 11 (centered at 8.6 μm) for two scenes where monthly precipitation varied from 0.5 mm (November, 2006) to 7.1 mm (December, 2006).

At all works previously mentioned the variation of TIR emissivity with SM it has been studied for just one type of textural soil and most of them sandy textures. This is the reason why Mira *et al.* (2007 and 2010) carried out a deeper study about the variation of TIR emissivity with SM for 14 samples of inorganic bare soils (IBS), covering nine of the twelve textural types defined by the United States Department of Agriculture (USDA). Both studies retrieved the TIR emissivity by means of the Box method (Rubio *et al.* 1997), for different SM levels at four spectral ranges inside the 8-14 µm atmospheric window using a CE 312-1 radiometer (Legrand *et al.* 2000) with the following bands: channel 1 (8-13.3 µm), channel 2 (11.5-12.4 µm), channel 3 (10.2-11.3 µm) and channel 4 (8.3-9.3 µm). Figure 1.1 shows the results of TIR emissivity variation with soil water content at CE312-1 spectral channels 1 and 4 for all IBS analyzed by Mira *et al.* (2007) and (2010). They show that at all the IBS samples TIR emissivity increases with SM at all spectral ranges. With these data and from statistical analysis, Mira *et al.* (2010) established a relationship between TIR emissivity (at all four CE 312-1 channels) and SM for any IBS, by means of the expression:

$$\varepsilon_i = a_i + b_i SM + c_i \ln(SM) + d_i OM + e_i OM^2 + f_i Q + g_i C \quad (1.1)$$

where a_i-g_i are regression coefficients for each spectral channel i (CE 312-1, 1 to 4), OM, Q and C are the organic matter, quartz and carbonate contents respectively, expressed as a percentage. Expression (1.1) allows for the retrieval of TIR emissivity from an IBS if the SM values and some textural and mineralogical parameter of the soil are previously known. Uncertainties associated with this equation vary between ±0.006 and ±0.019 according to spectral range.

1.3 Anisotropy of TIR emissivity

There are also few works related with the angular variation of TIR emissivity for IBS. Barton and Takashima (1986) used a broadband radiometer to measure the radiation of a sandy IBS between 30° and 70°. Results showed an emissivity decrease with the increase of zenith angle (θ) of around 3% from values close to nadir.

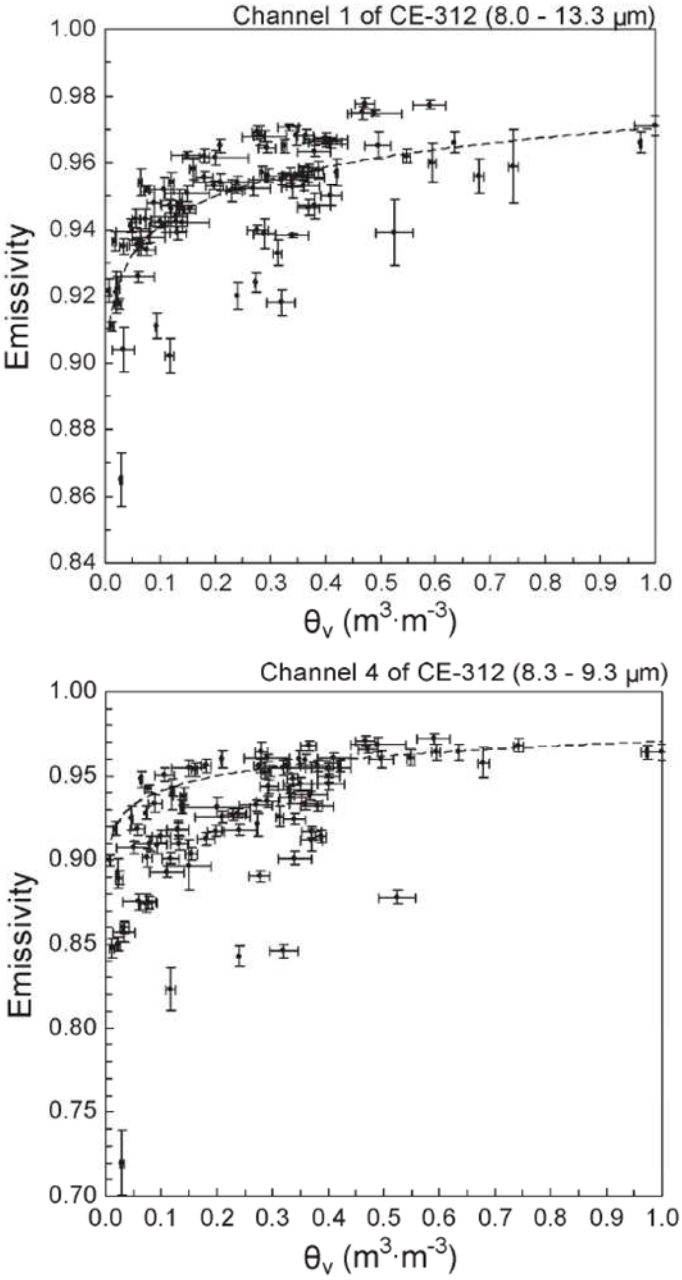

Figure 1.1 Results of TIR emissivity variation with soil water content at spectral ranges 8-13.3 μm and 8.3-9.3 μm (CE312-1 channels 1and 4, respectively), extracted from Figure 2 in Mira *et al.* (2010).

A thoroughly study about the anisotropy of TIR emissivity can be found in Labed and Stoll (1991), the authors analyzed the emissivity at all TIR spectral range for five IBS with different textures: sand (SiO_2), silt (Loess), silt-loam (Lehm), clay-loam (RB) and loam (AN). Figure 1.2 (show Figures 3, 4(a) and 6(a) from Labed and Stoll (1991)). The main result is that relative emissivity (ratio of emissivity at a specific θ and at nadir) decreases with θ over the whole TIR range, independently of the type of IBS; nevertheless, the magnitude of the emissivity decrease depends on the spectral range. For instance, Figure 1.2 (a) shows that the decrease of emissivity for the sandy IBS is more pronounced between 8-9 μm than at the rest of TIR wavelengths, nevertheless for a clay-loam IBS (Figure 1.2 b) there is no spectral effect on anisotropy of TIR emissivity (according to authors, this result can be extended to the rest of samples). From Labed and Stoll (1991) it is also concluded that the decrease of emissivity with θ is dependent on the type of IBS at a specific spectral range, for instance Figure 1.2 (c) shows that the emissivity, at spectral range 10-12 μm, decreases more or less pronounced depending on texture of the IBS.

It is worth to mention the works carried out by Sobrino and Cuenca (1999) and Cuenca and Sobrino (2004). In the first one, the authors analyzed the zenithal anisotropy of emissivity for three IBS (sandy, clayey and silty textures) with a broadband radiometer. Results showed that the relative emissivity of sandy soil decreases as much as 2% at θ=60° from nadir, and the other two IBS decreased around 1%. Cuenca and Sobrino (2004) extended the results of the previous study to narrower spectral ranges placed inside the 8-14 μm atmospheric window. The most relevant result from this second study is that sand emissivity decreases around 5% at θ=60° from nadir, at spectral range 8-9 μm.

There is not a deep enough study about the anisotropy of TIR emissivity of IBS, and it is not possible to find a work relating this anisotropy with the SM effect on emissivity. For this reason the present Thesis studied the emissivity dependence on viewing geometry and soil water content together.

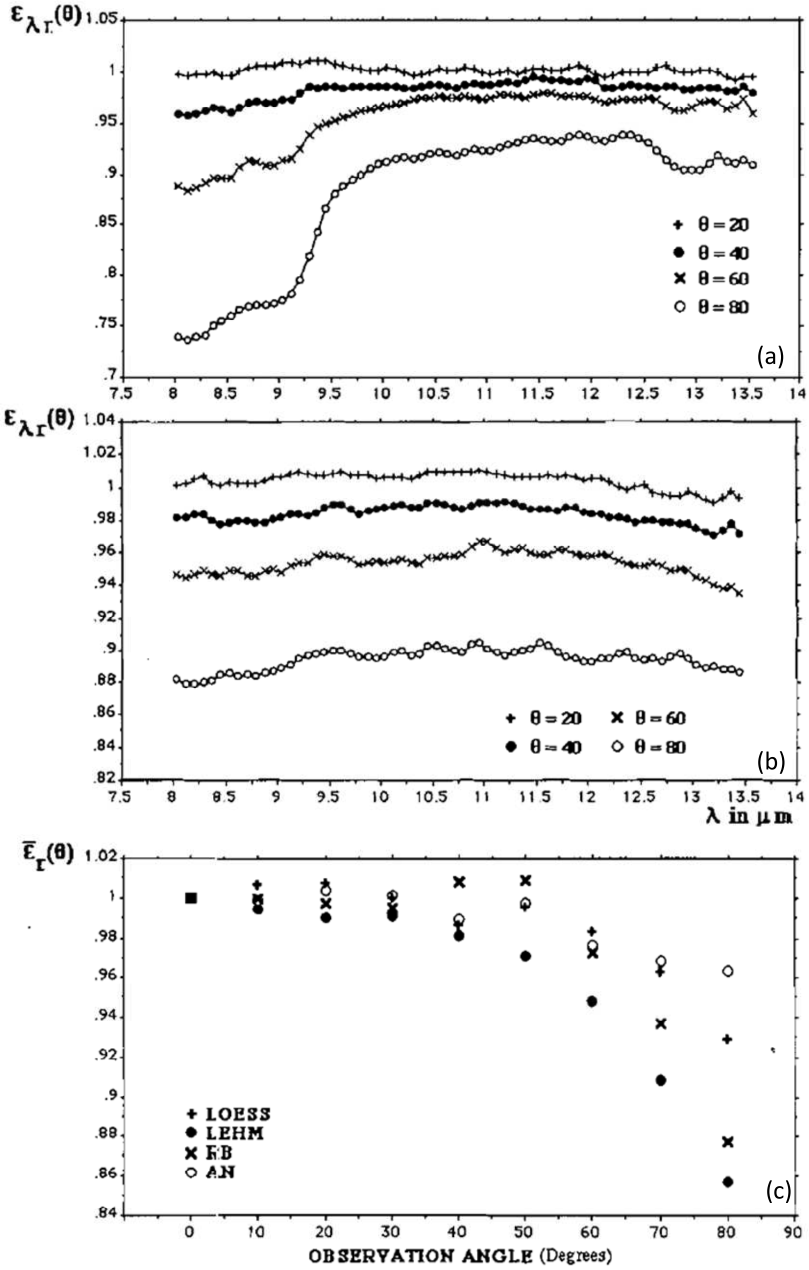

Figure 1.2 Results of TIR emissivity variation with zenith angle extracted from Figures 3, 4(a) and 6(a) from Labed and Stoll (1991): a) Relative spectral emissivity of sand at different observation angles at 8.0-13.5 μm. b) Relative spectral emissivity of sample RB at different observation angles at 8.0-13.5 μm. c) Relative angular emissivity $\varepsilon_r(\theta)$ (mean between values at λ= 10.6 μm and λ= 12.0 μm) of four bare soils versus the observation angle.

1.4 Main Thesis objectives

Considering the results of previous works on emissivity dependence on SM and viewing angle, the present Thesis has pursued the following main objectives:

1. To collect a set of IBS samples representative of a great number of existing textures on Earth to analyze the TIR emissivity anisotropy thoroughly.

2. Since the study is based on the measurement of accurate emissivities, the radiative effects of the surrounding elements and atmosphere must be accurately evaluated and considered. An analysis about which is the best method to take into account this contribution has been performed.

3. Once stipulated the methodology to carry out the emissivity measurements, the step has been to analyze the angular variation, both zenithal and azimuthally, of TIR emissivity for the set of IBS under completely dry conditions.

4. To check the evolution of that TIR emissivity anisotropy when SM is increasing from dry conditions.

5. Ignoring angular and soil moisture effects on TIR emissivity involves uncertainties retrieving other emissivity-dependent parameters such as LST or outgoing longwave radiation for instance. These uncertainties have been analyzed to assess how important is a precise knowledge of emissivity in the TIR region.

6. From results obtained analyzing the anisotropy of TIR emissivity at different SM levels, a regression with SM, viewing angle and some textural and mineralogical factors has been established in order to quantify all these effects on emissivity.

1.5 Thesis organization

This report has been organized in 6 chapters, structured as follow. Present **chapter 1** shows the *state of the art* of studies about anisotropy of TIR emissivity of mineral soils and the objectives pursued. **Chapter 2** describes main physical properties of selected mineral soils, specifying the roughness conditions required to carry out the anisotropy study on these soils. Water interaction on theses soils and methodology employed to take moisture measurements is also explained. **Chapter 3** explains the methodology followed to retrieve the TIR emissivity at different angular configurations; the main characteristics of multispectral thermal radiometer employed to carry out the study are also described in text. **Chapter 4** deals with the radiative environment contribution to emissivity measurements, where different methods to retrieve *in situ* hemispherical downwelling radiance from surrounding elements have been explained and compared, concluding which of them is the most suitable to be applied. **Chapter 5** shows the results of analyzing the anisotropy of TIR emissivity, at all mineral soils studied, both under dry conditions and at different moisture levels. Finally, **Chapter 6** summarizes the most important conclusions from the study.

Additionally, copies of the papers published in international journals achieved during the conduction of the present thesis are included in the annexes, those publications are referenced throughout this report.

Chapter 2

Moisture measurements on IBS

Next chapter explains the selection of several inorganic soils as representatives of a great variety of soils found in Earth, given their textural and mineralogical composition. Roughness status under dry conditions, and water saturation and drying process have been also explained as well as soil moisture retrievals.

2.1 Inorganic bare soils

Soils cover the first meters of the thinnest and external layers of Earth surface and comprise of a continuum of different mineral size particles. Since there exist a large variety of soils in nature a method is needed to classify these soils in different categories according to their properties. Two of the most important methods are: the soil taxonomy (Soil Survey Staff, 2010) elaborated by National Resources Conservation Service (NRCS) from United States Department of Agriculture (USDA). The second method is the World Reference Base developed by International Union of Soil Sciences (2006) in collaboration with Food and Agriculture Organization.

A set, composed of a total of 13 samples of soil with different compositions and properties, was selected to carry out the study about the anisotropy of TIR emissivity at different SM levels. The TIR spectrum is sensitive to radiation emitted by a surface from its first micrometers (Salisbury *et al.*, 1995), consequently our samples come from the first 15 cm of surface, called the organic-mineral A horizon. Depending on the soil’s bulk density it was necessary to acquire around 17 kg of each, a complex task since the origin of each sample is diverse: Samples B, C, D and F come from different places of Valencia (Spain), sample E comes from Galicia (Spain). Samples LW (03, 13, 45 and 52) and WS come from USA, LW from south of Oklahoma (Little Washita River Experimental Watershed) and WS from the White Sands National Monument (New Mexico). Samples BR1, BR2 and BR3 come from a rural area in São Paulo (Brazil).

Grain size analysis refers to inorganic composition (mineral fraction) of soils. According to USDA criterions three ranges of particle sizes are established: sand (particle diameter between 0.05 and 2 mm), silt (particle diameter between 0.002 and 0.05 mm) and clay (particle diameter lower than 0.002 mm). Percentages of sand, silt and clay of our soils were retrieved by means of the Bouyoucos method (Bouyoucos, 1962) according to ISO 11277:1998 regulation (ISO, 2002). Results of analysis showed that our samples cover ranges between 14% and 100% for sand and between 0% and 54% for silt and clay. Table 2.1 shows the granularity among other properties of our soils. USDA criterions established 12 different textural classes distributed in a triangle according to multiple combinations of sand, clay and silt percentages. Our soils represent 9 of these 12 textural classes. Figure 2.1 shows the distribution of these 13 soils in the texture triangle defined by the USDA. Textural distribution of inorganic soils around the world is mapped in Figure 2.2, according to this map there exist sandy-clay soils in the east part of china, silty-clay and silt soils can be found in small areas at any continent.

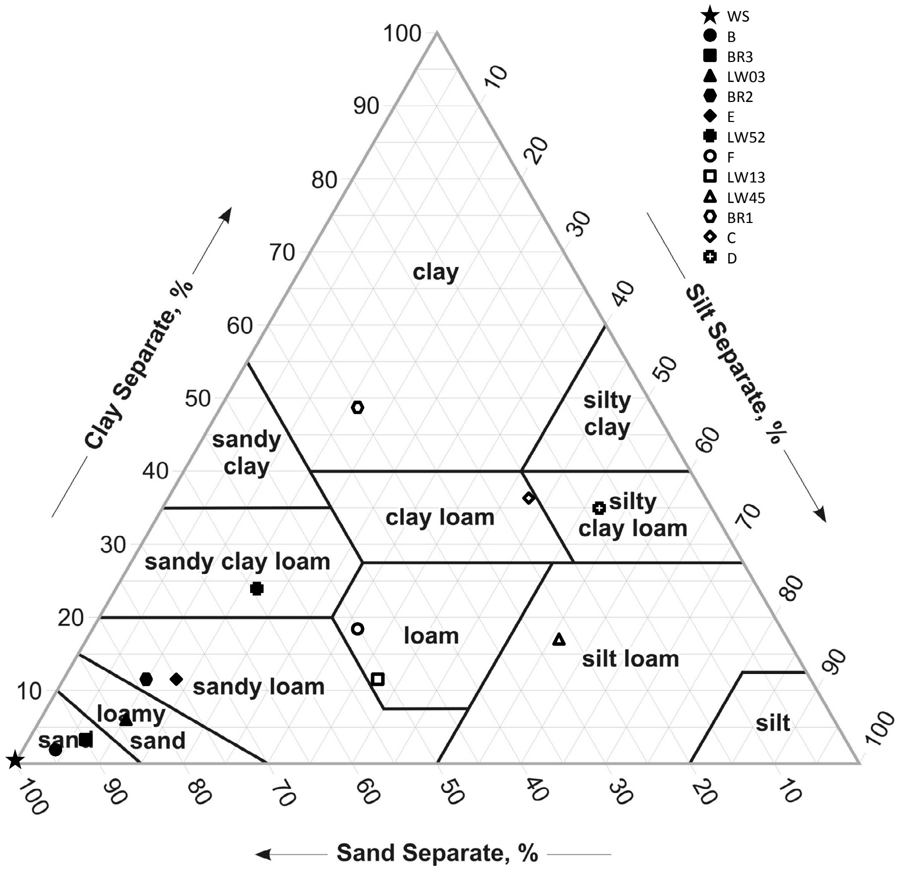

Figure 2.1 Distribution of the IBS analyzed in the texture triangle defined by USDA.

Inorganic components usually make up 95% of a dry soil mass, and it can be considered organic if the percentage of organic matter (OM) is greater than 37%. The most abundant minerals in soils are: silicates (quartz, feldspar, etc.), carbonates, oxides and sulfates. According to data of Table 2.1, our samples are considered Inorganic soils with quartz quantities covering ranges of sand fraction between 0% and 100%, OM in our soils reaches a maximum of 8.9%.

Tavble 2.1 Organic matter (OM) content, and textural and mineralogical features of the thirteen IBS selected for the analysis. Additional details can be found in Mira *et al.* (2007, 2010)

Soil code	USDA Texture type	OM (%)	Textural classification (%)			Mineral classification (%)						
			Sand	Silt	Clay	Quartz	Feldspar	Filosilicate	Hematite	Calcite	Gibbsite	Gypsum
B	sand	0.1	99	0.9	0.1	95.3	2.9	-	-	-	-	-
BR3	sand	1.69	92	2	6	100	-	-	-	-	-	-
WS	sand	0.21	100	0	0	1	-					99
LW03	loamy sand	0.73	77	18	5	53.7	46.3	-	-	-	-	-
BR2	sandy loam	1.47	69	15	16	82.3	16.8	0.8	-	-	-	-
E	sandy loam	1.5	67	20	13	72	21.4	3.2	-	-	-	-
LW52	sandy clay loam	1.71	62	15	23	58.4	32.2	9.4	-	-	-	-
LW13	loam	1.61	51	35	14	76	16.7	4.8	2.6	-	-	-
F	loam	3.5	50	30	20	19.9	4.5	4.1	8.7	62.9	-	-
BR1	clay	2.93	40	6	54	37.9	-	-	13.1	-	49	-
LW45	Silty loam	1.15	29	54	17	72.4	23.4	4.2	-	-	-	-
C	clay loam	8.9	20	43	37	29.4	5.5	9	-	56.1	-	-
D	Silty clay loam	4.5	14	50	35	19.3	3.5	6	8.9	62.3	-	-

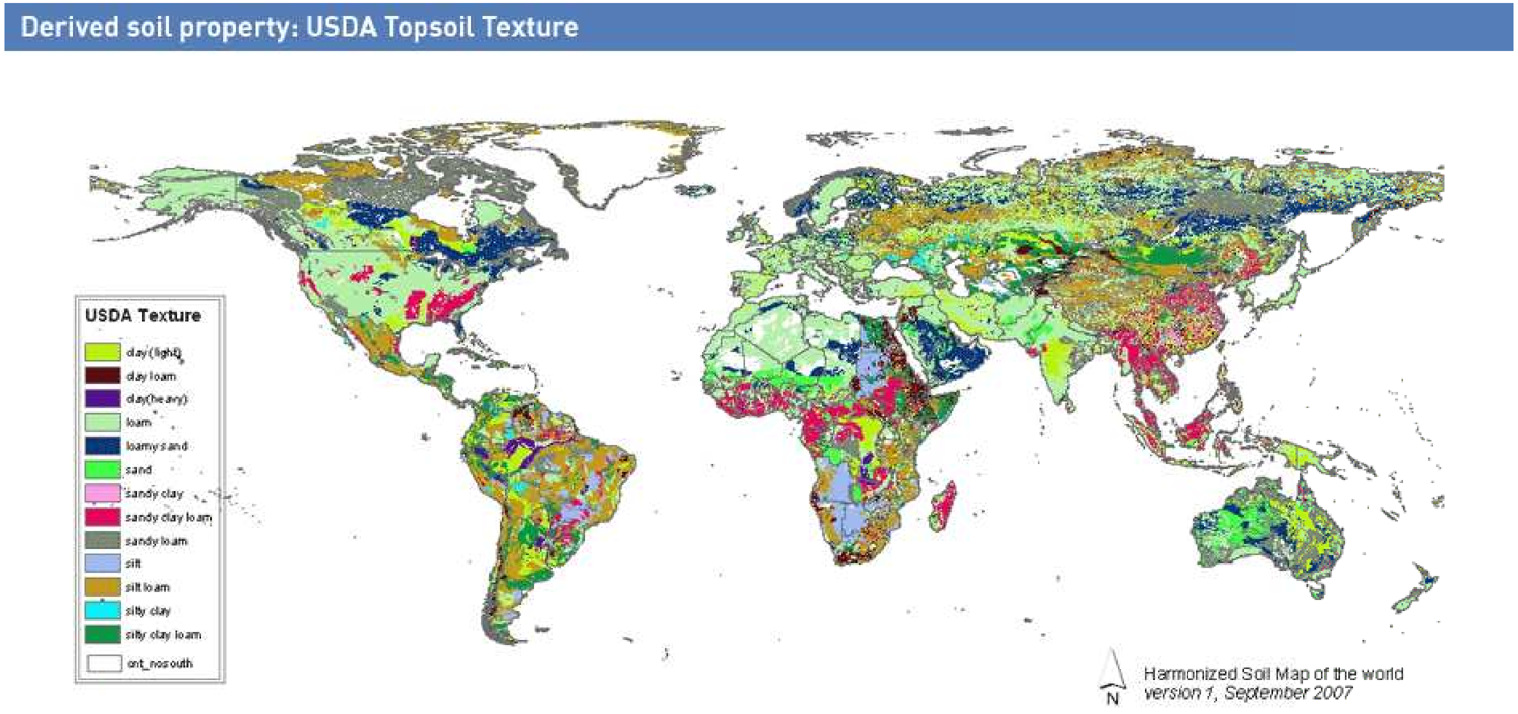

Figure 2.2 Global Distribution of soil textural classes according to FAO (http://www.fao.org/nr/water/news/soil-db.html).

2.2 Roughness condition of samples

As the present study attempts to analyze in field work conditions the anisotropy of TIR emissivity of IBS under different water content status, radiance measurements (chapter 3) were made very close to the IBS surface. For this reason our samples, once completely dry, were sieved to particle sizes lower than 0.5 cm. Lagouarde *et al.* (1995) analyzed the angular variation of brightness temperature (T_b) for different type of surfaces. Measurements were made at different zenith angles in a range from 0° to 180°, the zenith measurement process was carried out in a complementary and a perpendicular sun plane, and the complete process was repeated at different sun elevations. Three of these type of surfaces were IBSs with different roughness levels: a deeply ploughed soil with clod sizes up to 20-25 cm, a second soil, ploughed and harrowed, (with a vibrating harrow) which presented an average cold size around 4-5 cm, and a third sandy-stony IBS, very smooth due to several perpendicular passes of a heavy roller; for this last soil 70% of the clod size was around 200 µm. Figure 2.3 shows results of T_b angular variation for these three soils.

According to the results of Lagouarde *et al.* (1995), for IBSs whose roughness implies particle sizes of greater than 4–5 cm, effects associated with angular measurements of T_b are caused by sun elevation, since the distance between surface and sensor is short enough to be influenced by sunlight or shadow parts of the clods (Figure 2.3 (I) and (II)). Nevertheless, when IBS is very smooth to be considered both as a very rough, random surface with respect to the observation angle and a perfectly flat surface at the scale of landscape, the angular difference of T_b presented a similar shape (Figure 2.3 (III)) with no significant difference between measurements in the complementary and perpendicular plane. Since a surface with this roughness level exhibits no geometrical pattern, differences between nadir and oblique observation on T_b can only be attributed to the existence of angular variations in emissivity of the IBS. Present work tries to study the angular emissivity of IBS with an almost constant roughness (particles size no greater than 0.5 cm). The objective is to evaluate the behavior of angular emissivity for each textural class defined in the text, with no influence of other factors.

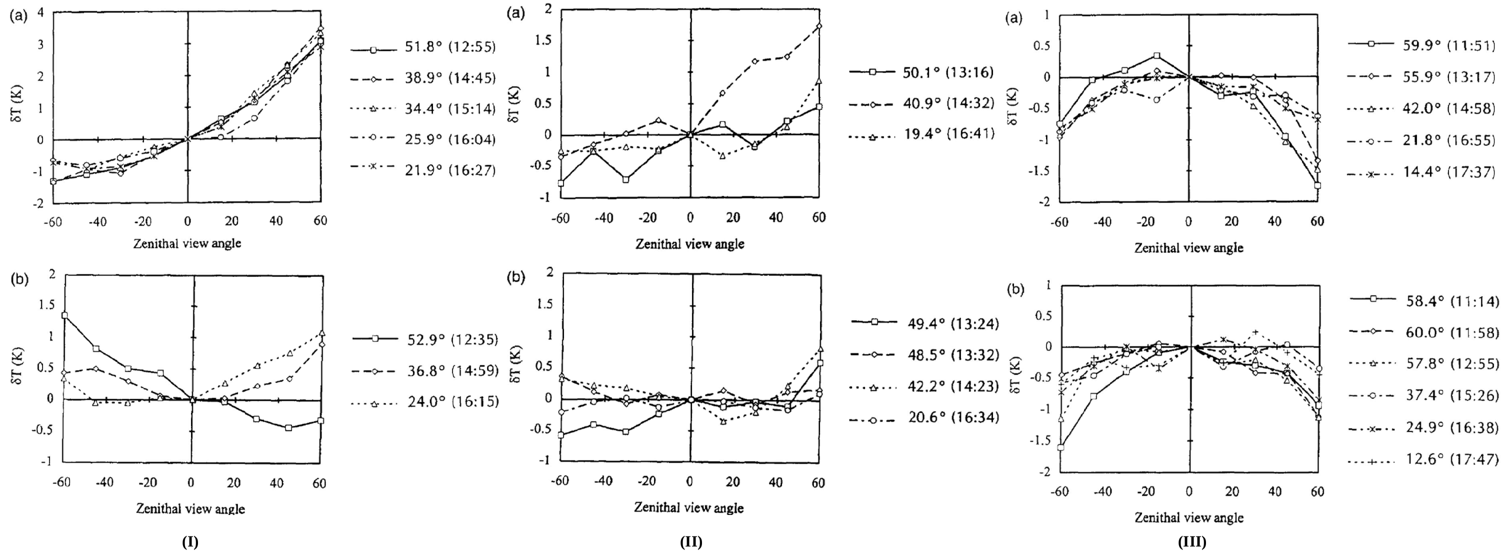

Figure 2.3 Influence of the zenithal view angle on $\delta T = T_b(\theta) - T_{b0}$ over: (I) Ploughed soil; (II) Harrowed soil; (III) Smooth soil, for various sun elevations, in the complementary (a) and perpendicular (b) sun planes. Solar elevations are displayed next to the figures and the times of the measurements are Local Solar Times appear within parentheses. These results have been extracted from Figures 9, 10 and 11 in Lagouarde *et al.* (1995)

2.3 Moisture content in IBS

The spectral effect of water on soils is important since it is highly absorbent of TIR radiation, with emissivity values close to 1 and therefore significantly affecting emission of wet soils (Mira *et al.*, 2007 and 2010). Water can be found related with soil in three ways; (i) *Hygroscopic water*, a molecular film absorbed by soil directly from air and superficially attached, it is not useful for plants since it cannot be absorbed. (ii) *capillary water*, is used by plants as hydrological reserve, this water is retained by soil micro-pores (particle space < 250 µm); and *gravitational water*, is retained by macro-pores (particle space ≥ 250 µm) sometimes saturating the soil, it is percolated through soil by means of gravitational force into deeper aquifers.

Saturation and Drying process of IBS

Completely dry and sieved IBS samples (see section 2.2) were put in a circular container with a 52 cm diameter and they remained flooded for 24 hours to get the saturation. Figure 2.4 shows the process for IBS BR3 as an example. Afterwards, saturation samples were freely air dried and TIR emissivity measurements (see chapter 3) were taken both under dry and saturated conditions as well as under different SM levels during the drying process. Some silt and clayey IBSs presented some cracks during this drying process (Figure 2.4), the soil cracks were sealed when moisture conditions allowed it. Otherwise emissivity measurements were not taken since cavity effects (Valor and Caselles, 1996) could probably appear.

Figure 2.4 Saturation process of an IBS sample. During drying some silt and clayey samples presented cracks.

Delta-T SM200 probe

The *time domain reflectometry* (TDR) technique allows fast and more accurate retrievals of SM based on the large difference between the dielectric constant of water ($k \approx 80$) and other soil components ($k \approx 1$ for air and $k \approx 2$ to 5 for solids). TDR-based instrumentation uses a high frequency voltaic pulse, propagated through a transmission line (usually limited by two steel rods) to measure its attenuation or propagation speed across the soil present between the rods. The ratio of the time propagation pulse between soil and air (t/t_{air}) is similar to the square root of the dielectric constant ($k^{1/2}$). An empirical relation called the *Topp equation* (Topp *et al.*, 1980; Malicki *et al.*, 1996; Topp and Reynolds, 1998) allows the retrieval of SM given the previous knowledge of k.

The TDR sensor used for the present study was a Delta-T SM200 probe. Figure 2.5 shows this sensor composed of the probe with two 5 cm rods and a data-logger used to simultaneously store and display the SM readings. According to the manufacturer these sensors can retrieve the volumetric SM value of any soil with an uncertainty of ± 0.03 $m^3 \cdot m^{-3}$ (Delta-T Devices Ltd., 2006).

(a) (b)

Figure 2.5 Delta-T SM200: (a) probe with 5 cm rods, (b) data-logger able to store and display simultaneously the SM readings.

A parallel calibration was made in our laboratory to test manufacturer equations. IBS samples BR2, LW03, E, D and LW45 were selected to carry out the comparison of SM200 probe measurements with SM volumetric values obtained multiplying IBS bulk density and laboratory SM gravimetric measurements (Day, 1965; chapter 2 from Mira, 2010). Gravimetric SM values (SM_G) were retrieved by measuring the weight of the soil when it is completely dry (m_s) and when it is wet (m_w), measurements of wet soil are made several times during the drying procces. Finally the gravimetric measurements are obtained from expression.

$$SM_G(kg \cdot kg^{-1}) = \frac{m_W - m_s}{m_s} \tag{2.1}$$

Figure 2.6 shows calibration results, comparing SM values measured with the SM200 Delta-T probe and SM laboratory retrievals through gravimetric method explained above. It is interesting to check that IBS samples centered in the USDA texture triangle (LW03, BR2 and E) show SM measured values that match better with laboratory measurements than soils situated in the border of the triangle (D and LW45). Nevertheless standard deviation (σ) of measurements in the regression shows a value of ± 0.03 $m^3 \cdot m^{-3}$, concluding that the Delta-T SM200 works correctly within the fabrication uncertainty.

SM measurements were made at different points of the IBS surface samples before and after the emissivity retrieval process (chapter 3) in order to check the possible spatial and temporal variations of SM in the sample. The gap time between two SM samplings was around one hour, average and standard deviation (SD) values were calculated and the SD was always lower than the Delta-T SM200 measurement error, assuring moisture homogeneity in the soil during the radiance measuring process. The emissivity retrieval process was repeated at different times during the drying of sample, allowing emissivity measurements at different SM values until the sample was completely dry. The sequence of soil saturation and drying was repeated one more time in order to check the validity and reproducibility of the results.

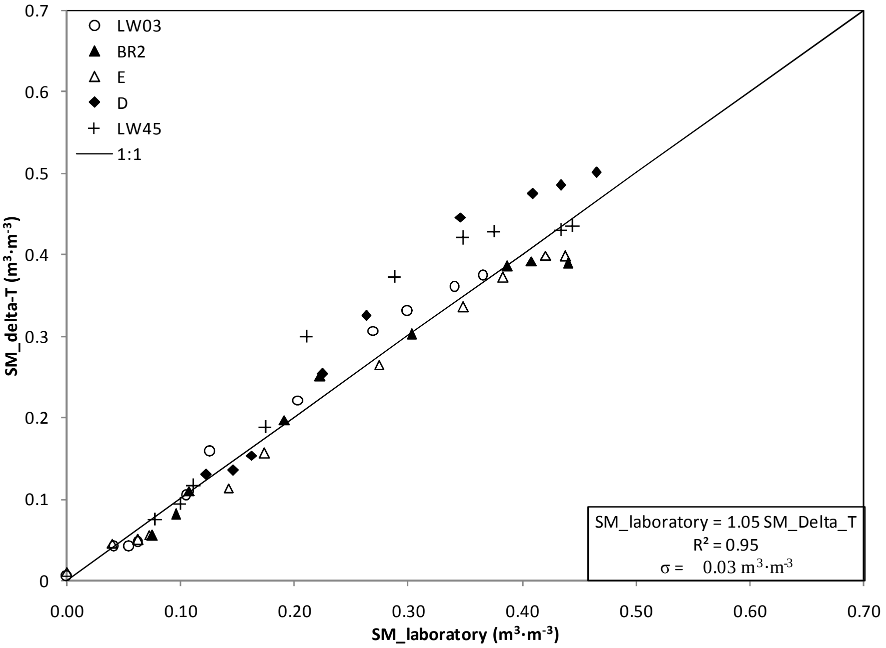

Figure 2.6 Calibration results for the 6 textural IBS samples selected. It is also represented the linear adjustment, regression coefficient and RMSE value.

Chapter 3

TIR emissivity retrievals

This chapter explains the methodology followed as well as the instrumentation employed, to carry out soil emissivity retrievals in this study. It is also included an exhaustive laboratory calibration of the multispectral thermal radiometer used, calibration checked by an experimental campaign carried out in April 2009 at the National Physical Laboratory in London, UK. The chapter ends with a sensitivity analysis of the uncertainty produced on emissivity retrievals, related with the methodology.

3.1 Relative-to-nadir TIR emissivity

For a thermal sensor onboard a spatial satellite, measuring the radiance coming from a surface within the 8-14 μm spectral region, the radiative transfer equation can be modeled with three terms: direct surface emission, surface reflected environmental radiation (hemispheric downwelling radiance), and atmospheric absorption and emission effects:

$$L_i(\theta,\varphi) = \left[\varepsilon_i(\theta,\varphi)B_i(LST) + \rho_i(\theta,\varphi)L_i^{\downarrow}\right]\tau_i(\theta,\varphi) + L_{atm,i}^{\uparrow}(\theta,\varphi) \qquad (3.1)$$

where $L_i(\theta,\varphi)$ is the band radiance measured directly by the sensor from surface at zenith angle θ and azimuthal angle φ; B_i is the Planck function for blackbody radiance at LST; $L^{\downarrow}_i$ is the hemispheric downwelling radiance made up from the atmosphere and surrounding element contributions, $\rho(\theta,\varphi)$ is the hemispherical-directional band reflectance (Nicodemus *et al.*, 1977), $\varepsilon_i(\theta,\varphi)$ is the absolute band emissivity of the surface, τ_i is the atmosphere spectral transmisivity and $L^{\uparrow}_{atm,i}$ is the direct atmosphere emission towards the sensor. Subscript *i* stands for the spectral band where measurements have been taken.

However, for this study, where sensor-surface distances are short, some atmospheric contributions can be neglected (τ=1 and $L^{\uparrow}_{atm}$=0) and reduced to the reflected term of hemispheric downwelling radiance. The spectral radiance can be modeled after Norman and Becker (1995):

$$L_i(\theta,\varphi) = \varepsilon_i(\theta,\varphi)B_i(LST) + \rho_i(\theta,\varphi)L_i^{\downarrow} \qquad (3.2)$$

A relationship between surface emissivity and hemispherical-directional reflectance for a surface opaque to radiation in thermal equilibrium can be established by means of Kirchhoff's law (Nicodemus, 1965) as:

$$\varepsilon_i(\theta,\varphi) = 1 - \rho_i(\theta,\varphi) \qquad (3.3)$$

This relation can be applied in two cases, either for anisotropic radiation over a Lambertian surface or for the inverse situation, with a non-Lambertian surface receiving isotropic radiation from its surroundings (Nicodemus *et al.*, 1977).

From Eqs (3.2) and (3.3) emissivity is retrieved as:

$$\varepsilon_i(\theta,\varphi) = \frac{L_i(\theta,\varphi) - L_i^{\downarrow}}{B_i(LST) - L_i^{\downarrow}} \qquad (3.4)$$

However, emissivities from Eq. (3.4) are often inaccurate due to difficulties in retrieving accurate measurements of the LST, from which the B(LST) is calculated, since this radiative temperature corresponds to a thin superficial layer of the order of a few micrometers (Salisbury *et al.*1995).

This problem is solved by retrieving relative-to-nadir values of $\varepsilon(\theta,\varphi)$ (Labed and Stoll, 1991), taking simultaneous measurements of radiance at nadir and an arbitrary angular configuration from the surface, besides the hemispheric radiance from the surrounding contribution. Taking measurements in a time period short enough to avoid significant changes of LST or $L^{\downarrow}_i$ during the measurement process, it is possible to obtain relative-to-nadir emissivity measurements by dividing Eq. (3.4), considered at a given angle (θ,φ) and at nadir viewing (0,0):

$$\varepsilon_{ri}(\theta,\varphi)=\frac{\varepsilon_i(\theta,\varphi)}{\varepsilon_i(0,0)}=\frac{L_i(\theta,\varphi)-L_i^{\downarrow}}{L_i(0,0)-L_i^{\downarrow}} \tag{3.5}$$

where $\varepsilon_{ri}(\theta,\varphi)$ is the relative-to-nadir emissivity and $L_i(0,0)$ is the radiance measured by the sensor at nadir viewing.

Given that Eq. (3.5) is the quotient between absolute emissivity from an angular configuration and nadir, a previous knowledge of absolute emissivity at nadir allows estimation of the absolute value of emissivity in that specific angular configuration by:

$$\varepsilon_i(\theta,\varphi)=\varepsilon_i(0,0)\varepsilon_{ri}(\theta,\varphi) \tag{3.6}$$

Absolute emissivity values close to nadir can be retrieved using several techniques: such as the Box method (Rubio *et al.* 1997; Mira *et al.* 2007) or the TES algorithm (Gillespie *et al.* 1998; Mira *et al.* 2009).

3.2 Experimental set-up to retrieve $\varepsilon_r(\theta,\varphi)$

Multispectral thermal radiometer CLIMAT 312-2B

Radiances were taken with two multispectral thermal CIMEL Electronique model CLIMAT 312-2B radiometers (CE312-2; Brogniez *et al.*, 2003). Figure 3.1(a) shows a picture of CE312-2 components made up by: a computer for data storage, treatment and visualization of the measured data as well as the computation of results; a power supply box with a buffer battery that could be power charged and a 6-band radiometric sensor head simulating 5 ASTER thermal bands (Gillespie *et al.* 1998). The instrument makes successive measurements of the target through various spectral filters, compensating the influence of its own temperature by means of measurements of its own thermal image on an automated mirror.

CE312-2 works in six different spectral bands, one of them operating in the broad range 7.7-14.3 μm (channel 1) and the other five channels working in narrow bands allocated within the previous broadband: 8.2-8.7 μm (channel 6), 8.4-8.9 μm (channel 5), 8.9-9.4 μm (channel 4), 10.1-11.1 μm (channel 3) and 10.9-11.9 μm (channel 2). Figure 3.1(b) shows a graph of spectral response function of six CE312-2 filters.

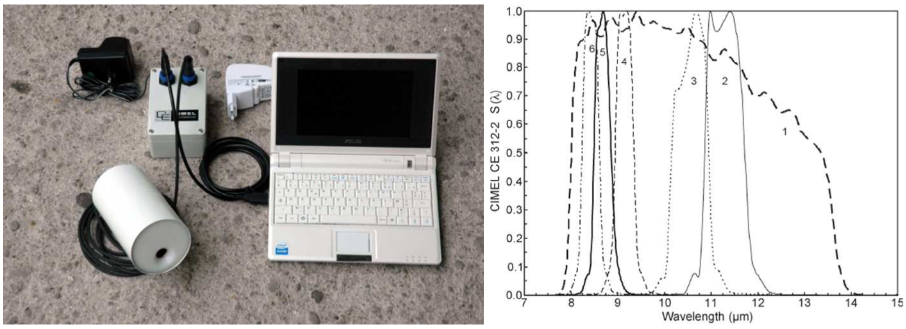

(a) (b)

Figure 3.1 (a) CE312-2 components. (b) Normalized spectral response of 6 CE312-2 filters

Calibration of CE312-2

Two CE312-2 were calibrated with a thermal near-blackbody behavior source, LandCal Blackbody Source model P80P (http://www.landinst.com/infrared/products/p80p) to check the accuracy and precision of this radiometer, at 5 °C intervals. The thermal radiometer calibration lies in a comparison of the blackbody CE312-2 temperature measurements with the blackbody temperatures, registered through an external probe connected to internal surface of LANDCAL P80P. Temperatures range of the calibration covers values from -5 °C to 45 °C taking measurements with the CE 312-2 every 5 °C increase.

Results in Figure 3.2 represent the comparison between LANDCAL P80P thermometric temperature and CE 312-2 temperature registered at each radiometer spectral channel. From these results it is concluded that the accuracy of channels 1 to 6 of CE 312-2 with regard to the blackbody temperature is: ±0.07 °C, ±0.11 °C, ±0.10 °C, ±0.10 °C, ±0.07 °C and ±0.09 °C, respectively.

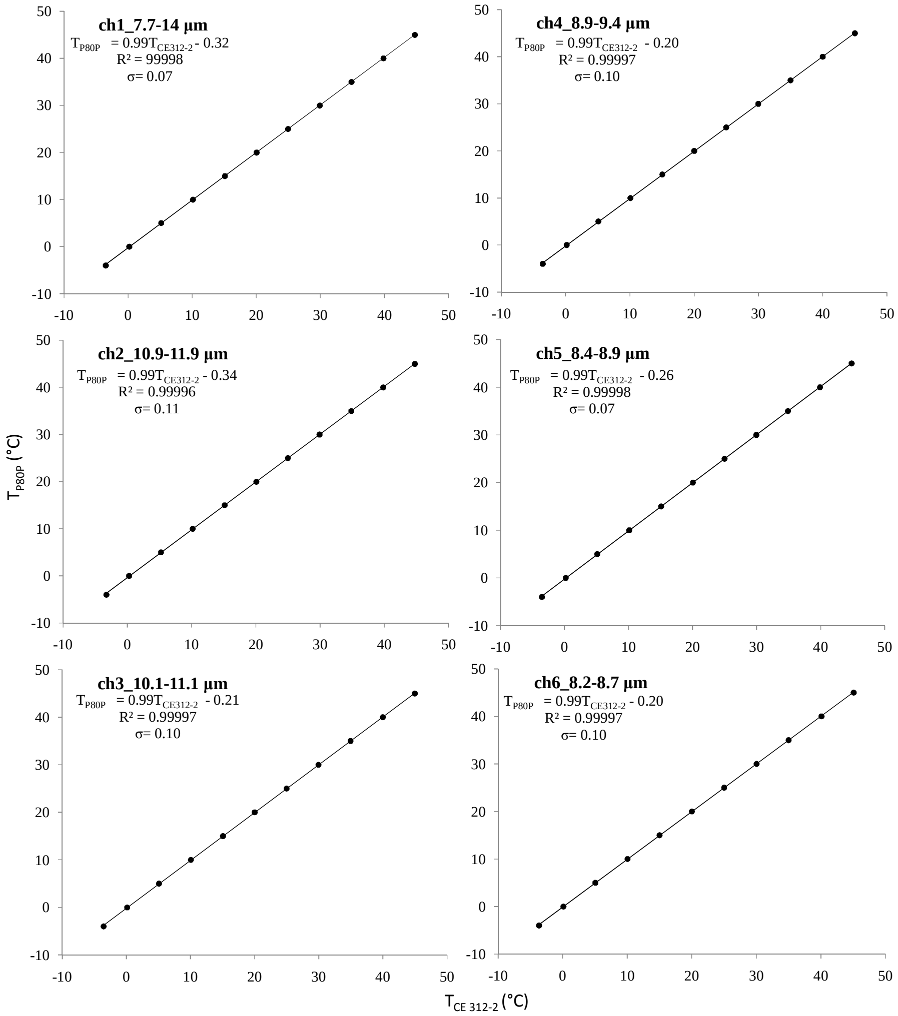

Figure 3.2 Calibration curves of CE312-2 temperatures vs P80P temperatures. Correlation coefficient and standard deviation are also included.

The P80P blackbody source was in turn calibrated at the *National Physics Laboratory* (London, UK) during a comparison and validation of TIR instruments campaign, organized by the *Working Group on Calibration and Validation* from *Committee on Earth Observation Satellites* in April 2009 (Theocharous and Fox, 2010). Results showed that P80P agreed with the NPL reference radiometer with an accuracy of ±0.19 °C at the three different reference temperatures of 10 °C, 20 °C and 30 °C. Therefore, the absolute accuracy of CE 312-2 channels is within ±0.19 °C.

$\varepsilon_r(\theta,\varphi)$ retrieval process

Angular radiance measurements over the IBS samples were carried out on the roof of the Physics Faculty of the University of Valencia, Spain (13°30’25’’N, 0°25’13’’W), and angular TIR emissivity was retrieved by means of equation (3.5). A goniometer was used to perform simultaneous radiance measurements on each sample at different viewing directions, by means of two identical CE 312-2 radiometers (see Figure 3.3), one at nadir (CE1) and the second one in a given direction (θ,φ) (CE2). This last radiometer could be moved along the arm of the goniometer varying the field of view (FOV) over the sample, in order to measure the same area as the nadir radiometer. Radiance measurements were taken at different combinations of zenith and azimuth angles. Zenith angles were considered from θ=10° to θ=70° at intervals of 10°. For each zenith angle, the IBS emissivity was measured at three different azimuthal orientations turning the samples 120° each time, instead of turning the goniometer-radiometer system. This process was repeated two times for each zenith angle, so it took around 3 minutes to finish all the measurement processes for a given zenithal angle. Azimuthal rotation of the sample, instead of the goniometer framework, was done to speed up data collection and to ensure that observations were made using the same surrounding conditions (i.e. solar elevation, atmosphere contribution, etc.). In this way any difference in retrieving emissivity by equation (3.5) at different azimuthal angles, can be attributed exclusively to the sample.

All IBS samples were placed in a circular container 52 cm in diameter and 10 cm in height (Figure 3.3). The container had multiple holes in the bottom designed for water drainage. Moreover, a sieve was attached to the bottom (between the holes and the sample) to avoid the loss of the finest particles. For each soil, the measurement process started with a completely dry sample for which the angular radiance measurements were performed. Then, the sample was flooded allowing filtration through the container, and freely air dried. During the drying process, angular radiance measurements were performed at several times so that the relative-to-nadir TIR emissivity could be measured at different SM levels from saturation to completely dry conditions. For a given sample at a specific SM level, the whole set of angular radiance measurements lasted 50 min. These measurements were repeated at different times during the drying of the sample, allowing emissivity measurements at different SM values until the sample was completely dry.

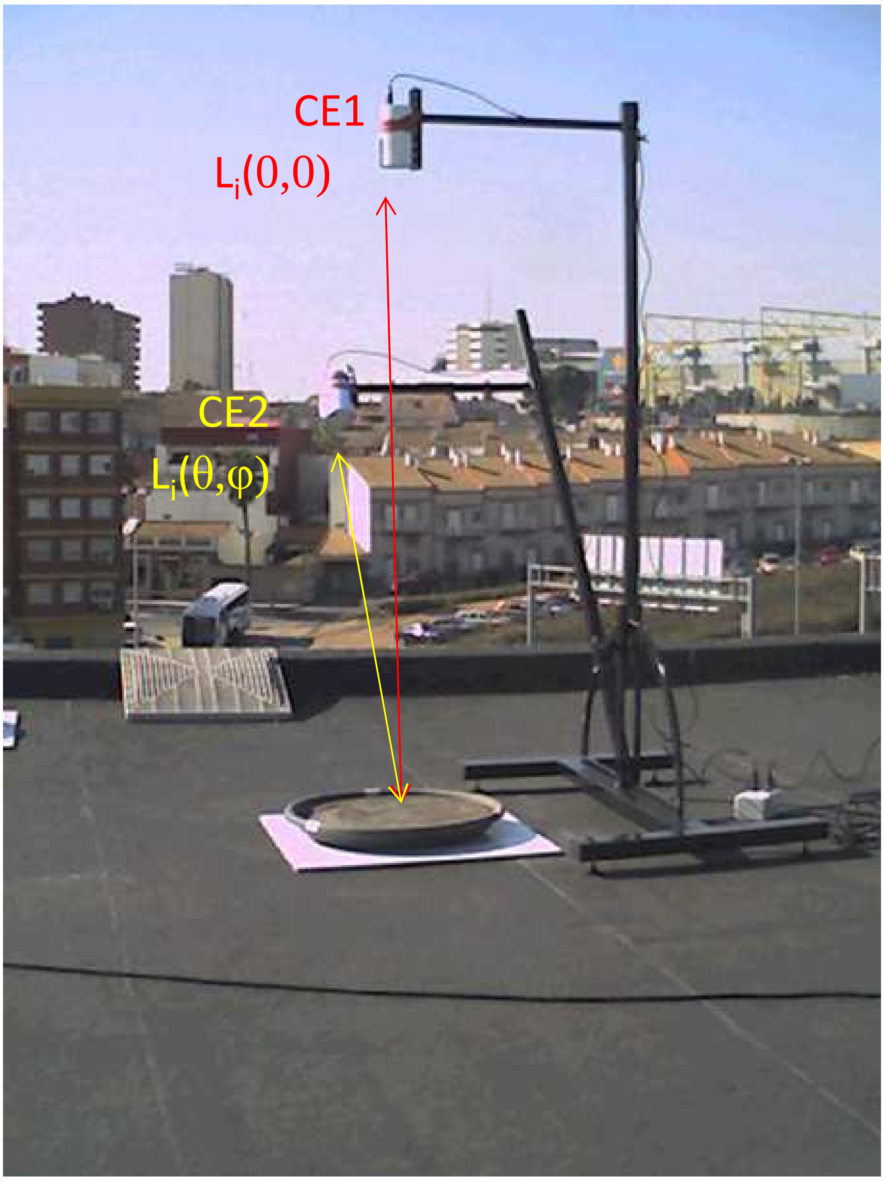

Figure 3.3 Experimental ensemble used in the study during two simultaneous measurements at nadir (CE1) and at viewing direction (θ, φ) (CE2).

Since we only disposed of two CE312-2, it was not possible to simultaneously measure the IBS radiance at nadir and a given direction (θ,φ) and the hemispherical radiance coming from the atmosphere and surrounding elements in Eq. (3.5), this was the reason for which we took only $L_i(0,0)$ and $L_i(\theta,\varphi)$ measurements simultaneously. $L^{\downarrow}_i$ was measured after the CE1(0°)-CE2(10°), CE1(0°)-CE2(30°), CE1(0°)-CE2(50°) and CE1(0°)-CE2(70°) measurement configurations, placing a gold diffuse reflectance panel inside the FOV of CE1 at 0°. The time period between both panel measurements was less than 18 minutes, which implied an average $L^{\downarrow}_i$ fluctuation of ±4%; this relative value was obtained from the quotient of the difference between the $L^{\downarrow}_i$ values measured before and after the 18 minutes interval, and the average value of both measurements, multiplying all by 100.

3.3 Sensitivity analysis of $\varepsilon_r(\theta,\varphi)$

Uncertainties associated with $\varepsilon_r(\theta,\varphi)$ retrievals are explained in this section. The error of relative-to-nadir emissivity ($\delta\varepsilon_r(\theta,\varphi)$) was calculated as the maximum value of three errors:

i) Propagation error through equation (3.5), associated to CE312-2 temperature uncertainty of ±0.19°C (see section 3.2), except in case of $L^{\downarrow}_i$, which is given by 4% fluctuation of the radiance as it was measured at 18 minutes interval.

ii) Standard deviation calculated from three $\varepsilon_r(\theta,\varphi)$ values retrieved for a specific (θ,φ) configuration, since radiance from IBS at this configuration is measured three times.

iii) Difference between maximum and minimum value of $\varepsilon_r(\theta,\varphi)$ at a specific (θ,φ), divided by four.

Figure 3.4 shows the histogram of these $\delta\varepsilon_r(\theta,\varphi)$ values for all six CE312-2 spectral channels, viewing configurations and SM levels. Results show that $\varepsilon_r(\theta,\varphi)$ can be retrieved in the field with an average error of ±0.003 (56 % of values). Nevertheless, we defined a threshold of ±0.01 in emissivity to consider the existence of significant anisotropy effects on $\varepsilon_r(\theta,\varphi)$ both when it varies with θ or φ (at all SM levels) since almost all $\delta\varepsilon_r(\theta,\varphi)$ values (97 %) are equal to or lower than this threshold. Thus, only emissivity changes larger than ±0.01 have been considered as real emissivity variations with viewing angle or soil moisture, well beyond the established emissivity measurement errors.

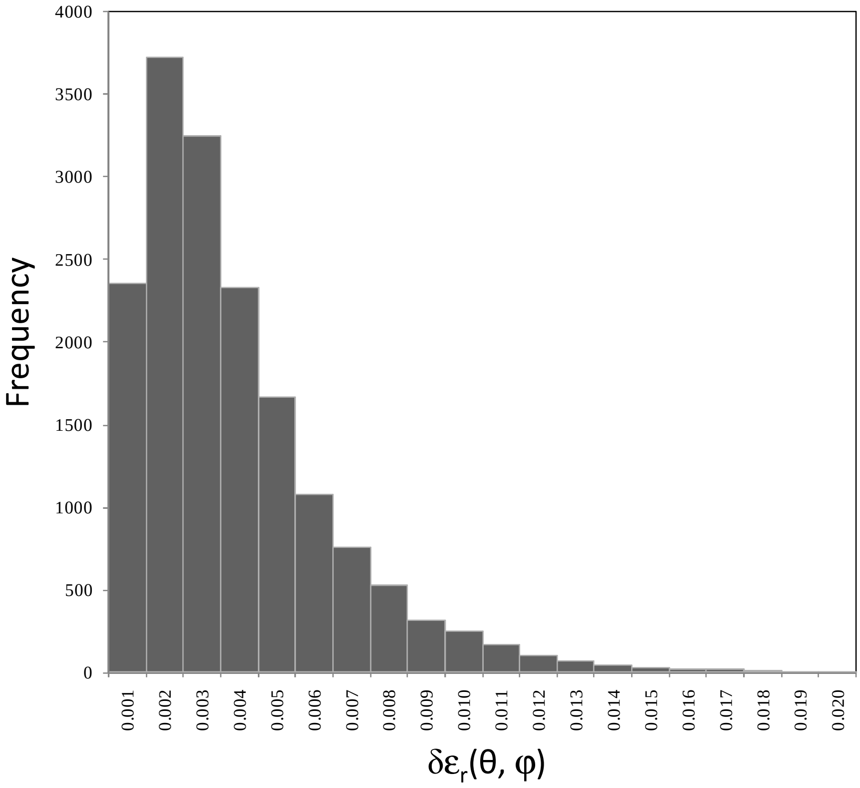

Figure 3.4 Histogram of error associated to specific angular configuration, $\delta\varepsilon_r(\theta, \varphi)$, for all the IBS studied at all spectral ranges, SM contents and (θ, φ) configurations (almost 16700 values)

It is also interesting to analyze the effect of $L^{\downarrow}_i$ fluctuation on $\varepsilon_r(\theta,\varphi)$ over time during the measurement process. Hemispheric downwelling measurements were made every 18 minutes using a gold diffuse reflectance panel, fluctuating around 4% from its average value. So we decided to consider this fluctuation as a relative error of $L^{\downarrow}_i$ and $\delta\varepsilon_r(\theta,\varphi)$ was retrieved when only this error was considered, from the propagation error in equation (3.5). Measurements were made for $\varepsilon_r(\theta,\varphi)$ at all CE312-2 spectral channels, SM levels and viewing configurations. Results showed that retrieved $L^{\downarrow}_i$ with a relative accuracy of 4% implies a retrieval of $\varepsilon_r(\theta,\varphi)$ with an uncertainty of ±0.0005, a value that is six times lower than the average error and twenty times lower than the maximum $\delta\varepsilon_r(\theta,\varphi)$ considered. So it was concluded that taking simultaneous radiance measurements from an IBS at nadir and another viewing geometry, instead of taking simultaneous measurements of $L^{\downarrow}_{i}$ is more convenient since ε_r errors associated to the fluctuations of $L^{\downarrow}_{i}$ over time are not significant. However, possible LST changes when IBS radiance is measured at nadir and a time later at a given (θ,φ) configuration, could lead to more significant errors.

Chapter 4

Method for the atmospheric downwelling radiance measurement

Present chapter goes into detail about the radiative contribution of soil sample surrounding, both atmosphere and surrounding elements. A comparison study of *in situ* hemispherical downwelling radiance retrieval methods was carried out. The comparison was made under different environment conditions to assess *a posteriori* possible effect on emissivity retrievals.

4.1 *In situ* methods to retrieve $L^{\downarrow}_{i}$

Radiative contribution from the atmosphere and possible surrounding elements must be taken into account when measuring LST or surface emissivity, since surfaces are usually grey bodies ($\varepsilon < 1$), and a part of the incident hemispheric irradiance is reflected towards the sensor. Thus, inaccurate measurement of $L^{\downarrow}_{i}$ can give rise to significant errors in ε_r retrievals, since from Eq. (3.5) this radiance appears at both sides of the quotient. For this reason, a precise value of $L^{\downarrow}_{i}$ is needed; the most exact way to obtain $L^{\downarrow}_{i}$ is to measure the incoming spectral radiance from all possible zenithal and azimuthal directions $L^{\downarrow}_{i}(\theta,\varphi)$ later retrieving an integrated value according to:

$$L_i^{\downarrow} = \frac{\int_0^{2\pi} d\varphi \int_0^{\pi/2} L_i^{\downarrow}(\theta,\varphi) \sin\theta \cos\theta d\theta}{\int_0^{2\pi} d\varphi \int_0^{\pi/2} \sin\theta \cos\theta d\theta} \qquad (4.1)$$

These measurement processes takes a long time to be performed, which is particularly critical when retrieving ε_r values under cloudy skies, there exist some alternative methods to obtain $L^{\downarrow}_{i}$ values faster than the process of equation (4.1). These methods are dependent on atmospheric and surrounding conditions. For this reason, an intercomparison study between the different available methods were carried out (Garcia-Santos *et al.* 2012a) to check which of them is the most suitable to be performed in our study.

In situ measurements of $L^{\downarrow}_{i}$ in the present intercomparison study was conducted using a radiometer CIMEL Electronique (CE312-1, Brogniez *et al.* 2003), which is a multi-spectral sensor that measures the radiance emitted by a surface in the TIR region at four different spectral channels: channel 1(8.0 µm - 13.3 µm), channel 2 (11.5 µm - 12.4 µm),channel 3 (10.2 µm - 11.3 µm) and channel 4 (8.3 µm - 9.3 µm). A previous calibration of the CE312-1 thermal radiometer with a primary reference blackbody was carried out in April 2009 at the National Physical Laboratory in London, UK, organized by the Committee on Earth Observation Satellites (CEOS, Theocharous *et al.* 2010). Calibration results showed an uncertainty for measured radiative temperatures at four CE 312-1 spectral channels of: ±0.5 K, ±0.6 K, ±0.3 K and ±0.6 K, respectively.

Kondratyev approximation

Kondratyev (1969) showed that a single measurement taken pointing the radiometer at a zenith angle of 53 ± 3° from vertical, in any azimuthal directions, gave a close value of the hemispherical downwelling radiance of the current atmosphere:

$$L_{i\_Kond}^{\downarrow} = L_i^{\downarrow}(53°) \tag{4.2}$$

However, the Kondratyev approximation requires a specific atmospheric condition. This technique is applicable only under homogeneous skies (a sky completely clear or overcast). Moreover this method does not take into account the possible radiative contributions from surrounding elements such as buildings, cars, trees, etc.

Rubio approximation

Rubio *et al.* (1997) analyzed the angular dependence of downwelling atmosphere radiation. They carried out an experimental study from September 1991 to August 1992, measuring the atmospheric temperature for a total of 130 atmospheric conditions, ranging from completely clear days to overcast days with a uniform distribution of horizontal cloud layers. Rubio *et al.* (1997) carried out for a fixed φ orientation, several scans of the atmospheric temperatures, varying the zenithal inclination θ from 0° to 85° with5° intervals in both descending and ascending directions. They repeated zenithal measurements in two perpendicular orientations, north-south and east-west.

Figure 4.1 shows the zenithal evolution of atmospheric temperature at different atmospheric conditions for a fixed φ. Results show that the anisotropy of atmospheric radiation is much greater on clear days than on cloudy days. Moreover, temperature shows not significant changes in measurements performed close to the zenith. Results from Figure 4.2 show that dependence of atmospheric radiation on the azimuth is almost negligible. Rubio *et al.* (1997) integrated all these measurements according to Eq. (4.1) for all the 130 atmospheric conditions. Results showed that hemispherical downwelling radiance can be retrieved by measuring the atmospheric radiance at nadir (0°) and multiplying this radiance by a factor (γ), dependent on spectral range and atmospheric water vapor content (W, in cm), using the following relationship:

$$L_{i\_Rub}^{\downarrow} = \gamma_i(W) L_i^{\downarrow}(0°) \tag{4.3}$$

W is the amount of water (depth of vertical column of unit-crossectional area) which would be obtained if all the water vapor in a specified column of the atmosphere were condensed to liquid.

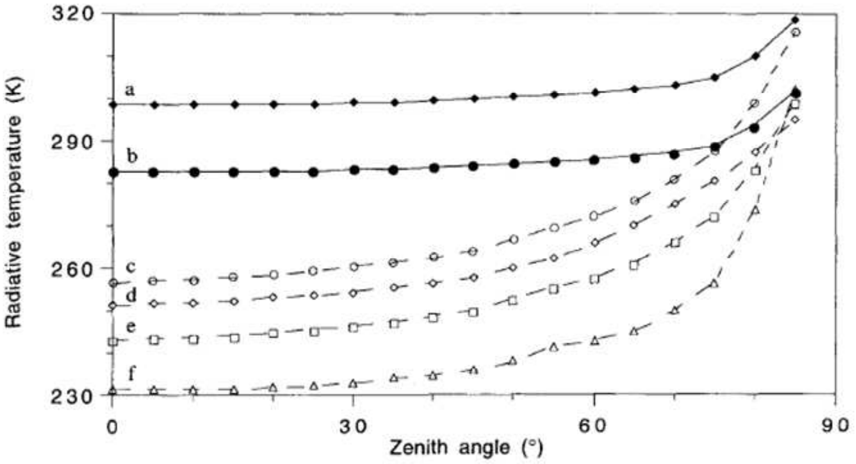

Figure 4.1 Dependence of the radiative temperature of the atmosphere on the zenith angle, for measurements in the 8-14 μm wave band, for days with different levels of cloudiness. Curves (a) and (b) correspond to days completely overcast (8 and 7 oktas, respectively), and curves (c), (d), (e), and (f) correspond to days completely clear (1, 0, 0, and 0 oktas, respectively). Results extracted from Figure 12 in Rubio *et al.* (1997).

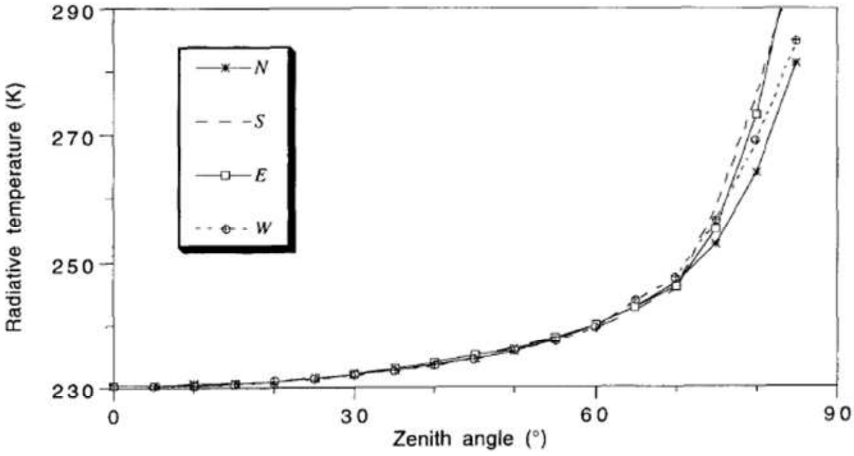

Figure 4.2 Dependence of the radiative temperature of the atmosphere on the zenith angle, for measurements in the range 8-14 μm, for four main orientations: north, south, east, and west. Results extracted from Figure 13 in Rubio *et al.* (1997).

Rubio *et al.* (1997) also corrected the diffusive zenithal angle stipulated by Kondratyev (1969) from 53 ± 3° to 55.4 ± 1.8°.

An adequate value of the γ coefficient is needed in Eq. (4.3), for this reason a simulation study (Garcia-Santos *et al.* 2012b) was previously carried out previously using the radiosounding data contained in the *Cloudless Land Atmosphere Radiosonde* (CLAR) database (Galve *et al.* 2008), which spans a W uniform interval from 0.02 to 5.61 cm and extends up to nearly 7 cm. The CLAR database is composed of 382 atmospheric profiles which are distributed in three latitude ranges, 40% of them placed at low latitudes (0°–30°), another 40% at mid-latitudes (30°–60°), and 20% placed at high latitudes (>60°). In this study only the profiles with W ranging from 0.7 to 5.5 cm were considered to simulate the same atmospheric conditions found in the experimental work of Rubio *et al.* (1997). The selected profiles were introduced into the radiative transfer code (RTC) MODTRAN 4v3r (Berk *et al.* 1999) to simulate values of $L^{\downarrow}_{i\_Rub}$ and $L^{\downarrow}_{i}(0°)$. According to Eq. (4.3), from these two sets of simulated radiances a γ(W) value was retrieved, which were regressed versus the corresponding W values obtained from each of the 180 atmospheric profiles. In addition to W, γ also depends on the spectral range, so this process was followed at the following four spectral ranges within TIR domain, which are coincident with the four spectral channels of CE 312-1 (Brogniez *et al.* 2003): 8-13 µm (Ch1), 11.5-12.5 µm (Ch2), 10.5-11.5 µm (Ch3) and 8.2-9.2 µm (Ch2). As a result of the described process, four empirical relationships were obtained to get each channel γ value from the value of W previously known by other means:

$$\gamma_{8-13\mu m} = 1.43 - 0.04W \tag{4.4}$$

$$\gamma_{11.5-12.5\,\mathrm{\mu m}} = 1.61 - 0.09W \tag{4.5}$$

$$\gamma_{10.5-11.5\,\mathrm{\mu m}} = 1.73 - 0.09W \tag{4.6}$$

$$\gamma_{8.2-9.2\,\mathrm{\mu m}} = 1.44 - 0.03W \tag{4.7}$$

These four relationships were validated with *in situ* measurements of W carried out with a CIMEL Electronique CE 318 sunphotometer (Holben *et al.* 1998) and with $L^{\downarrow}_{i}$ and $L^{\downarrow}_{i}(0°)$ measurements taken with two CE 312-1 Validation results of equations (4.4)-(4.7) with *in situ* data showed that these expressions enable γ values to be obtained with an uncertainty of ± 0.03. For more details, the published study of García-Santos *et al.* (2012b) can be found in *appendix A*.

Atmospheric profiles

As commented above, an alternative way to retrieve $L^{\downarrow}_{i}$ values is introducing atmospheric profiles into a RTC to obtain a simulated value of the atmosphere radiative contribution. In the present study, atmospheric profiles have been used, provided by the National Centers for Environmental Prediction (NCEP). These NCEP profiles, resulting from reanalysis techniques (Kalnay *et al.* 1995), were obtained from a Web-based tool Atmospheric Correction Parameter Calculator (Barsi *et al.* 2003), which needs a previous specification of date, time, and location to interpolate the desired atmospheric profile temporally and spatially at the time and place of the measurements. NCEP profiles generated by this system to incorporate satellite and ground data to characterize a global atmosphere at 28 altitudes, these profiles are sampled on a 1°×1° grid and are provided every 6h. From two options offered by this web-tool calculator, "*Use interpolated atmospheric profile for given lat/long*" was chosen; this option extracts a profile from the four grid corners which surround the input location for the two times before and after the input time, so corner profiles are interpolated for each time resulting in the desired time profiles.

Profiles obtained were processed with the MODTRAN 4v3r code (Berk *et al.* 1999), which provided $L^{\downarrow}_{i}(\theta)$ values for the zenith angles: 0.0°, 11.6°, 26.1°, 40.3°, 53.7°, 65.0°, 70.0°, 75.0°, 80.0°, 87.0° and 89.0°(the so-called Gaussian angles, Galve *et al.* 2008). Finally, $L^{\downarrow}_{i\_NCEP}$ was retrieved by integrating these values following Eq. (4.1). According to Barsi *et al.* (2003), uncertainties of ±6% and ±2 K were assigned to relative humidity and atmospheric temperature, respectively, on the NCEP atmospheric profiles. The difference of $L^{\downarrow}_{i\_NCEP}$, obtained with the original atmospheric profile and that obtained with a profile modified with the previous uncertainties, implies a relative error of 20% in $L^{\downarrow}_{i\_NCEP}$ values for all the spectral channels of CE312-1.

Diffuse reflectance plate

According to Kubelka and Munk (1931) theory, a material is able to reflect the spectral incoming radiance in a diffusive manner, if it presents a weak absorption for the incoming radiance which penetrates into the material with deepness greater than its own wavelength. One of the most reflective materials in the TIR region is gold, so for this reason a gold coated surface which presents a roughness larger than 14 μm (since TIR radiation ranges between 8-14 μm), must be able to reflect TIR incoming radiance from surroundings (atmosphere, buildings, objects, etc.). In the present study a gold diffuse panel was used with near-Lambertian behavior, able to retrieve $L^{\downarrow}_{i}$ by taking a single measurement of the reflected radiance on the panel. The panel model used was the *Infragold Reflectance Target IRT-94-100* (Figure 4.3), a gold rugged surface (0.5 cm deepness) of 25.4 x 25.4 cm^2 and 1 cm of thickness.

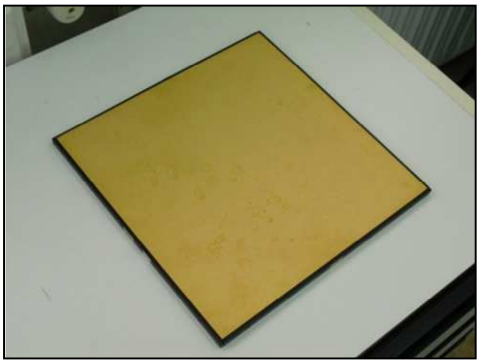

Figure 4.3 *Infragold Reflectance Target IRT-94-100*, diffusive gold panel.

The Gold diffusive panel also has a contribution to the measured signal due to the small emissivity of the gold rugged surface. This contribution must be removed from the direct measurements made over the panel according to Korb *et al.* (1996) through the expression:

$$L^{\downarrow}_{i\_panel} = \frac{L^{\downarrow}_{panel} - \varepsilon_{panel} B(T_{panel})}{(1 - \varepsilon_{panel})} \tag{4.8}$$

where $L^{\downarrow}_{panel}$ is the radiance measured directly on the panel, ε_{panel} is its emissivity, and T_{panel} is the temperature of the panel that must be known to calculate Planck function $B(T_{panel})$. A contact thermometer, with an accuracy of ±1 °C, was used to measure the temperature of the panel, this accuracy implies an error in estimating $L^{\downarrow}_{i\_panel}$ of ±0.09 $Wm^{-2}sr^{-1}\mu m^{-1}$ for all the channels of CE 312-1.

An intercomparison study of these four methods was carried out (García-Santos *et al.* 2012a). The four methods were compared under three different conditions: (i) For a cloudless day in a location with a minimal contribution of surrounding elements, (ii) for the same cloudless day but in a location with significant presence of contributive surrounding elements, and iii) in the same location as (i) but for a day with time-changing cloud coverage. For more details, the published study of García-Santos *et al.* (2012a) can be found in *appendix B*.

4.2 Comparison of $L^{\downarrow}_{i}$ retrieval methods in different environments

The first evaluation was made at two different places with a significant difference of surrounding elements between them (Figure 4.4). The aim was to check possible differences between methods due to the presence of radiative surrounding elements with temperatures comparable to the observed surface. Both locations chosen were located in the University of Valencia’s Burjassot campus, Spain (39°30’25’’N, 0°18’15’’W). The first location was located at the roof of the Physics Faculty (*roof*, Figure 4.4(a)), this site is characterized by the minimal presence of surrounding elements (scientific instrumentation and roves of surrounding buildings higher than this building). The second location was located near the campus library (*library*, Figure 4.4(b) and (c)), where the presence of surrounding elements is significantly greater than those on the *roof* (trees, cars, and different buildings).

The four analyzed methods to retrieve $L^{\downarrow}_{i}$ were compared using measurements performed during four days with cloud-free sky conditions, by means of two CE 312-1 (see *Rubio approximation* in section 4.1). Figure 4.4 shows the experimental setup, where $L^{\downarrow}_{i\_panel}$ was obtained taking radiance measurements on the diffuse reflectance panel, correcting the panel emissivity according to Eq. (4.8). Simultaneously to the panel radiance measurements, the other CE312-1 took radiance measurements of the sky, $L^{\downarrow}_{i}(0°)$, required in Eq. (4.3) to obtain $L^{\downarrow}_{i\_Rub}$, and at 55° to obtain $L^{\downarrow}_{i\_Kond}$. The time period between the two consecutive radiance measurements was around 3 minutes, short enough to consider that $L^{\downarrow}_{i}$ between both methods is comparable to the panel measurements. In each case the measurements were performed within time intervals of 15 minutes, during this period of time $L^{\downarrow}_{i}$ should not change significantly considering the stable atmospheric conditions (cloud free, no wind).

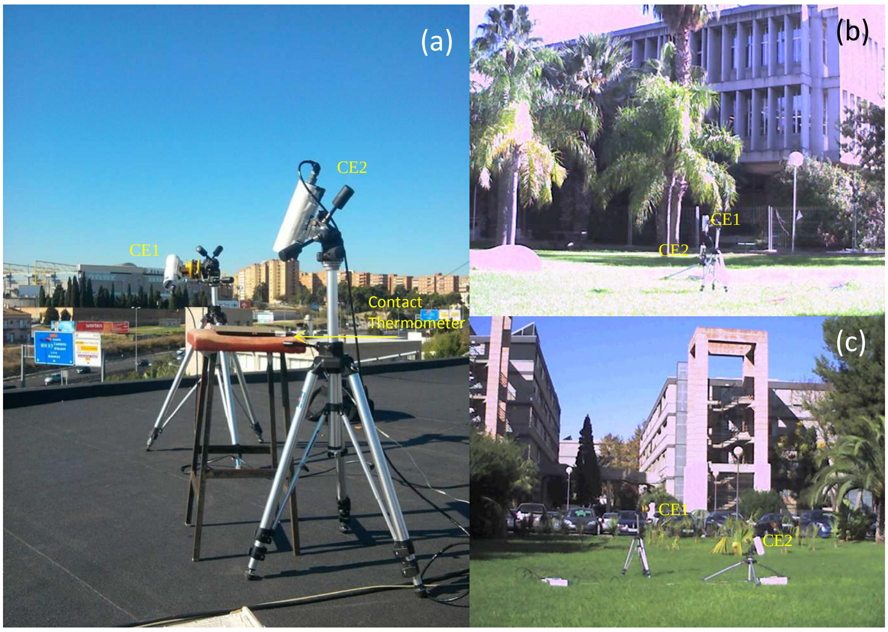

Figure 4.4 Experimental assemblies used to perform the irradiance measurements on the diffuse reflectance panel, with a CE312-1 radiometer (CE2) mounted on a tripod and measuring to the panel, at 25° zenith angle. A second CE312-1 radiometer (CE1) was mounted on a tripod for measuring the irradiance from sky, pointing it at 0° and 55°. This assembly was mounted in two different places: (a) Roof of the Physics Faculty (with minimal presence of surrounding elements), and (b) and (c) close to the University Library (with presence of surrounding elements such as buildings, trees, and cars).

Table 4.1 shows the $L^{\downarrow}_{i}$ average values measured during the 15-minutes time interval at the *roof* location, for the four considered days and different methods (including the $L^{\downarrow}_{i\_NCEP}$ retrieved from NCEP profiles and the MODTRAN RTC). Differences between methods are less than 0.38 $Wm^{-2}sr^{-1}\mu m^{-1}$, and mostly within the measurement errors. NCEP method presents the largest differences at all spectral channels (with exception of channel 3 placed at 10.2–11.3 μm) with regard to the three other methods, nevertheless these differences can be explained in terms of the errors associated to the $L^{\downarrow}_{i\_NCEP}$ methodology. From these results, it may be concluded that, under clear-sky conditions and in places where the surrounding elements have a minimal radiative contribution, the different approaches produce comparable results.

Table 4.1. $L^{\downarrow}_{i}$ average values measured at the roof of the Physics Faculty building (*roof*) for four measurement days, with their errors given in brackets, using the three analyzed *in situ* methods. The $L^{\downarrow}_{i}$ value retrieved from NCEP profiles and the MODTRAN RTC is also given.

Date (dd/mm/yyyy)	$L^{\downarrow}_{i}$ (Ch1: 8-13.3 μm) [W m^{-2} sr^{-1} μm^{-1}]				$L^{\downarrow}_{i}$ (Ch2: 11.5-12.4 μm) [W m^{-2} sr^{-1} μm^{-1}]			
	$L^{\downarrow}_{i\_panel}$	$L^{\downarrow}_{i\_Kond}$	$L^{\downarrow}_{i\_Rub}$	$L^{\downarrow}_{i\_NCEP}$	$L^{\downarrow}_{i\_panel}$	$L^{\downarrow}_{i\_Kond}$	$L^{\downarrow}_{i\_Rub}$	$L^{\downarrow}_{i\_NCEP}$
12/10/2011	**3.69** [0.13]	**3.63** [0.10]	**3.6** [0.3]	**3.4** [0.6]	**3.31** [0.09]	**2.86** [0.09]	**3.0** [0.2]	**2.7** [0.5]
19/10/2011	**3.63** [0.10]	**3.66** [0.13]	**3.5** [0.3]	**3.5** [0.6]	**3.37** [0.09]	**3.15** [0.13]	**3.2** [0.2]	**3.0** [0.6]
25/10/2011	**2.83** [0.10]	**2.87** [0.10]	**3** [0.2]	**2.6** [0.5]	**2.58** [0.09]	**2.39** [0.09]	**2.6** [0.2]	**2.1** [0.4]
9/11/2011	**2.71** [0.10]	**2.68** [0.10]	**2.9** [0.2]	**2.9** [0.5]	**2.42** [0.10]	**2.13** [0.10]	**2.26** [0.19]	**2.3** [0.5]
	$L^{\downarrow}_{i}$ (Ch3: 10.2-11.3 μm) [W m^{-2} sr^{-1} μm^{-1}]				$L^{\downarrow}_{i}$ (Ch4: 8.3-9.3 μm) [W m^{-2} sr^{-1} μm^{-1}]			
	$L^{\downarrow}_{i\_panel}$	$L^{\downarrow}_{i\_Kond}$	$L^{\downarrow}_{i\_Rub}$	$L^{\downarrow}_{i\_NCEP}$	$L^{\downarrow}_{i\_panel}$	$L^{\downarrow}_{i\_Kond}$	$L^{\downarrow}_{i\_Rub}$	$L^{\downarrow}_{i\_NCEP}$
12/10/2011	**2.26** [0.10]	**1.97** [0.06]	**1.9** [0.2]	**2.1** [0.4]	**3.34** 0.16	**3.09** [0.13]	**3.2** [0.4]	**2.7** [0.5]
19/10/2011	**2.36** [0.13]	**2.29** [0.10]	**2.2** [0.3]	**2.3** [0.4]	**3.06** [0.13]	**2.71** [0.16]	**2.5** [0.4]	**2.7** [0.5]
25/10/2011	**1.72** [0.06]	**1.66** [0.06]	**1.81** [0.19]	**1.5** 0.3	**2.39** [0.13]	**2.01** [0.13]	**2.0** [0.3]	**2.0** [0.4]
9/11/2011	**1.53** [0.06]	**1.46** [0.06]	**1.40** [0.16]	**1.8** [0.4]	**2.29** [0.16]	**1.91** [0.13]	**2.01** [0.3]	**2.2** [0.4]

Table 4.2. $L^{\downarrow}_{i}$ average values measured close to the university library building (*library*) for four measurement days, with their errors given in brackets, using the three analyzed *in situ* methods. The $L^{\downarrow}_{i}$ value retrieved from NCEP profiles and the MODTRAN RTC is also given.

Date	$L^{\downarrow}_{i}$ (Ch1: 8-13.3 μm) [W m^{-2} sr^{-1} μm^{-1}]				$L^{\downarrow}_{i}$ (Ch2: 11.5-12.4 μm) [W m^{-2} sr^{-1} μm^{-1}]			
(dd/mm/yyyy)	$L^{\downarrow}_{i\_panel}$	$L^{\downarrow}_{i\_Kond}$	$L^{\downarrow}_{i\_Rub}$	$L^{\downarrow}_{i\_NCEP}$	$L^{\downarrow}_{i\_panel}$	$L^{\downarrow}_{i\_Kond}$	$L^{\downarrow}_{i\_Rub}$	$L^{\downarrow}_{i\_NCEP}$
12/10/2011	**4.6** [0.2]	**3.69** [0.13]	**3.7** [0.3]	**3.4** [0.6]	**4.0** [0.2]	**2.96** [0.13]	**3.0** [0.2]	**2.7** [0.5]
19/10/2011	**4.17** [0.10]	**3.95** [0.10]	**3.7** [0.3]	**3.5** [0.6]	**3.82** [0.10]	**3.37** [0.10]	**3.3** [0.3]	**3.0** [0.6]
25/10/2011	**3.88** [0.10]	**3.0** [0.2]	**2.9** [0.2]	**2.6** [0.5]	**3.47** [0.10]	**2.51** [0.13]	**2.6** [0.2]	**2.1** [0.4]
9/11/2011	**3.66** [0.10]	**2.86** [0.10]	**3.1** [0.2]	**2.9** [0.6]	**3.25** [0.10]	**2.32** [0.10]	**2.5** [0.2]	**2.3** [0.5]
	$L^{\downarrow}_{i}$ (Ch3: 10.2-11.3 μm) [W m^{-2} sr^{-1} μm^{-1}]				$L^{\downarrow}_{i}$ (Ch4: 8.3-9.3 μm) [W m^{-2} sr^{-1} μm^{-1}]			
	$L^{\downarrow}_{i\_panel}$	$L^{\downarrow}_{i\_Kond}$	$L^{\downarrow}_{i\_Rub}$	$L^{\downarrow}_{i\_NCEP}$	$L^{\downarrow}_{i\_panel}$	$L^{\downarrow}_{i\_Kond}$	$L^{\downarrow}_{i\_Rub}$	$L^{\downarrow}_{i\_NCEP}$
12/10/2011	**3.2** [0.2]	**2.07** [0.15]	**2.0** [0.3]	**2.1** [0.4]	**4.2** [0.2]	**3.2** [0.2]	**3.3** [0.5]	**2.7** [0.5]
19/10/2011	**2.96** [0.06]	**2.51** [0.06]	**2.4** [0.3]	**2.3** [0.4]	**3.66** [0.13]	**2.90** [0.13]	**2.6** [0.4]	**2.7** [0.5]
25/10/2011	**2.83** [0.06]	**1.75** [0.10]	**1.8** [0.2]	**1.5** [0.3]	**3.44** [0.13]	**2.1** [0.2]	**2.0** [0.3]	**2.0** [0.4]
9/11/2011	**2.55** [0.06]	**1.59** [0.06]	**1.5** [0.2]	**1.8** [0.4]	**3.25** [0.13]	**2.04** [0.13]	**2.1** [0.3]	**2.2** [0.4]

Things are different when the surface roughness is significant and the surrounding elements cannot be avoided, for instance, when measuring in areas with buildings or vegetation elements such as trees, which are placed close to the surface being measured. Table 4.2 shows the same results for $L^{\downarrow}_{i}$ as in Table 4.1, but from the *library* location (see Fig. 4.4 (b) and (c)). It is interesting to check that for a place surrounded by important radiative contributive elements, $L^{\downarrow}_{i}$ values provided by Kondratyev, Rubio *et al.*, and NCEP methods are all close to each other showing differences lower than 0.48 W m^{-2} $sr^{-1}\mu m^{-1}$ and similar to the *roof* location (Table 4.1), since the time difference between the measurements at the *roof* and *library* places was less than 40 minutes (time needed to move instrumentation from one to another place). However, panel measurements present a significant increase in the *library* compared to the *roof* place (on the order of 0.95 $Wm^{-2}sr^{-1}\mu m^{-1}$) that produces a significant difference with regard to the rest of the methods.

The explanation of this increase is quite simple; the panel has proven to take into account the surrounding radiative contribution coming from close elements. Differences between $L^{\downarrow}_{i\_panel}$ and $L^{\downarrow}_{i}$ from the other methods, for all the measurement days, show an average increase for CE 312-1 channels 1–4 of: 0.83, 0.89, 0.95, and 1.15 $Wm^{-2}sr^{-1}\mu m^{-1}$, respectively. These increases mean that not taking into account the environment contribution can lead to an underestimation of the true $L^{\downarrow}_{i}$ value at four CE 312-1 spectral channels of 37%, 43%, 68% and 66%, respectively, for the case analyzed in this work. From these results it may be concluded that, under clear-sky conditions for places where presence of surrounding elements is important, measuring $L^{\downarrow}_{i}$ using a diffuse reflectance panel is the most recommended option, since it takes into account the radiative contributions of the existing surroundings elements.

4.3 Comparison of $L^{\downarrow}_{i}$ retrieval methods under a changing cloud cover sky

A second comparison was carried out at the *roof* location to evaluate $L^{\downarrow}_{i}$ retrieval methods under a sky with a cloud coverage changing over time, since clouds can probably modify $L^{\downarrow}_{i}$ considerably. The choice of the r*oof* location was based on the minimal contribution of the surroundings elements as has been shown previously. The four methods to retrieve $L^{\downarrow}_{i}$ were compared under different percentages of clouds occupying the sky for two different days; the first day with the presence of cumulus clouds and the second one with the presence of cirrus clouds. In both cases clouds were moving through the sky over time. A CE 312-1 instrument was measuring continuously, pointing at the panel, and the other radiometer was simultaneously measuring pointing at the sky at 55° ($L^{\downarrow}_{i\_Kond}$), every 30–60 min. The CE 312-1 radiometer taking measurements at 55°, was pointed at the sky at 0° to retrieve $L^{\downarrow}_{i\_Rub}$. Atmospheric profiles from NCEP (unavailable for the day with presence of cirrus) were downloaded every 30 min and also processed. Additionally, a camera SONA Automatic Cloudiness Observation System located on the *roof* (Serrano *et al.* 2013), took a photograph of the upper hemisphere every 5 minutes, these photos were processed to retrieve the percentage of cloud coverage with an error of ±10%.

Figure 4.5 shows the evolution over time of $L^{\downarrow}_{i}$ retrieved using each one of the methods considered in this work at four CE 312-1 spectral channels, for the two measurement days. Figure 4.5(a) shows the results for a sky with cumulus clouds. $L^{\downarrow}_{i\_Kond}$ and $L^{\downarrow}_{i\_Rub}$ present large fluctuations of their values not following the cloud coverage evolution. Sharp changes observed for these two methods are due to the accidental passage of a cloud in front of the radiometer's FOV. It is shown that when the cloud is out of the FOV the measured values fall suddenly to lower values corresponding to clear-sky areas (see $L^{\downarrow}_{i\_Kond}$ values at 10:40 A.M., 11:27 A.M. and 12:17 P.M., and $L^{\downarrow}_{i\_Rub}$ values at 12:30 P.M. and 1:00 P.M., for instance). Thus, for partial cloud cover conditions, the Kondratyev and Rubio approaches are not able to capture the real value of $L^{\downarrow}_{i}$, since these methods measure radiance in excess when viewing a cloud, and by defect when they are viewing the clear sky. Results from NCEP atmospheric profiles are also unsuccessful, since this simulated value cannot take into account the presence of clouds, matching up with the other methods just when the cloud coverage is lower than 10%. On the contrary, $L^{\downarrow}_{i\_panel}$ retrievals follow the cloud coverage evolution over time almost concurrently. Results from the panel measurements show that this technique takes into account the decrease and increase of clouds in the sky, making its radiance values representative of real sky conditions.

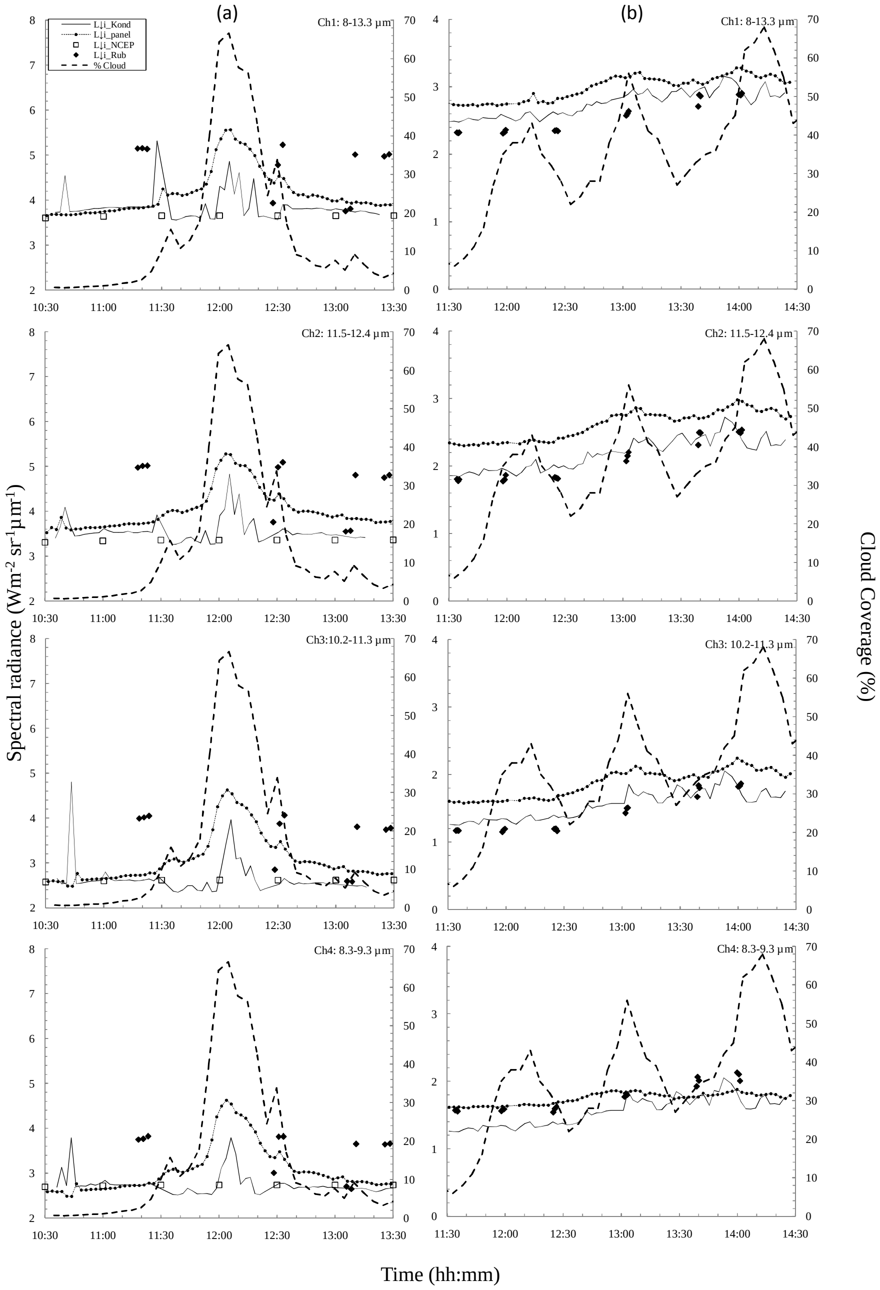

Figure 4.5 Measurements of L$^{\downarrow}_{i}$ over time obtained with Kondratyev approximation(solid line), (solid line) Rubio *et al.* approximation(solid line), NCEP profiles with the MODTRAN code(empty squares), and the diffuse reflectance panel(dotted line), on a day with (a) heterogeneous sky with presence of cumulus clouds, and (b) heterogeneous sky with cirrus clouds. Cloud coverage given in percent (dashed line), retrieved from a camera SONA Automatic Cloudiness Observation System (Serrano *et al.* 2013) is also presented.

For instance, $L^{\downarrow}_{i\_panel}$ value from 11:40 A.M. to 12:00 P.M. increases around +1.46 $Wm^{-2}sr^{-1}\mu m^{-1}$ in the four CE 312-1 channels, for an increase of 56% in cloud coverage. These increases can lead to the underestimation of the true $L^{\downarrow}_{i}$ values at four CE 312-1 spectral channels of 53%, 49%, 71% and 72%, respectively. The magnitude of that error will depend on the cloud coverage percentage, cloud type, cloud temperature, etc. For instance, Figure 4.5(b) shows the results for a sky with cirrus clouds present, where: (i) the magnitude of the irradiance is half the irradiance for the cumulus case, and (ii) the four methods used to measure the radiance present more comparable values in this case, with differences to each other within ±0.32 $Wm^{-2}sr^{-1}\mu m^{-1}$at the four CE312-1 spectral channels, being almost independent of cloud coverage. Thus, for this type of clouds each methodology proposed can be used since systematic errors produced are lower than in the cumulus case. In any case, an important conclusion is that under changing cloud coverage conditions, only a diffuse reflectance panel guarantees an adequate measurement of $L^{\downarrow}_{i}$.

4.4 Effects of $L^{\downarrow}_{i}$ inaccuracies on TIR emissivity retrievals

It has been shown in chapter 3 (section 3.3) that $L^{\downarrow}_{i}$ measurements taken every 18 minutes with a diffusive panel, fluctuate around ±4% from their average value. This fluctuation taken as relative error implies that to retrieve $\varepsilon_r(\theta,\varphi)$ through Eq. (3.5) with an uncertainty of ±0.0005, a value six times lower than the average error, and twenty times lower than the maximum $\delta\varepsilon_r(\theta,\varphi)$ must be considered.

Nevertheless, the present chapter has shown that using an inadequate method can lead to significant inaccuracies in $L^{\downarrow}_{i}$ retrievals. More specifically, not using a diffusive panel under heterogeneous skies, or when the presence of radiative surrounding elements is important, can underestimate $L^{\downarrow}_{i}$ up to 72% from its true value, depending on the spectral region. Since we used a panel to retrieve $L^{\downarrow}_{i}$, and subsequently $\varepsilon_r(\theta)$ by Eq. (3.5), it is interesting to check the effect on $\varepsilon_r(\theta)$ when $L^{\downarrow}_{i}$ is underestimated by the mentioned percentages at each spectral interval. Figure 4.6 shows the difference between $\varepsilon_r(\theta,\varphi)$ retrieved through Eq. (3.5) when the $L^{\downarrow}_{i}$ value is reduced by the maximum underestimated percentage (given for the case of a sky with cumulus clouds), and $\varepsilon_r(\theta,\varphi)$ for the $L^{\downarrow}_{i}$ originally measured. These differences were calculated at each specific zenithal angle measured for all IBS samples at all CE 312-2 spectral channels and SM values. Results show that the underestimation effect is important from θ=20° (overestimating ε_r more than 0.01), and the difference increases with θ overestimating ε_r up to values close to 0.09 at θ=70°. The main conclusion from this study is that an adequate measurement of $L^{\downarrow}_i$ needs to take into account both the contribution of the surroundings, as well as the possible presence of clouds, which is particularly important in field measurements performed continuously over a given area, for this reason the use of a diffusive reflectance panel could be the best alternative.

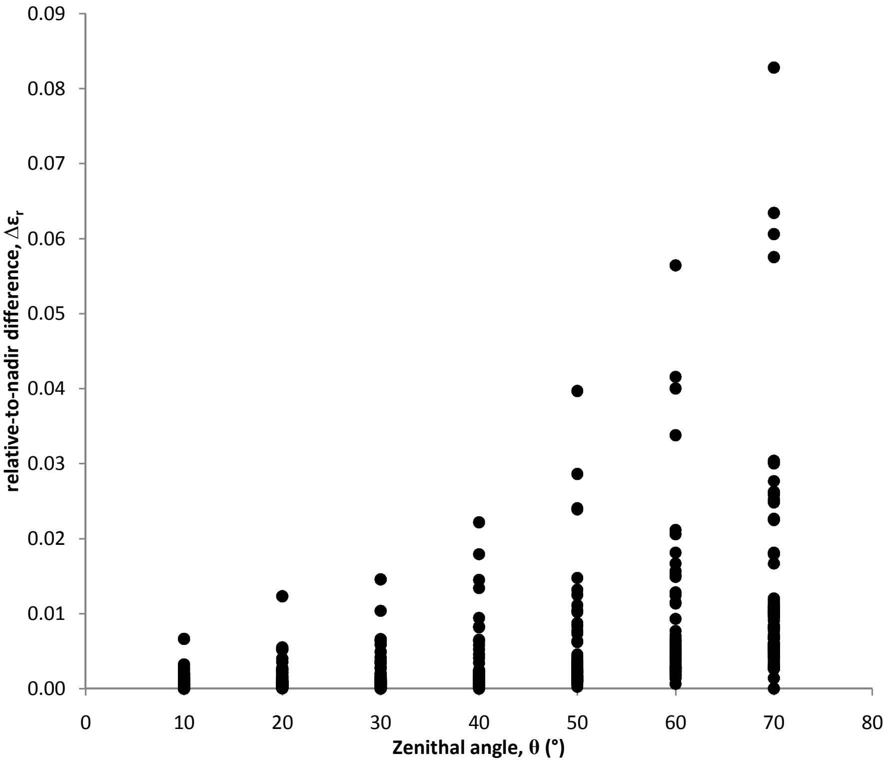

Figure 4.6 Difference between $\varepsilon_r(\theta,\varphi)$ when $L^{\downarrow}_i$ measured value is reduced by the maximum underestimated percentage, and $\varepsilon_r(\theta,\varphi)$ for the $L^{\downarrow}_i$ originally measured, at each specific zenithal angle measured for all IBS samples, CE 312-2 spectral channels and SM values.

Chapter 5

Anisotropy of IBS emissivity

Next chapter shows the results of the relative-to-nadir emissivity anisotropy study for chosen mineral soils, both for azimuth and zenith angles. Subsequently effect of soil moisture on emissivity anisotropy is evaluated and a regressed equation is implemented to calculate an emissivity value with a previous knowledge of soils moisture, viewing angle and some soil compositional parameters. Chapter ends with a simulation study that evaluates the error retrieving the surface temperature or the outgoing longwave flux when soil moisture and anisotropy effects are not taken into account.

5.1 Azimuthal variation of ε_r

In studies of Labed and Stoll (1991), or Sobrino and Cuenca (1999), it is supposed that TIR emissivity of IBS is azimuthally isotropic; only in Lagouarde *et al.* (1995), for a specific roughness level of a single IBS it is shown that emissivity is unchanging with azimuth. The present study checks the possible azimuthal variations of our IBS samples by means of next reasoning.

For a given θ, TIR relative emissivity was retrieved at three different azimuths (turning the IBS sample 120° each time, see chapter 3), and from these three ε_r values it was calculated the difference:

$$\Delta\varepsilon_r(\theta) = MAX[\varepsilon_r(\theta,\varphi)] - min[\varepsilon_r(\theta,\varphi)] \tag{5.1}$$

where $MAX[\varepsilon_r(\theta,\varphi)]$ is the maximum ε_r value obtained changing the φ angle, and $min[\varepsilon_r(\theta,\varphi)]$ is the minimum ε_r value obtained at other φ, always for the same zenith angle θ. Figure 5.1 shows the histogram of these differences for all CE 312-2 spectral channels, at all IBS samples, SM levels and θ angles.

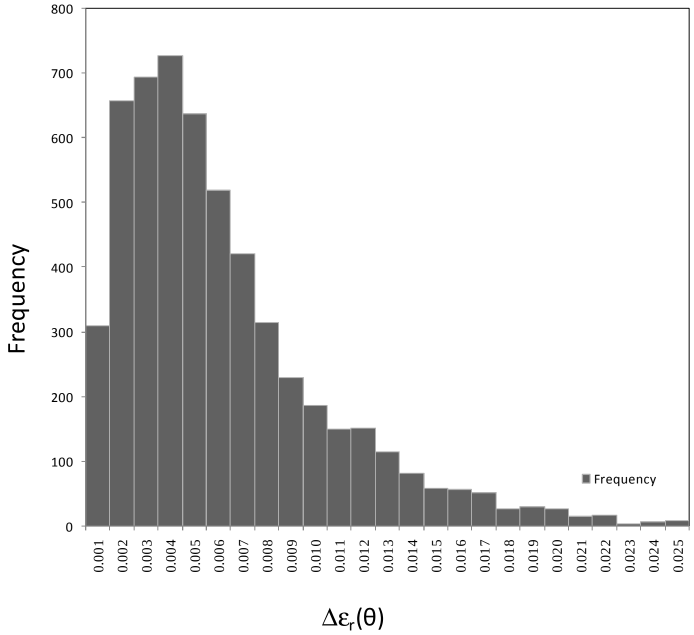

Figure 5.1 Maximum difference between $\varepsilon_r(\theta, \varphi)$ at different azimuth angles φ for a specific zenith angle θ. Values of $\Delta\varepsilon_r(\theta)$ are for all IBS, at the six spectral CE 312-2 channels, for all SM contents, and all zenith angles θ values considered (around 5500 values).

Results from Figure 5.1 show that 85.3 % of $\Delta\varepsilon_r(\theta)$ values are lower or equal than 0.01 (maximum error associated to ε_r measurements, section 3.3 in chapter 3) and the average value is 0.006 with a standard deviation $\sigma = \pm0.004$. So it could be concluded that IBS can be considered almost invariant azimuthally, since changes between two different φ orientations seldom is greater than 0.01.

Hereafter only variation of ε_r with θ is considered in the present work, since it was measured nine times $\varepsilon_r(\theta)$ (3 repetitions x 3 φ) an average value of these nine measurements was retrieved and error associated to this averaged $\varepsilon_r(\theta)$ value was the greatest of:

i) Propagation error through Eq. (3.5), associated to CE312-2 temperature uncertainty of ±0.19°C (see section 3.2). Except in case of $L^{\downarrow}_{i}$, which is given by ±4% fluctuation of this radiance, because it was measured at 18 minutes intervals.

ii) Standard Deviation calculated from nine $\varepsilon_r(\theta,\varphi)$ values retrieved for a specific (θ,φ) configuration, since radiance from IBS at this configuration is measured three times.

iii) Difference between maximum and minimum value of $\varepsilon_r$at a specific θ, divided by four.

5.2 Zenithal variation of ε_r under dry conditions

Figure 5.2 shows the zenithal variation of ε_r for the thirteen IBS samples studied at all six spectral intervals covered by CE 312-2 channels under dry conditions, for additional details see published work of Garcia-Santos *et al.* (2012c) which can be found in *appendix C*. Results show as main conclusion that emissivity decreases with θ for all IBS studied at all spectral ranges within the TIR region (8-14 µm). Nevertheless, the scale of this decreasing is strongly affected by the spectral range and soil composition.

Results of Figure 5.2 lead to another important conclusion: the decrease of ε_r with θ becomes significant from 60° independently on soil composition or spectral range where it is measured. However, analyzing in detail zenithal decrease of ε_r at specific spectral range it is shown how important IBS composition is.

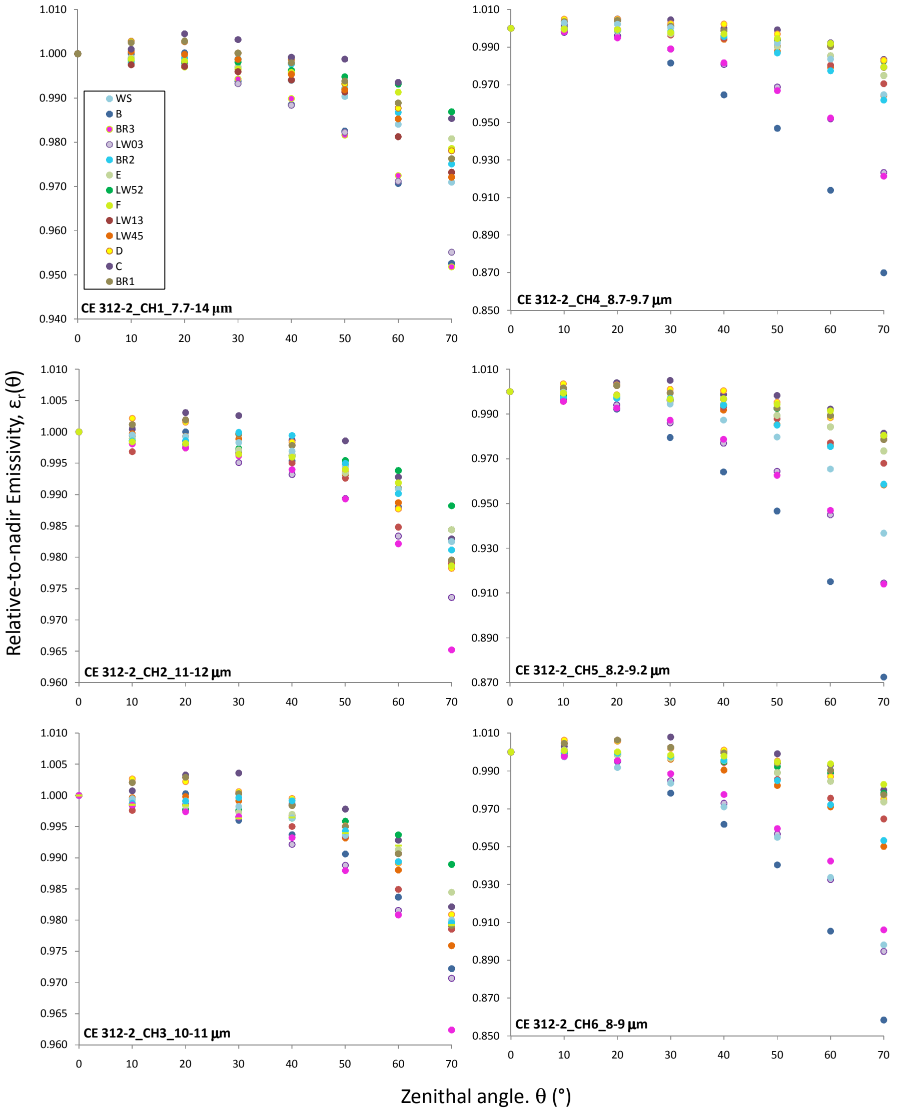

Figure 5.2 Zenithal variation of relative-to-nadir emissivity for the thirteen IBS samples studied, under dry conditions, at all six spectral channels of CE 312-2.

8-14 µm (CE 312-2 channel 1)

Within the so called *atmospheric window* it is observed that zenithal variation of ε_r is significant from $\theta \geq 60°$. Sandy samples with high quartz content (B, BR3 and LW03) showed significant decreases of their emissivities from 40°, probably on account of quartz reststrahlen band effect (Elachi et. al. 2006) at 8-9 µm range. Significant falls of ε_r from nadir range between 1-5 %, depending on soil composition.

10-12 µm (CE 312-2 channels 2 and 3)

IBSs present the lowest decrease of ε_r with θ respect to nadir at this spectral range, being significant from 60° (except samples BR3 and LW03, being at 50°). Emissivity falls between 1-4 % from its nadir values.

8-9.4 µm (CE 312-2 channels 4, 5 and 6)

Decrease of ε_r with θ acquires a great interest at spectral range 8-9.4 µm. Results from Figure 5.2 show a variety of different conclusions at each IBS composition type.

Clayey and loamy-clayey IBS samples (BR1, LW52, F, C and D) show decreases of ε_r from 60° with relative falls of 1-3 %. Loamy-sandy and loamy-silty soils (BR2, LW13, E and LW45) show a significant fall of ε_r from 50°, with drops between 1-5 %. Finally, sandy soils (WS, B, BR3 and LW03) give the most interesting results. Decreases of ε_r with θ for these soils are significant from 30° and present falls of its emissivity from nadir values up to 14%. Possibly the reason of such decreases can be attributed to high percentages of quartz (B, BR3 and LW03) and gypsum (WS) in their sand content. Quartz and gypsum present a characteristically molecular absorption in TIR region, reflectivity of these minerals between 7.7-9.7 µm increases at the so called *reststrahlen frequency* (Elachi et. al. 2006).

In summary, when a mineral soil presents dehydration conditions, the emissivity is relatively isotropic when clay is present; on the contrary, sand composed by quartz or gypsum makes the emissivity to decrease with increasing zenith angles, being significant for angles greater than 30°.

5.3 Effect of SM on zenithal variation of TIR ε

Effect of SM on $\varepsilon_r(\theta)$ shows dissimilar results at different type of IBS and at different spectral ranges. Discussions about this study, carried out during a whole year campaign, are exposed straightaway classified by IBS textural class (Garcia-Santos *et al.* 2013). Additional details of this study, currently under revision, can be found in *appendix D.*

Sandy soils

Figure 5.3 shows graphs of ε_r versus SM at six spectral intervals covered by CE 312-2 channels. Results are retrieved from IBS sample B since this sample is representative of sandy soils: WS, BR3 and LW03.

Starting from conclusions exposed in section 5.2 for a soil under dry conditions, when SM increase in a sandy IBS, anisotropy of ε_r shows a strong dependence on spectral range in which it has been measured. From results of Figure 5.3 it can be concluded that the increase of SM does not show noticeable effect on TIR ε_r at spectral ranges 8-14 μm and 10-12 μm. However, the increase of water content produces a reduction of the decrease of ε_r with zenith angle θ at spectral range 8-9.4 μm; the difference in the emissivity decrease between dry and saturated conditions reaches relative values between 1-7 % from $\theta \geq 40°$.

The reason of this behavior can be understood through the anisotropy study of water ε_r. In Cuenca and Sobrino (2004) it was observed that ε_r of a water sample decreased from nadir around a 4 % at spectral ranges 8-14 μm and 10-12 μm, and around a 6 % at 8-9.4 μm for a zenith angle θ=60°. Decrease of ε_r for a sandy soil at θ=60° is around 2 % at spectral ranges 8-14 μm and 10-12 μm, and between 4-9 % at 8-9.4 μm. When water content increases in an IBS, the emissivity measured is an effective value composed of ε_r of sandy soil and that of water weighted by the percentage of each one, in a first approximation.

For instance, in sandy soils (for which water retention is usually lower than 40 %), it is not appreciated the effect of SM on ε_r for a given θ (for instance 60°) at spectral ranges 8-14 μm and 10-12 μm, since the zenithal decrease of ε_r of water is not greater than that of the soil. However, SM effect on ε_r is quite noticeable at 8-9.4 μm, since emissivity decrease of water at 60° is usually much lower than emissivity of sandy soils at the same zenith angle, resulting in a lower decrease of ε_r with increasing viewing angle θ, as long as SM is increasing. SM effect is much noticeable at 70° showing difference of ε_r between saturated and dry conditions around 4 %.

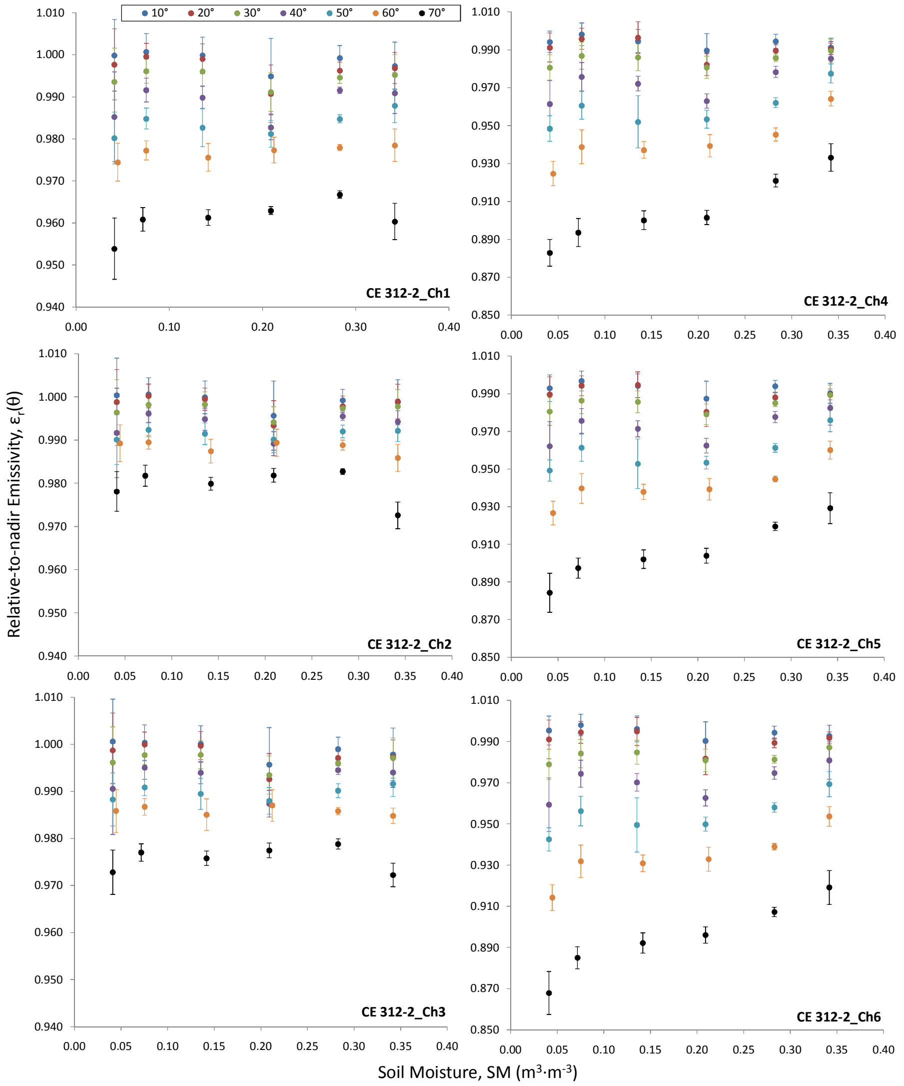

Figure 5.3 Zenithal variation of relative-to-nadir emissivity for IBS sample B as function of SM content at six CE 312-2 spectral channels. Results of sample B are representative of sandy soils and can be extended to the other sandy IBS samples: WS, BR3 and LW03.

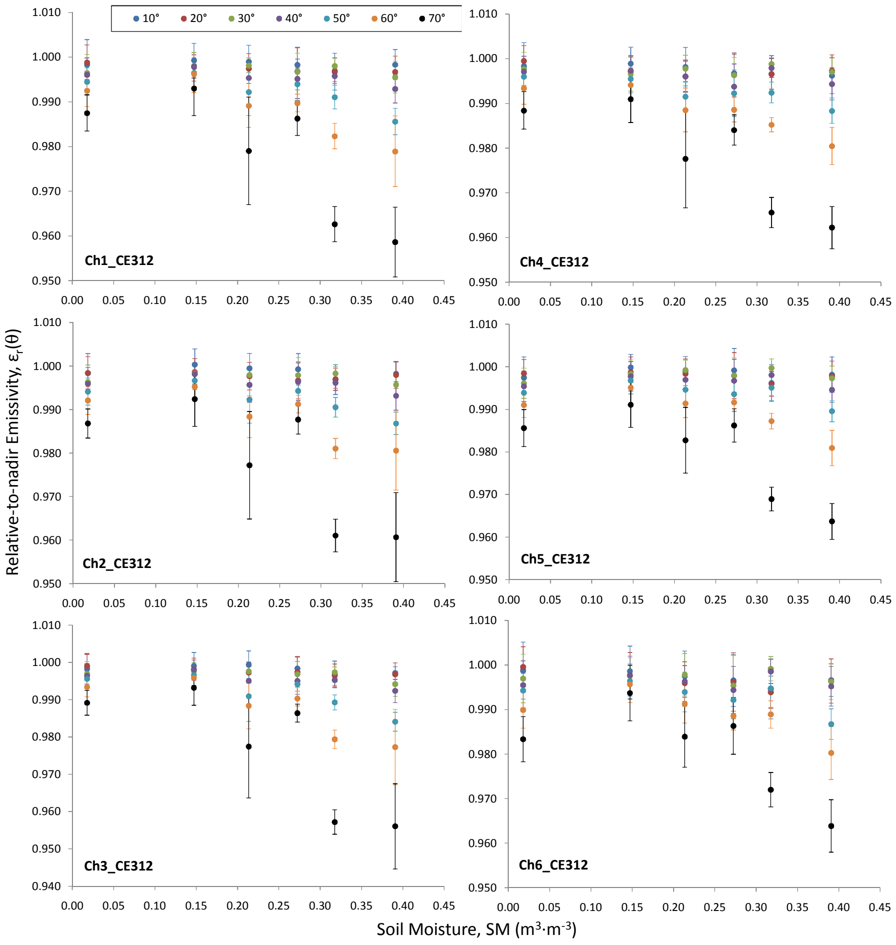

Figure 5.4 Zenithal variation of relative-to-nadir emissivity for IBS sample F as function of SM content at six CE 312-2 spectral channels. Results of sample B are representative of loamy soils and can be extended to the other loamy IBS samples: E, LW52, BR2, LW13, LW45, C and D.

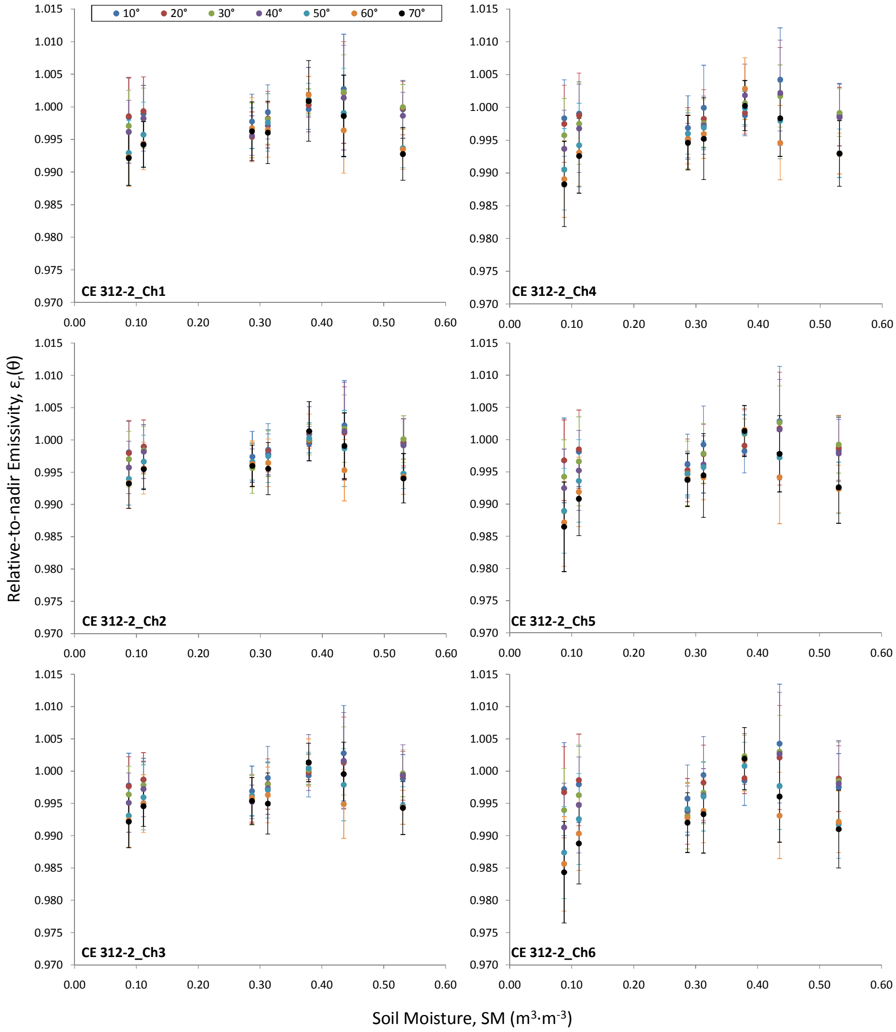

Figure 5.5 Zenithal variation of relative-to-nadir emissivity for IBS sample BR1 as function of SM content at six CE 312-2 spectral channels

Nevertheless, for a clayey soil, for which emissivity decreases with θ is almost negligible under dry conditions (ε_r decreases up to 2% at θ=70°, from nadir values at all spectral ranges), increasing the water content does not make to decrease the emissivity more significantly than at drier conditions; conversely, the increase of water content in our clayey soil makes to decrease its ε_r at θ=70°, much lower than under dry conditions. Obviously, the relation between TIR emissivity of soil and water is not necessarily linear, and some behaviors can be explained linearly only in a first approximation.

Loamy soils

Figure 5.4 shows the effect of water on IBS BR2 representative of loamy soils: E, F, LW52, F, LW13, LW45, C and D, at all six CE 312-2 spectral channels. Results show that SM produces a more pronounced decrease of ε_r with θ at all spectral ranges studied, in relation to the dry samples behavior. Such an accentuated decrease of ε_r with the increase of water content becomes significant from $\theta = 50°$. Loamy soils have a higher water retention than sandy soils because of their texture, reaching values of 50 % (samples D and C), therefore it is not surprising that ε_r (at θ=60°) decreases 2 % under dry conditions and 5 % when IBS is saturated, since water ε_r anisotropy (Cuenca and Sobrino, 2004) contributes to the effective soil emissivity.

Clayey soils

Results of SM effects on zenithal values of ε_r can be observed in Figure 5.5 for the clayey sample BR1 at all six spectral intervals studied. The main conclusion is that ε_r shows a complete isotropy with increase of SM. Just for a dehydrated state and for a $\theta \geq 60°$ it is appreciated significant decreases of zenithal ε_r, but this conclusion was achieved in section 5.2.

In summary, presence of water retained both by macropores and micropores of IBS, tends to homogenize the angular behavior of ε_r. Anisotropy of water ε_r (Cuenca and Sobrino, 2004) mitigates the decrease of ε_r with θ for soils with high quartz content at 8-9.4 μm spectral range. But that anisotropy also produces a higher decrease of ε_r with θ at all TIR region for IBS, with high water retention capacity (usually loamy soils), which zenithal decrease of ε_r under dry conditions is lower than water ε_r decreases. Finally, it seems that anisotropy of ε_r water cannot influence on soils with high clay percentages, being these kinds of IBS which present an almost isotropic behavior of angular ε_r regardless the SM content.

5.4 A global parameterization of TIR ε_r (SM, θ)

A parameterization of ε_r varying with SM and θ was addressed from results retrieved through the experimental measurements shown above. The model that best fits these results at each spectral channel and IBS sample is:

$$\varepsilon_r(SM,\theta) = a + b\,SM + c\,\theta + d\,SM^2 + e\,SM\,\theta + f\,\theta^2 \qquad (5.2)$$

Expression (5.2) has been regressed at each IBS for a number of points ranging from 28 to 56, the obtained average values of R^2 and RMSE range from 0.83 to 0.86 and from ±0.003 to ±0.004, respectively. However, it is of great interest to find a global expression that explains how ε_r changes with SM and θ with the aim of being applicable to any bare soil type. Consequently, variances of coefficients *a* - *f* in equation (5.2) were evaluated, using statistical factor analysis (Field, 2009), for all data available in Table 2.1 about IBS samples. Results of this statistical analysis can be understood in Table 5.1 and Figure 5.6, as way of example, for coefficient *a* in the spectral channel 6 of CE312-2.

Factor analysis consists in applying to factors studied (one of the coefficients *a-f* plus data included in Table 5.1) an extraction, which provides options pertaining to the retention of factors, and a rotation, which maximizes the loading of each variable on one of the extracted factors whilst minimizing the loading on all other factors. After extraction, it is applied a rotation, which works through changing the absolute values of the variables whilst keeping their differential values constant (Field, 2009). For the extraction technique, factors selected to be extracted were those whose *eigenvalues* are greater than 1, according to *Kaiser's recommendation* (Field, 2009).

Table 5.1 shows the result of the statistical factor analysis for coefficient *a* in the CE312-2 channel 6 (8.2-8.7 μm). First column (*initial Eigenvalues*) lists the *eigenvalues* associated with each factor before extraction; these *eigenvalues* represent the variance explained by that particular linear component. Sub-column titled *% of variance* represents the percentage of variance explained by that particular factor not explained by the other factors. Sub-column titled *Cumulative %,* is the addition of total variance explained by each factor. Same sub-columns are displayed after extraction (column *Extraction Sums of Squared Loadings*) and after rotation (column

Rotation Sums of Squared Loadings). Final results of the statistical analysis retrieved from Table 5.1 conclude that three factors (a, clay and quartz) are able to explain 86.6% of the total variance. Scree plot (Figure 5.6) reinforces the decision of extracting only three factors; this plot represents the curve drawn by the *eigenvalues* of each factor. According to Field (2009) the number of factors to be extracted is determined by the inflexion on the curve (when the slope becomes almost horizontal), so from Scree plot of Figure 5.6 it is easily deduced that only the three first factors should be extracted.

Table 5.1 Results of the statistical factor analysis for coefficient a in the CE312-2 channel 6 (8.2-8.7 µm). First column lists the *eigenvalues* associated with each factor before extraction. Sub-column *% of variance* represents the percentage of variance explained by that particular factor not explained by the other factors. Sub-column *Cumulative %*, is the addition of total variance explained by each factor. Same sub-columns are displayed after extraction (column *Extraction Sums of Squared Loadings*) and after rotation (column *Rotation Sums of Squared Loadings).*

Component	Initial Eigenvalues			Extraction Sums of Squared Loadings			Rotation Sums of Squared Loadings		
	Total	% of Variance	Cumulative %	Total	% of Variance	Cumulative %	Total	% of Variance	Cumulative %
a	3.6	51.2	51.2	3.6	51.2	51.2	3.0	42.3	42.3
Clay	1.4	20.6	71.8	1.4	20.6	71.8	1.7	23.7	66.0
Quartz	1.0	14.8	86.6	1.0	14.8	86.6	1.4	20.6	86.6
Feldspar	.4	5.9	92.4	-	-	-	-	-	-
OM	.3	4.3	96.7	-	-	-	-	-	-
Sand	.2	3.3	100.0	-	-	-	-	-	-
Silt	.0	.0	100.0	-	-	-	-	-	-

Statistical factor analysis stated that coefficient a can be parameterized in terms of clay and quartz percentages at spectral range 8.2-8.7 µm (channel 6 of CE312-2) since these two factors explain almost 87% of the variance in a. Subsequent factor analysis extended the conclusions of coefficient a to coefficients b-f at spectral channel 6. Moreover, coefficients a-f at spectral channels 4 and 5 are also dependent on clay and quartz, which explain a total variance of these coefficients ranging from 82.2% to 87.9%. In summary, coefficients a-f are dependent on clay and quartz at the spectral range 8-9.4 µm by means of the expression:

$$a - f_{ch4-6}(C,Q) = p_0 + p_1 C + p_2 Q + p_3 C^2 + p_4\, C\, Q + p_5 Q^2 \tag{5.3}$$

where p_0-p_5 are coefficients of polynomial (5.3) which values can be found in Table 5.2 together with R^2 and RMSE of the regression, and C and Q are the percentages of clay and quartz, respectively.

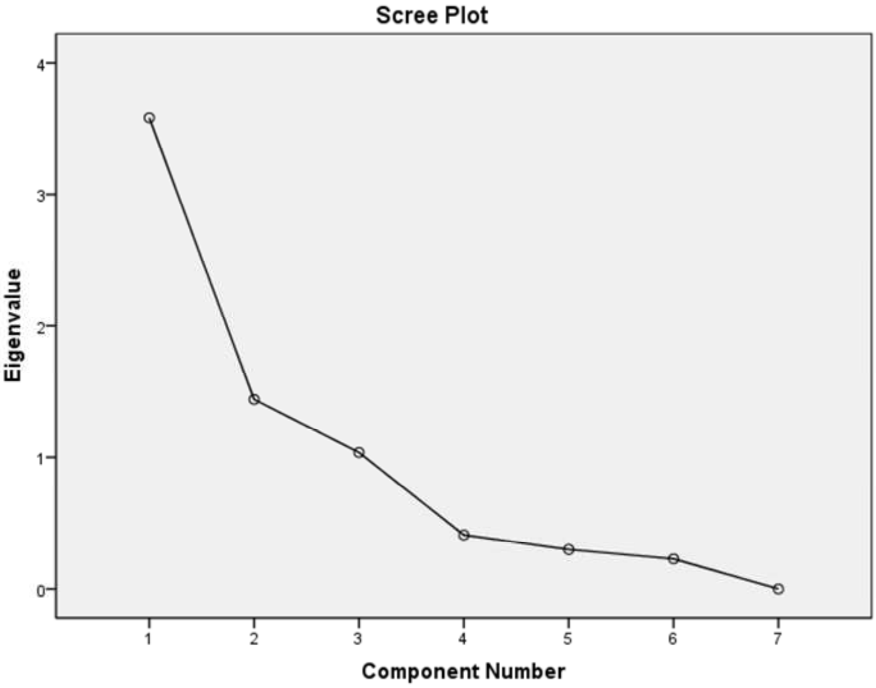

Figure 5.6 Scree plot of coefficient *a*, Eq. (5.3) for CE 312-2 spectral channel 6. Plot represents the curve drawn by the *eigenvalues* of each factor, according to Field (2009) the number of factors to be extracted is determined by the inflexion on the curve (when the slope becomes almost horizontal).

Coefficients a-f at spectral range 10-12 μm (CE312-2 channels 2 and 3) were found, after factor analysis, dependent on clay and organic matter (OM) contents (explaining a total variance ranging between 83.1% and 86.5%). The expression for these coefficients, similar to polynomial (5.3), is given by:

$$a - f_{ch2,3}(C, OM) = p_0 + p_1 C + p_2 OM + p_3 C^2 + p_4\, C\, OM + p_5 OM^2 \quad (5.4)$$

Table 5.2 summarizes results for coefficients p_0-p_5 of Eq. (5.3) and Eq. (5.4) at all six spectral ranges, statistics R^2 and RMSE are also included.

Table 5.2 Coefficientsp_0-p_5 of polynomials expressions (5.3) and (5.4) at all six spectral channels. R^2 and RMSE are also included.

	a	b $(m^3\cdot m^{-3})^{-1}$	c	d $(m^3\cdot m^{-3})^{-2}$	e $(m^3\cdot m^{-3})^{-1}$	f	a	b $(m^3\cdot m^{-3})^{-1}$	c	d $(m^3\cdot m^{-3})^{-2}$	e $(m^3\cdot m^{-3})^{-1}$	f
	Ch1: 7.7-14.3 µm						**Ch4: 8.7-9.4 µm**					
p_0	0.998	-0.005	0.00018	-0.02	0.0005	-0.00001	1.001	-0.04	0.0003	0.02	0.0007	-0.00001
p_1	-0.0006	0.0019	0.00003	-0.0004	-0.00008	$-1.3\cdot10^{-7}$	-0.0006	0.003	0.00004	-0.003	-0.00012	$-2\cdot10^{-8}$
p_2	-0.00022	0.0018	-0.00005	-0.003	-0.0002	$1.6\cdot10^{-6}$	-0.0003	0.0005	$3\cdot10^{-6}$	0.0012	0.000011	$-1.8\cdot10^{-7}$
p_3	0.000012	-0.00005	$-1.5\cdot10^{-6}$	0.00005	$1.9\cdot10^{-6}$	$1.4\cdot10^{-8}$	0.000012	-0.00006	$-8\cdot10^{-7}$	0.00006	$3\cdot10^{-6}$	$9\cdot10^{-11}$
p_4	$-4\cdot10^{-7}$	0.000017	0.000019	-0.00003	$-9\cdot10^{-6}$	$-2\cdot10^{-7}$	$-1.0\cdot10^{-6}$	0.00004	$-5\cdot10^{-8}$	-0.00006	$-1.1\cdot10^{-6}$	$8\cdot10^{-9}$
p_5	$2\cdot10^{-6}$	-0.00002	-0.00006	0.00004	0.00006	$7\cdot10^{-7}$	$4\cdot10^{-6}$	-0.000013	$-4\cdot10^{-8}$	$3.\cdot10^{-6}$	$7\cdot10^{-8}$	$5\cdot10^{-10}$
R^2	0.76	0.86	0.96	0.69	0.89	0.86	0.83	0.80	0.67	0.63	0.87	0.75
RMSE	0.004	0.016	0.00008	0.04	0.0003	$2\cdot10^{-6}$	0.004	0.04	0.0003	0.07	0.0006	$5\cdot10^{-6}$
	Ch2: 10.9-11.9 µm						**Ch5: 8.4-8.9 µm**					
p_0	0.997	0.00004	0.00018	-0.004	0.00005	$-5\cdot10^{-6}$	0.996	0.011	0.0003	-0.12	0.0016	-0.000014
p_1	-0.0010	0.007	0.00003	-0.011	-0.00006	$-3\cdot10^{-7}$	-0.0004	0.0019	0.00004	0.0015	-0.00017	$2\cdot10^{-7}$
p_2	0.003	-0.017	-0.00007	0.03	-0.00011	$8\cdot10^{-7}$	-0.00017	-0.0003	$-3\cdot10^{-7}$	0.003	$8\cdot10^{-6}$	$-1.2\cdot10^{-7}$
p_3	0.00002	-0.00010	$-1.3\cdot10^{-6}$	0.00011	$1.8\cdot10^{-06}$	$1.5\cdot10^{-8}$	0.00001	-0.00004	$-8\cdot10^{-7}$	-0.000010	$3\cdot10^{-6}$	$-3\cdot10^{-9}$
p_4	-0.00013	-0.0002	0.000017	0.0015	-0.000015	$-2\cdot10^{-7}$	$-6.1\cdot10^{-7}$	0.000023	$-1.0\cdot10^{-7}$	-0.00003	$-6\cdot10^{-7}$	$7\cdot10^{-9}$
p_5	0.0003	0.0017	-0.00005	-0.007	0.00006	$7\cdot10^{-7}$	$2\cdot10^{-6}$	$-7\cdot10^{-6}$	$-8\cdot10^{-9}$	$-6\cdot10^{-6}$	$1.4\cdot10^{-8}$	$9\cdot10^{-11}$
R^2	0.84	0.66	0.93	0.54	0.86	0.95	0.70	0.75	0.63	0.64	0.88	0.81
RMSE	0.003	0.02	0.00010	0.05	0.0003	$1\cdot10^{-6}$	0.004	0.03	0.0002	0.07	0.0006	$5\cdot10^{-6}$
	Ch3: 10.1-11.1 µm						**Ch6: 8.2-8.7 µm**					
p_0	0.998	-0.007	0.00018	0.003	0.00019	$-6\cdot10^{-6}$	0.992	0.07	0.00009	-0.3	0.002	-0.000017
p_1	-0.0011	0.007	0.00003	-0.011	-0.00007	$-3\cdot10^{-7}$	-0.00014	-0.0003	0.00004	0.009	-0.0002	$4\cdot10^{-7}$
p_2	0.002	-0.012	-0.00005	0.02	-0.0002	$1.1\cdot10^{-6}$	-0.00004	-0.002	$4\cdot10^{-7}$	0.008	$6\cdot10^{-6}$	$-7\cdot10^{-8}$
p_3	0.00002	-0.00010	$-1.5\cdot10^{-6}$	0.00011	$2\cdot10^{-6}$	$1.6\cdot10^{-8}$	$5.\cdot10^{-6}$	-0.000018	$-7\cdot10^{-7}$	-0.00006	$3\cdot10^{-6}$	$-5\cdot10^{-9}$
p_4	-0.00013	-0.0004	0.000019	0.0015	-0.000012	$-2\cdot10^{-7}$	$-3\cdot10^{-6}$	0.00006	$-2\cdot10^{-7}$	-0.00016	$-6\cdot10^{-8}$	$7\cdot10^{-9}$
p_5	0.0003	0.0019	-0.00006	-0.006	0.00007	$7\cdot10^{-7}$	$1.4\cdot10^{-6}$	$8.\cdot10^{-6}$	$1.1\cdot10^{-8}$	$-4\cdot10^{-5}$	$-6\cdot10^{-8}$	$-3\cdot10^{-10}$
R^2	0.80	0.64	0.96	0.45	0.88	0.96	0.61	0.80	0.72	0.83	0.89	0.86
RMSE	0.003	0.03	0.00008	0.06	0.0003	$1\cdot10^{-6}$	0.004	0.03	0.0002	0.07	0.0006	$4\cdot10^{-6}$

Factor statistical analysis of coefficients for the broad range 7.7-14.3 μm (CE312-2 channel 1) showed dependence of some of them (*a*, *b* and *d*) on clay and quartz contents, following expression (5.3), and the rest coefficients (*c*, *e* and *f*) showed dependence on clay and OM, following expression (5.4).

Figure 5.7 shows the comparison between the observed $\varepsilon_{ri}(SM, \theta)$ values and those modeled using expressions (5.2), (5.3) and (5.4) at the six considered spectral ranges. Results show a R^2 ranging between 0.85 and 0.92, with an average value of 0.88 and a RMSE ranging between ±0.003 and ±0.006, with an average of ±0.005. Considering that these RMSE are lower than the maximum uncertainty showed when ε_r of IBS is retrieved, regardless the azimuth angle φ(±0.01), it could be concluded that $\varepsilon_r(SM, \theta)$ of IBS can be retrieved from expressions (5.2), (5.3) and (5.4) with a maximum error of ±0.01.

Values of clay content could be estimated remotely using radar data. As shown in Singh and Kathpalia (2007), applying a Genetic Algorithm technique to radar data retrieved from Synthetic Aperture Radar onboard European Remote Sensing 2, percentages of clay are obtained with standard errors ranging between 0.07% - 0.08%. On the other hand, OM and quartz contents can be estimated using visible/infrared data. As shown in Ninomiya and Fu (2001), quartz content can be derived by means of spectral indices for lithologic mapping with TIR data from the Advanced Spaceborne Thermal Emission and Reflection radiometer (ASTER). Quartz minerals can be detected using bands 10 (8.3 μm), 11 (8.6 μm), and 12 (9.1 μm). According to Ninomiya and Fu (2001), the result of applying the indices to level 1B ASTER TIR data sets observing a study site at various seasons indicates that they are robust against variations in atmospheric conditions and surface temperatures. Regarding OM content, it can be estimated from Landsat Enhanced Thematic Mapper (ETM) bands 2 (0.52–0.60 μm) and 7 (2.08–2.35 μm) following a regression equation with a coefficient of correlation $R^2 = 0.51$ (Nanni and Dematte, 2006). Frazier and Cheng (1989) obtained $R^2 = 0.98$ for predictive OM equations, using the ratio between the ETM's bands 5 (1.55–1.75 μm) and 4 (0.76–0.90 μm). Wu *et al.* (2009) found that the highest correlation ($R^2 = 0.59$) between OM of 131 soil samples and the corresponding digital number of ETM reflective bands was with band 1 (0.45–0.52 μm).

A last possibility is the previous knowledge of clay, quartz and OM contents from ancillary data. In these cases the parameterizations given in expressions (5.2), (5.3) and (5.4), depending on the channel, could be applied to classification-based emissivity mapping, such as the one used in MODIS (Snyder *et al.* 1998), SEVIRI (Trigo *et al.* 2008), or more recently AATSR data (Caselles *et al.* 2012), in order to refine their algorithms.

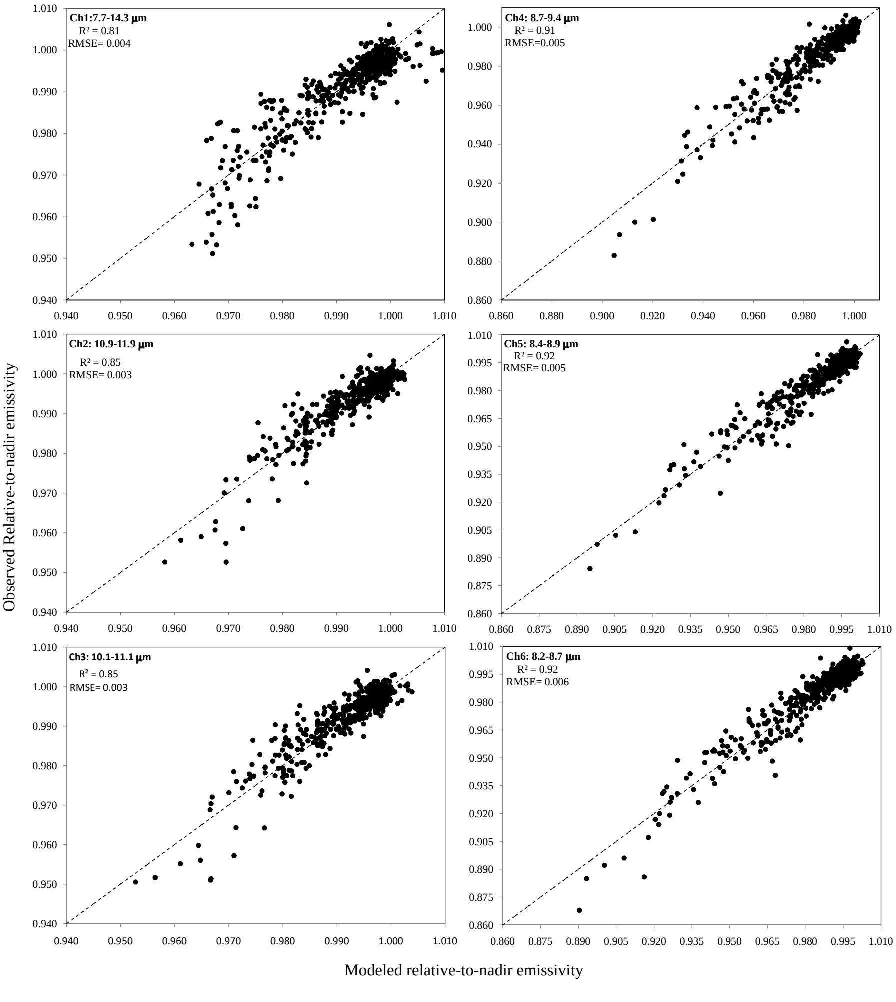

Figure 5.7 Self-validation of model represented by Expression (5.2), comparing ε_{ri} values measured with those calculated from the model, at six spectral ranges. R^2 and RMSE values of the regression are also included in each sub-plot.

5.5 Effect of emissivity anisotropy on LST and longwave radiation flux retrievals

Implications for LST accuracy

Ignoring angular effects on emissivity when measuring LST from space were addressed by means of a simulation study, using one of the available split-window algorithms that present explicit dependence on emissivity (Galve *et al.* 2008). The proposed algorithm, based on MODIS spectral bands 31 and 32, retrieves a LST, corrected from emissivity and atmospheric effects, as:

$$LST = T_{31} + \ a_0 + a_1(T_{31} - T_{32}) + a_2(T_{31} - T_{32})^2 + \alpha(1 - \bar{\varepsilon}) - \beta\Delta\bar{\varepsilon} \tag{5.5}$$

where T_{31} and T_{32} are brightness temperatures measured in MODIS bands 31 and 32, respectively; a_0, a_1 and a_2 are regression coefficients that can be found in Galve *et al.* (2008); coefficients α and β establish the weight of the emissivity correction and are dependent on W; and $\bar{\varepsilon}$ and $\Delta\bar{\varepsilon}$ are the average and emissivity difference of MODIS bands 31 and 32, respectively.

MODIS spectral bands 31 and 32 are similar to CE312-2 channels 2 (10.9-11.9 μm) and 3 (10.1-11.1 μm), although the results may be similar for other comparable algorithms and instruments. Since relative-to-nadir emissivities in CE312-2 channels 2 and 3 show almost the same angular variation (see Figures 5.2-5.5), emissivity difference $\Delta\bar{\varepsilon}$ will remain almost constant at any angle, and therefore the impact of this term on LST is negligible at any angular configuration. However, it is not the case with $\bar{\varepsilon}$, which uncertainty gives the next LST error propagation:

$$\delta LST(\theta) = \alpha\Delta\overline{\varepsilon(\theta)} \tag{5.6}$$

where $\Delta\overline{\varepsilon(\theta)}$ is the difference between the average emissivity values of CE312-2 spectral channels 2 and 3 at nadir and zenith angle θ.

As mentioned above, α is a W-dependent parameter following a quadratic relationship expressed in Galve *et al.* (2008) as:

$$\alpha = 45.99 + 4.67W - 1.446W^2 \tag{5.7}$$

Table 5.3 shows the difference between absolute emissivity at nadir and θ=65º, for all the analyzed samples, and for CE312-2 broad channel 1 (7.7-14 μm) and channels 2 and 3 (10-12 μm). The emissivity differences in this last case were used in Eq. (5.6) to assess the possible impact of ignoring the angular variation of emissivity on LST, at large observation angles, if emissivity values at nadir are used instead of the correct off-nadir value.

Table 5.3 Absolute emissivity values retrieved from expression (4) in Mira *et al.* (2010) at spectral ranges 7.7-14 μm and 10-12 μm (third and fourth columns), for all the IBS at the specific SM value given at the second column. Fifth and sixth columns show the maximum difference between relative-to-nadir emissivity between nadir and 60° zenith angle for all IBS at both spectral ranges selected.

IBS	**SM(m^3m^{-3})**	$\varepsilon_{7.7\text{-}14\,\mu m}$(0°)	$\varepsilon_{10\text{-}12\,\mu m}$(0°)	$\Delta\varepsilon_{7.7\text{-}14\,\mu m}$(65°)	$\Delta\varepsilon_{10\text{-}12\,\mu m}$(65°)
B	0.04	0.906	0.951	0.032	0.018
BR1	0.09	0.963	0.956	0.024	0.015
BR2	0.42	0.958	0.975	0.024	0.015
BR3	0.04	0.927	0.950	0.027	0.025
C	0.55	0.946	0.945	0.034	0.033
D	0.53	0.973	0.974	0.037	0.037
E	0.03	0.928	0.949	0.029	0.030
F	0.39	0.965	0.972	0.016	0.011
LW03	0.37	0.952	0.973	0.009	0.007
LW13	0.42	0.961	0.975	0.012	0.011
LW45	0.43	0.956	0.976	0.035	0.037
LW52	0.03	0.934	0.949	0.024	0.022
WS	0.01	0.915	0.943	0.018	0.016

Figure 5.8 shows LST error values from equation (5.6) for different W (i.e. for different values of α), ranging from 0 to 7 cm at intervals of 0.1 cm. For sandy soil LW45, LST errors reaches values up to +1.8 K for atmospheres with W values lower than 3 cm, and sample LW03 presents LST errors lower than +0.5 K independently on W. Overall results show that retrieving LST for pixels of a IBS at θ=65°, implies to make a systematic error between +0.4 K and +1.8 K for an atmosphere with W values lower than 4 cm. For extremely wet atmospheres (W ≥ 7 cm), errors in LST are lower than +0.5 K for each IBS studied here, being almost insignificant. In summary, the drier the atmosphere is the larger the error on LST retrievals are, for a pixel observed at a large zenith angle, if it is ignored the angular effect of IBS emissivity.

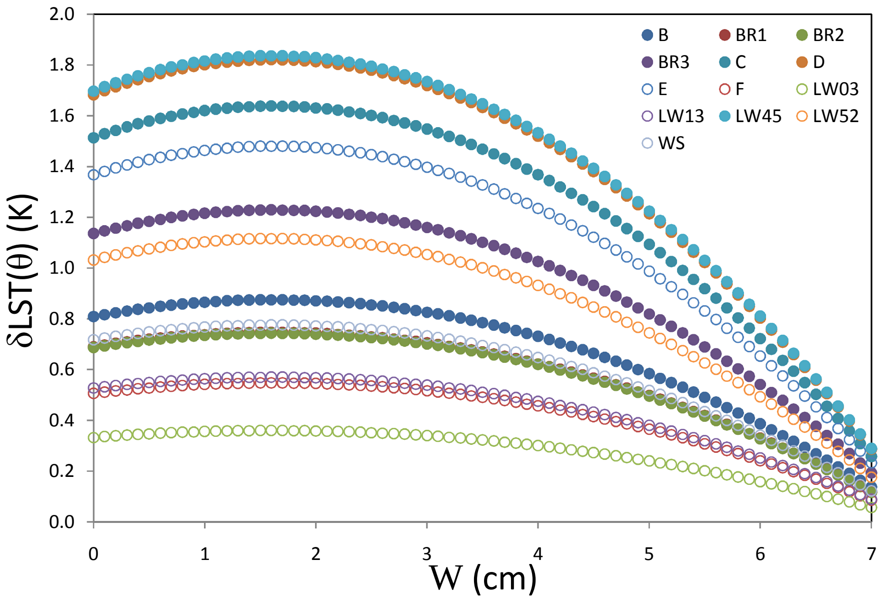

Figure 5.8 LST errors obtained applying a split-window algorithm (Eq. 5.5) for all IBS if angular emissivity effect at θ=65° is ignored. δLST(65°) values, calculated through Eq. (5.6), are represented for W values ranging from 0 to 7 cm at intervals of 0.1 cm.

Implications for $F^{\uparrow}$ accuracy

Another parameter that could be affected by the angular variation of emissivity is the outgoing longwave radiation ($F^{\uparrow}$), which can be calculated as follows:

$$F^{\uparrow} = \varepsilon \sigma T^4 \tag{5.7}$$

where ε is the hemispherical emissivity value for the whole TIR range, σ is the Stefan-Boltzmann constant and T is the thermodynamic surface temperature. Usually ε is considered not dependent on viewing angle, and thus its value at nadir is taken as representative of the hemispherical one, but the present work has shown that this value varies with zenith angle. Ignoring this effect could lead to errors in retrieving $F^{\uparrow}$, for this reason we have evaluated this error studying the relative sensitivity of $F^{\uparrow}$ to the emissivity angular variation ($S_{F^{\uparrow}}(\Delta\varepsilon)$) following Zhang *et al.* (1996):

$$S_{F^{\uparrow}}(\Delta\varepsilon) = \left|\frac{F_{-}^{\uparrow} - F_{+}^{\uparrow}}{F_{0}^{\uparrow}}\right| 100 \tag{5.8}$$

where $\Delta\varepsilon$ is the difference of 7.7-14.3 μm emissivity between $\theta=0°$ and $\theta=65°$ (Table 5.3), $F^{\uparrow}_0$ is the outgoing longwave radiation when the 7.7-14.3 μm emissivity value at nadir is introduced in equation (5.8), and $F^{\uparrow}_-$ and $F^{\uparrow}_+$ are the outgoing longwave radiation values when emissivity in Eq. (5.8) is decreased and increased by $\Delta\varepsilon$, respectively. Table 5.3 shows the values used to retrieve $S_{F^{\uparrow}}(\Delta\varepsilon)$ in each IBS sample. A fixed temperature value of 320 K was chosen in equation (5.8) for this sensitivity analysis.

Table 5.4 Sensitivity of $F^{\uparrow}$ to the emissivity angular variation ($\boldsymbol{S_{F^{\uparrow}}(\Delta\varepsilon)}$) retrieved from equation (5.8) for all IBS studied.

IBS	B	BR1	BR2	BR3	C	D	E	F	LW03	LW13	LW45	LW52	WS
$S_{F\uparrow}(\Delta\varepsilon)$ (%)	7	5	5	6	7	8	6	3	2	2	7	5	4

Results from Table 5.4 show that accuracy of $F^{\uparrow}$ can suffer variation between 2% - 8%, depending on IBS type, which may lead to significant errors in the estimation of the different terms of the surface energy balance, as shown in the sensitivity analysis of the two-source models carried out by Sánchez *et al.* (2008).

Measurements of radiation made over surfaces at high viewing angles by TIR sensors onboard satellites, could probably be more affected by atmospheric attenuation or non-linear effects in radiative transfer modeling, especially retrieving LST. But the present simulation study has shown that ignoring angular effects of surface emissivity may lead also to significant errors in retrieving parameters such as LST or $F^{\uparrow}$, even if this parameter has a secondary role in the radiative transfer budget.

Chapter 6

Conclusions

The last chapter summarizes the most important conclusions achieved from the different studies carried out, during the elaboration of the present PhD Thesis.

The main conclusions drawn from the analyses carried out throughout this Thesis report are summarized in the following:

1. Inorganic Bare Soil (IBS) samples employed in the present thesis are representative of a great number of existing textures on Earth according to USDA classification system, and therefore the presented results on the effect of anisotropy and SM on TIR emissivity can be applied to a wide variety of mineral soil types.

2. Present work studied the angular emissivity of completely dry IBS with an almost constant roughness (particles size no greater than 0.5 cm) and at different moisture levels. The methodology applied to retrieve angular emissivity allowed obtaining relative emissivity values with a maximum uncertainty of ±0.01.

3. The radiative contribution from the atmosphere and possible surrounding elements is an important parameter when retrieving factors such as temperature or surface emissivity, and therefore must be measured very accurately. From comparison between four different available methods to obtain the hemispherical downwelling radiance at different surrounding conditions it was concluded that:

    - Under clear-sky conditions and in places where the surrounding elements have a minimal radiative contribution, the different approaches produce comparable results, but for places where presence of surrounding elements is important, measuring hemispherical downwelling radiance by means of a diffuse reflectance panel is the most recommended option, since it takes into account the radiative contributions of the existing surroundings elements.

    - Under changing cloud coverage conditions, only a diffuse reflectance panel guarantees an adequate measurement of the hemispherical downwelling radiance, since it takes into account both the contribution of the surroundings, as well as the effects of clouds.

- An adequate value of hemispherical downwelling radiance is particularly important in field measurements since an underestimation of 72% of this radiative contribution means an overestimation of ε_r up to values close to 0.09.For this reason the use of a diffusive reflectance panel is the most suitable alternative.

4. Regarding the anisotropy of TIR emissivity for an IBS, the most important conclusions reached in this study are:

    - TIR emissivity of IBS can be considered almost invariant azimuthally, but not with zenith angle, since emissivity decrease becomes significant beyond60° independently on soil composition or spectral range.

    - However, the zenithal decrease is strongly affected by the spectral range and soil composition. The TIR emissivity of IBS under dry conditions is relatively isotropic when clay is present at all spectral ranges studied. On the contrary, sandy soils composed by quartz or gypsum present the most significant decreases of the emissivity when increasing zenith angles, being significant for instance, at zenith angles greater than 30° within 8-9.4 μm spectral region.

    - The effect of soil moisture on anisotropy of ε_r shows also a strong dependence on IBS type and spectral range in which it has been measured. Soil moisture increase on sandy soils does not show noticeable effect on TIR ε_r anisotropy at spectral ranges 8-14 μm and 10-12 μm. However, at spectral range 8-9.4 μm the increase of water content produces a reduction between 1-7 % from $\theta \geq 40°$of the decrease of ε_r with zenith angle. Effect of soil moisture increase on loamy soil produces a more pronounced decrease of ε_r with θ at all spectral ranges studied, in relation to the dry conditions, that becomes significant from $\theta = 50°$.For clayey sample, the main conclusion is that ε_r shows a complete isotropy with increase of SM and just for a dehydrated state and θ ≥ 60° it is appreciated significant decreases of zenithal ε_r.

5. A parameterization of ε_r varying with SM and θ was addressed, The model that best fits these results at each spectral channel and IBS sample is:

   $$\varepsilon_r(SM,\theta) = a + bSM + c\theta + dSM^2 + eSM\theta + f\theta^2$$

   Coefficients *a* - *f* were evaluated, using statistical factor analysis, and they were found dependent on clay and quartz at the spectral range 8-9.4 µm; at spectral range 10-12 µm they were found dependent on clay and organic matter contents; and for the broad range 7.7-14.3 µm some of them (*a*, *b* and *d*) showed dependence on clay and quartz contents, and the rest of the coefficients (*c*, *e* and *f*) showed dependence on clay and organic matter contents.

6. Ignoring angular effects on emissivity when measuring LST implies to make a systematic error between +0.4 K and +1.8 K for atmospheres with water content values lower than 4 cm. The drier the atmosphere is, the larger the error on LST retrievals are for a pixel observed at a large zenith angle, if angular effects of IBS emissivity are ignored. Outgoing longwave radiation fluxes can also suffer variation between 2% - 8%, depending on IBS type, if the emissivity anisotropy is not taken into account leading to significant errors in the estimation of the different terms of the surface energy balance.

References

Barsi J.A., J.L. Barker, J.R. Schott (2003). An Atmospheric Correction Parameter Calculator for a Single Thermal Band Earth-Sensing Instrument. *IGARSS03*, 21-25 July, Centre de Congres Pierre Baudis, Toulouse, France.

Barton I. J. and T. Takashima (1986). An AVHRR investigation of surface emissivity near Lake Eyre, Australia, *Remote Sens. Environ.*, 20(2), 153-163, ISSN 0034-4257, doi: 10.1016/0034-4257(86)90020-9.

Berk G. P. Anderson, P. K. Acharya, J. H. Chetwynd, L. S. Bernstein, E. P. Shettle, M. W. Matthew and S. M. Adler-Golden (1999). MODTRAN 4 user's manual, *Air Force Research Laboratory, Space Vehicles Directorate, Air Force Materiel Command*, Hascom AFB, MA, 95.

Bouyoucos G. (1962). Hydrometer method improved for making particle size analysis of soil. *Journal of Agronomy*, 54, 464-465.

Brogniez G., C. Pietras, M. Legrand, P. Dubuisson and M. Haeffelin (2003). A high-accuracy multiwavelength radiometer for in situ measurements in the thermal infrared. Part II: Behavior infield experiments, *J. Atmos. Ocean. Tech.*, 20, 1023-1033.

Caselles E., E. Valor, F.J. Abad and V. Caselles (2012). Automatic classification-based generation of thermal infrared land surface emissivity maps using AATSR data over Europe., *Remote Sens. Environ.*, 124, 321-333, doi: 10.1016/j.rse.2012.05.024.

Chen J. M., B. J. Yang, and R. H. Zhang (1989). Soil thermal emissivity as affected by its water content and surface treatment. *Soil Science*, 148(6), 433-435.

Cuenca J. and J. A. Sobrino (2004). Experimental Measurements for Studying Angular and Spectral Variation of Thermal Infrared Emissivity, *Applied Optics*, 43, 4598-460, doi:10.1364/AO.43.004598.

Day P. R. (1965). Methods of soil analysis, part I. Physical and mineralogical properties, including statistics of measurement and sampling, *Agronomy Series. American Society of Agronomy*, 9, 545-567.

Delta-T Devices Ltd (2006). User manual for the SM200 soil moisture sensor. SM200-UM-1.1, 36.

Elachi C. and J. J. Van Zyl (2006). Introduction to the Physics and Techniques of Remote Sensing, *Wiley Series in Remote Sensing & Image Processing, John Wiley & Sons Inc, 2nd Revised edition*, ISBN-13: 978-0471475699.

Field A. (2009). Discovering Statistics Using SPSS (3rd edition). *SAGE Publications Ltd*, 2455 Teller Road Thousand Oaks, CA 91320.

Frazier B. E. and Y. Cheng (1989). Remote sensing of soils in the eastern Palouse region with Landsat Thematic Mapper, *Remote Sens. Environ.*, 28, 317-325.

Galve J.M., C. Coll, V. Caselles, and E. Valor (2008). An Atmospheric Radiosounding Database for Generating Land Surface Temperature Algorithms, *IEEE Trans. Geosci. Remote Sens.*, 46(5), 1547-1557, doi: 10.1109/TGRS.2008.916084.

García-Santos V., E. Valor, V. Caselles, M. Mira, J. M. Galve and C. Coll. (2012a). Evaluation of different methods to retrieve the hemispherical downwelling irradiance in the thermal infrared region for field measurements, *IEEE Trans. Geosci. Remote Sens.*, 51(4), 2155-2165, doi:10.1109/TGRS.2012.2209891.

García-Santos V., J. M. Galve, E. Valor, V. Caselles, and C. Coll (2012b). Estimation of atmospheric water vapour content from direct measurements of radiance in the thermal infrared region, *Remote Sensing Letters*, 3(1), 31-38.

García-Santos V., E. Valor, V. Caselles, M.A. Burgos and C. Coll (2012c). On the angular variation of thermal infrared emissivity of inorganic soils, *J. Geophys. Res.*, 117, (D19116), doi:10.1029/2012JD017931.

García-Santos V., E. Valor, V. Caselles, M. A. Burgos and C. Coll (2013). Effect of soil moisture on the angular variation of thermal infrared emissivity of inorganic soils, *IEEE Geosci. and Remote Sens. Letters*, (under review).

Gillespie A., S. Rokugawa, T. Matsunaga, J.S. Cothern, S. Hook, and A.B. Kahle (1998). A temperature and emissivity separation algorithm for Advanced Spaceborne Thermal Emission and Reflection Radiometer (ASTER) images, *IEEE Trans. Geosci. Remote Sens*., 36(4), 1113-1126, doi: 10.1109/36.700995.

Holben B. N., T. F. Eck, I. Slutsker, D. Tanré, J. P. Buis, A. Setzer, E. Vermote, J. A. Reagan, Y. J. Kaufman, T. Nakajima, F. Lavenu, I. Jankowiak, and A. Smirmov (1998). AERONET - A federated instrument network and data archive for aerosol characterization. *Remote Sens. Environ.*, 66, 1-16.

International Union of Soil Sciences (2006). World Reference Base for Soil Resources, A framework for international classification, correlation and communication, *World Soil Resources Reports, FAO*, 103, 1-128.

ISO (2002). Soil quality, determination of particle size distribution in mineral soil material. Method by sieving and sedimentation (ISO 11277:1998/TC190). *International Organization for Standardization*, 30.

Kalnay E., M. Kanamitsu, R. Kistler, W. Collins, D. Deaven, L. Gandin, M. Iredell, S. Saha, G. White, J. Woollen, Y. Zhu, M. Chelliah, W. Ebissuzaki, W. Higgins, J. Janowiak, K. C. Mo, C. Ropelewski, J. Wang, A. Leetmaa, R. Reynolds, R. Jenne and D. Joseph (1995). NCEP/NCAR 40 Year Reanalysis Project, *B. Am. Meteorol. Soc.*, 437-471.

Kondratyev K.Y. (1969). Radiation in the Atmosphere. *New York and London: Academic Press*.

Korb A.R., P. Dybwad, W. Wadsworth and J.W. Salisbury (1996). Portable Fourier transform infrared spectroradiometer for field measurements of radiance and emissivity, *Applied Optics*, 35(10), 1679-1692.

Kubelka P. and F. Munk (1931). Ein Beitrag zur Optik der Farbanstriche, *Zeits. f. Techn. Physik*, 12, 593-601.

Labed J. and M. P. Stoll (1991). Angular variation of land surface spectral emissivity in the thermal infrared: laboratory investigations on bare soils. *Int. J. Remote Sens.*, 12, 2299-2310. doi:10.1080/01431169108955259.

Lagouarde J. P., Y. H. Kerr and Y. Brunet (1995). An experimental study of angular effects on surface temperature for various plant canopies and bare soils, Agricultural and Forest Meteorology, 77(3-4), *Thermal Remote Sensing of the Energy and Water Balance over Vegetation*, 167-190, doi: 10.1016/0168-1923(95)02260-5.

Legrand M., C.Pietras, G. Brogniez, M. Haefelin, N. K. Abuhassan and M. Sicard (2000). A high-accuracy multiwavelength radiometer for in situ measurements in the thermal infrared: Part 1. Characterization of the instrument, *Journal of Atmospheric and Oceanic Technology*, 17, 1203-1214.

Malicki M. A., R. Plagge, and C. H. Roth (1996). Improving the calibration of dielectric TDR soil moisture determination taking into account the solid soil. *European Journal of Soil Science*, 47, 357-366.

Mira M., E. Valor R. Boluda, V. Caselles, and C. Coll (2007). Influence of soil water content on the thermal infrared emissivity of bare soils: Implication for land surface temperature determination, *J. Geophys. Res.*, 112, F04003, doi:10.1029/2007JF000749.

Mira M., T.J. Schmugge, E. Valor, V. Caselles, C. Coll (2009). Comparison of Thermal Infrared Emissivities Retrieved With the Two-Lid Box and the TES Methods With Laboratory Spectra, *IEEE Trans. Geosci. Remote Sens.*, 47(4), 1012-1021, doi:10.1109/TGRS.2008.2008901.

Mira, M., E. Valor, V. Caselles, E. Rubio, C. Coll, J. M. Galve, R. Niclos, J.M. Sánchez, and R. Boluda (2010). Soil Moisture Effect on Thermal Infrared (8–13-μm) Emissivity, *IEEE Trans. Geosci. Remote Sens.*, 48(5), 2251-2260, doi:10.1109/TGRS.2009.2039143.

Mira M. (2010). Efecto de la humedad sobre la emisividad de los suelos en el infrarrojo térmico, *PhD Thesis*, Department of Earth’s Physic and Thermodynamic, Physics Faculty, University of Valencia.

Mira M., T. J. Schmugge, E. Valor, V. Caselles, and C. Coll (2011). Analysis of ASTER emissivity product over an arid area in southern New Mexico, USA, *IEEE Trans. Geosci. Remote Sens.*, 49(4), 1012-1021, doi:10.1109/TGRS.2008.2008901.

Nanni M. R. and J. A. Demattê (2006). Spectral reflectance methodology in comparison to traditional soil analysis, *Soil Sci. Soc. Amer.*, 70(2), 393-407.

Nicodemus F. E. (1965). Directional Reflectance and Emissivity of an Opaque Surface, *Applied Optics*, 4, 767-773, doi:10.1364/AO.4.000767.

Nicodemus F.E., J.C. Richmond, J.J. Hsia, I.W. Ginsberg, and T. Limperis (1977). Geometrical considerations of nomenclature for reflectance, *National Bureau Standards Monograph 160.*US Department of Commerce, Washington DC, 52.

Ninomiya Y. and B. Fu (2001). Spectral indices for lithologic mapping with ASTER thermal infrared data applying to a part of Beishan Mountains, Gansu, China, in *Proc. IEEE Int. Geosci. Remote Sens. Symp.*, 7, 2988–2990.

Norman J. M. and F. Becker (1995). Terminology in thermal infrared remote sensing of natural surfaces, *Agricultural and Forest Meteorology*, 77(3-4), 153-166, doi:10.1016/0168-1923(95)02259-Z.

Ogawa K., T. Schmugge and S. Rokugawa (2006). Observations of the dependence of the thermal infrared emissivity on soil moisture. *Geophysical Research Abstracts*, 8, 04996.

Ogawa K., T. Schmugge and S. Rokugawa (2008). Estimating broadband emissivity of arid regions and its seasonal variations using thermal infrared remote sensing. *IEEE Transactions on Geoscience and Remote Sensing*, 46(2), 334-343.

Rowan L. C. and J. C. Mars (2002). Lithologic mapping in the Mountain Pass, California area using Advanced Spaceborne Thermal Emission and Reflection radiometer (ASTER) data, *Remote Sens. Environ.*, 84, 350-366.

Rubio E., V. Caselles and C. Badenas (1997). Emissivity Measurements of Several Soils and Vegetation Types in the 8-14 µm Wave Band, *Remote Sens. Environ.*, 59, 490-521.

Salisbury J. W., and D. M. D’Aria (1992), Infrared (8–14 μm). Remote sensing of soil particle size, *Remote Sens. Environ.*, 42, 157-165, doi: 10.1016/0034-4257(92)90099-6.

Salisbury J. W., D. G., Murcray, Williams, W. J., and Blatherwick, R. D. (1995). Thermal infrared spectra of the Moon, *International Journal of Solar System Studies*, 115, 181-190.

Sánchez J. M., W. P. Kustas, V. Caselles, and M. C. Anderson, (2008). Modelling surface energy fluxes over maize using a two source patch model and radiometric soil and canopy temperature observations, *Remote Sens. Environ.*, 112, 1130-114. doi:10.1016/j.rse.2007.07.018.

Serrano D., M. Núñez, M.P. Utrillas, M.J. Marín and J.A. Martínez-Lozano, (2013). Cloud optical depth in the erythemal band for overcast conditions, *International Journal of Climatology*, (under review).

Singh D. and A. Kathpalia (2007). An efficient modeling with GA approach to retrieve soil texture, moisture and roughness from ERS-2 SAR data, *Progress In Electromagnetics Research*, 77, 121-136. doi:10.2528/PIER07071803.

Snyder W.C., Z. Wan, Y. Zhang and Y.Z. Feng (1998). Classification-based emissivity for land surface temperature measurement from space. *International Journal of Remote Sensing* 19, 2753-2774.

Sobrino J. A. and J. Cuenca (1999). Angular Variation of Thermal Infrared Emissivity for Some Natural Surfaces from Experimental Measurements, *Applied Optics*, 38, 3931-3936. http://dx.doi.org/10.1364/AO.38.003931.

Soil Survey Staff (2010). Keys to Soil Taxonomy. USDA-Natural Resources Conservation Service, Washington, DC., 11th edition.

Theocharous E., E. Usadi and N. P. Fox (2010). CEOS comparison of IR brightness temperature measurements in support of satellite validation. Part I: Laboratory and ocean surface temperature comparison of radiation thermometers. *NPL REPORT OP4*, Teddington, UK, National Physical Laboratory, ISSN: 1754-2944.

Theocharous E. and N. P. Fox (2010). CEOS comparison of IR brightness temperature measurements in support of satellite validation. Part II: Laboratory comparison of the brightness temperature of blackbodies, *NPL REPORT OP4*, Teddington, UK, National Physical Laboratory, ISSN: 1754-2944.

Topp G. C., J. L. Davis and A. P. Annan (1980). Electromagnetic determination of soil water content: Measurements in coaxial transmission lines. *Water Resources Research*, 16(3), 574-582.

Topp G. C. and W. D. Reynolds (1998). Time domain re_ectometry: a seminal technique for measuring mass and energy in soil. *Soil and Tillage Research*, 47, 125-132.

Trigo I.F., L.F. Peres, C.C. DaCamara and S.C. Freitas (2008). Thermal land surface emissivity retrieved from SEVIRI/Meteosat. *IEEE Transactions on Geoscience and Remote Sensing* 46, 307-315.

Valor E. and V.Caselles (1996). Mapping land surface emissivity from NDVI: Application to European, African, and South American areas. *Remote Sens. Environ.*, 57, 167-184.

Van Bavel C. H. M. and D. Hillel (1976). Calculating potential and actual evaporation from a bare soil surface by simulation of concurrent _ow of water and heat. Agricultural Meteorology, 76, 453-476.

Vaughan R. G., S. J. Hook, W. M. Calvin and J. V. Taranik (2005). Surface mineral mapping at Steamboat Springs, Nevada, USA, with multiwavelength thermal infrared images. *Remote Sens. Environ.*, 99(1/2).

Wu C., J. Wu, Y. Luo, L. Zhang, and S. D. DeGloria (2009), Spatial prediction of soil organic matter content using cokriging with remotely sensed data, *Soil Sci. Soc. Amer. J.*, 73(4), 1202-1208.

Zhan, X., W. P. Kustas, and K. S. Humes (1996). An intercomparison study on models of sensible heat flux over partial canopy surfaces with remotely sensed surface temperature. *Remote Sens. Environ.*, 58, 242-256. http://dx.doi.org/10.1016/S0034-4257(96)00049-1.

Appendix A

“Estimation of atmospheric water vapour content from direct measurements of radiance in the thermal infrared region”

Next study was published in *International Journal of remote Sensing* in April, 2011. This Journal has an *Impact Factor* of **1.117**, occupying the position 10 of the 24 journals in *Remote Sensing* category according to *ISI-Journal of Citation Reports Science Edition 2011*.

Remote Sensing Letters
Vol. 3, No. 1, January 2012, 31–38

Estimation of atmospheric water vapour content from direct measurements of radiance in the thermal infrared region

VICENTE GARCÍA-SANTOS*, JOAN MIQUEL GALVE, ENRIC VALOR,
VICENTE CASELLES and CÉSAR COLL
Department of Earth Physics and Thermodynamics, Faculty of Physics, University of Valencia, Burjassot 46100, Valencia, Spain

(*Received 7 July 2010; in final form 4 October 2010*)

Downloaded By: [García-Santos, Vicente García-Santos] At: 08:18 3 May 2011

Atmospheric water vapour content is a required parameter in thermal infrared (TIR) to carry out processes such as atmospheric correction or retrieving atmospheric factors (downwelling or upwelling irradiance, transmittance of the atmosphere and so on). This study proposes an alternative method to the ones already in use to measure water vapour content from direct measurements of downwelling atmospheric radiance in the TIR range. It was possible to estimate a linear relationship between atmospheric water vapour and downwelling atmospheric radiance using a simulated study, based on data from a radiosounding database. A subsequent validation concludes that it is possible to obtain water vapour content with an uncertainty of 0.5 cm using *in situ* measurements of downwelling atmospheric radiance in the TIR range of 11.5–12.5 μm.

1. Introduction

Currently, it is possible to estimate a value of the atmospheric water vapour content (W) using *in situ* measurements with instruments such as sun photometers (Estellés *et al.* 2007) with an uncertainty of ±0.15 cm. This direct technique usually works in the visible or the near-infrared spectral range. It is also possible to obtain W through satellite sensors, for instance the Medium Resolution Imaging Spectrometer (Guanter *et al.* 2008), the Michelson Interferometer for Passive Atmospheric Sounding (Milz *et al.* 2009) or the SCanning Imaging Absorption spectroMeter for Atmospheric CartograpHY (Noël *et al.* 2004), all onboard the Environmental Satellite platform. This study offers an alternative method to measure W if a sun photometer or satellite data are not available. The proposed method consists of estimating W with direct measurements of the sky radiance using a radiometer working in the thermal infrared (TIR) region of 8–14 μm.

The original idea started from the *diffusive approximation* proposed by Rubio *et al.* (1997), which states that the atmospheric downwelling radiance in the upper hemisphere ($L^{\downarrow}{}_{\mathrm{atm},\lambda}$) can be obtained from a direct measurement of the sky radiance at a nadir view ($L^{\downarrow}{}_{\mathrm{atm},\lambda}(0°)$) by

$$L^{\downarrow}_{\mathrm{atm},\lambda} = \gamma_\lambda L^{\downarrow}_{\mathrm{atm},\lambda}(0^\circ) \tag{1}$$

where λ indicates the spectral character of the measurements and γ_λ is a parameter that depends on both the spectral range of the measurements and the atmospheric

---

*Corresponding author. Email: vicente.garcia-santos@uv.es

Remote Sensing Letters
ISSN 2150-704X print/ISSN 2150-7058 online © 2012 Taylor & Francis
http://www.tandf.co.uk/journals
DOI: 10.1080/01431161.2010.531060

conditions. Between the parameters γ_λ and W exists a linear relationship that allows determining the atmospheric water vapour content using these measurements of radiance in the TIR region.

The aim of this study is divided into two stages. The first stage is centred on a simulation study that determines a mathematical relation between W and γ_λ in four spectral ranges in the TIR region using radiosounding data obtained from the Cloudless Land Atmosphere Radiosounding (CLAR) database (Galve *et al.* 2008). The second stage is focused on validating the previous relationship using direct measurements of W (in cm) and γ_λ.

2. Modelling a relationship between W and γ_λ

Starting from 180 different atmospheric conditions, included in the CLAR database, values of W were calculated from measurements of relative humidity (Φ) obtained for each radiosounding (see section 2.2); on the contrary, simulated values of γ_λ were possible by introducing these 180 atmospherics profiles into the radiative transfer code (RTC) MODTRAN 4v3r (Berk *et al.* 1999). From both the measured (W) and simulated (γ_λ) values, a linear relationship was established that allows the calculation of atmospheric water vapour content with sky radiance measurements.

Downloaded By: [García-Santos, Vicente García-Santos] At: 08:18 3 May 2011

2.1 *CLAR database*

The CLAR database is made up of radiosoundings compiled by the Atmospheric Science Department from the University of Wyoming (Laramie, WY, USA). The radiosoundings in the database are available through the website: http://weather.uwyo.edu/upperair/sounding.html.

CLAR contains a total of 382 radiosounding profiles, measured in land meteorological stations distributed relatively uniformly for the entire world. The profiles were filtered to remove all those that contained clouds. A radiosounding with a layer of more than 90% humidity and a subsequent layer of more than 85% humidity was considered cloudy and removed. A radiosounding with more than 80% humidity in the first 2 km was considered foggy and also removed. The CLAR database possesses a good distribution of atmospheric water vapour content, with approximately uniformly distributed values up to 5.5 cm. Forty percent of the radiosoundings is located in the low latitudes ($<30°$), 40% in middle latitudes (30°–60°) and the remaining 20% in high latitudes ($>60°$).

Once the filtration has been done as described above, a total of 180 cloud-free radiosoundings were chosen from the CLAR database, distributed between the months of June and August during the years 2003–2008.

2.2 *Simulated values of W and γ_λ*

Each one of the 180 radiosoundings corresponds to an atmospheric profile, with measured values of air temperature and relative humidity, which facilitates incorporation into a RTC to obtain calculated values of W and simulated values of γ_λ. With these data, it was possible to produce a graph of W versus γ_λ. This study introduced atmospheric profiles into the RTC model to obtain values for W, and the atmospheric downwelling radiance measured at a zenithal range of 0°–90°, which is independent of azimuthal angle (Rubio 1998).

To obtain γ_λ in this study, the atmospheric downwelling radiance was filtered for 11 zenithal observation angles (θ) corresponding to Gaussians angles (Wan and Dozier 1989), namely, 0.0°, 11.6°, 26.1°, 40.3°, 53.7°, 65.0°, 70.0°, 75.0°, 80.0°, 87.0° and 89.0°. The value of radiance at 0° corresponds to the parameter $L^{\downarrow}{}_{\mathrm{atm},\lambda}(0°)$ in equation (1), and the parameter $L^{\downarrow}{}_{\mathrm{atm},\lambda}$ at the same equation is obtained in integral form:

$$L^{\downarrow}_{\mathrm{atm},\lambda} = 2\int_{0}^{\pi/2} L^{\downarrow}_{\mathrm{atm},\lambda}(\theta)\cos\theta\sin\theta\,\mathrm{d}\theta \tag{2}$$

With these two values it is possible to calculate γ_λ from equation (1) by calculating the ratio:

$$\gamma_\lambda = \frac{L^{\downarrow}_{\mathrm{atm},\lambda}}{L^{\downarrow}_{\mathrm{atm},\lambda}(0°)} \tag{3}$$

where γ_λ is spectrally dependent.

In the simulation study, W was obtained from the measurements of relative humidity (Φ, in %), air temperature (T_a, in K) and atmospheric pressure (P, in mbar) made by each radiosounding of the CLAR database at different altitudes. First we calculate the saturation vapour pressure (e_s, in mbar) using the Clausius–Clapeyron equation:

$$e_\mathrm{s} = 6.11\exp\left\{\frac{L}{R_\mathrm{v}}\left(\frac{1}{273} - \frac{1}{T_\mathrm{a}}\right)\right\} \tag{4}$$

where $L = 2.453 \times 10^6$ J kg^{-1} is the latent heat of vaporization and $R_\mathrm{v} = 461$ J K^{-1} kg^{-1} is the gas constant for moist air. Once this parameter is calculated, the next step is to calculate the water vapour pressure (e, in mbar) as

$$e = \frac{\Phi}{100}e_\mathrm{s} \tag{5}$$

Now the mixing ratio is calculated as

$$r = \frac{0.622\,e}{P - e} \tag{6}$$

Finally, we obtain the water vapour content using the following integration:

$$W = \frac{1}{g_0}\int_{0}^{P_0} r(z)\,\mathrm{d}P \tag{7}$$

where $g_0 = 9.8$ m s^{-2} is the Earth's gravity constant, z represents the altitude of the radiosounding and P_0 is the atmospheric pressure at the surface level. In summary, with the previous processes we obtain 180 values of W and the corresponding simulated value of γ_λ.

Drawing on Hook *et al.* (2004) we assigned an uncertainty of ±10% to the Φ of the radiosounding and ±1 K to the T_a. These uncertainties imply a potential error of ±0.5 cm in determining W and ±0.3 in determining γ_λ for each of the four spectral channel of the CE 312 thermal radiometer.

Figure 1 presents W versus γ_λ, for the 180 different atmospheric conditions in four different thermal spectral bands corresponding to the four spectral channels of the

Downloaded By: [García-Santos, Vicente García-Santos] At: 08:18 3 May 2011

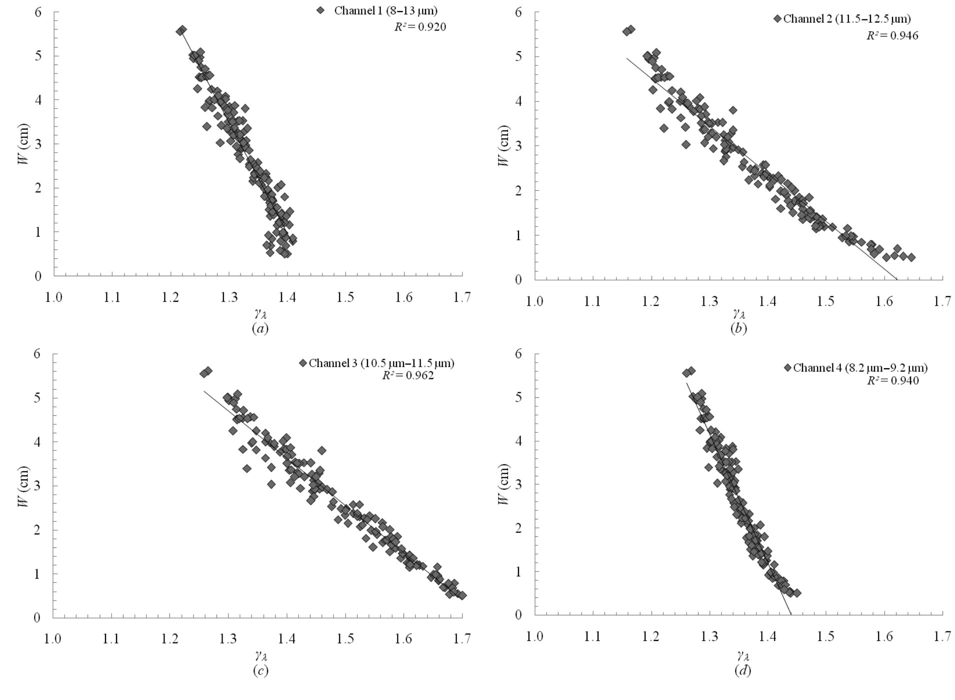

Figure 1. W versus γ_λ obtained from the 180 atmospheric situations extracted from the radiosoundings database CLAR, after analysis with the RTC. The expressions of the linear regression represented at each spectral range: (*a*) 8–14 μm, (*b*) 11.5–12.5 μm, (*c*) 10.3–11.3 μm and (*d*) 8.2–9.2 μm. The graphs correspond to equations (8)–(11), respectively.

multispectral radiometer CIMEL Electronique[†] model CE 312 used in this study (Brogniez *et al.* 2003). Those four spectral channels are located at 8–14 μm (channel 1), 11.5–12.5 μm (channel 2), 10.5–11.5 μm (channel 3) and 8.2–9.2 μm (channel 4). From the linear regression of the graphs in figure 1, for each spectral band, it is possible to establish a mathematical expression that relates the atmospheric water vapour content with γ_λ:

$$W = 36.4 - 25.3\gamma_{\mathrm{ch1}} \tag{8}$$

$$W = 17.3 - 10.7\gamma_{\mathrm{ch2}} \tag{9}$$

$$W = 18.7 - 10.7\gamma_{\mathrm{ch3}} \tag{10}$$

$$W = 42.8 - 29.7\gamma_{\mathrm{ch4}} \tag{11}$$

where the subscripts ‘ch*i*’ ($i = 1$–4) denote the corresponding spectral channel of the CE 312 thermal radiometer.

With the relationships obtained from figure 1, it is possible to calculate W with the availability of an instrument that works in one of the four aforementioned spectral bands. The relationships from equations (8)–(11) have uncertainties for W of ±0.4 cm (channel 1), ±0.3 cm (channel 2), ±0.2 cm (channel 3) and ±0.3 cm (channel 4).

[†] Trade and company names are given for the benefit of the reader and imply no endorsement by University of Valencia.

Downloaded By: [García-Santos, Vicente García-Santos] At: 08:18 3 May 2011

The next step is to validate the previous relationships using direct measurements of W and γ_λ, the latter calculated with measurements of atmospheric downwelling radiance using equation (3).

3. Validation of modelled relation

With the aim of validating the relationships extracted from figure 1, it was decided to take *in situ* measurements of $L^{\downarrow}{}_{\mathrm{atm},\lambda}(0°)$ and $L^{\downarrow}{}_{\mathrm{atm},\lambda}$ to calculate γ_λ using equation (3) and simultaneously to take measurements of W with another instrument. These measured values were compared to the simulated values of figure 1.

To measure the radiance $L^{\downarrow}{}_{\mathrm{atm},\lambda}(0°)$ and the hemispheric radiance $L^{\downarrow}{}_{\mathrm{atm},\lambda}$, we pointed the CE 312 radiometer to the sky and to a diffuse reflectance panel, respectively. This diffuse reflectance panel (García-Santos *et al.* 2010) has a rough gold surface capable of reflecting the atmospheric downwelling radiance in all angular directions, as it behaves in a Lambertian manner. The only correction applied to the measurements of the panel is to its spectral emissivity (Korb *et al.* 1996) to remove the panel contribution to the measured radiance. From measurements of thermodynamic temperature of the panel, taken *in situ* with a contact thermometer, the contribution of emissivity of the panel can be corrected by

$$L^{\downarrow}_{\mathrm{atm},\lambda} = \frac{L_{\mathrm{panel},\lambda} - \varepsilon_\lambda B_\lambda(T_{\mathrm{panel}})}{(1-\varepsilon_\lambda)} \tag{12}$$

where $L_{\mathrm{panel},\lambda}$ is the radiance measured directly over the panel, ε_λ is the spectral emissivity of the panel and $B_\lambda(T_{\mathrm{panel}})$ is the Planck function of the panel temperature T_{panel}.

Thus, the two needed radiances to calculate γ_λ using equation (3) are obtained. The uncertainties associated with γ_λ for channels 1–4 of CE 312 are ±0.03, ±0.04, ±0.06 and ±0.05, respectively.

To obtain W a CIMEL Electronique CE 318 sunphotometer was used (Holben *et al.* 1998). This instrument measures the atmospheric columnar water vapour in a channel centred at 940 nm, with an uncertainty of ±0.2 cm (Bruegge *et al.* 1992). The full width at half maximum of this channel is around 10 nm, and the sensor head is equipped with a double collimator with a 1.2° field of view.

Figure 2 shows a comparison of validation results with simulated results from figure 1 for the four spectral channels of the CE 312 thermal radiometer. Due to the few points of validation measured, taken in the months of February, March and May, the range of measured W was limited between 0.5 and 2.5 cm. It was therefore decided to compare the validation and simulation values of W and γ_λ in this range with their corresponding errors.

4. Results and discussion

Figure 2 shows that channel 2 is the only channel with simulated values coincident with the validation values. This is not strange because the effects of W are stronger in the spectral range of 11.5–12.5 µm (Varanasi 1988), which is the spectral range of channel 2 of the CE 312 thermal radiometer. It seems evident that this channel is the most sensitive to changes of W in the atmosphere, and therefore the most suitable from which to obtain W from measurements of atmospheric radiance in TIR region. Therefore, focusing solely on the spectral region 11.5–12.5 µm, and by considering the validation results as satisfactory, it is possible to establish a relationship between W and γ_λ.

Downloaded By: [García-Santos, Vicente García-Santos] At: 08:18 3 May 2011

Downloaded By: [García-Santos, Vicente García-Santos] At: 08:18 3 May 2011

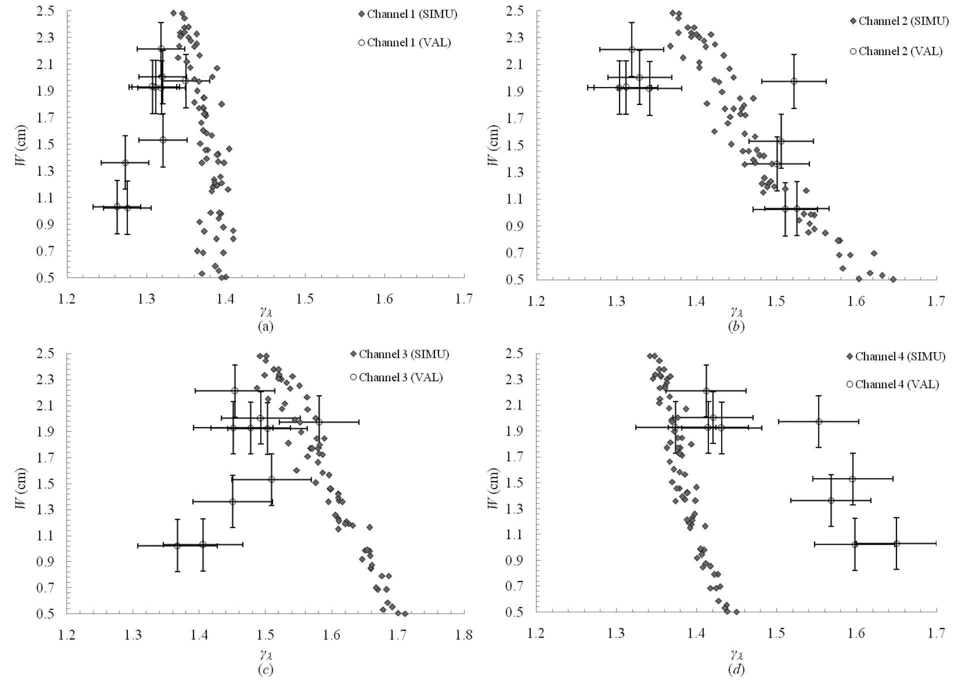

Figure 2. Comparison of validation results (VAL) and simulated values (SIMU) of W and γ_λ in the four spectral channels of the CE 312 (*a*) channel 1, (*b*) channel 2, (*c*) channel 3 and (*d*) channel 4. For the validation case, the errors of the measurements of γ_λ and W are included.

Considering equation (9) as the desired expression to obtain W, and obtaining measurements of the atmospheric downwelling radiance with a TIR instrument as has been explained, W can be estimated with an uncertainty of ±0.3 cm, which corresponds to the standard deviation. Furthermore, the difference between the calculated value of W using equation (9) for each of the 10 validation points, and the value of W measured directly by the sunphotometer CE 318, shows a bias of 0.4 cm. Overall, this methodology can be used to measure W with a root mean square error of ±0.5 cm.

We can conclude that there exists an expression that obtains the atmospheric water vapour content, equation (9), and by using that expression the uncertainty in the estimation of W is ±0.5 cm.

This study could probably be improved with more validation points, which is desired by the authors. In any case, this is the first approximation of an alternative method to those currently in use in determining W, which may be useful to an experimenter who has only TIR radiometers available.

5. Conclusions

In this study, an alternative method has been proposed to determine the atmospheric water vapour content using measurements *in situ* of atmospheric radiance in the TIR range. The proposed method is to use direct measurements of atmospheric downwelling radiance related with atmospheric water vapour content using the factor γ_λ present in the diffusive approximation proposed by Rubio *et al.* (1997). After a comparison of simulated values, obtained from the CLAR database, with *in situ* measurements of atmospheric water vapour content and γ_λ for the four spectral ranges in which the thermal radiometer CE 312 works, we come to the conclusion that it is possible to obtain W through measurements of atmospheric downwelling radiance in the TIR region of 11.5–12.5 μm with a root mean square error of ±0.5 cm.

Acknowledgements

This work was made possible with funding from the Spanish *Ministerio de Ciencia e Innovación* (grant of V. García-Santos associated to project CGL2007-64666/CLI and project CGL2007-29819-E/CLI, cofinanced by FEDER funds) and the finance of the *Conselleria d'Educació de la Generalitat Valenciana* (project PROMETEO/2009/086). The authors thank the CEAM foundation for its contribution to this work, the radiosounding data (project TRANSREG (CGL2007-65359/CLI)) and Dr. Victor Estellés, from the Solar Radiation Group in Department of Earth Physics and Thermodynamics (University of Valencia, Valencia, Spain), for providing us with atmospheric water vapour content measurements framed in projects CGL2007-60648 and CGL2010-07790.

Downloaded By: [García-Santos, Vicente García-Santos] At: 08:18 3 May 2011

References

Berk, A., Anderson, G.P., Acharya, P.K., Chetwynd, J.H., Bernstein, L.S., Shettle, E.P. Matthew, M.W. and Adler-Golden S.M., 1999, *MODTRAN 4 User's Manual.* (Bedford, MA: Air Force Research Laboratory's Space Vehicles Directorate, Air Force Materiel Command, Hascom AFB), p. 95.

Brogniez, G., Pietras, C., Legrand, M., Dubuisson, P. and Haeffelin, M., 2003, A high-accuracy multiwavelength radiometer for in situ measurements in the thermal infrared – part II: behavior in field experiments. *Journal of Atmospheric and Oceanic Technology*, **20**, pp. 1023–1033.

Bruegge, C.J., Conel, J.E., Green, R.O., Margolis, J.S., Holm, R.G. and Toon, G., 1992, Water vapor abundance retrievals during FIFE. *Journal of Geophysical Research*, **97**, pp. 18759–18768.

Estellés, V., Martínez-Lozano, J.A., Utrillas, M.P. and Campanelli, M., 2007, Columnar aerosol properties in Valencia (Spain) by ground-based Sun photometry. *Journal of Geophysical Research*, **112**, p. 9, doi: 10.1029/2006JD008167.

Galve, J.M., Coll, C., Caselles, V. and Valor, E., 2008, An atmospheric radiosounding database for generating land surface temperature algorithm. *Remote Sensing of Environment*, **46**, pp. 1547–1557, doi: 10.1109/TGRS.2008.916084.

García-Santos, V., Valor, E., Mira, M., Coll, C., Galve, J.M. and Caselles, V., 2010, Evaluación de distintos métodos de medida de la radiancia atmosférica descendente en el infrarrojo térmico. *Revista de Teledetección* (under review).

Guanter, L., Gómez-Chova, L. and Moreno, J., 2008, Coupled retrieval of aerosol optical thickness, columnar water vapor and surface reflectance maps from ENVISAT/ MERIS data over land. *Remote Sensing of Environment*, **112**, pp. 2898–2913, doi: 10.1016/j.rse.2008.02.001.

Holben, B.N., Eck, T.F, Slutsker, I., Tanré, D., Buis, J.P., Setzer, A., Vermote, E., Reagan, J.A., Kaufman, Y.J., Nakajima, T., Lavenu, F., Jankowiak, I. and Smirmov, A., 1998, AERONET—a federated instrument network and data archive for aerosol characterization. *Remote Sensing of Environment*, **66**, pp. 1–16.

Hook, S.J., Chander, G., Barsi, J.A., Alley, R.E., Abtahi, A., Palluconi, F.D., Markham, B.L., Richards, R.C., Schladow, S.G. and Helder, D.L., 2004, In-flight validation and recovery of water surface temperature with landsat-5 thermal infrared data using an automated high-altitude lake validation site at lake Tahoe. *IEEE Transactions on Geoscience and Remote Sensing*, **42**, pp. 2767–2776.

Korb, A.R., Dybwad, P., Wadsworth, W. and Salisbury, J.W., 1996, Portable Fourier transform infrared spectroradiometer for field measurements of radiance and emissivity. *Applied Optics*, **35**, pp. 1679–1692.

Milz, M., Clarmann, T.V., Bernath, P., Boone, C., Buehler, S.A., Chauhan, S., Deuber, B., Feist, D.G., Funke, B., Glatthor, N., Grabowski, U., Griesfeller, A., Haefele, A., Höpfner, M., Kämpfer, N., Kellmann, S., Linden, A., Müller, S., Nakajima, H., Oelhaf, H., Remsberg, E., Rohs, S., Russell III, J.M., Schiller, C., Stiller, G. P., Sugita, T., Tanaka, T., Vömel, H., Walker, K., Wetzel, G., Yokota, T., Yushkov, V. and Zhang, G., 2009, Validation of water vapour profiles (version 13) retrieved by the IMK/IAA scientific retrieval processor based on full resolution spectra measured by MIPAS on board Envisat. *Atmospheric Measurement Techniques*, **2**, pp. 379–399.

Noël, S., Buchwitz, M. and Burrows, J. P., 2004, First retrieval of global water vapour column amounts from SCIAMACHY measurements. *Atmospheric Chemistry and Physics*, **4**, pp. 111–125.

Rubio, E., 1998, Hacia la optimización de la medida de la emisividad y la temperatura en teledetección. PhD thesis, University of Valencia, Burjassot, Spain.

Rubio, E., Caselles, V. and Badenas, C., 1997, Emissivity measurements of several soils and vegetation types in the 8–14 µm wave band: analysis of two field methods. *Remote Sensing of Environment*, **59**, pp. 490–521.

Varanasi, P., 1988, Infrared absorption by water vapor in the atmospheric window. *SPIE Modeling of the Atmosphere*, **98**, pp. 213–230.

Wan, Z. and Dozier, J., 1989, Land-surface temperature measurement from space: physical principles and inverse modeling. *IEEE Transactions on Geoscience and Remote Sensing*, **27**, pp. 268–277.

Downloaded By: [García-Santos, Vicente García-Santos] At: 08:18 3 May 2011

Appendix B

“Evaluation of different methods to retrieve the hemispherical downwelling irradiance in the thermal infrared region for field measurements”

Next study was published in *IEEE Transactions on Geoscience and Remote Sensing* in August, 2012. This Journal has an *Impact Factor* of **3.467**, occupying the position 2 of the 27 journals in *Remote Sensing* category according to *ISI-Journal of Citation Reports Science Edition 2012*.

Evaluation of Different Methods to Retrieve the Hemispherical Downwelling Irradiance in the Thermal Infrared Region for Field Measurements

Vicente García-Santos, Enric Valor, Vicente Caselles, Maria Mira, Joan Miquel Galve, and César Coll

***Abstract*—The thermal infrared hemispherical downwelling irradiance (HDI) emitted by the atmosphere and surrounding elements contributes through reflection to the signal measured over an observed surface by remote sensing. This irradiance must be estimated in order to obtain accurate values of land-surface temperature (LST). There are some fast methods to measure the HDI with a single measurement pointing to the sky at a specified viewing direction, but these methods require completely cloud-free or cloudy skies, and they do not account for the radiative contribution of surrounding elements. Another method is the use of a diffuse reflectance panel (usually, a rough gold-coated surface) with near-Lambertian behavior. This method considers the radiative contribution of surrounding elements and can be used under any sky condition. A third possibility is the use of atmospheric profiles and a radiative transfer code (RTC) in order to simulate the atmospheric signal and to calculate the HDI by integration. This study compares the HDI estimations with these approaches, using measurements made on four different days with a completely clear sky and two days with a partially cloudy sky. The measurements were made with a four-channel CIMEL Electronique radiometer working in the 8–14-μm spectral range. The HDI was also estimated by means of National Centers for Environmental Prediction atmospheric profiles introduced in the MODTRAN RTC. Additionally, the measurements were made at two different places with very different environments to quantify the effect of the contributing surroundings. Results showed that, for a clear-sky day with a minimal contribution of the surroundings, all methods differed from each other between 5% and 11%, depending on the spectral range, and any of them could be used to estimate HDI in these conditions. However, in the case of making surface measurements in an area with significant surrounding elements (buildings, trees, etc.), HDI values retrieved from the panel present an increase of $+3\ \mathrm{W \cdot m^{-2} \cdot \mu m^{-1}}$ compared with the other methods; this increase, if ignored, implies to make an error in LST ranging from $+0.5\ ^\circ\mathrm{C}$ to $+1.5\ ^\circ\mathrm{C}$, depending on the spectral range and on surface emissivity and temperature. Comparison under heterogeneous skies with changing cloud coverage showed also large differences between the use of panel and the other methods, reaching a maximum difference of $+4.6\ \mathrm{W \cdot m^{-2} \cdot \mu m^{-1}}$, which implies to make an error on LST of $+2.2\,^\circ\mathrm{C}$. In these cases, the use of the diffuse reflectance panel is proposed, since it is the unique way to capture the contribution of the surroundings and also to adequately measure HDI for sky changing conditions.**

***Index Terms*—Angular measurements, diffuse reflectance panel, field measurements, hemispherical downwelling radiance, thermal infrared (TIR).**

I. INTRODUCTION

THE accurate measurement of land-surface temperatures (LSTs) using thermal infrared [(TIR), 8–14 μm] remote sensing measurements in the field needs to take into account two important factors: 1) land-surface emissivity $\varepsilon_{\mathrm{sur}}$ and 2) the hemispherical downwelling irradiance (HDI) $F_{\mathrm{HEM}}^{\downarrow}$ coming from the surroundings and the atmosphere, which is, in turn, reflected by the surface to the sensor. The land-leaving radiance from an observed area placed at surface level (L_{sur}), considering Lambertian behavior, is

$$L_{\mathrm{sur}} = \varepsilon_{\mathrm{sur}} B(T) + (1 - \varepsilon_{\mathrm{sur}}) \frac{F_{\mathrm{HEM}}^{\downarrow}}{\pi} \tag{1}$$

where B is Planck's radiance function for a blackbody emitting at the kinetic temperature T.

To correct L_{sur} measurements in (1) from the emissivity effect and to get accurate LST values, it is needed to measure $F_{\mathrm{HEM}}^{\downarrow}$ in addition to $\varepsilon_{\mathrm{sur}}$. The most exact way to obtain $F_{\mathrm{HEM}}^{\downarrow}$ is to measure the radiance from all possible zenithal and azimuthal directions $L^{\downarrow}(\theta, \varphi)$ and to integrate these measurements. Since this measurement process takes a long time to be performed, which is particularly critical when the sky is partially cloudy and can be changing over time, there exist other alternative faster methods allowing accurate measurement of $F_{\mathrm{HEM}}^{\downarrow}$. Hereinafter, these methods are presented.

The first method is based on taking a single measurement of the sky at a specific direction. For example, in [1], Kondratyev showed that a single measurement, pointing the radiometer at a zenith angle of $(53 \pm 3)^\circ$ measured from the vertical $(L_{\mathrm{sky}}^{\downarrow}(53^\circ))$, at any azimuth angle, gave a close value of the hemispherical irradiance of the atmosphere

$$F_{\mathrm{HEM\_Kond}}^{\downarrow} = \pi L_{\mathrm{sky}}^{\downarrow}(53^\circ). \tag{2}$$

Manuscript received November 8, 2010; revised May 10, 2011, December 8, 2011, and April 11, 2012; accepted July 10, 2012. Date of publication August 31, 2012; date of current version March 21, 2013. This work was supported in part by the Spanish Ministerio de Ciencia e Innovación and FEDER funds under projects CGL2007-64666/CLI, CGL2007-29819-E/CLI, and CGL2010-17577/CLI and in part by Conselleria d'Educació Formació i Ocupació of the Generalitat Valenciana under project PROMETEO/2009/086. The work of V. García-Santos was supported in part by the Spanish Ministerio de Ciencia e Innovación and in part by FEDER funds. The work of M. Mira was supported in part by Conselleria d'Educació Formació i Ocupació of the Generalitat Valenciana and in part by the Spanish Ministerio de Ciencia e Innovación.

V. García-Santos, E. Valor, V. Caselles, J. M. Galve, and C. Coll are with the Department of Earth Physics and Thermodynamics, Faculty of Physics, University of Valencia, 46100 Burjassot, Spain (e-mail: vicente.garcia-santos@uv.es; enric.valor@uv.es; vicente.caselles@uv.es; joan.galve@uv.es; cesar.coll@uv.es).

M. Mira is with the National Institute for Agricultural Research (INRA), 84914 Avignon, France (e-mail: Maria.Mira@uv.es)

Color versions of one or more of the figures in this paper are available online at http://ieeexplore.ieee.org.

Digital Object Identifier 10.1109/TGRS.2012.2209891

0196-2892/$31.00 © 2012 IEEE

Results from Kondratyev approximation were checked in [2] by Rubio *et al.*, using atmospheric radiances measured during a whole year with a goniometer that allowed scanning the atmosphere in several azimuth and zenith angles. The experiment included both clear and overcast days, and the measurements were performed from 0° to 85° in zenithal direction and in different azimuths. Results showed that the sky was, in all cases, almost isotropic in the azimuthal direction and showed a significant anisotropy in the zenithal direction. The authors also obtained that a single measurement at a zenith angle of $(55.4 \pm 1.8)^\circ$ could provide a way to obtain the atmospheric irradiance, as stated by (2), and in agreement (within the error) with the Kondratyev estimation. In addition, a modification of the Kondratyev approximation was proposed in [2], which only requires a single measurement of the sky radiance at nadir $L^{\downarrow}_{\text{sky}}(0^\circ)$ and multiplying this irradiance by a coefficient (γ) that depends on the TIR channel used and the atmospheric conditions, particularly atmospheric total water vapor content (W) [3]

$$F^{\downarrow}_{\text{HEM\_Rub}} = \gamma \pi L^{\downarrow}_{\text{sky}}(0^\circ) \tag{3}$$

where the values of γ can vary from 1.1 to 1.7. This version of the Kondratyev approximation is more practical in the field, because it does not require making an accurate measurement of the viewing zenith angle.

These two techniques are fast, but both require homogeneous atmospheric conditions (complete cloud cover or complete clear sky), and do not consider the possible radiative contribution of the surrounding elements. Moreover, the technique proposed by [2] needs an estimate of the water vapor content (W) to calculate γ, W being the total amount of water yielded by the vertical integration from the ground level to the top of the atmosphere; this dependence will be explained later.

A second method to obtain $F^{\downarrow}_{\text{HEM}}$ is the use of an atmospheric profile which can be introduced into a radiative transference code (RTC) such as MODTRAN 4v3r [4]. In this paper, atmospheric profiles resulting from reanalysis techniques have been used, provided by the National Centers for Environmental Prediction (NCEP). These profiles need to be interpolated temporally and spatially at the time and place of the measurements [5], using the coordinates of the desired area and the central time of the measurement session. Simulation procedures present also some drawbacks. NCEP profiles are predicted from data obtained from spatial and temporal interpolations, whereas the atmospheric conditions not only can be significantly different in the region nearest to the interest zone but also can change with time. Moreover, these profiles are representative of a 1° spatial resolution area.

The third methodology is the use of a gold diffuse panel with high reflectance and a near-Lambertian behavior, retrieving $F^{\downarrow}_{\text{HEM}}$ by measuring the reflected radiance on the panel from any viewing direction. The advantages of this methodology are that it can be used under any atmospheric condition and that its measurements take into account the radiative contribution of the surrounding elements in addition to the contribution of the atmosphere. Several works have made use of gold diffuse surfaces as a satisfactory alternative for measuring $F^{\downarrow}_{\text{HEM}}$ [6]–[14].

Different authors have made use of one or another methodology to estimate or calculate the HDI for different objectives, such as measuring surface emissivity [7]–[15], correcting satellite-based measurements for the atmospheric effect [16], measuring LST in the field for validation purposes [17], or obtaining emissivity and temperature from radiance measurements using emissivity–temperature separation algorithms [18], to give some examples. However, to our knowledge, there is not a work in the bibliography that does the following: 1) compares the different methods to check to what extent their estimations of $F^{\downarrow}_{\text{HEM}}$ in field are in agreement, pointing out the applicability conditions of each one, particularly in the case of different contributive surrounding elements, or under changing sky conditions with different cloud coverage and 2) explains, with detail, the practical procedure to measure $F^{\downarrow}_{\text{HEM}}$ using gold diffuse reflectance panels with reference to suitable viewing angles, effect of the surroundings, or changing skies. These are the main contributions of this paper to previously published work.

Thus, the objective of this paper is to make an evaluation of four different methodologies to estimate $F^{\downarrow}_{\text{HEM}}$, evaluating possible inaccuracies retrieving LST with the use of one or another method in field measurements. With this aim, a simple experimental setup was designed to perform $F^{\downarrow}_{\text{HEM}}$ measurements, from both a golden diffuse reflectance panel and the approximations given by (2) and (3), at two different places with a different number of surrounding elements and under different cloud coverage of the sky. Simulated values of $F^{\downarrow}_{\text{HEM}}$ calculated using atmospheric profiles provided by the NCEP in the MODTRAN RTC were also included.

This paper proceeds as follows. The instrumentation is presented first in Section II. Next, Section III describes the methodology to compare the previous techniques to obtain $F^{\downarrow}_{\text{HEM}}$. Section IV presents the results and their discussion. Finally, the most important conclusions drawn from this study are given in Section V.

II. INSTRUMENTATION

This work was conducted using a radiometer CIMEL Electronique (CE312-1) [19], which is a multispectral sensor that measures the radiance emitted by a surface in the TIR region (8–14 μm). It is composed of an optical head, which points to the observed surface, and a data logger joined to the optical head, which is responsible for recording the measurements. The CE312-1 has four filters that allow us to measure in a wide spectral interval (channel 1: 8.0–13.3 μm) and three narrow spectral intervals located within the wide channel (channel 2: 11.5–12.4 μm; channel 3: 10.2–11.3 μm; channel 4: 8.3–9.3 μm). The field of view (FOV) of the optical head is 10°. A previous calibration of the CE312-1 thermal radiometer with a primary reference blackbody carried out in April 2009 at the National Physical Laboratory, London, U.K., organized by the Committee on Earth Observation Satellites [20], showed uncertainties in spectral radiance for the channels 1–4 of ± 0.06,

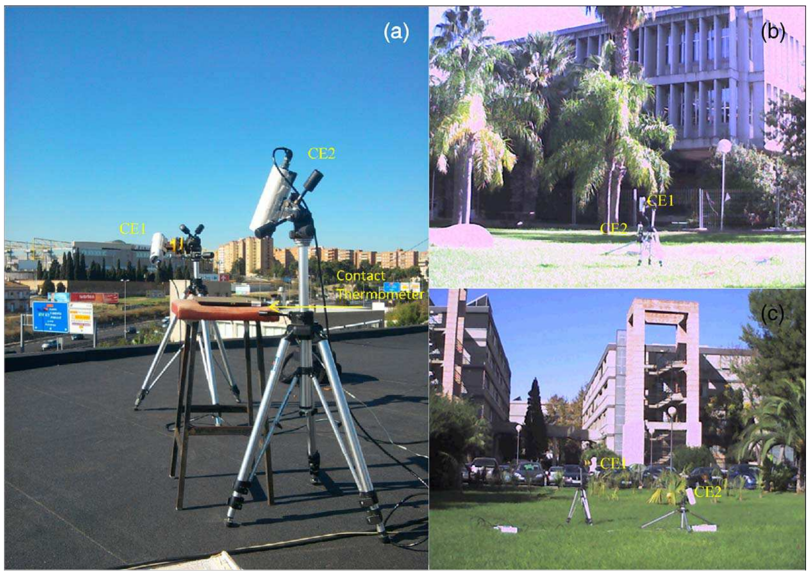

Fig. 1. Experimental assembly used to perform the irradiance measurements on the diffuse reflectance panel, with a CE312-1 radiometer (CE2) mounted on a tripod and measuring to the panel, at 25° zenith angle. A second CE312-1 radiometer (CE1) was mounted on a tripod for measuring the irradiance from sky, pointing it at 0° and 55°. This assembly was mounted in two different places: (a) Roof of the Physics Faculty (with minimal presence of surrounding elements) and (b) and (c) close to the University Library (with presence of surrounding elements such as buildings, trees, and cars).

± 0.06, ± 0.06, and $\pm 0.13\ \mathrm{W \cdot m^{-2} \cdot sr^{-1} \cdot \mu m^{-1}}$, respectively (or, equivalently, ±0.5 K, ±0.6 K, ±0.3 K, and ±0.6 K in radiative temperature).

The diffuse reflectance panel *Infragold Reflectance Target IRT-94-100* from Labsphere is a gold rugged surface of $25.4 \times 25.4\ \mathrm{cm}^2$ and 1 cm of thickness. This panel has high reflectivity in the TIR region, with CE312-1 four-channel values of 0.923, 0.925, 0.925, and 0.918, respectively. These channel reflectivity values are the result of filtering the spectral reflectance values provided by the manufacturer between 8 and 14 μm at 0.05-μm steps, using the filter functions of the four CE312-1 bands, with an error of ±0.009. Consequently, following Kirchhoff's law, the emissivities of the panel in each channel are 0.077, 0.075, 0.075, and 0.082, respectively.

III. METHODOLOGY

In order to compare different methods to retrieve $F^{\downarrow}_{\mathrm{HEM}}$, a previous characterization of the panel was made to check if it presented Lambertian behavior. For this purpose, the CE312-1 radiometer was used mounted on a goniometer taking angular measurements on the panel from 0° to 60° zenith angles (θ), at intervals of 10°. Three consecutive readings were made at each zenith angle, and at the end of these three readings, the panel was turned azimuthally 120° and 240° from its original orientation. Thus, three azimuths for each zenith angle and seven zenith angles that are 3×7 measurements were performed to check the Lambertian behavior of the panel. The zenithal variation was made with the radiometer placed 50 cm away from the panel at nadir view; this distance was chosen as a compromise between maintaining the radiometer's FOV within the panel's area, particularly for large zenith angles, and maximizing the distance of the radiometer from the surface, to avoid as much as possible its own radiative contribution, taking measurements of the maximum area possible.

Once the angular behavior of the panel was analyzed (see Section IV-A), the four methods to retrieve $F^{\downarrow}_{\mathrm{HEM}}$ were compared. The HDI was obtained with the panel $(F^{\downarrow}_{\mathrm{HEM\_panel}})$ taking radiance measurements on it, regardless the azimuth angle, and performing the correction for the panel emissivity (see Section III-A as follows). Simultaneous to panel radiance measurements, another identical radiometer CE312-1 took radiance measurements of the atmosphere measuring the sky both at nadir to retrieve $L^{\downarrow}_{\mathrm{sky}}(0^{\circ})$, required in (3) to obtain the HDI using the Rubio *et al.* approximation [2]$F^{\downarrow}_{\mathrm{HEM\_Rub}}$, and at 55° to get a value of $F^{\downarrow}_{\mathrm{HEM\_Kond}}$ according to the Kondratyev approximation through (2) [1]. The time period between two consecutive $L^{\downarrow}_{\mathrm{sky}}(0^{\circ})$ and $L^{\downarrow}_{\mathrm{sky}}(55^{\circ})$ measurements was around 3 min, a time short enough to consider $F^{\downarrow}_{\mathrm{HEM}}$, retrieved between both methods, comparable together with panel measurements. Fig. 1 shows the experimental setup.

Additionally, $F^{\downarrow}_{\mathrm{HEM}}$ values were calculated using atmospheric profiles, provided by NCEP reanalysis [5], and the MODTRAN 4v3r code [4]. The profiles were obtained from the Web-based tool Atmospheric Correction Parameter Calculator [22] which, with previous specification of date, time, and location, gives values of pressure, atmospheric temperature (T_a), and relative humidity (RH), interpolated spatially and temporally at the place and time of the radiance measurements. Atmospheric profiles generated by NCEP incorporate satellite and surface data to characterize a global atmosphere at 28 altitudes, and they are sampled on a $1^{\circ} \times 1^{\circ}$ grid and generated every 6 h. From two options offered by the calculator, "*Use interpolated atmospheric profile for given lat/long*" was chosen; this option extracts a profile from the four grid corners which surround the input location for the two times before and after the input time, so corner profiles are interpolated for each time resulting in the desired time profiles (see Fig. 3 in [22]). Profiles obtained were processed with the MOD-

TRAN code, which provided $L^{\downarrow}(\theta)$ values for the zenith angles 0.0°, 11.6°, 26.1°, 40.3°, 53.7°, 65.0°, 70.0°, 75.0°, 80.0°, 87.0°, and 89.0° (the so-called Gaussian angles, see [21]). Finally, $F^{\downarrow}_{\mathrm{HEM\_NCEP}}$ was retrieved integrating these values. According to [22], uncertainties of $\pm 6\%$ and ± 2 K were assigned to RH and T_a, respectively, on the NCEP atmospheric profiles. The difference of $F^{\downarrow}_{\mathrm{HEM}}$, obtained with the original atmospheric profile and obtained with a profile modified with the previous uncertainties, implies a relative error of 20% in $F^{\downarrow}_{\mathrm{HEM\_NCEP}}$ values for all the spectral channels of CE312-1.

The four different $F^{\downarrow}_{\mathrm{HEM}}$ values obtained from different procedures, using a panel, with the two approximation techniques, and by means of atmospheric profiles were compared under two different conditions.

The first evaluation was made at two different places with a significant difference of surrounding elements from one to the other place. In this case, the objective was to quantify the differences between the panel measurements and the other approaches due to the effect of surrounding elements with temperatures comparable to the observed surface. Both places were located in the University of Valencia campus in Burjassot, Spain (39° 30′ 25″ N, 0° 18′ 15″ W). The first one was located at the roof of the Physics Faculty, hereafter called *roof*; in this place, the presence of surrounding elements was minimal [scientific instrumentation and the roof of surrounding buildings a little higher than the faculty building, see Fig. 1(a)]. The second place was located near the campus library, hereafter *library*; in this place, the presence of surrounding elements was significantly greater than those in the *roof* [trees, cars, and different buildings such as the library building and the Physics and Chemistry Faculty buildings, see Fig. 1(b) and (c)].

A second evaluation was carried out at the *roof* (to minimize the effect of surroundings) for different cloud coverage conditions of the sky rapidly changing. The four methods to retrieve $F^{\downarrow}_{\mathrm{HEM}}$ were compared under different percentage of clouds occupying the sky. In this case, the objective was to quantify the differences between the panel measurements (that capture the contribution from the clouds) and the other approaches. Results of both comparisons are shown and analyzed in Section IV.

A. Panel Emissivity Correction

There are some questions that must be addressed before comparing the four methods to retrieve $F^{\downarrow}_{\mathrm{HEM}}$. The panel has also a contribution to the measured signal due to the small emissivity of the gold rugged surface (see Section II). This contribution must be removed from the direct measurements made over the panel according to [8]

$$L^{\downarrow}_{\mathrm{panel\_corr}} = \frac{L^{\downarrow}_{\mathrm{panel}} - \varepsilon_{\mathrm{panel}} B(T_{\mathrm{panel}})}{(1 - \varepsilon_{\mathrm{panel}})} \tag{4}$$

where $L^{\downarrow}_{\mathrm{panel}}$ is the radiance measured directly on the panel, $\varepsilon_{\mathrm{panel}}$ is its emissivity, and T_{panel} is the temperature of the panel that must be known to calculate Planck function $B(T_{\mathrm{panel}})$. The HDI is obtained finally as $F^{\downarrow}_{\mathrm{HEM\_panel}} = \pi L^{\downarrow}_{\mathrm{panel\_corr}}$. A contact thermometer, with an accuracy of ± 1 °C, was used to measure the temperature of the panel [see Fig. 1(a)]. This accuracy implies to make an error in estimating the radiance emitted by the panel, through $B(T_{\mathrm{panel}})$, of $\pm 0.09\ \mathrm{W} \cdot \mathrm{m}^{-2} \cdot \mathrm{sr}^{-1} \cdot \mu\mathrm{m}^{-1}$ for all the channels of CE 312-1. Errors associated to panel spectral irradiance measurements were obtained from error propagation applied to (4) due to errors of the CE 312-1 radiometers (see Section II) and of the contact thermometer. These errors gave maximum values for channels 1–4 of ± 0.3, ± 0.3, ± 0.3, and $\pm 0.4\ \mathrm{W} \cdot \mathrm{m}^{-2} \cdot \mu\mathrm{m}^{-1}$, respectively.

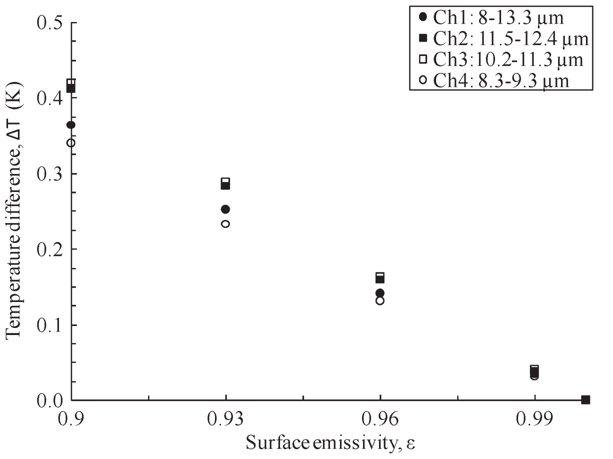

Fig. 2. Temperature difference (ΔT) in the surface temperature retrieved from remote sensing measurements using (1), when the diffuse reflectance panel emissivity and temperature are accounted for, and when they are not, for the measurement of $F^{\downarrow}_{\mathrm{HEM}}$ using the panel. A surface temperature of 303 K has been considered for this calculation, for a range of surface emissivities from 0.99 to 1. This graph shows the systematic error in the retrieved temperature if the emissivity of the panel is neglected.

The impact of ignoring the panel emissivity in the measurement of a surface temperature in the field (for example, when measuring soil or vegetation temperatures) has been estimated. The LST difference obtained from (1), when it is used, the measurement taken directly from the panel ($L^{\downarrow}_{\mathrm{panel}}$ multiplied by π), or the value corrected for the panel emissivity ($F^{\downarrow}_{\mathrm{HEM\_panel}}$), for a given value of surface brightness temperature, has been calculated. Fig. 2 shows the case of a surface with a brightness temperature of 303 K and for different values of surface emissivity. The parameter $\Delta T = LST_{\mathrm{corr}} - LST_{\mathrm{ign}}$ represents the difference between the LST when the panel emissivity is considered and corrected (LST_{corr}) and the surface temperature when the panel emissivity is ignored (LST_{ign}). The difference between the LSTs increases when the surface emissivity decreases. For instance, for a surface emissivity of 0.9, the temperature difference is around ± 0.5 K, for all the channels; however, for surface emissivities larger than 0.94, the effect of the panel emissivity is not significant. In any case, when the emissivity effect is corrected, a better agreement between the measurements of the panel and the other approaches is obtained.

B. Estimation of the γ Coefficient

Another point to be considered is the selection of an adequate value of the γ coefficient needed in (3). Since it depends on the channel and also on W, a previous simulation study [3]

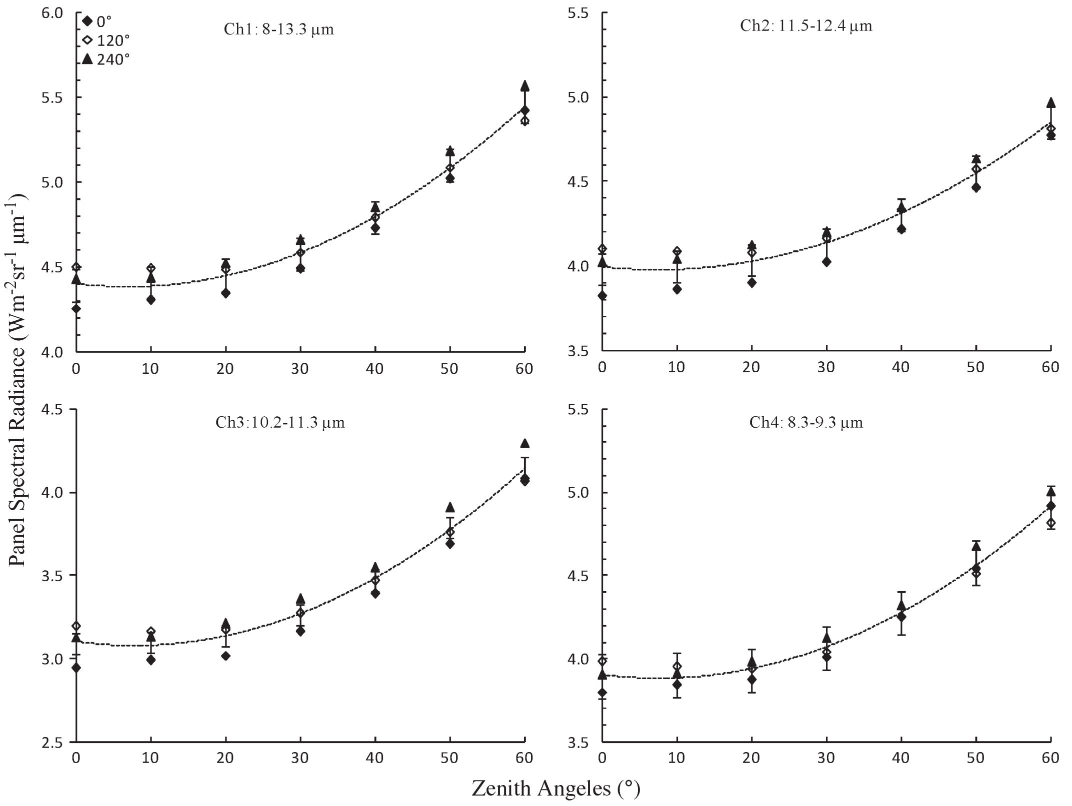

Fig. 3. Panel spectral radiance measurements made for the four channels of CE 312-1, taken at three different azimuth angles, namely, 0°, 120°, and 240°, and for zenith angles from 0° to 60° at 10° steps. Measurements were made at the *roof*, in cloud-free sky conditions. (Dotted line) Average value of the three azimuth values for each zenith angle, together with its uncertainty, is also shown.

was carried out using the radiosounding data contained in the Cloudless Land Atmosphere Radiosonde database [21], which spans a W interval from 0.02 to 5.61 cm. For each of these atmospheric profiles, the parameters W, $L_{\text{sky}}^{\downarrow}(0^\circ)$, and $F_{\text{HEM}}^{\downarrow}$ were calculated, from which the γ coefficient was derived. A linear relationship was obtained between γ and W (in centimeters) using the data for the four channels of the CE312-1

$$\begin{aligned}\gamma_{\text{ch1}} &= 1.43 - 0.04\ \text{W}\\ \gamma_{\text{ch2}} &= 1.61 - 0.09\ \text{W}\\ \gamma_{\text{ch3}} &= 1.73 - 0.09\ \text{W}\\ \gamma_{\text{ch4}} &= 1.44 - 0.03\ \text{W}.\end{aligned} \tag{5}$$

The dependence of γ with W is weak, particularly for spectral channels 1 and 4. These relationships were checked with direct measurements of γ and W. The γ coefficients were also determined using (3) by measuring, under cloudless sky condition, $L_{\text{sky}}^{\downarrow}(0^\circ)$ pointing the radiometer to the sky at 0° and $F_{\text{HEM}}^{\downarrow}$ pointing it at 55°; while W was measured with a sunphotometer CIMEL Electronique model CE318 [23], the same is used in this study to retrieve the W applied to (5). These relationships allow adjusting γ from W with error values of ±0.09, ±0.09, ±0.16, and ±0.18, for the channels 1–4 of CE312-1, respectively. The HDI error associated to the approximation of Rubio *et al.* is retrieved from error propagation through (3).

IV. RESULTS AND DISCUSSION

A. Panel Characterization

Fig. 3 shows channel radiance measurements retrieved with (4), at three different azimuth angles (0°, 120°, and 240°) for a zenithal variation from 0° to 60° at 10° steps. These angular measurements were made for several days at the *roof* place (see Section III and Fig. 1), with cloud-free sky conditions. The measurements show a significant zenithal dependence, while the azimuthal dependence is almost negligible. In fact, the standard deviation of the three azimuthal values for each zenith angle was calculated, and the maximum standard deviations obtained were ± 0.11, ± 0.13, ± 0.11, and $\pm 0.08\ \text{W} \cdot \text{m}^{-2} \cdot \text{sr}^{-1} \cdot \mu\text{m}^{-1}$ for CE312-1 channels 1–4, respectively. These deviations are of the same order of magnitude than the measurement uncertainty (see Section III). Thus, it may be concluded that the panel shows azimuthal isotropy in radiance measurements. For that reason, the average values of the azimuthal measurements for each zenith angle were calculated, which are shown in the dotted line in Fig. 3. This line shows a significant zenith variation of the measured radiances, which is higher than the measurement uncertainty, beyond 30°. Considering the limited size of the panel $(25.4 \times 25.4\ \text{cm}^2)$ and the FOV of the radiometer (see Section II), this radiance increase could be due to a partial viewing of the surface out of the panel. Nevertheless, radiance measurements made from 0° to 25° zenith angles are measured most likely inside the surface of the panel. For this reason, it was decided to make the radiance measurements with a viewing zenith angle of 25°, regardless of the azimuthal

TABLE I

$F^{\downarrow}_{\mathrm{HEM}}$ Average Values Measured at the Roof of the Physics Faculty Building (*Roof*) for Four Measurement Days, With Their Errors Given in Brackets, Using the Three Analyzed *In Situ* Methods. The $F^{\downarrow}_{\mathrm{HEM}}$ Value Retrieved From NCEP Profiles and the MODTRAN RTC Is Also Given

Date (dd/mm/yyyy)	$F^{\downarrow}_{\mathrm{HEM}}$ (CH1: 8-13.3 μm) [$\mathrm{Wm^{-2}\mu m^{-1}}$]				$F^{\downarrow}_{\mathrm{HEM}}$ (CH2: 11.5-12.4 μm) [$\mathrm{Wm^{-2}\mu m^{-1}}$]			
	$F^{\downarrow}_{\mathrm{HEM\_panel}}$	**$F^{\downarrow}_{\mathrm{HEM\_Kond}}$**	**$F^{\downarrow}_{\mathrm{HEM\_Rub}}$**	**$F^{\downarrow}_{\mathrm{HEM\_NCEP}}$**	**$F^{\downarrow}_{\mathrm{HEM\_panel}}$**	**$F^{\downarrow}_{\mathrm{HEM\_Kond}}$**	**$F^{\downarrow}_{\mathrm{HEM\_Rub}}$**	**$F^{\downarrow}_{\mathrm{HEM\_NCEP}}$**
12/10/2011	11.6 [± 0.4]	11.4 [± 0.3]	11.3 [± 0.9]	10.7 [± 2]	10.4 [± 0.3]	9.0 [± 0.3]	9.4 [± 0.7]	8.6 [± 1.7]
19/10/2011	11.4 [± 0.3]	11.5 [± 0.4]	11.0 [± 0.8]	10.9 [± 2]	10.6 [± 0.3]	9.9 [± 0.4]	9.9 [± 0.7]	9.4 [± 1.9]
25/10/2011	8.9 [± 0.3]	9.0 [± 0.3]	9.3 [± 0.7]	8.2 [± 1.6]	8.1 [± 0.3]	7.5 [± 0.3]	8.3 [± 0.7]	6.5 [± 1.3]
9/11/2011	8.5 [± 0.3]	8.4 [± 0.3]	9.1 [± 0.7]	9.0 [± 1.6]	7.6 [± 0.3]	6.7 [± 0.3]	7.1 [± 0.6]	7.3 [± 1.5]
	$F^{\downarrow}_{\mathrm{HEM}}$ (CH3: 10.2-11.3 μm) [$\mathrm{Wm^{-2}\mu m^{-1}}$]				$F^{\downarrow}_{\mathrm{HEM}}$ (CH4: 8.3-9.3 μm) [$\mathrm{Wm^{-2}\mu m^{-1}}$]			
12/10/2011	7.1 [± 0.3]	6.2 [± 0.2]	6.1 [± 0.7]	6.5 [± 1.3]	10.5 [± 0.5]	9.7 [± 0.4]	10.2 [± 1.4]	8.6 [± 1.7]
19/10/2011	7.4 [± 0.4]	7.2 [± 0.3]	7.0 [± 0.8]	7.2 [± 1.4]	9.6 [± 0.4]	8.5 [± 0.5]	7.9 [± 1.2]	8.5 [± 1.7]
25/10/2011	5.4 [± 0.2]	5.2 [± 0.2]	5.7 [± 0.6]	4.8 [± 1	7.5 [± 0.4]	6.3 [± 0.4]	6.4 [± 1.0]	6.2 [± 1.2]
9/11/2011	4.8 [± 0.2]	4.6 [± 0.2]	4.4 [± 0.5]	5.5 [± 1.1]	7.2 [± 0.5]	6.0 [± 0.4]	6.3 [± 0.9]	6.9 [± 1.4]

angle. This zenith angle was chosen as a compromise between assuring that the radiometer's FOV was placed well within the panel's area and measuring the radiance from the panel covering as much surface as possible.

B. Comparison of Methods for $F^{\downarrow}_{\mathrm{HEM}}$ Measurement

The four analyzed methods for the HDI estimation were compared using measurements performed during four days with cloud-free sky conditions. The measurements were made in two places (*roof* and *library*, see Fig. 1) with very different environments, to quantify the effect of the surroundings in the irradiance measurement (see Section III). In each case, the measurements were performed within time intervals of 15 min, during which $F^{\downarrow}_{\mathrm{HEM}}$ should not change significantly considering the stable atmospheric conditions (cloud free, no wind). However, possible fluctuations in $F^{\downarrow}_{\mathrm{HEM}}$ were accounted for as part of the measurement error $\delta F^{\downarrow}_{\mathrm{HEM}}$ which was given by

$$\delta F^{\downarrow}_{\mathrm{HEM}} = \sqrt{\delta F^{2}_{\mathrm{mes}} + \sigma^{2}} \qquad (6)$$

where δF_{mes} is the error given by error propagation through (4) in the case of irradiance measurements using the panel, error propagation through (3) in the case of irradiance measurements using Rubio *et al.* approximation, or the instrumental error given by radiometer accuracy (see Sections II and III) in the case of the Kondratyev approximation. The quantity σ is the standard deviation of the measurements set over the 15-min interval, accounting for possible fluctuations in $F^{\downarrow}_{\mathrm{HEM}}$.

Table I shows the channel $F^{\downarrow}_{\mathrm{HEM}}$ average values measured during the 15-min time interval in the *roof* place, with the uncertainties calculated using (6) given in brackets, for the four considered days and the different methods (including the $F^{\downarrow}_{\mathrm{HEM}}$ value retrieved from NCEP profiles and the MODTRAN RTC, see Section III). Difference between $F^{\downarrow}_{\mathrm{HEM\_panel}}$ and the rest of the methods was evaluated at each spectral channel by means of retrieving the average $F^{\downarrow}_{\mathrm{HEM}}$ difference of all measurement days. The average differences between $F^{\downarrow}_{\mathrm{HEM\_panel}}$ and $F^{\downarrow}_{\mathrm{HEM\_Kond}}$ methods on the CE 312-1 channels 1–4 are 0.03, 0.9, 0.4, and 1.1 $\mathrm{W \cdot m^{-2} \cdot \mu m^{-1}}$, respectively. Differences between $F^{\downarrow}_{\mathrm{HEM\_panel}}$ and $F^{\downarrow}_{\mathrm{HEM\_Rub}}$ are −0.06, 0.5, 0.4, and 1.0 $\mathrm{W \cdot m^{-2} \cdot \mu m^{-1}}$, respectively. Finally, differences between $F^{\downarrow}_{\mathrm{HEM\_panel}}$ and $F^{\downarrow}_{\mathrm{HEM\_NCEP}}$ are 0.4, 1.2, 0.18, and 1.2 $\mathrm{W \cdot m^{-2} \cdot \mu m^{-1}}$, respectively. As shown, differences between methods are less than 1.2 $\mathrm{W \cdot m^{-2} \cdot \mu m^{-1}}$, and most of them are within the measurement errors. NCEP method presents the largest differences at all spectral channels (with exception of channel 3 placed at 10.2–11.3 μm) with regard to the two other methods; nevertheless, these differences are explained in terms of the errors associated to the $F^{\downarrow}_{\mathrm{HEM\_NCEP}}$ methodology. Channels 4 and 2 present the largest differences at all three $F^{\downarrow}_{\mathrm{HEM}}$ retrieving methods in comparison to the panel measurements, with an average value of 1.1 and 0.9 $\mathrm{W \cdot m^{-2} \cdot \mu m^{-1}}$, respectively. Taking into account the differences between $F^{\downarrow}_{\mathrm{HEM\_panel}}$ and the rest methods shown earlier, for the case of a surface with a kinetic temperature of 30 °C and an emissivity of 0.8 in all channels, these differences on HDI would produce a difference ranging between 0.05 °C and 0.4 °C at the four channels of CE 312-1, in the measured surface temperature after correcting the emissivity effect with (1). These temperature differences would decrease for increasing emissivity; for instance, for an emissivity of 0.9 and the same kinetic temperature, the differences in measured temperature would be ranging between 0.01 °C and 0.2 °C. From these results, it may be concluded that, under clear-sky conditions and in places where the surrounding elements have a minimal contribution, the different approaches produce comparable results in terms of surface kinetic temperatures.

TABLE II

$F^{\downarrow}_{\mathrm{HEM}}$ AVERAGE VALUES MEASURED CLOSE TO THE UNIVERSITY LIBRARY BUILDING (*LIBRARY*) FOR FOUR MEASUREMENT DAYS, WITH THEIR ERRORS GIVEN IN BRACKETS, USING THE THREE ANALYZED *IN SITU* METHODS. THE $F^{\downarrow}_{\mathrm{HEM}}$ VALUE RETRIEVED FROM NCEP PROFILES AND THE MODTRAN RTC IS ALSO GIVEN

Date (dd/mm/yyyy)	$F^{\downarrow}_{\mathrm{HEM}}$ (CH1: 8-13.3 μm) [Wm-2μm-1]				$F^{\downarrow}_{\mathrm{HEM}}$ (CH2: 11.5-12.4 μm) [Wm-2μm-1]			
	$F^{\downarrow}_{\mathrm{HEM\ panel}}$	$F^{\downarrow}_{\mathrm{HEM\ Kond}}$	$F^{\downarrow}_{\mathrm{HEM\ Rub}}$	$F^{\downarrow}_{\mathrm{HEM\ NCEP}}$	$F^{\downarrow}_{\mathrm{HEM\ panel}}$	$F^{\downarrow}_{\mathrm{HEM\ Kond}}$	$F^{\downarrow}_{\mathrm{HEM\ Rub}}$	$F^{\downarrow}_{\mathrm{HEM\ NCEP}}$
12/10/2011	14.4 [± 0.7]	11.6 [± 0.4]	11.5 [± 1.0]	10.6 [± 2]	12.6 [± 0.5]	9.3 [± 0.4]	9.5 [± 0.7]	8.5 [± 1.7]
19/10/2011	13.1 [± 0.3]	12.4 [± 0.3]	11.7 [± 0.9]	10.9 [± 2]	12.0 [± 0.3]	10.6 [± 0.3]	10.5 [± 0.8]	9.3 [± 1.9]
25/10/2011	12.2 [± 0.3]	9.4 [± 0.5]	9.2 [± 0.7]	8.2 [± 1.6]	10.9 [± 0.3]	7.9 [± 0.4]	8.3 [± 0.6]	6.5 [± 1.3]
9/11/2011	11.5 [± 0.3]	9.0 [± 0.3]	9.6 [± 0.7]	9.0 [± 1.8]	10.2 [± 0.3]	7.3 [± 0.3]	7.7 [± 0.6]	7.3 [± 1.5]
	$F^{\downarrow}_{\mathrm{HEM}}$ (CH3: 10.2-11.3 μm) [Wm-2μm-1]				$F^{\downarrow}_{\mathrm{HEM}}$ (CH4: 8.3-9.3 μm) [Wm-2μm-1]			
12/10/2011	10.0 [± 0.6]	6.5 [± 0.4]	6.2 [± 0.8]	6.5 [± 1.3]	13.3 [± 0.7]	10.0 [± 0.5]	10.3 [± 1.5]	8.5 [± 1.7]
19/10/2011	9.3 [± 0.2]	7.9 [± 0.2]	7.5 [± 0.8]	7.1 [± 1.4]	11.5 [± 0.4]	9.1 [± 0.4]	8.3 [± 1.2]	8.5 [± 1.7]
25/10/2011	8.9 [± 0.2]	5.5 [± 0.3]	5.6 [± 0.6]	4.8 [± 1]	10.8 [± 0.4]	6.6 [± 0.5]	6.4 [± 1.0]	6.2 [± 1.2]
9/11/2011	8.0 [± 0.2]	5.0 [± 0.2]	4.8 [± 0.6]	5.5 [± 1.1]	10.2 [± 0.4]	6.4 [± 0.4]	6.6 [± 1.0]	6.9 [± 1.4]

Things are different when the surface roughness is significant and the surrounding elements cannot be avoided, for instance, when measuring in areas with buildings or vegetation elements such as trees, which are placed close to the surface being measured. Table II shows the channel $F^{\downarrow}_{\mathrm{HEM}}$ average values measured during the 15-min interval in the *library* place [see Fig. 1(b) and (c)], with the uncertainties calculated using (6) given in brackets, for the four considered days and the different methods (including the $F^{\downarrow}_{\mathrm{HEM}}$ value retrieved from NCEP profiles and the MODTRAN code, see Section III). In this case, the HDI values provided by the methods of Kondratyev, Rubio *et al.*, and NCEP are all close to each other showing differences lower than 1.5 $\mathrm{W \cdot m^{-2} \cdot \mu m^{-1}}$, similar to the *roof* case presented in Table I. In fact, the values of these methods are almost the same in both tables, since the time difference between the measurements at the *roof* and at the *library* places was less than 40 min (the time needed to move the instrumentation from one place to the other one). However, the measurements performed with the panel present a significant increase in the *library* place compared to the *roof* place (on the order of $+3\ \mathrm{W \cdot m^{-2} \cdot \mu m^{-1}}$) that produces a significant difference between the panel results with regard to the rest of the methods, which is beyond the measurement error. This increase is the effect of the radiative contribution coming from the surrounding elements to the measurement area [trees and buildings mainly, see Fig. 1(b) and (c)]. Differences between $F^{\downarrow}_{\mathrm{HEM\_panel}}$ and the rest of the methods for all the measurement days show average values of +2.6, +2.8, +3.0, and $+3.6\ \mathrm{W \cdot m^{-2} \cdot \mu m^{-1}}$, for channels 1–4 of CE 312-1, respectively. For a surface with a kinetic temperature of 30 °C and an emissivity of 0.8 in all channels, these differences on HDI would produce a difference of +1.0 °C, +1.5 °C, +1.3 °C, and +1.3 °C for channels 1–4 of CE 312-1, respectively, in the measured surface temperature after correcting the emissivity effect with (1). For an emissivity of 0.9 and the same kinetic temperature, the differences in measured temperature would be +0.5 °C, +0.7 °C, +0.6 °C, and +0.6 °C, respectively. From these results, it may be concluded that, under clear-sky conditions and in places where the surrounding elements have a significant contribution, only the use of a diffuse reflectance panel accounts for the radiative contribution of the surroundings, which can produce a significant systematic error in the LST measurement, particularly in the case of low-emissivity land surfaces. Thus, in these cases, the use of a panel for the HDI measurement is preferable over the other approaches to avoid these systematic errors.

C. Evaluation of $F^{\downarrow}_{\mathrm{HEM}}$ Under Heterogeneous Skies

A comparison of the four methods under skies with cloud coverage changing over time was made, since clouds can modify considerably the HDI. Measurements were taken at the *roof* place for minimizing the contribution of the surroundings as has been shown in Section IV-B, on two days, one with the presence of cumulus clouds and the second one with the presence of cirrus clouds; in both cases, clouds were moving through the sky over time. The CE2 instrument was measuring continuously pointing to the panel (with a zenith viewing angle of $\theta = 25^{\circ}$ $F^{\downarrow}_{\mathrm{HEM\_panel}}$), and the radiometer CE1 was measuring simultaneously pointing to the sky at 55° ($F^{\downarrow}_{\mathrm{HEM\_Kond}}$). $F^{\downarrow}_{\mathrm{HEM\_Rub}}$ was retrieved pointing the CE1 instrument to the sky at 0° every 30–60 min. Atmospheric profiles from NCEP were downloaded (from Web-based tool, see [22]) and also processed using MODTRAN (see Section III) every 30 min (NCEP profiles were unavailable for the day with presence of cirrus), retrieving an HDI value from each profile. Additionally, a camera SONA Automatic Cloudiness Observation System, located in the *roof*, took a photograph of the upper hemisphere every 5 min; these photos were processed to get the cloud coverage (in percent) with an error of ±10%.

Fig. 4 shows the measurements obtained with each procedure over time, at the four channels of CE 312-1, for the two measurement days. The results of a sky with cumulus clouds

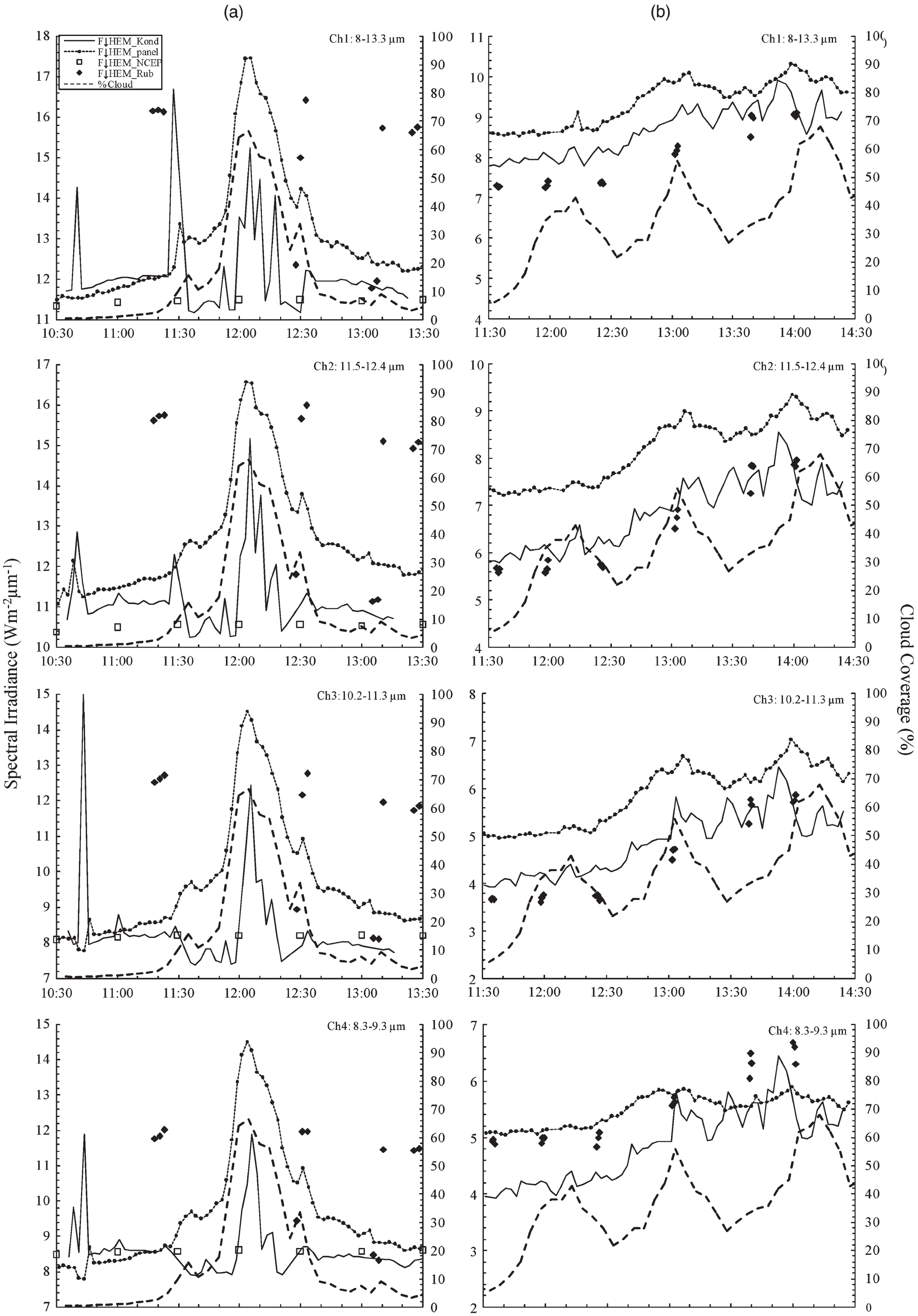

Fig. 4. Measurements of $F^{\downarrow}_{\mathrm{HEM}}$ over time obtained with (solid line) Kondratyev approximation, (black diamonds) Rubio *et al.* approximation, (empty squares) NCEP profiles with the MODTRAN code, and (dotted line) the diffuse reflectance panel, on a day with (a) heterogeneous sky with presence of cumulus clouds and (b) heterogeneous sky with cirrus clouds. (Dashed line) Cloud coverage (in percent), retrieved from a camera SONA Automatic Cloudiness Observation System, is also presented.

[Fig. 4(a)], show that $F^{\downarrow}_{\mathrm{HEM\_Kond}}$ and $F^{\downarrow}_{\mathrm{HEM\_Rub}}$ present large fluctuations of their values, not following the actual evolution of the cloud coverage. The sharp changes observed are due to the passage of a cloud in front of the radiometer's FOV; when the cloud is out of the FOV, the measured values fall suddenly to lower values corresponding to clear-sky areas. This can be seen for $F^{\downarrow}_{\mathrm{HEM\_Kond}}$ at 10:40 A.M., 11:27 A.M., or 12:17 P.M., for instance, and for $F^{\downarrow}_{\mathrm{HEM\_Rub}}$ at 12:30 P.M. or 1:00 P.M. Thus, in partial cloud cover conditions, the approximations of Kondratyev and Rubio *et al.* are not able to capture the real value of the HDI, since they measure in excess when viewing a cloud and by defect when they are viewing the clear sky. Results from NCEP atmospheric profiles are also unsuccessful, given that this approach cannot take into account the presence of clouds, matching up with the other methods just when the cloud coverage is lower than 10%.

On the contrary, the HDI retrieved using the diffuse reflectance panel is able to follow the cloud coverage evolution over time. These results show that the panel takes into account the decrease and increase of clouds in the sky, being its irradiance values more representative of real sky conditions. For instance, $F^{\downarrow}_{\mathrm{HEM\_panel}}$ value from 11:40 A.M. to 12:00 P.M. increases around $+4.6\ \mathrm{W}\cdot\mathrm{m}^{-2}\cdot\mu\mathrm{m}^{-1}$ in the four CE 312-1 channels, for an increase of 56% in cloud coverage. This increase of irradiance, considered as a systematic error if it is not taken into account in (1) (as would happen using one of the other three methods), introduces significant errors in retrieving LST. For a given surface with an emissivity of 0.8 in all channels and with a kinetic temperature of 30 °C, an error in $F^{\downarrow}_{\mathrm{HEM}}$ of $-4.6\ \mathrm{W}\cdot\mathrm{m}^{-2}\cdot\mu\mathrm{m}^{-1}$ implies making an error in retrieving LST of -1.7 °C, -2.1 °C, -2.2 °C, and -1.5 °C, for channels 1–4 of CE 312-1, respectively. The magnitude of that error will depend on the cloud coverage percentage, the cloud types present in the sky, and the cloud temperature. For instance, Fig. 4(b) shows the results for a sky with cirrus clouds, showing the following: 1) The magnitude of the irradiance is half the irradiance for the cumulus case, and 2) the three methods used to measure the irradiance present more comparable values in this case, with differences to each other that are within $\pm 1\ \mathrm{W}\cdot\mathrm{m}^{-2}\cdot\mu\mathrm{m}^{-1}$ at the four spectral channels of CE312-1, almost independent of the cloud coverage (that shows values from 6% to 68% during the measurements). Thus, for this type of clouds, the use of the different methodologies would produce much lower systematic errors than in the cumulus case. In any case, the conclusion is that, with cloud coverage changing conditions, only the use of a diffuse reflectance panel guarantees an adequate measurement of the HDI to avoid significant systematic errors in the surface temperature measurement. This is particularly important in field measurements performed continuously over a given area.

V. SUMMARY AND CONCLUSION

TIR HDI emitted by the atmosphere must be accurately estimated in order to obtain precise values of LST in the field, using fast and reliable methods, particularly when the sky is partially cloudy and can be changing over time. Four methods to retrieve $F^{\downarrow}_{\mathrm{HEM}}$ were compared at two different environments with a different number of surrounding elements and under different cloud coverage of the sky: Two of them were based on taking a single measurement of the sky at 0° (Rubio *et al.* method) or at 55° (Kondratyev method), another one is based on using a gold diffuse panel with high reflectance and a near-Lambertian behavior, and the last one is based on using atmospheric profiles provided by the NCEP, interpolated temporally and spatially, introduced in an RTC.

Previous to the comparison, a characterization of the panel was made concluding that it shows azimuthal isotropy in radiance measurements while showing a significant increase of the measured radiances with the increase of the viewing zenith angle. This radiance increase could be due to a partial viewing of the surface out of the panel; for this reason, measurements with a viewing zenith angle not larger than 25°, regardless the azimuthal angle, were used. Moreover, the panel has also a contribution to the measured signal due to the small emissivity of the gold rugged surface. This contribution must be removed from the direct measurements made on the panel with the help of contact temperature measurements taken on the panel gold surface.

The four methods were first compared under cloud-free sky conditions in a place with minimal contribution of surrounding elements. In this case, differences between methods lower than $2\ \mathrm{W}\cdot\mathrm{m}^{-2}\cdot\mu\mathrm{m}^{-1}$ were obtained, being these differences within the measurement errors of each method. In consequence, it may be concluded that, under clear-sky conditions and in places where the surrounding elements have a minimal contribution, the different approaches produce comparable results in terms of HDI.

When the surface roughness is significant and the surrounding elements cannot be avoided, HDI values provided by the methods of Kondratyev, Rubio *et al.*, and from NCEP profiles are all close to each other. However, the measurements performed with the panel increase, showing a significant difference between the panel results with regard to the rest of the methods, which is not explained by measurement error. This increase is the effect of the radiative contribution to the measurement area coming from the surrounding elements. Differences between $F^{\downarrow}_{\mathrm{HEM\_panel}}$ and the other methods for all the measurements days show average values of $+3\ \mathrm{W}\cdot\mathrm{m}^{-2}\cdot\mu\mathrm{m}^{-1}$, for all channels of CE 312-1, which would produce a significant difference in the retrieval of LST. Thus, under clear-sky conditions and in places where the surrounding elements have a significant contribution, only the use of a diffuse reflectance panel accounts for the radiative contribution of the surroundings, avoiding significant systematic error in the LST measurement.

The four methods were also compared under a sky with changing cumulus cloud coverage over time, in a place with minimal contribution of the surroundings. Results showed that neither the methods of Kondratyev and Rubio *et al.* nor NCEP atmospheric profiles are able to capture the real value of the HDI. On the contrary, HDI retrieved using the diffuse reflectance panel follows the cloud coverage evolution over time, taking into account the decrease and increase of clouds in the whole sky, being its irradiance value more representative of real sky conditions, which is crucial for accurate LST measurements in the field. Nevertheless, for a sky with changing cirrus cloud coverage, all the methods studied to retrieve HDI presented similar results with differences within $\pm 1\ \mathrm{W} \cdot \mathrm{m}^{-2} \cdot \mu\mathrm{m}^{-1}$, so the magnitude of the error due to partial cloud coverage will depend on factors such as the cloud type, cover percentage, and temperature. However, it could be concluded that the use of a diffuse reflectance panel is the best alternative since it ensures an adequate measurement of HDI and takes into account both the contributions of the surroundings as well as the possible presence of clouds, which is particularly important in field measurements performed continuously over a given area.

ACKNOWLEDGMENT

The authors would like to thank Dr. Estellés at the Solar Radiation Group, Department of Earth Physics and Thermodynamics, University of Valencia, for providing us with atmosphere water vapor content and cloud coverage data, framed in projects CGL2007-60648 and CGL2010-07790. They would also like to thank three anonymous reviewers for their useful comments and suggestions.

REFERENCES

[1] K. Y. Kondratyev, *Radiation in the Atmosphere*. New York: Academic, 1969.

[2] E. Rubio, V. Caselles, and C. Badenas, "Emissivity measurements of several soils and vegetation types in the 8–14 μm wave band," *Remote Sens. Environ.*, vol. 59, no. 3, pp. 490–521, Mar. 1997.

[3] V. García-Santos, J. M. Galve, E. Valor, V. Caselles, and C. Coll, "Estimation of atmospheric water vapour content from direct measurements of radiance in the thermal infrared region," *Remote Sens. Lett.*, vol. 3, no. 1, pp. 31–38, Jan. 2012.

[4] A. Berk, G. P. Anderson, P. K. Acharya, J. H. Chetwynd, L. S. Bernstein, E. P. Shettle, M. W. Matthew, and S. M. Adler-Golden, *MODTRAN 4 User's Manual*. Hascom AFB, MA: Air Force Res. Lab., Space Veh. Dir., Air Force Mater. Comm., 1999, p. 95.

[5] E. Kalnay, M. Kanamitsu, R. Kistler, W. Collins, D. Deaven, L. Gandin, M. Iredell, S. Saha, G. White, J. Woollen, Y. Zhu, M. Chelliah, W. Ebisuzaki, W. Higgins, J. Janowiak, K. C. Mo, C. Ropelewski, J. Wang, A. Leetmaa, R. Reynolds, R. Jenne, and D. Joseph, "NCEP/NCAR 40 year reanalysis project," *Bull. Amer. Meteor. Soc.*, vol. 77, no. 3, pp. 437–471, Mar. 1996.

[6] R. M. Narayanan, S. E. Green, and D. R. Alexander, "Soil classification using mid-infrared off-normal active differential reflectance characteristics," *Photogramm. Eng. Rem. Sens.*, vol. 58, no. 2, pp. 193–199, Feb. 1992.

[7] J. W. Salisbury and D. M. D'Aria, "Infrared (8–14 μm) remote sensing of soil particle size," *Remote Sens. Environ.*, vol. 42, no. 2, pp. 157–165, Nov. 1992.

[8] A. R. Korb, P. Dybwad, W. Wadsworth, and J. W. Salisbury, "Portable Fourier transform infrared spectroradiometer for field measurements of radiance and emissivity," *Appl. Opt.*, vol. 35, no. 10, pp. 1679–1692, Apr. 1996.

[9] Rivard, P. J. Thomas, and J. Giroux, "Precise emissivity of rock samples," *Remote Sens. Environ.*, vol. 54, no. 2, pp. 152–160, Nov. 1995.

[10] S. J. Hook and A. B. Khale, "The micro Fourier transform interferometer (μFTIR)—A new field spectrometer for acquisition of infrared data of natural surfaces," *Remote Sens. Environ.*, vol. 56, no. 3, pp. 172–181, Jun. 1996.

[11] K. A. Horton, J. R. Johnson, and P. G. Lucey, "Infrared measurements of pristine and disturbed soils 2. Environmental effects and fields data reduction," *Remote Sens. Environ.*, vol. 64, no. 1, pp. 47–52, Apr. 1998.

[12] A. R. Korb, J. W. Salisbury, and D. M. D'Aria, "Thermal-infrared remote sensing and Kirchhoff's law 2. Field measurements," *J. Geophys. Res.*, vol. 104, no. B7, pp. 15 339–15 350, Jul. 1999.

[13] M. Hori, T. Aoki, T. Takinawa, H. Motoyoshi, A. Hachikubo, K. Sugiura, T. J. Yasunari, H. Eide, R. Storvold, Y. Nakajima, and F. Takahashi, "In situ measured spectral directional emissivity of snow and ice in the 8–14 μm atmospheric window," *Remote Sens. Environ.*, vol. 100, no. 4, pp. 486–502, Feb. 2006.

[14] Y. Zhang, Z. Rong, X. Hu, J. Liu, L. Zhang, Y. Li, and X. Zhang, "Field measurements of Gobi surface emissivity using and Infragold Board at Dunhuang calibration site of China," in *Proc. IEEE Int. Geosci. Remote Sens. Symp.*, 2007, pp. 358–360.

[15] M. Mira, T. J. Schmugge, E. Valor, V. Caselles, and C. Coll, "Comparison of thermal infrared emissivities retrieved with the two-lid box and the TES methods with laboratory spectra," *IEEE Trans. Geosci. Remote Sens.*, vol. 47, no. 4, pp. 1012–1021, Apr. 2009.

[16] J. C. Jiménez-Muñoz, J. Cristóbal, J. A. Sobrino, G. Sòria, M. Ninyerola, and X. Pons, "Revision of the single-channel algorithm for land surface temperature retrieval from Landsat thermal-infrared data," *IEEE Trans. Geosci. Remote Sens.*, vol. 47, no. 1, pp. 339–349, Jan. 2009.

[17] Coll, J. M. Galve, J. M. Sánchez, and V. Caselles, "Validation of Landsat-7/ETM+ thermal-band calibration and atmospheric correction with ground-based measurements," *IEEE Trans. Geosci. Remote Sens.*, vol. 48, no. 1, pp. 547–555, Jan. 2010.

[18] N. Wang, H. Wu, F. Nerry, C. Li, and Z.-L. Li, "Temperature and emissivity retrievals from hyperspectral thermal infrared data using linear spectral emissivity constraint," *IEEE Trans. Geosci. Remote Sens.*, vol. 49, no. 4, pp. 1291–1303, Apr. 2011.

[19] G. Brogniez, C. Pietras, M. Legrand, P. Dubuisson, and M. Haeffelin, "A high-accuracy multiwavelength radiometer for in situ measurements in the thermal infrared. Part II: Behavior infield experiments," *J. Atmos. Ocean. Tech.*, vol. 20, pp. 1023–1033, Jul. 2003.

[20] E. Theocharous, E. Usadi, and N. P. Fox, "CEOS comparison of IR brightness temperature measurements in support of satellite validation. Part I: Laboratory and ocean surface temperature comparison of radiation thermometers," Nat. Phys. Lab., Middlesex, U.K., NPL Rep. OP 3, Jul. 2010.

[21] J. M. Galve, C. Coll, V. Caselles, and E. Valor, "An atmospheric radiosounding database for generating land surface temperature algorithms," *IEEE Trans. Geosci. Remote Sens.*, vol. 46, no. 5, pp. 1547–1557, May 2008.

[22] J. A. Barsi, J. L. Barker, and J. R. Schott, "An atmospheric correction parameter calculator for a single thermal band Earth-sensing instrument," in *Proc. IEEE IGARSS*, Toulouse, France, 2003, pp. 3014–3016.

[23] V. Estellés, J. A. Martínez-Lozano, M. P. Utrillas, and M. Campanelli, "Columnar aerosol properties in Valencia (Spain) by ground-based Sun photometry," *J. Geophys. Res.*, vol. 112, no. D11, pp. D11201-1–D11201-9, Jun. 2007.

Vicente García-Santos received the B.Sc. and M.Sc. degrees in physics from the University of Valencia, Burjassot, Spain, in 2007 and 2010, respectively, where he is currently working toward the Ph.D. degree in physics in the Thermal Remote Sensing Group, Department of Earth Physics and Thermodynamics, Faculty of Physics.

His research interest focuses on the physical processes of thermal infrared remote sensing, land-surface emissivity, and atmospheric parameter measurement and characterization.

Enric Valor received the B.Sc., M.Sc., and Ph.D. degrees in physics from the University of Valencia, Burjassot, Spain, in 1992, 1994, and 1997, respectively.

He is currently an Associate Professor of Earth physics with the Department of Earth Physics and Thermodynamics, Faculty of Physics, University of Valencia. He has 20-year expertise in the physical processes involved in temperature measurement using remote sensing techniques, which have been documented through four books, three doctoral theses, 45 papers in international journals, and 60 conference papers. His research interest focuses on the physical processes of thermal infrared remote sensing, emissivity measurement and characterization, atmospheric and emissivity corrections, and temperature–emissivity separation algorithms.

Dr. Valor was the recipient of the Norbert Gerbier—MUMM International Award in 2010, conferred by the Executive Council of the World Meteorological Organization.

Vicente Caselles received the B.Sc., M.Sc., and Ph.D. degrees in physics from the University of Valencia, Burjassot, Spain, in 1979, 1980, and 1983, respectively.

He is currently a Professor in Earth physics and the Head of the Thermal Remote Sensing Group, Department of Earth Physics and Thermodynamics, Faculty of Physics, University of Valencia. He has 34-year expertise in the physical processes involved in both temperature measurement and evapotranspiration using remote sensing techniques, which has been documented through ten books, 20 doctoral theses, 100 papers in international journals, 60 conference papers, and 30 reports.

Dr. Caselles was the recipient of the Norbert Gerbier—MUMM International Award in 2010, conferred by the Executive Council of the World Meteorological Organization. He was collaborating with the European Space Agency as a member of the Advisory Group for the Land-Surface Processes and Interactions Mission. He was the Chairman of the Spanish Remote Sensing Society and is currently the Manager of Human Resources and Researchers Mobility General Direction, Spanish Ministry of Economy and Competitiveness.

Maria Mira received the B.Sc. (first-class honors), M.Sc., and Ph.D. degrees in physics from the University of Valencia, Burjassot, Spain, in 2005, 2007, and 2010, respectively.

She was a Visiting Student with New Mexico State University, Las Cruces, from December 2007 to March 2008 and with the National Institute for Agricultural Research (INRA), Bordeaux, France, from September 2009 to December 2009. She is currently a Postdoctoral Researcher with the INRA, Avignon, France. She has published 12 papers in international journals and more than 45 conference papers. He has participated in more than 14 national and international projects. Her research interest focuses on the thermal infrared remote sensing in general and the estimation of evapotranspiration using remote sensing in particular.

Joan Miquel Galve was born in Benifaio, Spain, in July 1978. He received the B.Sc. degree in physics and the M.Sc. degree in Earth physics and thermodynamics from the University of Valencia, Burjassot, Spain, in 2004 and 2006, respectively, where he is currently working toward the Ph.D. degree in physics in the Department of Earth Physics and Thermodynamics, Faculty of Physics.

His research includes the derivation and validation of land-surface temperatures from remote sensing sensors in thermal infrared.

César Coll received the B.Sc., M.Sc., and Ph.D. degrees in physics from the University of Valencia, Burjassot, Spain, in 1989, 1992, and 1994, respectively.

He is currently a Professor of Earth physics with the Department of Earth Physics and Thermodynamics, Faculty of Physics, University of Valencia. He has published 50 papers in international journals and 70 conference papers. His research interest focuses on the physical processes of thermal infrared (TIR) remote sensing, atmospheric and emissivity corrections, temperature–emissivity separation, and ground validation of Advanced Along-Track Scanning Radiometer, Moderate Resolution Imaging Spectroradiometer, and Advanced Spaceborne Thermal Emission and Reflection Radiometer TIR products.

Appendix C

“On the angular variation of thermal infrared emissivity of inorganic soils”

Next study was published in *Journal of Geophysical Research-Atmospheres* in October, 2012. This Journal has an *Impact Factor* of **3.174**, occupying the position 23 of the 170 journals in *Geosciences and Multidisciplinary* category according to *ISI-Journal of Citation Reports Science Edition 2012*.

JOURNAL OF GEOPHYSICAL RESEARCH, VOL. 117, D19116, doi:10.1029/2012JD017931, 2012

On the angular variation of thermal infrared emissivity of inorganic soils

Vicente García-Santos,[1] Enric Valor,[1] Vicente Caselles,[1] M. Ángeles Burgos,[1]
and César Coll[1]

Received 12 April 2012; revised 27 August 2012; accepted 5 September 2012; published 10 October 2012.

[1] Land surface temperature (LST), a key parameter for many environmental studies, can be most readily estimated by using thermal infrared (TIR) sensors onboard satellites. Accurate LST are contingent upon simultaneously accurate estimates of land surface emissivity (ε), which depend on sensor viewing angle and the anisotropy of optical and structural properties of surfaces. In the case of inorganic bare soils (IBS), there are still few data that quantify emissivity angular effects. The present work deals with the angular variation of TIR emissivity for twelve IBS types, representative of nine of the twelve soil textures found on Earth according to United States Department of Agriculture classification. Emissivity was measured with a maximum error of ±0.01, in several spectral ranges within the atmospheric window 7.7–14.3 μm, at different zenithal (θ) and azimuthal (φ) angles. Results showed that ε of all IBS studied is almost azimuthally isotropic, and also zenithally up to $\theta = 40°$, from which ε values decrease with the increase of θ. This decrease is most pronounced in sandy IBS which is rich in quartz reaching a maximum difference from nadir of +0.101 at $\theta = 70°$. On the other hand, clayey IBS did not show a significant decrease of ε up to $\theta = 60°$. A parameterization of the relative-to-nadir emissivity in terms of θ and sand and clay percentage was established. Finally, the impact of ignoring ε angular effects on the retrievals of LST, using split-window-type algorithms, and of outgoing longwave radiation, was analyzed. Results showed systematic errors ranging between ±0.4 K to ±1.3 K for atmospheres with water vapor values lower than 4 cm in the case of LST, and errors between 2%–8%, in the estimation of different terms of the surface energy balance.

Citation: García-Santos, V., E. Valor, V. Caselles, M. Ángeles Burgos, and C. Coll (2012), On the angular variation of thermal infrared emissivity of inorganic soils, *J. Geophys. Res.*, *117*, D19116, doi:10.1029/2012JD017931.

1. Introduction

[2] Land surface temperature (LST) is a key parameter, essential for numerous studies related to terrestrial surface processes such as the atmosphere-surface energy budget [*Sánchez et al.*, 2008], wildfire risk studies [*Yi et al.*, 2009], weather and climate predictions, or soil moisture measurements [*Wen et al.*, 2003]. An accurate LST measurement from satellite radiometry critically depends upon corrections for atmospheric and land surface emissivity (ε) effects. Emissivity and LST are coupled in a remote sensing radiance measurement in the thermal infrared (TIR) spectral domain, so the knowledge of the emissivity behavior with respect to factors such as soil composition and texture [*Salisbury and D'Aria*, 1992], soil moisture [*Mira et al.*, 2007, 2010; *Ogawa et al.*, 2006,] or viewing geometry [*Takashima and Masuda*, 1987; *Labed and Stoll*, 1991; *Sobrino and Cuenca*, 1999] are important when analyzing satellite TIR data.

[3] In the last two decades different satellite-based sensors have taken terrestrial measurements from different viewing angles. Sensors such as Moderate Resolution Imaging Spectroradiometer (MODIS), onboard Terra and Aqua satellites [*Barnes et al.*, 1998], and Advanced Very High Resolution Radiometer (AVHRR), onboard National Oceanic and Atmospheric Administration 17/18 (NOAA) [*Goodrum et al.*, 2001] collect observations with at-sensor view up to 55° (actually 65° at the surface due to Earth's curvature) from nadir because of their field-of-view (FOV) scanning. Other instruments with large observation angles are Advanced Along-Track Scanning Radiometer (AATSR) onboard the Environmental Satellite (ENVISAT) [*Llewellyn-Jones et al.*, 2001] that collects biangular observations at two zenithal angles in the forward direction (close to nadir and 55°), or the Spinning Enhanced Visible and Infrared Imager (SEVIRI) on board Meteosat Second Generation (MSG) [*Aminou et al.*, 1997] that can reach viewing angles of ±50°. The knowledge of the angular effects on

---

[1] Department of Earth Physics and Thermodynamics, Faculty of Physics, University of Valencia, Burjassot, Spain.

Corresponding author: V. García-Santos, Department of Earth Physics and Thermodynamics, Faculty of Physics, University of Valencia, 50, Dr. Moliner, ES-46100 Burjassot, Spain. (vicente.garcía-santos@uv.es)

©2012. American Geophysical Union. All Rights Reserved.
0148-0227/12/2012JD017931

Table 1. List of Previous Studies on the Angular Variation of TIR Emissivity of IBS, Which Are Referenced in the Main Text[a]

	IBS Number and Types	Main Findings
Barton and Takashima [1986]	1 sample beach sand	Emissivity of a sand sample decreases by 3% with the increase of zenith angle from nadir to $\theta = 70°$.
Takashima and Masuda [1987]	2 samples quartz and Sahara dust powders	Difference between temperatures of channels 4 and 5 of NOAA-AVHRR are significant at different zenithal angles. This difference is attributed to angular variation of the emissivity
Becker et al. [1985]	3 samples quartz sand lehm Al_2O_3 powders	Sand and loam showed a decrease of 3% and 2%, respectively. Evidence of strong spectral effects, and important and specific roles of the surface roughness and nature medium on the emissivity change
Labed and Stoll [1991]	4 samples SiO2 sand Loam soil Loess (silty) AN (silty)	Sand does not present angular dependence up to $\theta = 50°$. For larger viewing angles emissivity decrease does not exceed 4.5%. Loam soil exhibits the largest angular variation (a decrease of 9% at $\theta = 70°$) and the effect is appreciable at $\theta = 20°$. Silty soils exhibit a maximum decrease from $\theta = 0°$ of 3% at $\theta = 70°$.
Snyder et al. [1997]	2 samples Sand Silt-loam	Sand shows a decrease around 4% at spectral range 8–9 μm. This decrease is less than 2% at 10–12 μm. Silt-loam soil presents a decrease less than 1%.
Sobrino and Cuenca [1999]	3 samples Clay, sand and silt	Clay and silt show a decrease of 0.5% and 0.9%, respectively at $\theta = 70°$. Sand shows a decrease of 2% at $\theta = 70°$.
Cuenca and Sobrino [2004]	3 samples Clay, sand and silt	Sand presents decrease around 2% at spectral ranges: 8–14 μm, 11.5–12.5 μm and 10.3–11.3 μm, but presents a pronounced decrease (around 5%) at spectral range 8.2–9.2 μm. Clay and silt present a decrease in emissivity of 1 and 2%, respectively at four spectral channels. The pattern of the curve corresponding to a specific sample is conserved if we are operating at different wavelengths.
Present study	12 samples Comprise 9 of the 12 textural classes defined by USDA texture triangle	Emissivity decreases with the increase of zenith angle and is azimuthally isotropic, depending on soil texture and composition. A parameterization of the emissivity variation with view angle is proposed for different spectral channels. The impact of this variation on LST and outgoing longwave radiation assessment is provided.

[a] The second column presents the number and soil types analyzed in each case, and the third column summarizes the main conclusions obtained.

surface thermal infrared emission can be important to evaluate different geophysical parameters. For instance, *Lagouarde et al.* [2000, 2004] during a flight campaign found a hot spot effect in angular measurements of LST over a forest and in an urban area, in which a significant increase in temperature was observed at certain observation angles. This hot spot was dependent on tree height, LAI and size of leaves, in the case of forest, and on sunlit and shaded faces due to the structure of buildings, in the case of the urban area, concluding that this effect plays an important role when retrieving LST from satellite at different view angles; moreover, this effect can be important for understanding the relationship between LST distributions and the surface energy budget. *Niclòs et al.* [2007] showed that sea surface temperature (SST) can be more accurately measured when the emissivity angular variation is taken into account. They obtained an emissivity-dependent split-window equation for MODIS Terra/Aqua sensors, which takes into account the decrease of sea surface emissivity with viewing angle. This algorithm was validated with in situ SST measurements with an accuracy of ±0.3 K. *Chehbouni et al.* [2001] showed that, under clear sky and constant vegetation conditions, difference between nadir and off-nadir temperature is well correlated with surface soil moisture. Finally, *Ball and Pinkerton* [2006] showed the benefit of angular measurements of basalt temperature in volcanology studies to establish the location of the most active parts of the lava domes and lava flows. These applications, among others, show that accurate angular temperature measurements are needed to have access to different biophysical and geophysical quantities.

[4] Closely related to angular variations of LST are angular variations in thermal emissivity, denoted as $\varepsilon(\theta, \varphi)$, where θ represents zenith angle, and φ represents azimuth angle. Previous works have analyzed these variations for water [*Rees and James*, 1992; *Niclòs et al.*, 2005] showing that it is important to select the suitable emissivity for the accurate retrieval of SST; snow [*Dozier and Warren*, 1982; *Hori et al.*, 2006] for which emissivity is also important for the nighttime cloud detection over cold snow/ice surfaces needed for radiation budget studies; and vegetation [*McAtee et al.*, 2003; *Cuenca and Sobrino*, 2004] in which brightness temperature (T_b) is evidently affected by a relationship between solar illumination and viewing angle through differential heating and shading. The present study is focused on a specific type of surface, inorganic bare soils (IBS), which are mineralogical soils with low organic matter (OM) content (less than 9%). There exist few studies about the angular variation of thermal emissivity for IBS. Table 1 summarizes the most important conclusions drawn from these works. *Barton and Takashima* [1986] used a single channel radiometer to measure the radiation from the sand for zenith

angles between 30° and 70°. *Takashima and Masuda* [1987] took measurements of $\varepsilon(\theta, \varphi)$ for a sandy soil with high quartz content from Sahara desert on the spectral range 7–17 μm evaluating the effect of particle size on emissivities. *Becker et al.* [1985] investigated experimentally the reflectance of various soils at different zenithal angles, expanding the number of samples to a lehm agricultural soil and Al_3O_2 powders. *Labed and Stoll* [1991] dealt with the study of the relative-to-nadir value of $\varepsilon(\theta, \varphi)$, measured under laboratory conditions for both sandy and silty soils, plus three agricultural soils with different texture and organic content. In addition to these soils *Snyder et al.* [1997] measured a relative value of $\varepsilon(\theta, \varphi)$ between $\theta = 10°$ and $\theta = 53°$, with a Fourier transform spectrometer in the 3–14 μm range for an organic soil plus another one vegetated and gravel. *Sobrino and Cuenca* [1999] added results of clay and grass, expanding their results from the broadband 8–14 μm to narrower spectral bands [*Cuenca and Sobrino*, 2004].

[5] The present work extends these results limited to specific types of textural IBS to a wider range, retrieving $\varepsilon(\theta, \varphi)$ for twelve soils classified in nine of the twelve textural classes defined by the United States Department of Agriculture (USDA) texture triangle. With this aim, experimental measurements were carried out through the ensemble of a goniometer together with two multispectral thermal radiometers which allowed taking simultaneous angular measurements of radiance from IBS in two different angular configurations.

[6] In section 2 we discuss the theory followed to obtain $\varepsilon(\theta, \varphi)$ for the studied IBS. Section 3 presents the methodological details implemented to obtain the angular measurements. Section 4 presents results of $\varepsilon(\theta, \varphi)$ for each IBS, discussing the results obtained, as well as regression analyses to retrieve the relative-to-nadir emissivity for any IBS. Section 5 presents the impact of ignoring angular effects of IBS emissivity on the retrieval of LST using the split-window algorithm, and on the estimation of the outgoing longwave radiation. Finally, conclusions are presented in section 6.

2. Theory

[7] For a thermal sensor spanning the 8–14 μm atmospheric window the radiative transfer can be modeled with three terms: direct surface emission, surface reflected environmental radiation (hemispheric downwelling radiance), and atmospheric absorption and emission effects. However, for this study, where sensor-surface distances are short, atmospheric effects can be reduced to the reflected term of hemispheric downwelling radiance. The spectral radiance can be modeled after *Norman and Becker* [1995]:

$$L_i(\theta,\varphi) = \varepsilon_i(\theta,\varphi)B_i(T) + \rho_i(\theta,\varphi)L_i^{\downarrow} \tag{1}$$

where $L_i(\theta, \varphi)$ is the band radiance measured directly by the sensor from surface at θ and φ; B_i is the Planck function for blackbody radiance at temperature T; $L_i^{\downarrow}$ is the hemispheric downwelling radiance made up from atmosphere and surrounding elements contribution, $\rho(\theta, \varphi)$ is the hemispherical-directional band reflectance [*Nicodemus et al.*, 1977], and $\varepsilon_i(\theta, \varphi)$ is absolute band emissivity of the surface. Subscript *i* stands for the spectral band where measurements have been taken.

[8] A relationship between surface emissivity and hemispherical-directional reflectance for a surface opaque to radiation in thermal equilibrium can be established by means of Kirchhoff's law [*Nicodemus*, 1965] as:

$$\varepsilon_i(\theta,\varphi) = 1 - \rho_i(\theta,\varphi) \tag{2}$$

This relation can be applied in two cases, either for anisotropic radiation over a Lambertian surface or for the inverse situation, with a non-Lambertian surface receiving isotropic radiation from its surroundings [*Nicodemus et al.*, 1977].

[9] From equations (1) and (2) emissivity is retrieved as:

$$\varepsilon_i(\theta,\varphi) = \frac{L_i(\theta,\varphi) - L_i^{\downarrow}}{B_i(T) - L_i} \tag{3}$$

However, emissivities from equation (3) are often inaccurate because of the difficulties in obtaining accurate measurements of the surface temperature T from which the Planck's radiance, B(T), is calculated as this radiative temperature corresponds to a thin superficial layer on the order of a few micrometers.

[10] A way to avoid this problem is to calculate relative-to-nadir values of $\varepsilon(\theta, \varphi)$ [*Labed and Stoll*, 1991], by taking two or more measurements, one of them at nadir and the rest at an arbitrary angular configuration, simultaneously or in a time period short enough to avoid significant changes of T or $L_i^{\downarrow}$ during the measurement process. It is possible to obtain relative-to-nadir emissivity measurements by dividing equation (3) considered at a given angle (θ, φ) and at nadir viewing (0, 0):

$$\varepsilon_{ri}(\theta,\varphi) = \frac{\varepsilon_i(\theta,\varphi)}{\varepsilon_i(0,0)} = \frac{L_i(\theta,\varphi) - L_i^{\downarrow}}{L_i(0,0) - L_i^{\downarrow}} \tag{4}$$

where $\varepsilon_{ri}(\theta, \varphi)$ is the relative-to-nadir emissivity and $L_i(0, 0)$ is the radiance measured by the sensor at nadir viewing.

[11] Given that equation (4) is the quotient between absolute emissivity from an angular configuration and nadir, a previous knowledge of absolute emissivity at nadir allows estimation of the absolute value of emissivity in that specific angular configuration by:

$$\varepsilon_i(\theta,\varphi) = \varepsilon_i(0,0)\varepsilon_{ri}(\theta,\varphi) \tag{5}$$

Equation (5) was used in the present study to retrieve the angular value of absolute emissivity.

3. Methodology

3.1. IBS Samples

[12] In this study we used twelve IBS samples, all with OM content lower than 9%, and spanning a wide range of textural compositions. Table 2 lists the textural and mineralogical features for the twelve IBS selected to carry out the study, all of them with a low roughness, after sieving particles size is between 0.2 cm and 1 cm, and almost completely dry with volumetric soil moisture values lower than 0.02 $m^3 \cdot m^{-3}$ [*Mira et al.*, 2007, 2010]. Figure 1 shows the distribution of the twelve IBS in the different subclasses given by the texture triangle defined by the USDA, and according to the *International Organization for Standardization* [2002]. Samples studied here present a wide percentage of sand content

Table 2. Organic Matter (OM) Content, and Textural and Mineralogical Features of the Twelve IBS Selected for the Analysis[a]

			Textural Classification (%)			Mineral Classification (%)					
Soil Code	USDA Texture Type	OM (%)	Sand	Silt	Clay	Quartz	Feldspar	Filosilicate	Hematite	Calcite	Gibbsite
B	sand	0.10	99	0.9	0.1	95.3	2.9	-	-	-	-
BR3	sand	1.69	92	2	6	100	-	-	-	-	-
LW03	loamy sand	0.73	77	18	5	53.7	46.3	-	-	-	-
BR2	sandy loam	1.47	69	15	16	82.3	16.8	0.8	-	-	-
E	sandy loam	1.50	67	20	13	72	21.4	3.2	-	-	-
LW52	sandy clay loam	1.71	62	15	23	58.4	32.2	9.4	-	-	-
LW13	loam	1.61	51	35	14	76	16.7	4.8	2.6	-	-
F	loam	3.50	50	30	20	19.9	4.5	4.1	8.7	62.9	-
BR1	clay	2.93	40	6	54	37.9	-	-	13.1	-	49
LW45	Silty loam	1.15	29	54	17	72.4	23.4	4.2	-	-	-
C	clay loam	8.90	20	43	37	29.4	5.5	9	-	56.1	-
D	Silty clay loam	4.50	14	50	35	19.3	3.5	6	8.9	62.3	-

[a] Additional details can be found in *Mira et al.* [2007, 2010].

(14–99%), the most common constituent of this sand is silica in the form of quartz, which also spans a wide range (19–100%); the other textures, silt and clay, present a percentage range from 0% to 54%. Additional details about these IBS can be found in the works of *Mira et al.* [2007, 2010].

[13] According to *Lagouarde et al.* [1995], for samples whose texture implies particles size less than 4–5 cm, the effects associated with angular measurements of T_b are caused by the emissivity of the IBS. On the other hand, in soils with coarse granularity and presence of particles which size is greater than 5 cm, angular effects in retrieving T_b are caused additionally by measuring shadowed or sunlit parts. Present work tries to study the angular emissivity of IBS with a roughness almost constant (particles size ranging between 0.2 and 1 cm). The objective is to evaluate the behavior of angular emissivity for each textural class defined in the text.

3.2. Instrumentation

[14] Angular radiance measurements over the IBS samples described in Table 2 were carried out on the roof of the Physics Faculty of the University of Valencia, Spain (13°30′25″N, 0°25′13″W) to determine the angular behavior of thermal emissivity by means of equation (5). Radiances were taken with two multispectral thermal radiometers CIMEL Electronique model CE312-2 [*Brogniez et al.*, 2003]. This radiometer works in six different spectral bands, one of them

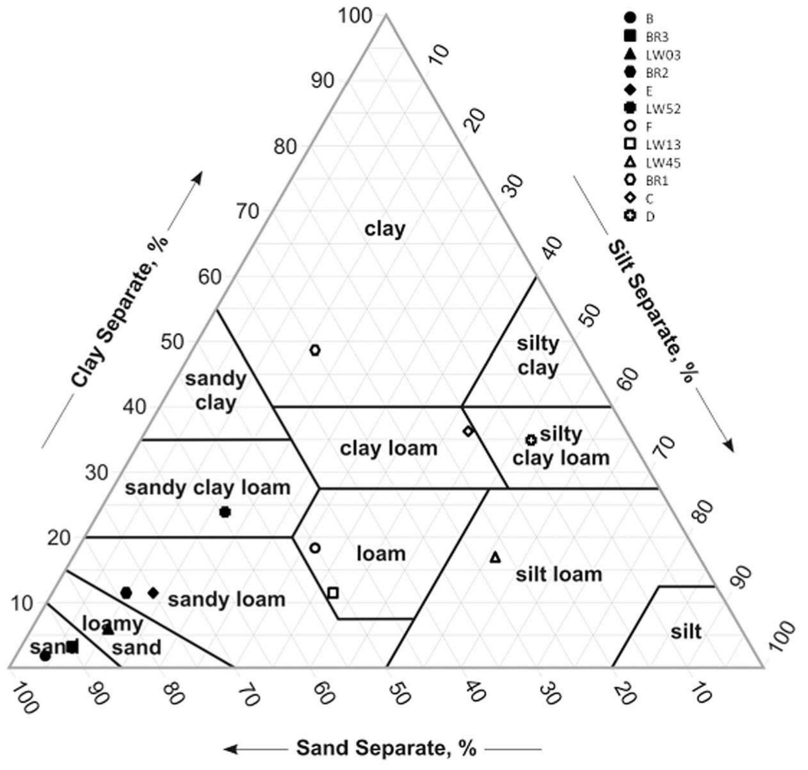

Figure 1. Distribution of the IBS analyzed in the texture triangle defined by USDA.

operating in the broad range 7.7–14.3 μm (channel 1) and the other five channels working in narrow bands allocated within the previous broadband: 8.2–8.7 μm (channel 6), 8.4–8.9 μm (channel 5), 8.9–9.4 μm (channel 4), 10.1–11.1 μm (channel 3) and 10.9–11.9 μm (channel 2).

3.2.1. Calibration

[15] Two CE312-2 radiometers used in the experiment were calibrated with a thermal source with near blackbody behavior, LandCal Blackbody Source model P80P (http://www.landinst.com/infrared/products/p80p), for a range temperature from 0°C to 30°C, to check the accuracy and precision of this radiometer. The P80P blackbody source in turn was calibrated in the National Physics Laboratory (NPL, London) during a comparison of TIR instruments, organized by the Committee on Earth Observation Satellites in April 2009 [*Theocharous and Fox*, 2010]. Results show that P80P agreed with the NPL reference radiometer with an accuracy of ±0.19°C at the three different reference temperatures of 10°C, 20°C and 30°C.

[16] Temperature measurements of CE312-2 against the P80P blackbody source were made at temperature values of 5°C, 10°C, 20°C and 30°C. Results showed that the accuracy of channels 1 to 6 of CE 312-2 with regard to the blackbody temperature is: ±0.03°C, ±0.02°C, ±0.03°C, ±0.018°C, ±0.03°C and ±0.02°C, respectively. Therefore, the absolute accuracy of CE 312-2 channels is within ±0.19°C.

[17] Measurements of $L_i^{\downarrow}$ in equation (4) were carried out by means of a panel with high diffuse reflectivity in the TIR, Infragold Reflectance Target (IRT-94-100) made by Labsphere. It is a squared panel with dimensions 25.4 × 25.4 cm^2 with a golden rough surface characterized by a high reflectance. The reflectance signature filtered for the six channels of the radiometer gives values of 0.926 (channel 1), 0.927 (channel 2), 0.926 (channel 3), 0.920 (channel 4), 0.917 (channel 5) and 0.918 (channel 6) (http://www.pro-lite.co.uk/File/Tech_Guide_-_Coatings_&_Materials.pdf), which imply small emissivities in all bands by virtue of Kirchhoff law. Nevertheless, direct measurements of radiance from the panel must be corrected by the radiative effect of this small emissivity, to get accurate values of $L_i^{\downarrow}$, using the following relationship:

$$L_i^{\downarrow} = \frac{L_{panel,i} - \varepsilon_{panel,i} B_{panel,i}\left(T_{panel}\right)}{1 - \varepsilon_{panel,i}} \qquad (6)$$

where $L_{\mathrm{panel,i}}$ is the direct measurement of radiance from panel, $\varepsilon_{\mathrm{panel,i}}$ is the emissivity of the panel and T_{panel} is the kinetic temperature of the golden surface which is measured by means of a contact thermometer, with an accuracy of ±1°C. This accuracy caused an error in $L_i^{\downarrow}$, of $\pm 0.09\ \mathrm{Wm^{-2}\ sr^{-1}}\ \mu\mathrm{m}^{-1}$ (or ±0.3 K in terms of environmental effective temperature) when $L_i^{\downarrow}$ is calculated in each of the six radiometer channels. It was decided to use a gold diffusive panel to retrieve the $L_i^{\downarrow}$ over other methods, such as direct sky measurements through using the diffusive approximation [*Kondratyev*, 1969; *Rubio et al.*, 1997], or the simulation of $L_i^{\downarrow}$ values obtained by introducing atmospheric profiles into radiative transfer codes, because in a previous study [*García-Santos et al.*, 2012] it was observed that all these methods agreed under clear sky conditions, but with the presence of clouds or surrounding elements (trees, buildings, instrumentation, etc.) only the gold panel took into account these radiative contributions that could lead to significant systematic errors in retrieving emissivity or LST [*García-Santos et al.*, 2012].

3.2.2. Angular Measurements

[18] A goniometer was used to perform the measurements on each sample at different viewing directions, together with two identical CE 312-2 radiometers (see Figure 2). In order to take relative-to-nadir emissivity measurements at different viewing angles using equation (4), radiance measurements were performed simultaneously setting one of the radiometers in the goniometer at nadir, and the second one in a viewing direction (θ, φ) (this last radiometer can be moved along the arc of the goniometer varying the viewing angle). With this configuration simultaneous measurements were readily achieved ensuring the stability of sample temperature. The experimental design of the ensemble can be seen in Figure 2, where the two radiometers are deployed to collect simultaneous measurements at nadir (CE1) and at a different angle (CE2).

[19] Angular measurements were taken at different combinations of zenith and azimuth angles. Zenith angles were considered from $\theta = 10°$ to $\theta = 70°$ at intervals of 10°. For each zenith angle, the IBS emissivity was measured at four different azimuthal orientations turning the samples 90° each time, instead of turning the goniometer-radiometer system. This process was repeated three times for each zenith angle. Azimuthal rotation of the sample, instead of the goniometer framework, was done to speed data collection and to ensure that observations were made using the same surrounding conditions (i.e., solar elevation, atmosphere contribution, etc.). In this way any difference in retrieving emissivity by equation (4) at different azimuthal angles, can be attributed exclusively to the sample.

[20] $L_i^{\downarrow}$ was measured before the CE1(0°)–CE2(10°) and after the CE1(0°)–CE2(70°) measurement configurations, placing the gold panel inside the FOV of CE1(0°). The period of time between both panel measurements was 30 min, which implied an average fluctuation of $L_i^{\downarrow}$ of ±7%; this relative value was obtained from the quotient of the difference between the $L_i^{\downarrow}$ values measured before and after the 30 min interval, and the average value of both measurements, given in percentage. This fluctuation, considered as an error of $L_i^{\downarrow}$ measurement, results in an equivalent emissivity error of ±0.0003, i.e., around ±0.03%. This error is much lower than the current accuracies in field emissivity measurements, and thus it was deemed appropriate to take the average value of $L_i^{\downarrow}$ for application to equation (4).

[21] Once the relative-to-nadir emissivity for each sample was measured, it is easy to obtain its absolute value by means of equation (5), provided that the absolute emissivity value at nadir is measured using one of the existing methodologies. In the present study the absolute emissivity at nadir was obtained by means of temperature-emissivity separation (TES) method originally developed for the ASTER instrument [*Gillespie et al.*, 1998], which was adapted to the field instrumentation taking into account that the radiometers have five bands that essentially fit those of ASTER [*Mira et al.*, 2009].

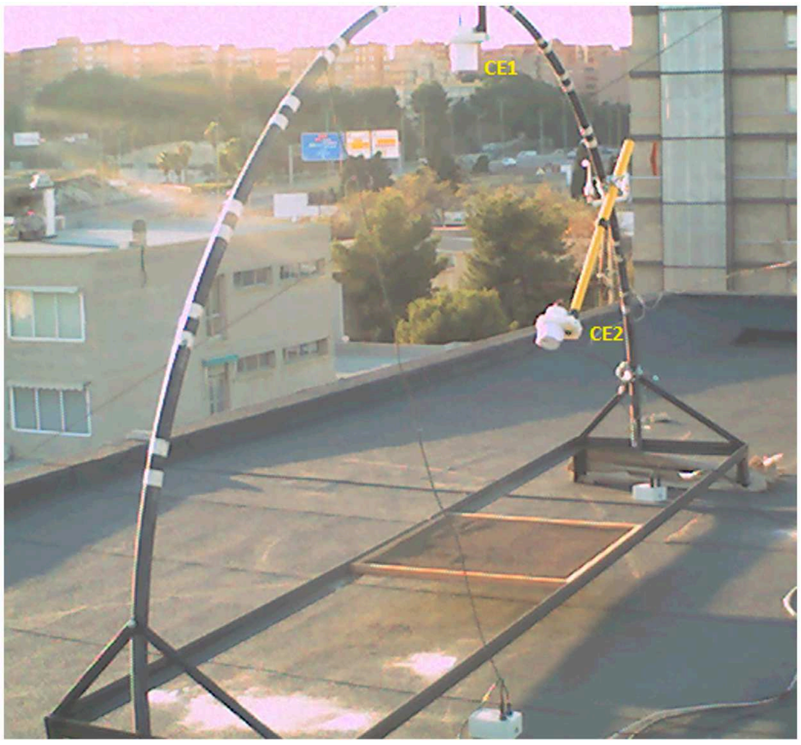

Figure 2. Experimental ensemble used in the study during two simultaneous measurements at nadir (CE1) and at zenithal angle (CE2).

[22] Errors associated with $\varepsilon_i(\theta, \varphi)$ were obtained through error propagation in equation (5) by means of expression:

$$\delta\varepsilon_i(\theta,\varphi) = \sqrt{\left[\varepsilon_i(0,0)\delta\varepsilon_{ri}(\theta,\varphi)\right]^2 + \left[\varepsilon_{ri}(\theta,\varphi)\delta\varepsilon_i(0,0)\right]^2} \qquad (7)$$

The term $\delta\varepsilon_i(0, 0)$ is the precision for emissivity values at nadir derived as the standard deviation of ten individual emissivity measurements for each IBS sample, made with the TES method; these errors showed an average value of ±0.005 at all spectral channels of CE 312-2 and for all the samples analyzed. On the other hand, the term $\delta\varepsilon_{ri}(\theta, \varphi)$ is the error of relative-to-nadir values of emissivity that are obtained as the maximum value of: (i) the values resulting from error propagation in equation (4), in which errors of each radiance measurement are given by the accuracy of the radiometer (see section 3.2.1), except in case of $L_i^{\downarrow}$ which is given by the standard deviation of the $L_i^{\downarrow}$ measurements made according to the methodology (see section 3.2.2); or (ii) the standard deviation of the three measurements made over a sample in each angular viewing direction. Results showed that the propagation error in equation (4), associated to accuracy of radiometers, was most of the time higher than the standard deviation of the three measurements; in addition, the maximum of these two errors, at a zenithal angle for all the azimuths measured, was very similar in all the spectral channels. As a result these values were averaged, taking all azimuth and channel error values in a specific zenithal angle obtaining, together with the standard deviation, the root-mean square deviation (RMSD) associated to $\varepsilon_{ri}(\theta, \varphi)$ for each IBS. As can be seen, results given in Table 3 show that values of RMSD are mostly lower than ±0.01, except in the case of sample B at 30°, and sample LW03 from 50° to 70°. Average error associated to $\varepsilon_{ri}(\theta, \varphi)$

Table 3. RMSD Obtained From the Average and Standard Deviation of $\delta\varepsilon_{ri}(\theta, \varphi)$ for All the Azimuthal Angles and Spectral Channels in a Specific Zenith Angle, for Each One of the IBS Studied

θ(°)	BR1	BR2	BR3	B	C	D	E	F	LW03	LW13	LW45	LW52
10	0.004	0.006	0.005	0.010	0.005	0.004	0.005	0.005	0.010	0.005	0.005	0.006
20	0.004	0.005	0.005	0.010	0.005	0.005	0.005	0.005	0.010	0.004	0.005	0.005
30	0.004	0.005	0.005	0.011	0.005	0.004	0.005	0.005	0.010	0.004	0.005	0.005
40	0.004	0.005	0.005	0.010	0.005	0.005	0.005	0.005	0.010	0.004	0.005	0.005
50	0.004	0.005	0.005	0.010	0.006	0.004	0.005	0.005	0.012	0.006	0.005	0.005
60	0.004	0.005	0.005	0.010	0.007	0.005	0.005	0.005	0.014	0.006	0.005	0.006
70	0.007	0.006	0.008	0.010	0.009	0.010	0.005	0.007	0.015	0.007	0.007	0.005

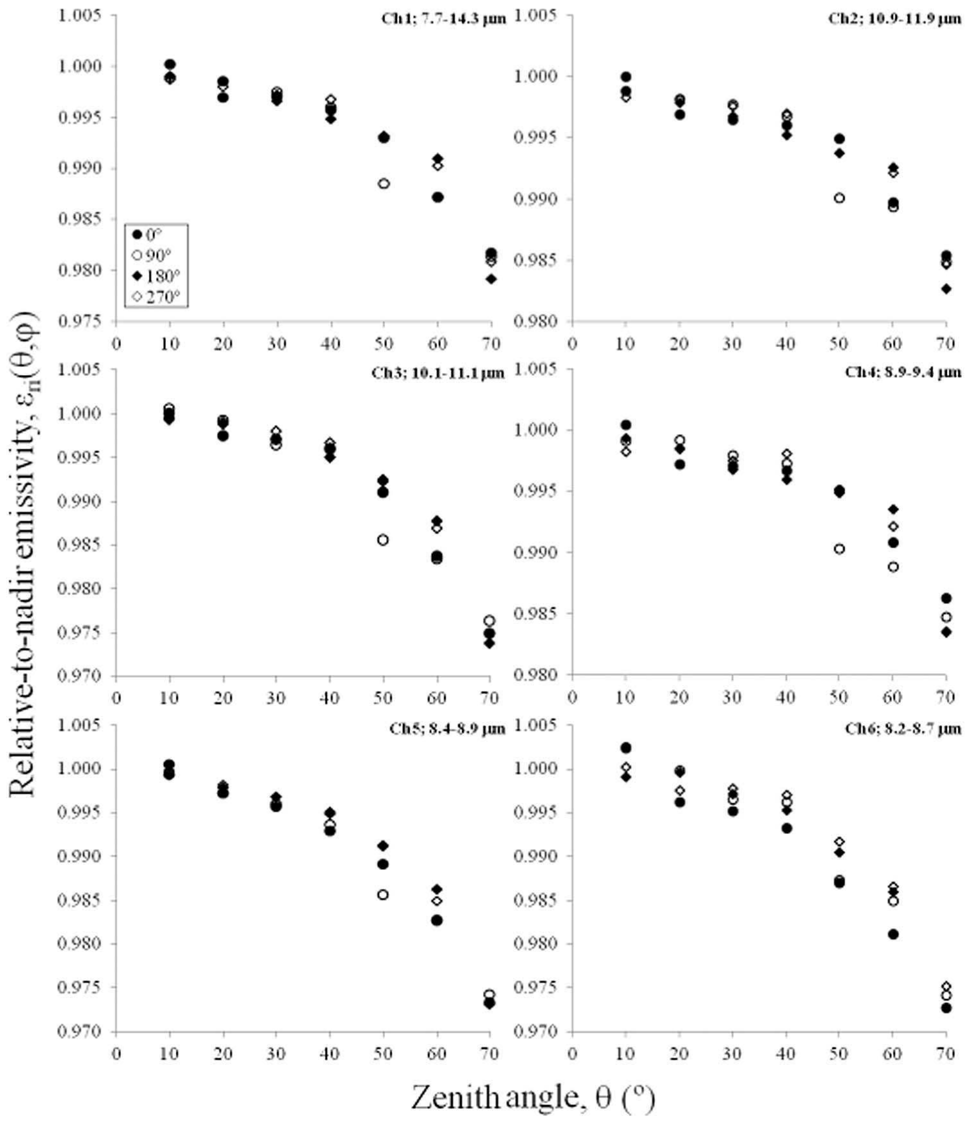

Figure 3. $\varepsilon_{\rm ri}(\theta, \varphi)$ for the E sample at the four azimuth angles, obtained turning azimuthally 90 degrees each time the sample for a specific zenith angle. Results are presented along the zenithal variation.

is ±0.006. Therefore we considered that only variations of $\varepsilon_{\rm ri}(\theta, \varphi)$ larger than ±0.01 imply significant changes of emissivity with viewing angle.

4. Results and Discussion

4.1. Azimuthal Variation of IBS Emissivity

[23] The azimuthal dependence of the IBS relative-to-nadir emissivity was first analyzed. $\varepsilon_{\rm ri}(\theta, \varphi)$ for the twelve samples was retrieved, at each zenith angle, at four different azimuthal orientations, turning the sample 90° each time. Figure 3 shows $\varepsilon_{\rm ri}(\theta, \varphi)$ for the sample E at the four azimuths along the zenithal variation. Results show emissivity almost azimuthally isotropic compared to the zenithal decrease. Given the results of Figure 3, it was calculated the standard deviation of the four $\varepsilon_{\rm ri}(\theta, \varphi)$ values retrieved in each azimuth, for a specific zenithal angle and spectral channel. Then, this standard deviation value was averaged at all six spectral channels, since it presented a very similar value in all cases, and their standard deviations were also calculated; with these two values it was obtained finally the RMSD for each one of the zenith angles studied here. Table 4 shows this last RMSD for the twelve IBS.

[24] Results of Table 4 show that the azimuthal variation of $\varepsilon_{\rm ri}(\theta, \varphi)$ (RMSD less than ±0.01) is in general lower than the measurement error associated (given in Table 3) with the exception of samples BR3, from $\theta = 50°$ to $\theta = 70°$, and LW45 at $\theta = 50°$. According to this result, azimuthal variation of $\varepsilon_{\rm ri}(\theta, \varphi)$ for a IBS (with a roughness lower than 5 mm) could be ignored, assuming an uncertainty in the measurement lower than ±0.01.

4.2. Zenithal Variation of IBS Emissivity

[25] Considering the relatively low azimuthal variation of IBS emissivity in comparison to the zenithal variation, the relative-to-nadir emissivities at each zenith angle were calculated as the average of the values measured at all azimuthal angles. This final $\varepsilon_{\rm ri}$ value was multiplied by an absolute nadir

Table 4. RMSD Obtained From the Average of the Standard Deviation Calculated for the Four Azimuth Angles and for All the Spectral Channels in a Specific Zenith Angle[a]

θ(°)	BR1	BR2	BR3	B	C	D	E	F	LW03	LW13	LW45	LW52
10	0.003	0.002	0.003	0.004	0.001	0.002	0.001	0.001	0.002	0.002	0.001	0.002
20	0.003	0.001	0.002	0.004	0.001	0.002	0.001	0.000	0.005	0.001	0.001	0.002
30	0.002	0.002	0.003	0.005	0.003	0.001	0.001	0.001	0.003	0.003	0.001	0.003
40	0.001	0.002	0.002	0.009	0.002	0.002	0.001	0.002	0.002	0.001	0.001	0.002
50	0.001	0.004	0.007	0.005	0.004	0.004	0.003	0.003	0.004	0.004	0.006	0.003
60	0.001	0.006	0.010	0.007	0.004	0.004	0.002	0.003	0.007	0.006	0.005	0.002
70	0.004	0.004	0.009	0.010	0.011	0.010	0.001	0.004	0.005	0.004	0.007	0.004

[a] Results are presented for the twelve IBS.

emissivity value calculated from TES method [*Gillespie et al.*, 1998] to retrieve the absolute value at a specific θ according to equation (5). Figures 4a–4d present the zenithal variation of absolute emissivity, for each of the twelve IBS samples, in all six channels of the radiometer. The errors have been calculated according to equation (7). The uncertainties obtained for all zenith angles, IBS samples and spectral channels were lower than ±0.015 in 98% of cases and lower than ±0.01 in 71% of cases. So, the average value of this error for all the channels and zenith angles for all samples was ±0.009 with a standard deviation of ±0.003, being the RMSD ±0.01. This value was established as a threshold to determine if the absolute emissivity of an IBS changes significantly with the zenith angle with respect to its nadir value.

4.3. Spectral Features of $\varepsilon_i(\theta, \varphi)$

[26] Results of Figures 4a–4d show that for all the IBS, the absolute emissivity decreases with increasing viewing angle. The magnitude of the decrease depends on IBS texture and composition. Analyzing the difference between the value of $\varepsilon_i(\theta, \varphi)$, hereafter referred as $\varepsilon_i(\theta)$, at nadir and other zenith angles, shows that no significant angular variation is observed for zenith angles lower than 40°, independently of IBS composition.

[27] In the broad interval 7.7–14.3μm (channel 1), Figures 4a–4d show that difference $\varepsilon_i(0°) - \varepsilon_i(\theta)$ becomes significant for IBS with sand and quartz content greater than 80% and 90%, respectively (samples B and BR3, Table 2) even for zenith angles lower than 50°. Angular effects in emissivity must be taken into account for zenithal angles above 60° for all IBS, independently of its textural or mineralogical composition. In this broad spectral range the maximum angular variation of emissivity from nadir appears at $\theta = 70°$, for the sandy soil B being the emissivity difference $\varepsilon_i(0°)–\varepsilon_i(70°)$ of +0.047. However, the minimum variation obtained is +0.012 (sample C), and therefore still significant. At $\theta = 60°$, just IBS with high percentage of sand and quartz (samples B, BR3, LW03 and BR2, see Table 2) show significant differences from nadir, ranging between +0.014 and +0.028.

[28] The angular effects in the range 10–12 μm (channels 2 and 3) are negligible for zenith angles up to 60°. For IBS with sand and quartz contents above 80% (B, BR2 and BR3), the emissivity angular variation becomes relevant at a zenith angle of 60°, ranging from +0.013 to +0.018. For zenith angles of 70°, the angular effects are important for all IBS, and are more pronounced for sandy soils with high quartz content; at this specific zenith angle, differences range from +0.011 to +0.036.

[29] Results for channels 4, 5 and 6, show that angular decrease of emissivity are strongly affected by sand composition and quartz content of the IBS, being significantly large for sandy soils with high quartz content (B and BR3), for zenith angles above 40°. If sand and quartz contents are higher than 50% (all samples except most clayey samples: BR1, C and D), the angular effects become important from 50°, whose differences from nadir range between +0.01 and +0.035. At $\theta = 60°$ these differences increase, ranging between +0.014 and +0.051. Maximum angular variation is reached at $\theta = 70°$, for sandy soils with a high quartz content (sample B). This difference is of +0.091.

[30] In order to quantify the zenithal dependence of emissivity on textural and mineralogical composition, we first calculated an average value of $\varepsilon_{ri}(\theta)$ for all IBS sample data analyzed at each specific zenith angle (12 values per angle), with the purpose of checking possible dependences on soil composition. Errors associated to these average values were calculated as the root mean square of (i) the average error of $\varepsilon_{ri}(\theta)$ at the specific zenithal angle derived from Table 3 values (Av($\delta\varepsilon_{ri}$)), and (ii) the standard deviation of the 12 $\varepsilon_{ri}(\theta)$ values ($\delta\varepsilon_\sigma$):

$$\delta\bar{\varepsilon}_r = \sqrt{Av(\delta\varepsilon_{ri})^2 + \delta\varepsilon_\sigma^2}. \tag{8}$$

[31] Results are presented in Table 5. For spectral ranges 7.7–14.3 μm (CE312-2 channel 1) and 10–12 μm (CE312-2 channels 2 and 3), $\varepsilon_{ri}(\theta)$ shows a decrease with the increase of θ, that can be considered independent of any IBS composition, since the observed uncertainties are lower, or of the same order than ±0.01, except for 70° at the broad channel 1. Therefore, specific values can be established to assess the angular variation of $\varepsilon_{ri}(\theta)$ for every IBS. For the spectral range 8–9.4 μm (CE312-2 channels 4, 5 and 6), averaged values of $\varepsilon_{ri}(\theta)$ show uncertainties lower than ±0.01 for zenith angles lower than 30°. Nevertheless, for $\theta \geq 40°$ the dispersion of results gave uncertainties larger than ±0.01, reaching values greater than ±0.03 for $\theta = 70°$. These large errors showed that the emissivity zenith variation has a strong dependence with soil composition, which is addressed in the next section.

4.4. Parameterization of $\varepsilon_{ri}(\theta)$

[32] A parameterization of the angular variation of emissivity was addressed from the results shown in Table 5. First, considering that the relative emissivity values are very similar for the spectral ranges 7.7–14.3 μm and 10–12 μm, a

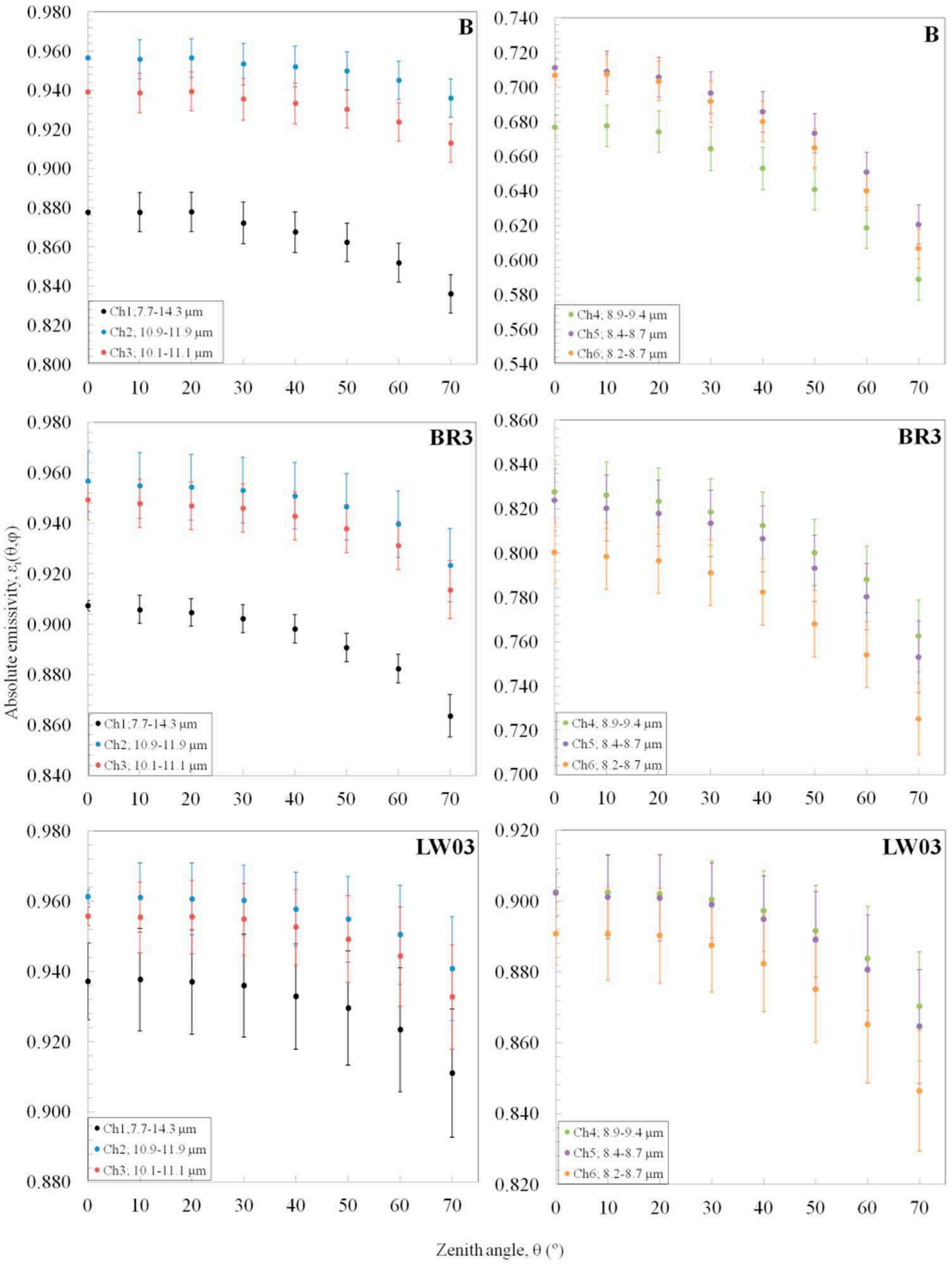

Figure 4a. Absolute angular emissivity values obtained for the IBS samples B, BR3 and LW03, and for the six spectral channels of the radiometer. First column of graphs shows results for channel 1 (black dots) that extends over 7.7–14.3 m, and for channels 2 (blue dots) and 3 (red dots) that are placed within the 10–12 m region. Second column of graphs shows the results for channels 4 (green dots), 5 (purple dots) and 6 (orange dots) that are allocated in the 8–9.5 m interval. The errors shown have been calculated using equation (7).

single relationship was derived for these spectral ranges that define the relative emissivity as a function of observation angle θ (in degrees):

$$\varepsilon_r(\theta) = 1 - 8.7 \times 10^{-9}\ \theta^{3.47} \tag{9}$$

The regression presents a determination coefficient of R^2 = 0.993 and a RMSE = ±0.001. Taking into account also the uncertainties in those channels given by equation (8), the final error using the parameterization of equation (9) ranges from ±0.002 (at θ = 10°–20°) to ±0.009 (at θ = 70°), with an average value of ±0.004.

[33] As mentioned previously, in the spectral range 8–9.4 μm $\varepsilon_{ri}(\theta)$ shows great discrepancies for $\theta \geq 40°$ considering the different types of IBS (see Figures 4a–4d and Table 5). Consequently, a parameterization that includes the IBS textural and mineralogical composition was set up. In a first step, the relevant parameters for the relative emissivity variation with viewing angle were assessed, by using a principal component analysis [*Field*, 2009] for all data

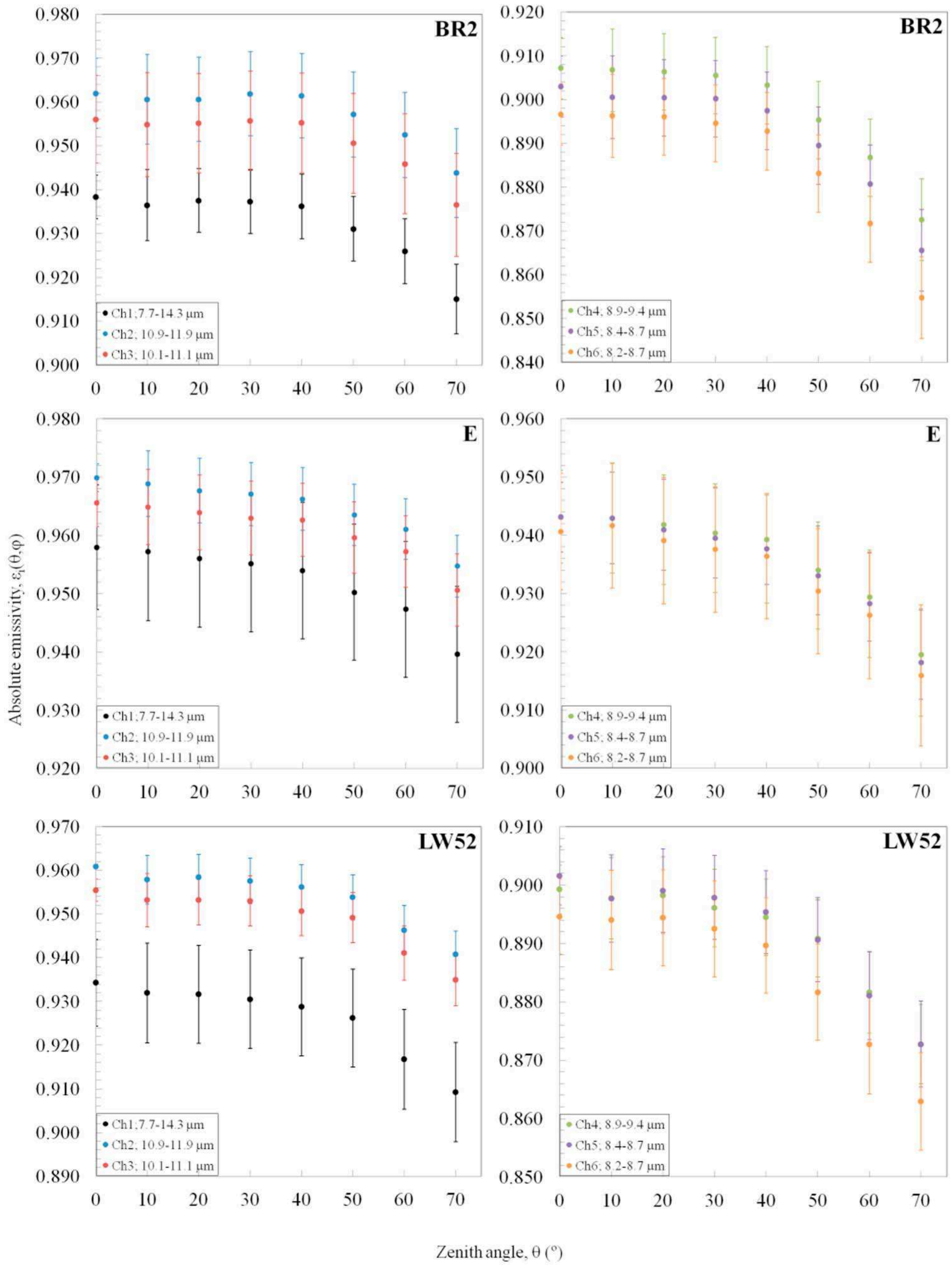

Figure 4b. Absolute angular emissivity values obtained for the IBS samples BR2, E and LW52, and for the six spectral channels of the radiometer. First column of graphs shows results for channel 1 (black dots) that extends over 7.7–14.3 m, and for channels 2 (blue dots) and 3 (red dots) that are placed within the 10–12 m region. Second column of graphs shows the results for channels 4 (green dots), 5 (purple dots) and 6 (orange dots) that are allocated in the 8–9.5 m interval. The errors shown have been calculated using equation (7).

available in Table 1 about IBS samples (except mineralogical data, excluding quartz and feldspar, since there was no complete information for all the samples), plus the measured values of $\varepsilon_{\mathrm{ri}}$. The most interesting statistical results are summarized in Figure 5.

[34] Figure 5a shows the Scree Plot, which according to *Field* [2009] shows how many factors are necessary to represent the total variance of data introduced. This quantity of factors is given by the number of components at which the slope becomes almost horizontal. Scree Plot presented here (see Figure 5a) shows that only four factors are enough. Results of the Total Variance Explained matrix (*Field* [2009], not included here) show that the first four factors represent a 90% of the variance.

[35] Once fixed how many factors are necessary, it is needed to know which ones are the most relevant, since

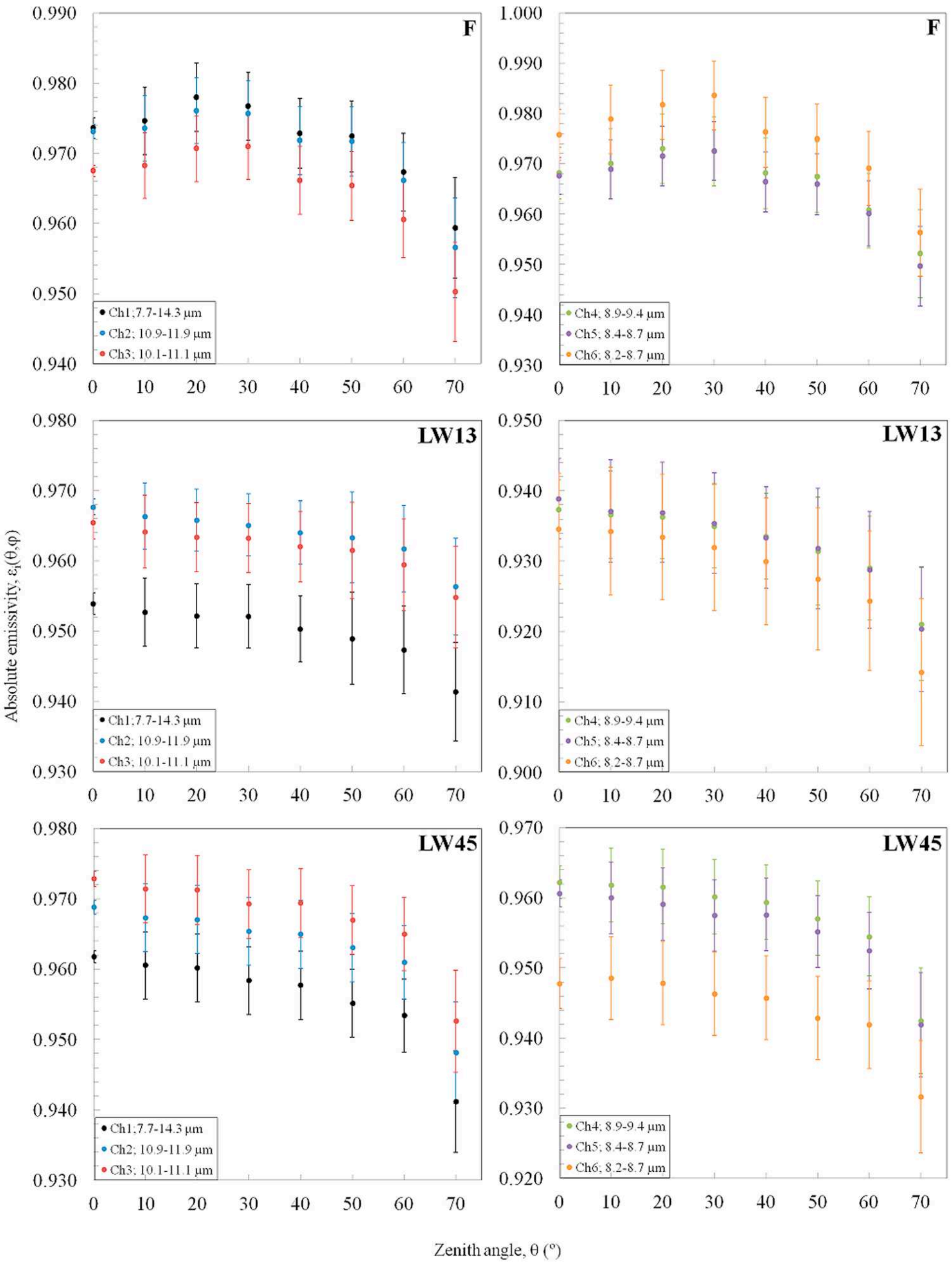

Figure 4c. Absolute angular emissivity values obtained for the IBS samples F, LW13 and LW45, and for the six spectral channels of the radiometer. First column of graphs shows results for channel 1 (black dots) that extends over 7.7–14.3 m, and for channels 2 (blue dots) and 3 (red dots) that are placed within the 10–12 m region. Second column of graphs shows the results for channels 4 (green dots), 5 (purple dots) and 6 (orange dots) that are allocated in the 8–9.5 m interval. The errors shown have been calculated using equation (7).

during the PCA it was applied an extraction of those factors whose Eigenvalues were greater than 1, according to Kaiser's recommendation [*Field*, 2009]. PCA found only two factors to be extracted, ε_r and θ, both represented in axes of rotated space, Figure 5b. The reason of this extraction is because ε_r explains the 60.5% of the total variance, being the most significant factor and θ is the second most significant, explaining a 16% of the total variance, different from that explained by ε_r. To select the two other factors, the plot of components in rotated space (Figure 5b) is used. This plot represents the correlation degree of each component to relative-to-nadir emissivity. According to *Field* [2009], values lower than ±0.5 are not well correlated with the component of interest, and all factors greater than ±0.5 could be taken into account. In Figure 5b, the factors to take under consideration for the relative-to-nadir emissivity are sand and quartz (negatively

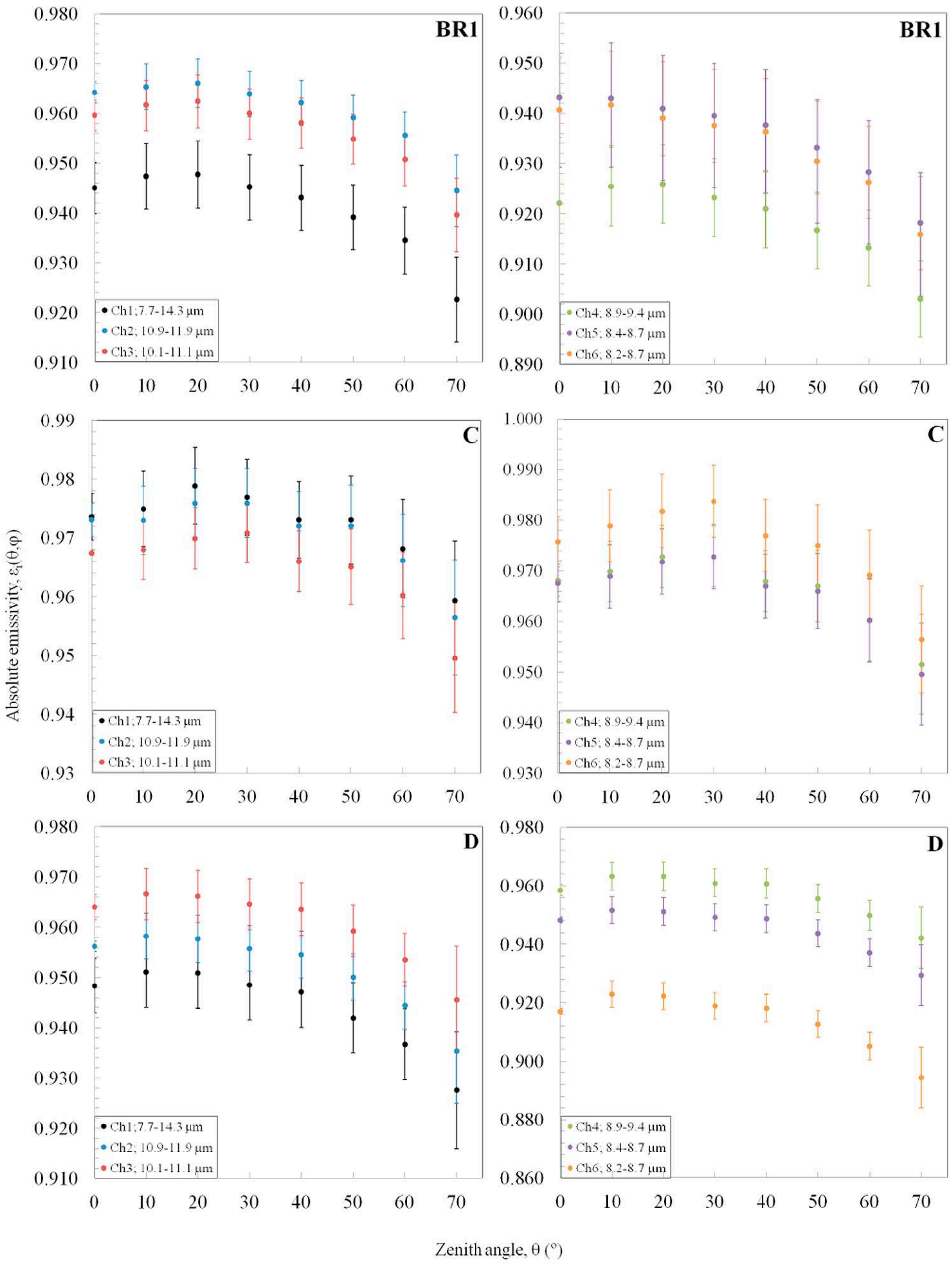

Figure 4d. Absolute angular emissivity values obtained for the IBS samples BR1, C and D, and for the six spectral channels of the radiometer. First column of graphs shows results for channel 1 (black dots) that extends over 7.7–14.3 m, and for channels 2 (blue dots) and 3 (red dots) that are placed within the 10–12 m region. Second column of graphs shows the results for channels 4 (green dots), 5 (purple dots) and 6 (orange dots) that are allocated in the 8–9.5 m interval. The errors shown have been calculated using equation (7).

correlated), which would be expected because the common constituent of sand of our IBS samples is silica in the form of quartz, and silt, clay and OM (positively correlated).Sand is the most correlated factor with ε_r followed by OM, Clay and Quartz, it is obvious that sand should be the first factor selected. Deciding to select which one will be the last factor is difficult because OM and Clay present similar correlation with ε_r, for this reason the parameterization was made including first OM and finally substituting OM by clay. Comparison between observed $\varepsilon_{ri}(\theta)$ values and those parameterized at the three considered spectral ranges showed that including clay results are slightly better than choose OM. Results showed a correlation coefficient (R^2) ranging between 0.97 and 0.98 and a RMSE ranging between ±0.003–±0.005 for the case of clay and a R^2 ranging between 0.95 and 0.96 and a RMSE ranging between ±0.005–±0.006 for the case of OM. Finally, sand and clay were the two factors chosen, the model to calculate the

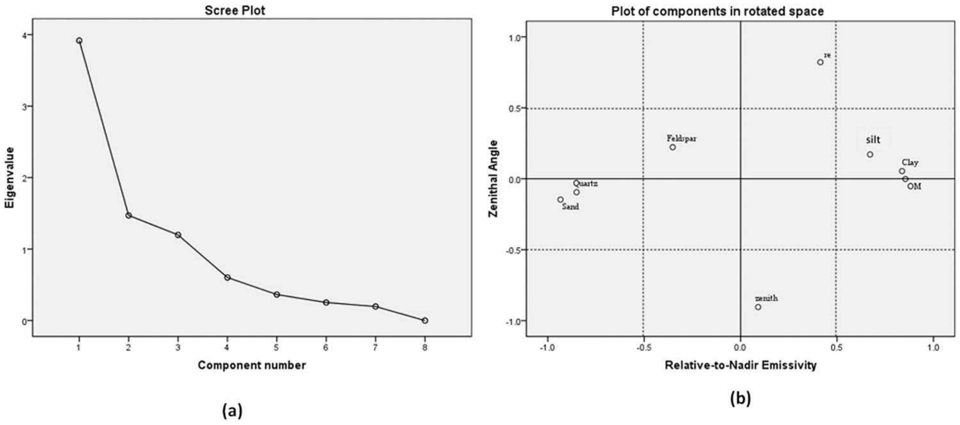

Figure 5. (a) Scree Plot of components that shows the number of components needed to explain most of the variance. (b) Plot of components in rotated space, which shows the correlation of the relevant components to relative-to-nadir emissivity. (See main text for details.)

relative-to-nadir emissivity obtained considering these parameters is:

$$\varepsilon_{ri}(\theta, S, C) = a_i(\theta) + b_i(\theta)S + c_i(\theta)C + d_i(\theta)S^2 + e_i(\theta)SC + f_i(\theta)C^2 \tag{10}$$

where *i* represents the spectral range (8.9–9.4 μm, 8.4–8.9 μm or 8.2–8.7 μm), S and C are sand and clay percentage, respectively and parameters a(θ) to f(θ) are quadratic zenith angle-dependent polynomials:

$$\begin{aligned} a_i(\theta) &= a_{0i} + a_{1i}\theta + a_{2i}\theta^2 \\ b_i(\theta) &= b_{0i} + b_{1i}\theta + b_{2i}\theta^2 \\ c_i(\theta) &= c_{0i} + c_{1i}\theta + c_{2i}\theta^2 \\ d_i(\theta) &= d_{0i} + d_{1i}\theta + d_{2i}\theta^2 \\ e_i(\theta) &= e_{0i} + e_{1i}\theta + e_{2i}\theta^2 \\ f_i(\theta) &= f_{0i} + f_{1i}\theta + f_{2i}\theta^2 \end{aligned} \tag{11}$$

Coefficients of polynomials in (11) are given in Table 6 for each spectral range, together with the determination coefficients and RMSE of the regressions.

[36] Values of S and C contents could be estimated remotely using radar data. As shown in *Singh and Kathpalia* [2007], applying a Genetic Algorithm technique to radar data retrieved from Synthetic Aperture Radar onboard European Remote Sensing 2, percentages of S and C are obtained with an standard error ranging between 0.07%–0.18%. Another possibility is to have a previous knowledge of S and C content from ancillary data. In these cases the parameterizations given above (equations (9) to (11), depending on the channel) could be applied to classification-based emissivity mapping, such as the one used in MODIS [*Snyder et al.*, 1998], SEVIRI [*Trigo et al.*, 2008], or more recently AATSR data [*Caselles et al.*, 2012], in order to refine their algorithms.

[37] Figure 6 shows the comparison between the observed $\varepsilon_{ri}(\theta)$ values and those modeled using equation (10) at the three considered spectral ranges. Results show an average correlation of 0.98 and an average RMSE of ±0.004. Considering also error propagation in equation (10), the final uncertainty showed an average value for all three spectral

Table 5. Averaged Relative-to-Nadir Emissivity Values at Each Zenith Angle (θ) for the Six Spectral Channels of CE312-2, for All the IBS[a]

θ(°)	$\varepsilon_{r\ ch1}(\theta)$ 7.7–14.3 μm	$\varepsilon_{r\ ch2}(\theta)$ 10.9–11.9 μm	$\varepsilon_{r\ ch3}(\theta)$ 10.1–11.1 μm	$\varepsilon_{r\ ch4}(\theta)$ 8.9–9.4 μm	$\varepsilon_{r\ ch5}(\theta)$ 8.4–8.9 μm	$\varepsilon_{r\ ch6}(\theta)$ 8.2–8.7 μm
10	1.000 ± (0.006)	0.999 ± (0.005)	1.000 ± (0.006)	1.000 ± (0.006)	0.999 ± (0.006)	1.001 ± (0.006)
20	1.000 ± (0.006)	0.999 ± (0.006)	1.000 ± (0.006)	1.000 ± (0.006)	0.998 ± (0.007)	1.000 ± (0.007)
30	0.998 ± (0.006)	0.998 ± (0.006)	0.999 ± (0.006)	0.996 ± (0.008)	0.995 ± (0.009)	0.996 ± (0.010)
40	0.995 ± (0.007)	0.996 ± (0.006)	0.996 ± (0.006)	0.992 ± (0.012)	0.990 ± (0.012)	0.991 ± (0.013)
50	0.991 ± (0.008)	0.994 ± (0.007)	0.993 ± (0.007)	0.985 ± (0.017)	0.983 ± (0.017)	0.981 ± (0.019)
60	0.984 ± (0.010)	0.989 ± (0.008)	0.988 ± (0.008)	0.98 ± (0.02)	0.97 ± (0.02)	0.97 ± (0.03)
70	0.972 ± (0.014)	0.979 ± (0.010)	0.978 ± (0.010)	0.96 ± (0.04)	0.96 ± (0.04)	0.95 ± (0.04)

[a] Errors obtained with equation (8) are included in parentheses. From $\theta \geq 40°$ and for channels 4, 5 and 6 of CE 312-2, the relative emissivity presents errors greater than ±0.01.

Table 6. Coefficients for the Quadratic Zenith-Dependent Polynomials a(θ) to f(θ) Included in Equation (10), Together With R^2 and RMSE Regression Parameters

	a(θ)	b(θ)	c(θ)	d(θ)	e(θ)	f(θ)
Channel 4 8.9–9.4 μm						
θ^2	−0.00004	$5\cdot10^{-7}$	$1.2\cdot10^{-6}$	$-4\cdot10^{-9}$	$-1.2\cdot10^{-10}$	$-1.6\cdot10^{-8}$
θ	0.0009	$-5\cdot10^{-6}$	−0.000018	$5\cdot10^{-8}$	$-4\cdot10^{-8}$	$1.9\cdot10^{-7}$
Offset	0.991	−0.000014	0.0003	$3\cdot10^{-7}$	$-3\cdot10^{-6}$	$-7\cdot10^{-7}$
R^2	0.990	0.965	0.993	0.979	0.098	0.998
RMSE	0.006	0.00017	0.0002	$1.2\cdot10^{-6}$	$4\cdot10^{-6}$	$1.4\cdot10^{-6}$
Channel 5 8.4–8.9 μm						
θ^2	−0.00005	$7\cdot10^{-7}$	$1.4\cdot10^{-6}$	$-6\cdot10^{-9}$	$-3\cdot10^{-9}$	$-1.6\cdot10^{-8}$
θ	0.0012	−0.000019	−0.00002	$1.5\cdot10^{-7}$	$1.4\cdot10^{-7}$	$1.4\cdot10^{-7}$
Offset	0.9833	0.0003	0.0005	$-1.7\cdot10^{-6}$	$-6\cdot10^{-6}$	$-1.4\cdot10^{-6}$
R^2	0.985	0.953	0.989	0.966	0.412	0.996
RMSE	0.008	0.0002	0.0003	$1.6\cdot10^{-6}$	$4\cdot10^{-6}$	$2\cdot10^{-6}$
Channel 6 8.2–8.7 μm						
θ^2	−0.00005	$7\cdot10^{-7}$	$1.6\cdot10^{-6}$	$-6\cdot10^{-9}$	$-3\cdot10^{-9}$	$-2\cdot10^{-8}$
θ	0.0012	−0.000019	−0.00002	$1.4\cdot10^{-7}$	$1.1\cdot10^{-7}$	$1.5\cdot10^{-7}$
Offset	0.985	0.0002	0.0005	$-1.4\cdot10^{-6}$	$-6\cdot10^{-6}$	$-5\cdot10^{-7}$
R^2	0.992	0.972	0.994	0.979	0.395	0.997
RMSE	0.008	0.00019	0.0002	$1.4\cdot10^{-6}$	$4\cdot10^{-6}$	$2\cdot10^{-6}$

ranges of ±0.009 for $\theta = 10°$ to $50°$, at $\theta = 60°$ the average error was ±0.011, and at $\theta = 70°$ it was ±0.013. The average error for all spectral channels and zenith angles was ±0.01, so this error could be considered as final error for results retrieved with equation (10).

5. Implications for LST and Longwave Radiation Retrieval Accuracy

5.1. Implications for LST Accuracy

[38] The impact of ignoring angular effects on emissivity when measuring LST from space were addressed using one of the available split-window algorithms that present explicit dependence on emissivity. To this end, the algorithm proposed by *Galve et al.* [2008] for the MODIS spectral bands 31 and 32 were used, these bands are similar to CE312-2 channels 2 (10.9–11.9 μm) and 3 (10.1–11.1 μm) in this study, although the results may be similar for other comparable algorithms and instruments. This algorithm gives LST corrected for emissivity and atmospheric effects as:

$$LST = T_{31} + a_0 + a_1(T_{31} - T_{32}) + a_2(T_{31} - T_{32})^2 + \alpha(1 - \bar{\varepsilon}) - \beta\Delta\bar{\varepsilon} \qquad (12)$$

where T_{31} and T_{32} are brightness temperatures measured in MODIS bands 31 and 32, respectively; a_0, a_1 and a_2 are regression coefficients that can be found in *Galve et al.* [2008]; coefficients α and β determine the weight of the emissivity correction and are dependent on atmospheric water vapor content or precipitable water (W in cm); and $\bar{\varepsilon}$ and $\Delta\bar{\varepsilon}$ are the average and emissivity difference in MODIS at bands 31 and 32, respectively.

[39] Since relative-to-nadir emissivities in CE312-2 channels 2 and 3 show almost the same angular variation (see Table 4), the emissivity difference $\Delta\bar{\varepsilon}$ will remain almost constant at any angle, and thus the impact in this term should be negligible. However, this is not the case for the average emissivity term $\bar{\varepsilon}$, for which error propagation gives:

$$\delta LST(\theta) = \alpha\left[1 - \Delta\overline{\varepsilon(\theta)}\right] \qquad (13)$$

where $\Delta\overline{\varepsilon(\theta)}$ is the difference between the average emissivity values of CE312-2 spectral channels 2 and 3 at nadir and at a zenith angle θ. As mentioned above, α is a W-dependent parameter following a quadratic relationship [*Galve et al.*, 2008]:

$$\alpha = 45.99 + 4.67W - 1.446W^2. \qquad (14)$$

[40] Table 7 shows the variation of absolute emissivity between nadir values and the values at $\theta = 40°$ and $\theta = 65°$, respectively, for all the analyzed samples, and for CE312-2 channels 2 and 3. The emissivity differences between 0° and 40° are generally small, but this is not the case for viewing angles of 65°. The emissivity differences in this last case were used in equation (13) to assess the possible impact of ignoring the angular variation of emissivity on LST, at large observation angles, if emissivity values at nadir are used instead of the correct off-nadir value. The results are shown in Figure 7, in which error values are represented for different W (i.e., for different values of α), ranging from 0 to 7 cm at intervals of 0.1 cm. For sandy soil BR3, LST errors reaches values up to +1.3 K for drier atmospheres, and sample LW52 presents LST errors lower than +0.5 K independently of W. Overall results show that retrieving LST for pixels of a IBS at $\theta = 65°$, implies to make a systematic error between +0.4 and +1.3 K for an atmosphere with W values lower than 4 cm. For wet atmospheres ($W \geq 6$ cm), errors in LST are lower than +0.5 K for each IBS studied here, and for extremely wet atmospheres ($W \geq 7$ cm), errors can be considered not significant, taking values lower than +0.1 K for each IBS. In summary, drier atmospheres have the largest effect in LST

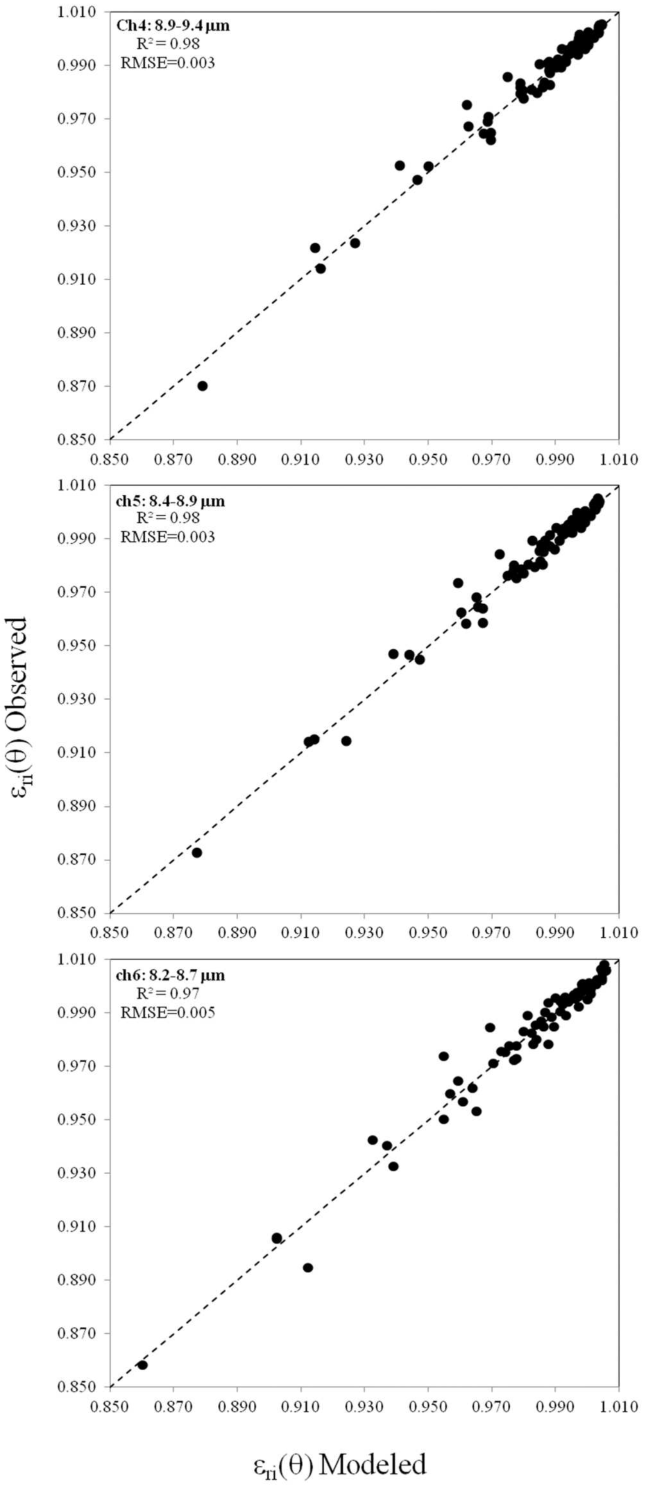

Figure 6. Self-validation of model represented by equation (10), comparing ε_{Π} values measured with those calculated from the model. The plots represent self-validation made at the three spectral channels: (top) Ch4 (8.9–9.4 μm), (middle) Ch5 (8.4–8.9 μm) and (bottom) Ch6 (8.2–8.7 μm), respectively. RMSE and R^2 values of the regression are also included in each plot.

Table 7. Averaged Emissivity Values of CE312-2 Channels 2 and 3 for the Twelve IBS Samples at Zenith Angles 0°, 40° and 65°[a]

	$\theta = 0°$		$\theta = 40°$		$\theta = 65°$			
Soil Code	ε	σ	ε	σ	ε	σ	$\Delta\varepsilon(40°)$	$\Delta\varepsilon(65°)$
B	0.945	0.000	0.939	0.004	0.926	0.006	0.005	0.018
BR1	0.962	0.003	0.960	0.004	0.948	0.007	0.002	0.014
E	0.968	0.003	0.965	0.005	0.956	0.007	0.003	0.012
C	0.970	0.002	0.969	0.004	0.958	0.007	0.001	0.012
LW45	0.959	0.001	0.955	0.004	0.942	0.006	0.003	0.016
LW03	0.969	0.001	0.964	0.004	0.951	0.007	0.006	0.019
LW 13	0.958	0.002	0.953	0.004	0.941	0.006	0.005	0.017
LW 52	0.955	0.002	0.951	0.004	0.947	0.006	0.004	0.009
D	0.960	0.002	0.959	0.004	0.945	0.006	0.001	0.015
F	0.950	0.002	0.946	0.004	0.936	0.006	0.004	0.014
BR2	0.980	0.009	0.979	0.010	0.965	0.011	0.001	0.015
BR3	0.990	0.010	0.983	0.011	0.962	0.012	0.006	0.027

[a] The right column of each averaged emissivity is the averaged emissivity error associated at both channels for a given θ. The last two columns are the difference of averaged emissivity at nadir and at zenith angles 40° and 65°, respectively.

retrieval accuracy, for a pixel observed at a large zenith angle, if it is ignored the angular effect of IBS emissivity.

5.2. Implications for Longwave Radiation Accuracy

[41] Another parameter that could be affected by the angular variation of the emissivity is the outgoing longwave radiation ($F^{\uparrow}$), which can be calculated as follows:

$$F^{\uparrow} = \varepsilon\sigma T^4 \tag{15}$$

where ε is the hemispherical emissivity value for the whole TIR range, σ is the Stefan-Boltzmann constant and T is the thermodynamic surface temperature. Usually ε is considered Lambertian and its value at nadir is taken as the hemispherical one, but the present work has shown that this value varies with the zenith angle. Ignoring this effect could lead to errors in retrieving $F^{\uparrow}$. For this reason we have evaluated

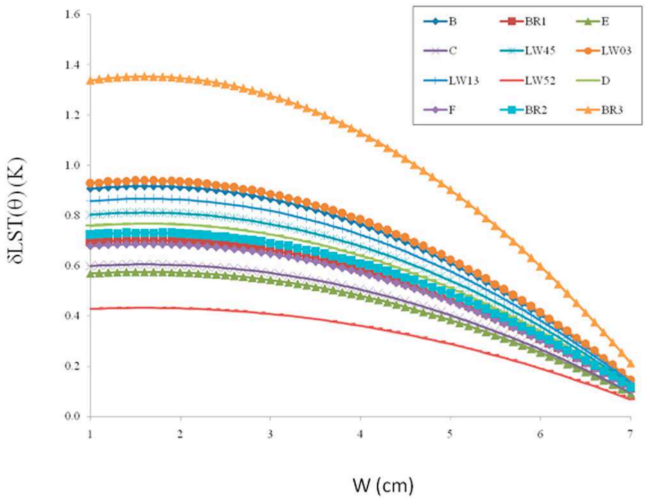

Figure 7. LST errors obtained applying split-window algorithm (equation (11)) for the twelve IBS if angular emissivity effect at θ = 65° is ignored. δLST(65°) values, calculated through equation (12), are represented for W values ranging from 0 to 7 cm at intervals of 0.1 cm.

Table 8. Sensitivity of $F^{\uparrow}$ to the Emissivity Angular Variation ($S_{F^{\uparrow}}(\Delta\varepsilon)$) Retrieved From Equation (16) for the Twelve IBS Studied[a]

IBS Sample	B	BR1	E	C	LW45	LW03	LW13	LW52	D	F	BR2	BR3
$\varepsilon_{7.7\text{–}14.3\mu m}$ (0°)	0.878	0.945	0.958	0.917	0.962	0.937	0.954	0.934	0.948	0.974	0.938	0.907
$\Delta\varepsilon$(0°–65°)	0.034	0.016	0.015	0.034	0.014	0.020	0.010	0.021	0.016	0.010	0.018	0.034
$S_{F\uparrow}(\Delta\varepsilon)$ (%)	8	3	3	7	3	4	2	5	3	2	4	8

[a]The table presents the values of nadir absolute emissivity in the spectral range 7.7–14.3 μm (first row), the difference of 7.7–14.3 μm emissivity between θ = 0° and θ = 65° (second row), and the relative sensitivity values of $F^{\uparrow}$ (third row).

this error studying the relative sensitivity of $F^{\uparrow}$ to the emissivity angular variation ($S_{F^{\uparrow}}(\Delta\varepsilon)$) following *Zhan et al.* [1996]:

$$S_{F^{\uparrow}}(\Delta\varepsilon) = \left|\frac{F_{-}^{\uparrow} - F_{+}^{\uparrow}}{F_{0}^{\uparrow}}\right| 100 \qquad (16)$$

where $\Delta\varepsilon$ is the difference of 7.7–14.3 μm emissivity between θ = 0° and θ = 65°, $F_0^{\uparrow}$ is the outgoing longwave radiation when the 7.7–14.3 μm emissivity value at nadir is introduced in (15), and $F_{-}^{\uparrow}$ and $F_{+}^{\uparrow}$ are the outgoing longwave radiation values when emissivity in (15) is decreased and increased by $\Delta\varepsilon$, respectively. Table 8 shows the values used to retrieve $S_{F^{\uparrow}}(\Delta\varepsilon)$ in each IBS sample. A fixed temperature value of 320 K was chosen in (15) for this sensitivity analysis.

[42] Results from Table 8 show that accuracy of $F^{\uparrow}$ can suffer variation between 2%–8%, depending on the type of IBS, which may lead to significant errors in the estimation of the different terms of the surface energy balance, as shown in the sensitivity analysis of the two-source models carried out by *Sánchez et al.* [2008]. Measurements of radiation made over surfaces at high viewing angles by TIR sensors onboard satellites, could probably be more affected by atmospheric attenuation or nonlinear effects in radiative transfer modeling, especially retrieving LST. But the present study has shown that ignoring angular effects of surface emissivity may lead also to significant errors in retrieving parameters such as LST or $F^{\uparrow}$, even if this parameter has a secondary role in the radiative transfer budget.

6. Conclusions

[43] Angular effects in TIR radiance measurements may have consequences for the retrieval of accurate LSTs or the outgoing longwave radiation, $F^{\uparrow}$, for instance. In the case of IBS, with organic matter content less than 9% and low roughness with a particle size between 0.2 and 1 cm, angular effects are mainly associated with the IBS emissivity. The present study measured the TIR emissivity of twelve different IBS samples, completely dry, and representative of a wide range of surface textures. Uncertainties associated to the methodology were lower than ±0.015 in the 98% of the cases and lower than ±0.01 in the 71% of cases, being the average value of ±0.009 and the standard deviation of ±0.003. So a threshold of ±0.01 was established to consider that the absolute emissivity of an IBS changes significantly with the observation angle respect to its nadir value.

[44] The emissivity of the analyzed samples presents a low azimuthal variation, and the zenithal emissivity change is also small for viewing angles lower than 40°, from which emissivity decreases significantly. The most influential factors in the decrease of emissivity are sand and quartz content. For all sensors operating within the spectral range 7.7–14.3 μm, emissivity of IBS with sand and quartz content larger than 80% change significantly at zenith angles larger than 60°, showing differences from the nadir value ranging from +0.011 to +0.101. In the specific spectral range 8–9.4 μm, this angular decrease of emissivity must be considered from zenith angles larger than 40°. On the other hand, clayey samples do not show significant decrease in emissivity with the increase of the zenith angle, in fact samples with a clay content ranging from 35% to 54%, and a sand content lower than 40%, present a negligible decrease in emissivity for zenith angles lower than 70°.

[45] Results also showed that the decrease of emissivity with increasing viewing angles can be considered independent of textural and mineralogical IBS composition at the broadband 7.7–14.3 μm, and at the spectral channels within 10–12 μm. This work established a single zenith-dependent relationship for these spectral ranges between relative-to-nadir emissivity and zenith viewing angle with a maximum uncertainty of ±0.009. However, in the spectral domain 8–9.4 μm, the decrease of emissivity is also dependent on IBS textural composition. A principal component analysis showed that sand and clay are the most influential factors, explaining a 90% of the variance. Sand is the main factor responsible to make the IBS emissivity decreases with the increase of θ, on the other hand emissivity of clayey soils remains almost constant with zenithal variation. It was possible to establish a relationship of relative-to-nadir emissivity as function of sand and clay percentage for an IBS, in which coefficients are zenithal-dependent quadratic polynomials. This relationship allows retrieving a relative-to-nadir emissivity value with a maximum error of ±0.01. The absolute emissivity value can be obtained later by multiplying the relative-to-nadir value by the absolute emissivity value at nadir, which can be retrieved using different methods.

[46] Finally, the impact of ignoring angular effects of emissivity on parameters such as LST or $F^{\uparrow}$ from satellite data was assessed. LST retrievals using an emissivity-dependent split-window algorithm applied to MODIS thermal bands 31 and 32, showed that for pixels measured at zenith angles larger than 65°, ignoring the angular dependence of emissivity could produce systematic errors on LST ranging from +0.4 K to +1.3 K, depending on the type of soil and for atmospheres with a water vapor content lower than 4 cm. Accuracy of $F^{\uparrow}$ retrieved from satellite can suffer variation between ±2%–±8%, depending on the type of IBS if the zenithal decrease of the TIR emissivity is not taken into account in the final hemispherical value of the emissivity. These inaccuracies in $F^{\uparrow}$ may lead to significant errors in the estimation of the different terms of the surface energy balance. TIR radiance measurements made over surfaces at high viewing angles could probably be more affected by atmospheric attenuation or nonlinear effects in radiative transfer

modeling. But ignoring angular effects of surface emissivity may lead to inaccuracies retrieving parameters such as LST or $F^{\uparrow}$, even if this parameter has a secondary role in the radiative transfer budget.

[47] Although most current moderate-resolution operational TIR instruments have at-satellite view angles up to 55 degrees, the view angle relative to the vertical at surface level (that is what actually is being measured in this study) might be larger depending on surface orientation and considering Earth's curvature, and in that case the emissivity angular effect could be significant as shown by the obtained measurements. It will be even more critical to account for this effect in future TIR instruments as long as their spatial resolutions are improved (for instance the HyspIRI mission will have a spatial resolution of 60 m [*Roberts et al.*, 2012]). The angular effects on soil emissivity may also be important for high spatial resolution instruments onboard airplanes, or also for field radiometers deployed viewing the surface with large observation angles. The results obtained in the present work will contribute to improve the accuracy and understanding of the measurements carried out by these range of instruments.

[48] **Acknowledgments.** This work was possible with the finance of the Spanish *Ministerio de Ciencia e Innovación* (grant of V. García-Santos associated to project CGL2007-64666/CLI) and projects CGL2007-29819-E/CLI and CGL2010-17577/CL, cofinanced by FEDER funds, and the financial support of the *Conselleria d'Educació de la Generalitat Valenciana* (project PROMETEO/2009/086). The authors want to thank Juan Manuel Sánchez at the University of Castilla La Mancha for his comments and suggestions made in the present work on the effect of angular emissivity in the accuracy retrieving the outgoing longwave radiation. Useful comments and suggestions made by three anonymous reviewers are also acknowledged.

References

Aminou, D. M. A., B. Jacquet, and F. Pasternak (1997), Characteristics of the Meteosat Second Generation Radiometer/Imager: SEVIRI, *Proc. SPIE Int. Soc. Opt. Eng.*, *3221*, 19–31, doi:10.1117/12.298084.

Ball, M., and H. Pinkerton (2006), Factors affecting the accuracy of thermal imaging cameras in volcanology, *J. Geophys. Res.*, *111*, B11203, doi:10.1029/2005JB003829.

Barnes, W. L., T. S. Pagano, and V. V. Salomonson (1998), Prelaunch characteristics of the moderate resolution imaging spectroradiometer (MODIS) on EOS-AM1, *IEEE Trans. Geosci. Remote Sens.*, *36*(4), 1088–1100.

Barton, I. J., and T. Takashima (1986), An AVHRR investigation of surface emissivity near Lake Eyre, Australia, *Remote Sens. Environ.*, *20*(2), 153–163, doi:10.1016/0034-4257(86)90020-9.

Becker, F., P. Ramanantsizehena, and M. P. Stoll (1985), Angular variation of the bidirectional reflectance of bare soils in the thermal infrared band, *Appl. Opt.*, *24*(3), 365–375, doi:10.1364/AO.24.000365.

Brogniez, G., C. Pietras, M. Legrand, P. Dubuisson, and M. Haeffelin (2003), A high-accuracy multiwavelength radiometer for in situ measurements in the thermal infrared. Part II: Behavior in field experiments, *J. Atmos. Oceanic Technol.*, *20*(7), 1023–1033, doi:10.1175/1520-0426(2003)20<1023:AHMRFI>2.0.CO;2.

Caselles, E., E. Valor, F. J. Abad, and V. Caselles (2012), Automatic classification-based generation of thermal infrared land surface emissivity maps using AATSR data over Europe, *Remote Sens. Environ.*, *124*, 321–333, doi:10.1016/j.rse.2012.05.024.

Chehbouni, A., Y. Nouvellon, Y. H. Kerr, M. S. Moran, C. Watts, L. Prevot, D. C. Goodrich, and S. Rambal (2001), Directional effect on radiative surface temperature measurements over a semiarid grassland site, *Remote Sens. Environ.*, *76*(3), 360–372, doi:10.1016/S0034-4257(01)00183-3.

Cuenca, J., and J. A. Sobrino (2004), Experimental measurements for studying angular and spectral variation of thermal infrared emissivity, *Appl. Opt.*, *43*, 4598–4602, doi:10.1364/AO.43.004598.

Dozier, J., and S. Warren (1982), Effect of viewing angle on the infrared brightness temperature of snow, *Water Resour. Res.*, *18*(5), 1424–1434, doi:10.1029/WR018i005p01424.

Field, A. (2009), *Discovering Statistics Using SPSS*, 3rd ed., SAGE, Thousand Oaks, Calif.

Galve, J. M., C. Coll, V. Caselles, and E. Valor (2008), An atmospheric radiosounding database for generating land surface temperature algorithms, *IEEE Trans. Geosci. Remote Sens.*, *46*(5), 1547–1557, doi:10.1109/TGRS.2008.916084.

García-Santos, V., E. Valor, V. Caselles, M. Mira, J. M. Galve, and C. Coll (2012), Evaluation of different methods to retrieve the hemispherical downwelling irradiance in the thermal infrared region for field measurements, *IEEE Trans. Geosci. Remote Sens.*, doi:10.1109/TGRS.2012.2209891, in press.

Gillespie, A., S. Rokugawa, T. Matsunaga, J. S. Cothern, S. Hook, and A. B. Kahle (1998), A temperature and emissivity separation algorithm for Advanced Spaceborne Thermal Emission and Reflection Radiometer (ASTER) images, *IEEE Trans. Geosci. Remote Sens.*, *36*(4), 1113–1126, doi:10.1109/36.700995.

Goodrum, G., K. B. Kidwell, and W. Winston (2001), *NOAA KLM User's Guide*, NOAA, Silver Spring, Md.

Hori, M., et al. (2006), In-situ measured spectral directional emissivity of snow and ice in the 8–14 μm atmospheric window, *Remote Sens. Environ.*, *100*(4), 486–502, doi:10.1016/j.rse.2005.11.001.

International Organization for Standardization (2002), Soil quality. Determination of particle size distribution in mineral soil material, Method by sieving and sedimentation, *Rep. ISO 11277:1998/TC190*, 30 pp., Geneva, Switzerland.

Kondratyev, K. Y. (1969), *Radiation in the Atmosphere*, Academic, New York.

Labed, J., and M. P. Stoll (1991), Angular variation of land surface spectral emissivity in the thermal infrared: Laboratory investigations on bare soils, *Int. J. Remote Sens.*, *12*, 2299–2310, doi:10.1080/01431169108955259.

Lagouarde, J. P., Y. H. Kerr, and Y. Brunet (1995), An experimental study of angular effects on surface temperature for various plant canopies and bare soils, *Agric. For. Meteorol.*, *77*(3–4), 167–190, doi:10.1016/0168-1923(95)02260-5.

Lagouarde, J. P., H. Ballans, P. Moreau, D. Guyon, and D. Coraboeuf (2000), Experimental study of brightness surface temperature angular variations of maritime pine (*Pinus pinaster*) stands, *Remote Sens. Environ.*, *72*(1), 17–34, doi:10.1016/S0034-4257(99)00085-1.

Lagouarde, J. P., P. Moreau, M. Irvine, J. M. Bonnefond, J. A. Voogt, and F. Solliec (2004), Airborne experimental measurements of the angular variations in surface temperature over urban areas: Case study of Marseille (France), *Remote Sens. Environ.*, *93*(4), 443–462, doi:10.1016/j.rse.2003.12.011.

Llewellyn-Jones, D., M. C. Edwards, C. T. Mutlow, A. R. Birks, I. J. Barton, and H. Tait (2001), AATSR: Global-change and surface temperature measurements from ENVISAT, *ESA Bull.*, *105*, 11–21.

McAtee, B. K., A. J. Prata, and M. J. Lynch (2003), The angular behavior of emitted thermal infrared radiation (8–12 μm) at a semiarid site, *J. Appl. Meteorol.*, *42*, 1060–1071, doi:10.1175/1520-0450(2003)042<1060:TABOET>2.0.CO;2.

Mira, M., E. Valor, R. Boluda, V. Caselles, and C. Coll (2007), Influence of soil water content on the thermal infrared emissivity of bare soils: Implication for land surface temperature determination, *J. Geophys. Res.*, *112*, F04003, doi:10.1029/2007JF000749.

Mira, M., T. J. Schmugge, E. Valor, V. Caselles, and C. Coll (2009), Comparison of thermal infrared emissivities retrieved with the two-lid box and the TES methods with laboratory spectra, *IEEE Trans. Geosci. Remote Sens.*, *47*(4), 1012–1021, doi:10.1109/TGRS.2008.2008901.

Mira, M., E. Valor, V. Caselles, E. Rubio, C. Coll, J. M. Galve, R. Niclos, J. M. Sánchez, and R. Boluda (2010), Soil moisture effect on thermal infrared (8–13-μm) emissivity, *IEEE Trans. Geosci. Remote Sens.*, *48*(5), 2251–2260, doi:10.1109/TGRS.2009.2039143.

Niclòs, R., E. Valor, V. Caselles, C. Coll, and J. M. Sánchez (2005), In situ angular measurements of thermal infrared sea surface emissivity-Validation of models, *Remote Sens. Environ.*, *94*(1), 83–93, doi:10.1016/j.rse.2004.09.002.

Niclòs, R., V. Caselles, C. Coll, and E. Valor (2007), Determination of sea surface temperature at large observation angles using an angular and emissivity-dependent split-window equation, *Remote Sens. Environ.*, *111*(1), 107–121, doi:10.1016/j.rse.2007.03.014.

Nicodemus, F. E. (1965), Directional reflectance and emissivity of an opaque surface, *Appl. Opt.*, *4*, 767–773, doi:10.1364/AO.4.000767.

Nicodemus, F. E., J. C. Richmond, J. J. Hsia, I. W. Ginsberg, and T. Limperis (1977), Geometrical considerations of nomenclature for reflectance, *Natl. Bur. Stand. Monogr. 160*, 52 pp., U.S. Dep. of Commerce, Washington, D. C.

Norman, J. M., and F. Becker (1995), Terminology in thermal infrared remote sensing of natural surfaces, *Agric. For. Meteorol.*, *77*(3–4), 153–166, doi:10.1016/0168-1923(95)02259-Z.

Ogawa, K., T. Schmugge, and S. Rokugawa (2006), Observations of the dependence of the thermal infrared emissivity on soil moisture, *Geophys. Res. Abstr.*, *8*, 04996.

Rees, W. G., and S. P. James (1992), Angular variation of the infrared emissivity of ice and water sea surfaces, *Int. J. Remote Sens.*, *13*, 2873–2886, doi:10.1080/01431169208904088.

Roberts, D. A., D. A. Quattrochi, G. C. Hulley, S. J. Hook, and R. O. Green (2012), Synergies between VSWIR and TIR data for the urban environment: An evaluation of the potential for the Hyperspectral Infrared Imager (HyspIRI) Decadal Survey mission, *Remote Sens. Environ.*, *117*, 83–101, doi:10.1016/j.rse.2011.07.021.

Rubio, E., V. Caselles, and C. Badenas (1997), Emissivity measurements of several soils and vegetation types in the 8–14 μm wave band, *Remote Sens. Environ.*, *59*, 490–521, doi:10.1016/S0034-4257(96)00123-X.

Salisbury, J. W., and D. M. D'Aria (1992), Infrared (8–14 μm) remote sensing of soil particle size, *Remote Sens. Environ.*, *42*, 157–165, doi:10.1016/0034-4257(92)90099-6.

Sánchez, J. M., W. P. Kustas, V. Caselles, and M. C. Anderson (2008), Modelling surface energy fluxes over maize using a two source patch model and radiometric soil and canopy temperature observations, *Remote Sens. Environ.*, *112*, 1130–1143, doi:10.1016/j.rse.2007.07.018.

Singh, D., and A. Kathpalia (2007), An efficient modeling with GA approach to retrieve soil texture, moisture and roughness from ERS-2 SAR data, *Prog. Electromagn. Res.*, *77*, 121–136, doi:10.2528/PIER07071803.

Snyder, W. C., Z. Wan, Y. Zhang, and Y. Z. Feng (1997), Thermal infrared (3–14 μm) bidirectional reflectance measurements of sands and soils, *Remote Sens. Environ.*, *60*(1), 101–109, doi:10.1016/S0034-4257(96)00166-6.

Snyder, W. C., Z. Wan, Y. Zhang, and Y. Z. Feng (1998), Classification-based emissivity for land surface temperature measurement from space, *Int. J. Remote Sens.*, *19*, 2753–2774, doi:10.1080/014311698214497.

Sobrino, J. A., and J. Cuenca (1999), Angular variation of thermal infrared emissivity for some natural surfaces from experimental measurements, *Appl. Opt.*, *38*, 3931–3936, doi:10.1364/AO.38.003931.

Takashima, T., and K. Masuda (1987), Emissivities of quartz and Sahara dust powders in the infrared region (7–17 μ), *Remote Sens. Environ.*, *23*(1), 51–63, doi:10.1016/0034-4257(87)90070-8.

Theocharous, E., and N. P. Fox (2010), CEOS comparison of IR brightness temperature measurements in support of satellite validation. Part II: Laboratory comparison of the brightness temperature of blackbodies, *NPL Rep. OP4*, Natl. Phys. Lab., Teddington, U. K.

Trigo, I. F., L. F. Peres, C. C. DaCamara, and S. C. Freitas (2008), Thermal land surface emissivity retrieved from SEVIRI/Meteosat, *IEEE Trans. Geosci. Remote Sens.*, *46*, 307–315, doi:10.1109/TGRS.2007.905197.

Wen, J., Z. Su, and Y. Ma (2003), Determination of land surface temperature and soil moisture from Tropical Rainfall Measuring Mission/Microwave Imager remote sensing data, *J. Geophys. Res.*, *108*(D2), 4038, doi:10.1029/2002JD002176.

Yi, S., et al. (2009), Interactions between soil thermal and hydrological dynamics in the response of Alaska ecosystems to fire disturbance, *J. Geophys. Res.*, *114*, G02015, doi:10.1029/2008JG000841.

Zhan, X., W. P. Kustas, and K. S. Humes (1996), An intercomparison study on models of sensible heat flux over partial canopy surfaces with remotely sensed surface temperature, *Remote Sens. Environ.*, *58*, 242–256, doi:10.1016/S0034-4257(96)00049-1.

Appendix D

“Impact of soil moisture on the angular variation of thermal infrared emissivity of inorganic soils”

Next study is now under reviewing process in *IEEE Geoscience and Remote Sensing Letters*. This Journal has an *Impact Factor* of **1.823**, occupying the position 8 of the 27 journals in *Remote Sensing* category according to *ISI-Journal of Citation Reports Science Edition 2012*.

Effect of Soil Moisture on the Angular Variation of Thermal Infrared Emissivity of Inorganic Soils

Vicente García-Santos, Enric Valor, Vicente Caselles, César Coll and Mª Ángeles Burgos

Departament of Earth Physics and Thermodynamics, Faculty of Physics, University of Valencia, 46100, Burjassot, Valencia, Spain

ABSTRACT

Emissivity is influenced by different factors, the present study deals with the effect of the soil moisture (SM) content on the zenithal (θ) variation of ratio-to-nadir emissivity (ε_r), for a wide variety of inorganic bare soils. To retrieve ε_r a goniometer assembly was used, together with two identical CIMEL CE312-2 radiometers working at six spectral bands within 7.7-14.3 μm, performing simultaneous radiance measurements at different combinations of zenith and azimuth angles. Results showed that the effect of SM upon $\varepsilon_r(\theta)$ is different depending on the spectral range and textural composition of the sample. Sandy soils showed a decrease of $\varepsilon_r(\theta)$ from nadir of 0.132 for $\theta \geq 40°$ at 8-9.4 μm under dry conditions, but this decrease was reduced to 0.093 with the increase of SM. Clayey samples did not present dependence of $\varepsilon_r(\theta)$ with SM. Loamy texture samples presented a more sharply decrease of $\varepsilon_r(\theta)$ with the increase of SM, reaching differences between nadir values and 70° up to 6%, at all spectral ranges studied. Finally, a parameterization of ε_r with SM and θ was derived allowing to obtain ratio-to-nadir emissivities with an accuracy of ±0.011.

Index Terms: Angular emissivity, bare soil, remote sensing, soil moisture, thermal infrared.

I. INTRODUCTION

Emissivity (ε) is a characteristic property of natural land surfaces that is coupled with land surface temperature (LST) in a radiance measurement in the thermal infrared (TIR) spectral domain. LST plays a key role in numerous geophysical processes such as long-wave surface energy fluxes in the atmosphere-surface interface, for instance. For this reason, a good knowledge of surface thermal emissivity and its influencing physical variables are needed. Factors such as soil composition and texture [1], soil moisture (SM) [2] or viewing geometry [3] must be taken into account when analyzing satellite TIR data, since their influence on ε is significant.

Recently, the effects of SM and viewing geometry on thermal ε for a wide variety of inorganic bare soils (IBS) with different texture, have been analyzed separately [2-3]. Regarding SM, it was observed in general an increase of ε with SM that was more notable for sandy soils, and in the 8-9 μm spectral range [2]. In relation to the angular variation of ε, results from [3] showed that ε of dry IBS is almost azimuthally isotropic, and decreases in the zenithal direction beyond 40°, with the maximum variation observed on sandy soils rich in quartz and within 8-9.4 μm.

The main objective of the present paper is to study the effect produced by SM on the anisotropy of thermal ε, extending the results obtained in the study carried out in a previous work [3], by combining the effect of SM and viewing angle for the same samples. In section II, IBS samples and instrumentation are presented together with the methodology followed to measure the radiance at different angles, and SM measurements.

Section III shows the retrievals of ratio-to-nadir band emissivity (ε_r) for different viewing angles and SM values at each IBS, and the results obtained are discussed. Section IV uses these results to retrieve an empirical regression of the ratio-to-nadir emissivity for any IBS as a function of SM and θ. Finally, conclusions are presented in section V.

II. EXPERIMENTAL SETUP

Twelve IBS samples were chosen to evaluate the variation of TIR ε_r with SM and viewing angles according to different soil texture. Table I lists the textural and mineralogical features for the IBS selected to carry out the study.

INSERT TABLE I

Radiances were taken with a multispectral thermal radiometer CIMEL Electronique model CE312-2 [4], working in six different spectral bands: 7.7-14.3 μm (channel 1), 8.2-8.7 μm (channel 6), 8.4-8.9 μm (channel 5), 8.9-9.4 μm (channel 4), 10.1-11.1 μm (channel 3) and 10.9-11.9 μm (channel 2) with an uncertainty temperature of ± 0.03 K, ± 0.02 K, ± 0.03 K, ± 0.018 K, ± 0.03 K and ± 0.02 K, for channels 1 to 6 respectively, obtained after comparison with temperatures from a reference blackbody whose values presented a maximum bias of -0.19 K with regard to a reference transfer radiometer. Ratio-to-nadir was retrieved taking two simultaneous radiance measurements, one at nadir and another at an arbitrary angular configuration (θ,φ), by means of equation:

$$\varepsilon_{ri}(\theta,\varphi)=\frac{\varepsilon_i(\theta,\varphi)}{\varepsilon_i(0,0)}=\frac{L_i(\theta,\varphi)-L_i^{\downarrow}}{L_i(0,0)-L_i^{\downarrow}} \qquad (1)$$

where $L_i^{\downarrow}$ is the spectral hemispherical downwelling radiance, measured by means of a gold diffuse reflectance panel ([3], [5]), which was placed inside the FOV of CE1 at 0°. The time interval between two consecutive panel measurements was less than 18 minutes. Given that Eq. (1) is the quotient between absolute emissivity from an angular configuration and nadir, a previous knowledge of absolute emissivity at nadir allows estimation of the absolute value of emissivity in that specific angular configuration.

To retrieve ε_r values, radiance measurements over the sample were taken simultaneously using a goniometer in which the two CE312-2 radiometers were placed (see Figure 1), one at nadir (CE1), and the second one in a specific direction (θ,φ) (CE2). The latter radiometer could be moved along the arm of the goniometer varying the field of view over the sample, in order to measure the same area as the nadir radiometer. Radiance measurements were taken at different combinations of zenith and azimuth angles. Zenith angles were considered from θ=10° to θ=70° at intervals of 10°. For each zenith angle, the IBS emissivity was measured at three different azimuthal orientations turning the samples 120° each time. Azimuthal rotation was repeated two more times for each zenith angle.

Each IBS samples was placed in a circular container 52 cm in diameter and 10 cm height (Fig.1) which had multiple holes in its bottom, designed for allowing the water drainage. Moreover, a sieve was attached to the bottom (between holes and sample) to avoid the loss of the finest particles. Samples were flooded allowing filtration through the container and straightaway freely air dried.

Radiance measurement process started with a completely dry sample and they were performed at several times during the drying process, after saturation, so the ratio-to-nadir band emissivity could be measured at different SM levels. If soil cracks appeared during the drying process, they were removed when possible. The sequence of soil saturation and drying was repeated one more time in order to check the validity and reproducibility of the results.

Volumetric SM content from moist IBS samples, was retrieved with a Delta-T SM200 sensor which has a calibration uncertainty of ±0.03 $m^3 \cdot m^{-3}$. SM was measured puncturing the rods (5 cm long) of the SM200, at different points of the IBS surface. SM measurements were taken before and after each set of radiance measurements, in order to check possible spatial and temporal variations of SM in the sample. Standard deviation of all these SM measurements was always lower than ±0.03 $m^3 \cdot m^{-3}$.

III. RESULTS AND DISCUSSIONS

The uncertainty in the ratio-to-nadir band emissivity, $\delta\varepsilon_{ri}(SM,\theta,\varphi)$, associated to a specific angular direction (θ, φ) was chosen as the maximum of three values: (i) average of the three values obtained for a single (θ, φ) configuration, which were calculated by applying error propagation to Eq. (1) with radiance uncertainties given by the radiometer calibration errors; (ii) standard deviation of these three ε_{ri} values; (iii) difference between maximum and minimum values of ε_{ri} at specific (θ, φ), divided by four. Results showed that 97% of $\delta\varepsilon_{ri}(SM,\theta, \varphi)$ ranged from ±0.001 to ±0.010. The azimuthal dependence of ε_{ri} in all cases was less than the maximum emissivity error (±0.010), concluding that ε_{ri} of an IBS can be retrieved, regardless the φ angle, with a maximum uncertainty of ±0.010, for a specific θ and SM content. The emissivity variation was more significant in terms of zenith angle and SM content. Figure 2 show the ratio-to-nadir emissivity variation with SM for different zenith angles, at channels 1 (7.7-14.3 μm), 3 (10.1-11.1 μm) and 5 (8.4-8.9 μm) of CE312-2, and for the samples: B (representative of sandy samples BR3, WS and LW03), F (representative of loamy textures samples BR2, LW13, D and C), BR1 and LW45 (as unique clayey and sitly samples, respectively), to summarize the observed behavior in all samples. Conclusions driven from channel 3 data can be extended to channel 2 (10.9-11.9 μm), and from band 5 to channels 4 (8.9-9.4 μm) and 6 (8.2-8.7 μm).

INSERT FIGURE 2

Results show that angular effect of SM on $\varepsilon_{ri}(\theta)$ exhibits different behavior as a function of the spectral range and textural composition of the sample. Sandy soils show significant decreases of $\varepsilon_{ri}(SM,\theta)$ at 8-9.4 μm for $\theta \geq 30°$, independently of SM. Under dry conditions, $\varepsilon_{ri}(SM, \theta)$ presents maximum decreases for sandy soils from nadir ranging between 0.021 (at θ=30°) to 0.132 (at θ=70°), for sample B at SM=0.04 $m^3 \cdot m^{-3}$. $\varepsilon_{ri}(SM, \theta)$ of sandy soils decrease from nadir in a less notable way under wet conditions, but it is still significant for $\theta \geq 30°$, ranging between 0.019 (at θ=30°) to 0.093 (at θ=70°), for sample B at SM=0.28 $m^3 \cdot m^{-3}$. It is possible that increasing soil water content results in a decrease of the spectral contrast of emissivity, because water is strongly absorbing in the region of the quartz reststrahlen bands [1], thus reducing the effect of quartz. Sample WS presents abundant content of gypsum (99%), which has a weak absorption in the spectral region 8-9 μm [6], so it is expected that water content acts with gypsum similarly than with quartz at the reststrahlen bands. The decrease of ε_{ri} with θ remains constant at spectral range 10-12 μm, regardless of water content in the soil, being significant only for $\theta \geq 60°$. This decrease has an average value of 0.012 at θ=60°, and 0.019 at θ=70°. Finally, ε_{ri} of sandy soils (B, WS, BR3 and LW03) at broad spectral range 7.7-14.3 μm also shows constant decrease with θ independently of SM, but at this spectral range ε_{ri} decreases significantly for $\theta \geq 50°$, with an average decrease of 0.012 for θ=50°, 0.019 (θ=60°) and 0.029 (θ=70°).

Clayey IBS BR1 shows a decrease of ε_r with θ nearly independent on both SM and the spectral ranges studied, being significant for $\theta \geq 50°$, with a maximum decrease of ε_r (under dry conditions) of 0.013 for θ=50°, 0.014 (θ=60°) and 0.016 (θ=70°).

Soil LW45 shows a similar behavior on $\varepsilon_{ri}(SM,\theta)$ as sandy soils, probably because the presence of high quartz content in its sand percentage. At 8-9.4 μm and under dry conditions, significant decrease of $\varepsilon_{ri}(SM,\theta)$ from nadir, begins at θ=40° ranging from 0.011(θ=40°) to 0.059 (θ=70°). For high SM values, decrease of $\varepsilon_{ri}(SM,\theta)$ from nadir is significant for $\theta \geq 50°$, ranging between 0.011 (θ=50°) and 0.036 (θ=70°). At spectral ranges 10-12 μm and 7.7-14.3 μm, decrease of ε_{ri} from nadir is independent on SM content, reaching significant differences of 0.014 and 0.017 (at θ=60°) and 0.023 and 0.028 (at θ=70°), respectively.

For the rest of IBS samples with loamy textures (BR2, LW13, F, D and C), the observed behavior is opposite to that of sandy soils, ε_{ri} decreases with θ more sharply with the increase of water content. Our results agreed with those of [3] under dry conditions, but the decrease of ε_{ri} with θ is more notable with the increase of SM, being significant at all spectral ranges for $\theta \geq 50°$. ε_{ri} has an average decrease respect to nadir of 0.013 (θ=50°), 0.020(θ=60°) and 0.035 (θ=70°), at all spectral ranges studied when IBS is saturated.

It is known that emissivity of water decreases with θ more than 7% from its nadir value [7]. Given the presence of OM content in those IBSs, which is the principal storage of plant available water due to the high percentage of water-stable aggregates, water content retained by these samples is usually greater than for sandy soils, so angular behavior of water emissivity probably influenced the decrease of ε_{ri} with θ for high SM contents at spectral ranges 8-9.4 μm, 10-12 μm and broadband range 7.7-14.3 μm.

IV. PARAMETERIZATION OF ε_{ri}(SM, θ)

A parameterization of ε_{ri} varying simultaneously with SM and θ was derived from all measurements. The IBS samples were split into two groups. The first one was composed of seven samples (WS, B, F, LW45, C, D and BR1) representing the full ranges of textural and mineralogical parameters, as well as OM. Data of this first group of samples were used to set up the parameterization. The other IBS samples (BR3, LW03, BR2, LW13 and LW52) were used to validate the parameterization model obtained from the first group.

The model that best fits the measurements is:

$$\varepsilon_{ri}(SM,\theta) = a_i + b_i\,SM + c_i\theta + d_i SM^2 + e_i\,SM\theta + f_i\theta^2 \tag{2}$$

where variance of coefficients a_i - f_i in (2) were evaluated, using statistical factor analysis, for all data available in Table I following the procedure used in [3].

The coefficients a_i - f_i are dependent on clay and quartz content at the spectral range 8-9.4 μm (CE 312-2 channels 4, 5 and 6) by means of the equation:

$$a - f_{8-9.4\,\mu m}(C,Q) = p_0 + p_1 Q + p_2 C + p_3\,CQ + p_4 C^2 \tag{3}$$

where p_0-p_5 are coefficients of the polynomial given in equation (3), whose values can be found in Table II, C and Q are the percentages of clay and quartz, respectively.

Coefficients a_i - f_i at spectral range 10-12 μm (CE312-2 channels 2 and 3) were found to be dependent on clay and OM content, following:

$$a - f_{10-12\ \mu m}(C, OM) = p_0 + p_1 OM + p_2 C + p_3 COM + p_4 C^2 \qquad (4)$$

For the broad range 7.7-14.3 μm (CE312-2 channel 1), coefficients *a*, *b* and *d* were dependent on clay and quartz contents, following equation (3), while coefficients *c*, *e* and *f* showed dependence on clay and OM, following Eq. (4). Table II summarizes the values for coefficients p_0-p_5 of (3) and (4) at all six spectral ranges; statistics R^2 and RMSE are also included.

INSERT TABLE II

Figure 3 shows the comparison between the observed ε_{ri}(SM, θ) values measured for the IBS samples BR3, LW03, BR2, LW13 and LW5 and those values modeled for the same samples using expressions (2), (3) and (4) at the three considered spectral ranges (see section III) Comparison was made for $\theta \geq 30°$, since at this zenith angle a decrease of ε_{ri} from nadir greater than 0.01 is observed. Results showed R^2 ranging between 0.65 and 0.84, and RMSE ranging between ±0.005 and ±0.011.

Estimation of clay, OM and quartz contents needed for equations (2)-(4) from remote sensing data was discussed in the works [2-3]. Another possibility is the previous knowledge of clay, quartz and OM contents from ancillary data. In these cases the parameterizations given in expressions (2), (3) and (4), depending on spectral channel, could be applied to classification-based emissivity mapping, such as the one used in MODIS, SEVIRI, or more recently AATSR data, in order to refine their algorithms. In relation to the SM estimations for equation (2), they could be obtained from recent sensors such as the Microwave Imaging Radiometer by Aperture Synthesis (MIRAS) aboard the Soil Moisture and Ocean Salinity (SMOS) mission [8], or the Advanced Microwave Scanning Radiometer (AMSR-E) on board the EOS-Aqua platform [9], with spatial resolutions of 40 km (SMOS) and 56 km (AMSR-E), and expected accuracies of ±0.04 $m^3 \cdot m^{-3}$.

CONCLUSIONS

Angular effects of emissivity under controlled SM contents were assessed for a wide variety of IBS according their textural classification. Ratio-to-nadir emissivity values were retrieved taking two simultaneous radiance measurements, one at nadir and another one at an angular direction (θ,φ), with a maximum uncertainty of ±0.01. Results showed that the effect of SM on $\varepsilon_{ri}(SM,\theta)$ exhibits three different behaviors as a function of the spectral range and textural composition of the sample. For sandy soils (B, BR3, WS and LW03) and the silty soil LW45, ε_{ri} decreases significantly with θ under dry conditions reaching differences up to 0.132 (sample B, θ=70°) from nadir values, but decreasing of $\varepsilon_{ri}(SM,\theta)$ with zenith angle is less notable when SM increases. It could be explained with the increase of water content in the soil, which results in a decrease of the spectral contrast of emissivity, because water is strongly absorbing in the region of the quartz retstrahlen bands. It is expected that water content interacts with gypsum (sample WS) similarly as quartz at reststrahlen bands. At spectral ranges 7.7-14.3 μm and 10-12 μm, decrease of $\varepsilon_{ri}(SM,\theta)$ with zenith angle for sandy soils is significant for $\theta \geq 50°$; however it is independent on water content. Clayey IBS showed an almost constant fall of ε_r with θ at all spectral ranges studied, regardless the SM content, being the decreases of ε_r with θ significant for observation angles greater than 50°. Finally loamy IBS samples presented an opposite behavior to that of sandy soils, ε_{ri} decreasing with θ more sharply with the increase of SM at all six spectral ranges studied and reaching differences from 0.011 for dry soils to 0.035 under saturated conditions.

In summary, the effect of SM on $\varepsilon_{ri}(SM,\theta)$ reduces its angular contrast under dry conditions up to 0.07 when sandy soil is saturated (because sandy soils are very poor water retainers) and counteracting the quartz and gypsum reststrahlen effects at 8-9.4 μm. On the other hand, SM makes the decrease of $\varepsilon_{ri}(SM,\theta)$ with θ more noticeable for loamy soils (which are very good water retainers due the presence of OM) because the decrease of water emissivity with observation angle, that may reach differences from its nadir value up to 0.04 at $\theta=70°$.

Finally, a parameterization of ε_r with SM and θ was obtained allowing to obtain ε_r with a maximum accuracy of ±0.011, by means of a quadratic-polynomial whose coefficients are dependent on percentages of clay and quartz and OM content at spectral range 8-9.4 μm, 10-12 μm and 7.7-14.3 μm.

Acknowledgments. This work was possible with the finance of the Spanish Ministerio de Ciencia e Innovación (grant of V. García-Santos associated to project CGL2007-

64666/CLI) and projects CGL2007-29819-E/ CLI and CGL2010-17577/CL, cofinanced by FEDER funds, and the financial support of the Conselleria d’Educació de la Generalitat Valenciana (project PROMETEO/2009/086). The ESA CAT-1 project SMOS AO-4748 is also acknowledged.

REFERENCES

[1] J. W. Salisbury and D. M. D’Aria, “Infrared (8–14 mm) remote sensing of soil particle size”, *Remote Sens. Environ.*, vol. 42, pp. 157–165, 1992.

[2] M. Mira, E. Valor, V. Caselles, E. Rubio, C. Coll, J. M. Galve, R. Niclos, J.M. Sánchez, and R. Boluda, “Soil Moisture Effect on Thermal Infrared (8–13-µm) Emissivity”, *IEEE Trans. Geosci. Remote Sens.*, vol. 48, no. 5, pp. 2251-2260, 2010, doi:10.1109/TGRS.2009.2039143.

[3] V. García-Santos, E. Valor, V. Caselles, M.A. Burgos and C. Coll, “On the angular variation of thermal infrared emissivity of inorganic soils”, *J. Geophys. Res.*, vol. 117 (D19116), 2012, doi:10.1029/2012JD017931.

[4] G. Brogniez, C. Pietras, M. Legrand, P. Dubuisson, and M. Haeffelin, “A high-accuracy multiwavelength radiometer for in situ measurements in the thermal infrared. Part II: Behavior in field experiments”, *J. Atmos. Ocean Technol.*, vol. 20, no. 7, pp. 1023–1033, 2003, http://dx.doi.org/10.1175/15200426(2003)20<1023:AHMRFI>2.0.CO;2.

[5] V. García-Santos, E. Valor, V. Caselles, M. Mira, J. M. Galve and C. Coll, “Evaluation of different methods to retrieve the hemispherical downwelling irradiance in the thermal infrared region for field measurements”, *IEEE Trans. Geosci. Remote Sens.*, 2012, doi:10.1109/TGRS.2012.2209891 (in press).

[6] A.M. Baldridge, S.J. Hook, C.I. Grove and G. Rivera, “The ASTER spectral library version 2.0”, *Remote Sens. Environ.*, vol. 113, no. 4, pp. 711–715, 2009, doi:10.1016/j.rse.2008.11.007.

[7] R. Niclòs, E. Valor, V. Caselles, C. Coll, and J. M. Sánchez, “In situ angular measurements of thermal infrared sea surface emissivity-Validation of models”, *Remote Sens. Environ.*, vol. 94, no. 1, pp. 83-93, 2005, doi: 10.1016/j.rse.2004.09.002.

[8] Y. H. Kerr, P. Waldteufel, J. P. Wigneron, J. M. Martinuzzi, J. Font, andM. Berger, “Soil moisture retrieval from space: The Soil Moisture and Ocean Salinity (SMOS) mission,” IEEE Trans. Geosci. Remote Sens., vol. 39, no. 8, pp. 1729–1735, Aug. 2001.

[9] T. Kawanishi, T. Sezai, Y. Ito, K. Imaoka, T. Takeshima, Y. Ishido,A. Shibata, M. Miura, H. Inahata, and R. W. Spencer, “The Advanced Microwave Scanning Radiometer for the Earth Observing System (AMSRE), NASDA’s constribution to the EOS for global energy and water cycle studies,” IEEE Trans. Geosci. Remote Sens., vol. 41, no. 2, pp. 184–194, Feb. 2003.

TABLES

TABLE I. Organic matter (OM) content, and textural and mineralogical features of the eleven IBS selected for the analysis.

Soil code	OM (%)	Textural classification (%)			Mineral classification (%)						
		S	L	C	Q	F	Fi	H	Ca	Gi	G
B	0.1	99	0.9	0.1	95.3	2.9	-	-	-	-	-
BR3	1.69	92	2	6	100	-	-	-	-	-	-
WS	0.21	100	0	0	1	-	-	-	-	-	99
LW03	0.73	77	18	5	53.7	46.3	-	-	-	-	-
BR2	1.47	69	15	16	82.3	16.8	0.8	-	-	-	-
LW52	1.71	62	15	23	58.4	32.2	9.4	-	-	-	-
LW13	1.61	51	35	14	76	16.7	4.8	2.6	-	-	-
F	3.5	50	30	20	19.9	4.5	4.1	8.7	62.9	-	-
BR1	2.93	40	6	54	37.9	-	-	13.1	-	49	-
LW45	1.15	29	54	17	72.4	23.4	4.2	-	-	-	-
C	8.9	20	43	37	29.4	5.5	9	-	56.1	-	-
D	4.5	14	50	35	19.3	3.5	6	8.9	62.3	-	-

Textural parameters S, L and C are percentages of sand, silt and clay, respectively. Mineralogical parameters Q, F, Fi, H, Ca, Gi and G are respectively percentages of quartz, feldspar, filosilicates, hematite, calcite, gibbsite and gypsum.

TABLE II. COEFFICIENTS p_0-p_4 OF POLYNOMIALS (3) AND (4) AT ALL SIX SPECTRAL CHANNELS. R^2 AND RMSE ARE ALSO INCLUDED

	a	**b $(m^3m^{-3})^{-1}$**	**c**	**d $(m^3m^{-3})^{-2}$**	**e $(m^3m^{-3})^{-1}$**	**f**	**a**	**b $(m^3m^{-3})^{-1}$**	**c**	**d $(m^3m^{-3})^{-2}$**	**e $(m^3m^{-3})^{-1}$**	**f**
	CH 1: 7.7-14.3 µm						**CH 4: 8.9-9.4 µm**					
p_0	0.998	-0.003	$16\cdot10^{-5}$	-0.03	0.0006	$-9\cdot10^{-6}$	1.001	-0.04	0.0003	0.03	0.03	$-1\cdot10^{-5}$
p_1	$2\cdot10^{-5}$	-0.0002	$-10\cdot10^{-5}$	0.0004	-0.0006	$4\cdot10^{-6}$	$3\cdot10^{-5}$	-0.0011	$14\cdot10^{-8}$	0.0019	0.0019	$-2\cdot10^{-7}$
p_2	-0.0007	0.003	$6\cdot10^{-5}$	-0.003	$-6\cdot10^{-5}$	$-7\cdot10^{-7}$	-0.0008	0.005	$4\cdot10^{-5}$	-0.004	$-13\cdot10^{-5}$	$-2\cdot10^{-8}$
p_3	$-3\cdot10^{-6}$	$3\cdot10^{-5}$	$12\cdot10^{-7}$	$-6\cdot10^{-5}$	$17\cdot10^{-6}$	$-7\cdot10^{-8}$	-410^{-6}	$6\cdot10^{-5}$	$-17\cdot10^{-8}$	$-10\cdot10^{-5}$	$-5\cdot10^{-7}$	$8\cdot10^{-9}$
p_4	$15\cdot10^{-5}$	$-7\cdot10^{-5}$	$-11\cdot10^{-7}$	$9\cdot10^{-5}$	$6\cdot10^{-7}$	$16\cdot10^{-9}$	$-16\cdot10^{-6}$	$-9\cdot10^{-5}$	$-8\cdot10^{-7}$	$9.6\cdot10^{-5}$	$2\cdot10^{-6}$	$5\cdot10^{-10}$
R^2	0.85	0.89	0.77	0.72	0.90	0.79	0.97	0.97	0.76	0.94	0.97	0.93
RMSE	0.004	0.018	0.0003	0.04	0.0004	$4\cdot10^{-6}$	0.002	0.018	0.0003	0.04	0.0004	$4\cdot10^{-6}$
	CH 2: 10.9-11.9 µm						**CH 5: 8.4-8.9 µm**					
p_0	0.998	-0.008	$13\cdot10^{-5}$	0.009	$16\cdot10^{-5}$	$-5\cdot10^{-6}$	0.996	0.010	0.0003	-0.12	0.0016	$-14\cdot10^{-6}$
p_1	0.003	0.006	$-11\cdot10^{-5}$	-0.03	-0.0003	$13\cdot10^{-7}$	$5\cdot10^{-5}$	-0.0011	$4\cdot10^{-7}$	0.002	$1.2\cdot10^{-5}$	$-16\cdot10^{-8}$
p_2	-0.0013	0.005	$6\cdot10^{-5}$	-0.004	$-6\cdot10^{-5}$	$-7\cdot10^{-7}$	-0.0006	0.003	$4\cdot10^{-5}$	0.0016	$-17\cdot10^{-5}$	$2\cdot10^{-7}$
p_3	$-5\cdot10^{-5}$	-0.0003	$12\cdot10^{-7}$	0.0011	$11\cdot10^{-6}$	$-11\cdot10^{-9}$	$-4\cdot10^{-6}$	$5\cdot10^{-5}$	$-3\cdot10^{-7}$	$-9\cdot10^{-5}$	$17\cdot10^{-7}$	$7\cdot10^{-9}$
p_4	$2\cdot10^{-5}$	$-7\cdot10^{-5}$	$-12\cdot10^{-7}$	$4\cdot10^{-5}$	$7\cdot10^{-7}$	$13\cdot10^{-9}$	$13\cdot10^{-6}$	$-6\cdot10^{-5}$	$-7\cdot10^{-7}$	$3\cdot10^{-5}$	$2\cdot10^{-6}$	$-3\cdot10^{-9}$
R^2	0.99	0.95	0.81	0.76	0.82	0.79	0.95	0.92	0.79	0.83	0.97	0.95
RMSE	0.0011	0.012	0.0002	0.04	0.0004	$3\cdot10^{-6}$	0.0019	0.02	0.0002	0.05	0.0004	$4\cdot10^{-6}$
	CH 3: 10.1-11.1 µm						**CH 6: 8.2-8.7 µm**					
p_0	0.999	-0.017	0.00011	0.018	0.0003	$-6\cdot10^{-6}$	0.992	0.066	$8\cdot10^{-5}$	-0.32	0.0024	$-17\cdot10^{-6}$
p_1	0.0012	0.015	$-3\cdot10^{-5}$	-0.04	-0.0006	$19\cdot10^{-7}$	$9.5\cdot10^{-5}$	-0.0017	$3\cdot10^{-6}$	0.004	$3\cdot10^{-6}$	$-13\cdot10^{-8}$
p_2	-0.0012	0.005	$6\cdot10^{-5}$	-0.004	$-6\cdot10^{-5}$	$-7\cdot10^{-7}$	-0.0003	-0.0006	$4\cdot10^{-5}$	0.011	-0.0002	$4\cdot10^{-7}$
p_3	$-6\cdot10^{-6}$	-0.0005	$-4\cdot10^{-7}$	0.0013	$18\cdot10^{-6}$	$-3\cdot10^{-8}$	$-7\cdot10^{-6}$	$8\cdot10^{-5}$	$-4\cdot10^{-7}$	-0.0002	$6\cdot10^{-7}$	$6\cdot10^{-9}$
p_4	$2\cdot10^{-5}$	$-6\cdot10^{-5}$	$-10\cdot10^{-7}$	$3\cdot10^{-5}$	$6\cdot10^{-7}$	$14\cdot10^{-9}$	$9\cdot10^{-6}$	-3·10-5	$-6\cdot10^{-7}$	$-4\cdot10^{-5}$	$2\cdot10^{-6}$	$-5\cdot10^{-9}$
R^2	0.97	0.96	0.74	0.83	0.87	0.73	0.99	0.98	0.84	0.99	0.98	0.94
RMSE	0.0017	0.011	0.0003	0.03	0.0004	$4\cdot10^{-6}$	0.0003	0.012	0.0002	0.02	0.0004	$4\cdot10^{-6}$

FIGURE CAPTIONS

Figure 1. Experimental ensemble used in the study for two simultaneous measurements at nadir (CE1) and at viewing direction (θ,φ) (CE2).

Figure 2. Angular variation of $\varepsilon_r(\theta)$, for θ=10°-70° at 10° intervals, for soil samples B, BR1, LW45 and F, as function of SM content for spectral channels 1, 3 and 5 of CE312-2. Uncertainty associated to $\varepsilon_r(\theta)$ is the standard deviation of 9 measurements (3 repetitions at a specific (θ,φ) configuration x 3 different φ angles). Legend of top left-corner graph can be applied to the other ones.

Figure 3. Validation of model represented by Eqs. (2), (3) and (4), comparing ε_{ri} values measured for samples samples BR3, LW03, BR2, LW13 and LW5 with those calculated from the model, at three spectral ranges. R^2, RMSE and BIAS values of the regression are also included in each plot.

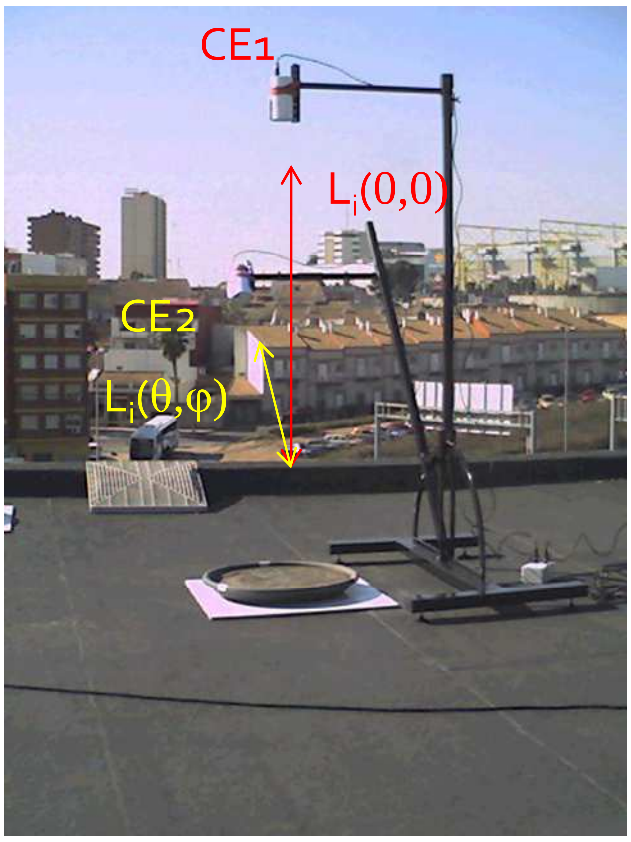

Figure 1.

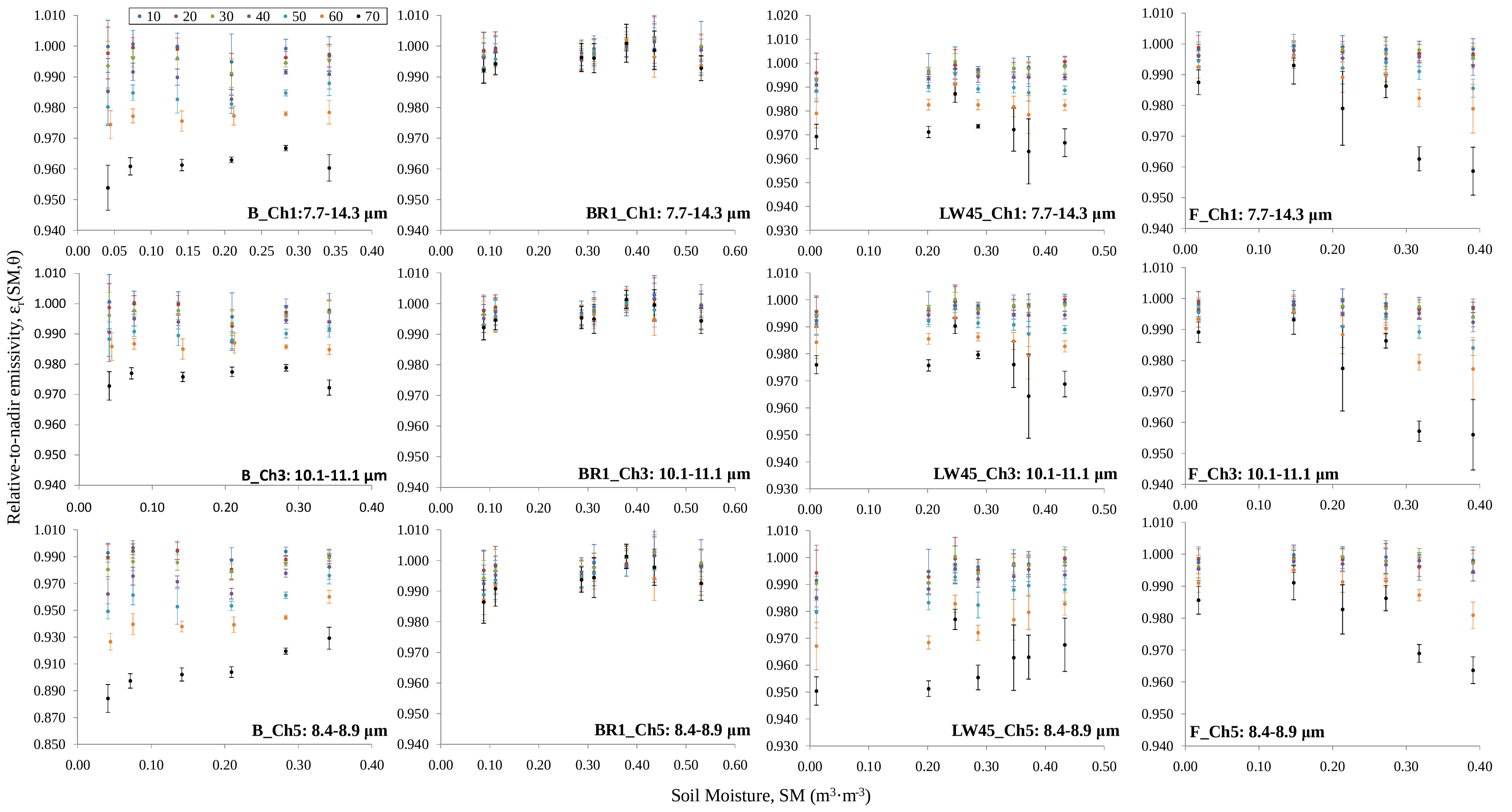
10
20
30
40
50
60
70
B_Ch1:7.7-14.3 µm
BR1_Ch1: 7.7-14.3 µm
LW45_Ch1: 7.7-14.3 µm
F_Ch1: 7.7-14.3 µm
B_Ch3: 10.1-11.1 µm
BR1_Ch3: 10.1-11.1 µm
LW45_Ch3: 10.1-11.1 µm
F_Ch3: 10.1-11.1 µm
B_Ch5: 8.4-8.9 µm
BR1_Ch5: 8.4-8.9 µm
LW45_Ch5: 8.4-8.9 µm
F_Ch5: 8.4-8.9 µm
Relative-to-nadir emissivity, εr(SM,θ)
Soil Moisture, SM (m3·m-3)

Figure 2.

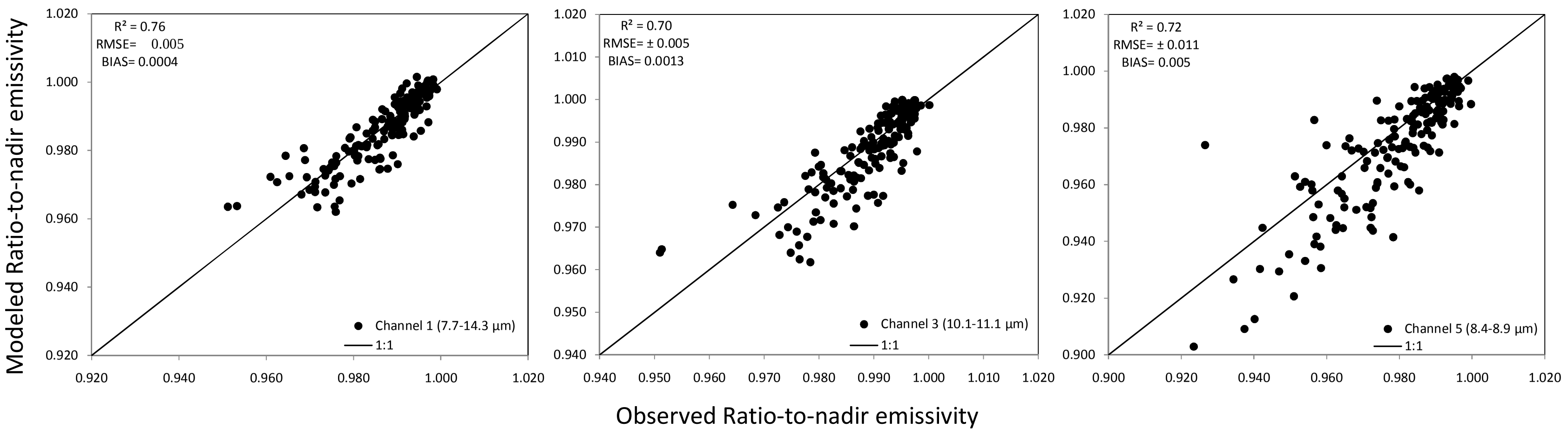
Modeled Ratio-to-nadir emissivity
Observed Ratio-to-nadir emissivity
R² = 0.76
RMSE= 0.005
BIAS= 0.0004
Channel 1 (7.7-14.3 µm)
1:1
0.920
0.940
0.960
0.980
1.000
1.020
R² = 0.70
RMSE= ± 0.005
BIAS= 0.0013
Channel 3 (10.1-11.1 µm)
1:1
0.940
0.950
0.960
0.970
0.980
0.990
1.000
1.010
1.020
R² = 0.72
RMSE= ± 0.011
BIAS= 0.005
Channel 5 (8.4-8.9 µm)
1:1
0.900
0.920
0.940
0.960
0.980
1.000
1.020

Figure 3.